Process-induced effects in material extrusion: From G-Code to printed polymer component

Zur Erlangung des akademischen Grades eines

Doktors der Ingenieurwissenschaften (Dr.-Ing.)

von der KIT-Fakultät für
Maschinenbau
des Karlsruher Instituts für Technologie (KIT)

angenommene

DISSERTATION

von

M.Sc. Felix Johannes Frölich
geb. in Bad-Dürkheim

Tag der mündlichen Prüfung:	05.12.2025
Hauptreferent:	Prof. Dr.-Ing. Luise Kärger
Korreferent:	Prof. Dr.-Ing. Thomas Hanemann

Abstract

Growing demands for functionality and efficiency require flexible and economical manufacturing technologies, particularly for complex components produced in small quantities. Material extrusion (MEX), an additive manufacturing process, offers great potential in this regard, enabling the tool-free production of application-specific, geometrically sophisticated components directly from digital models. However, the industrial application of MEX is challenged by the complex interplay between material behavior, process parameters, and machine-specific influences. This interplay, combined with the layer-by-layer material deposition, inherently produces anisotropic mechanical properties that are strongly dependent on material and process parameters, and may also result in process-induced defects such as poor strand adhesion or deformation.

This thesis addresses these challenges by developing experimental, analytical, and numerical methods to improve the predictive accuracy for MEX processes. The focus is on four central questions: (1) the effect of firmware interpretation of G-Code on real nozzle motion and local process conditions, (2) the reliable material characterization of components printed under real MEX conditions, (3) the consideration of structural anisotropy in process simulations of entire components, and (4) the coupling of simulations at the component level with high-resolution small-scale models in a multiscale framework.

The first part of the work involves developing a simulation framework that reconstructs real nozzle motion while considering firmware-specific motion planning, such as acceleration limits. The framework enables the quantification and analysis of deviations between the process conditions set in the slicer and the actual local conditions realized during printing. This capability allows process

simulations to incorporate the real implemented nozzle motion, improving the accuracy of predictions for process behavior and the resulting material and component properties.

The second part involves developing a standardized test procedure for mechanically characterizing PLA-based MEX components. Various specimen preparation methods are compared based on the reproducibility and representativeness of the determined mechanical properties. The results show that milled tensile specimens from printed plates are particularly suitable. Formulated recommendations provide a reliable basis for characterization and address inconsistencies in the literature.

The third part of the work maps the structural anisotropy typical of the process in simulations of entire components to predict process-induced deformation. To this end, a homogenization approach based on second- and fourth-order orientation tensors is developed. The local strand orientation is derived from the G-Code and converted into finite elements, which allows for realistic mapping of local stiffness distributions. Experimental investigations and numerical studies confirm the relevance of the considered effects.

The fourth part presents a multiscale simulation approach that couples process simulations at the component level with high-resolution small-scale models. Submodeling is used to transfer time-dependent boundary conditions from the large-scale simulation to local detail areas. This method is numerically verified and experimentally validated. This approach enables precise and still efficient prediction of local temperature profiles and local effects, such as interface strengths, within entire components.

Overall, this thesis contributes to the physic-based simulation of MEX processes. The developed methods enable more precise prediction of process-induced effects and lay the groundwork for efficient virtual process chains for designing and manufacturing customized polymer components.

Kurzfassung

Steigende Anforderungen an Funktionalität und Effizienz erfordern flexible und wirtschaftliche Fertigungstechnologien, insbesondere für komplexe Bauteile in kleinen Stückzahlen. Das Materialextrusionsverfahren (MEX) als additiver Fertigungsprozess bietet hierfür großes Potenzial, da es die werkzeuglose Herstellung geometrisch anspruchsvoller, anwendungsspezifischer Komponenten direkt aus digitalen Modellen ermöglicht. Die industrielle Nutzung von MEX wird jedoch durch die komplexe Wechselwirkung zwischen Materialverhalten, Prozessparametern und maschinenspezifischen Einflüssen erschwert. Dieses Zusammenspiel und der schichtweise Materialauftrag führen zwangsläufig zu anisotropen mechanischen Eigenschaften, die stark von Material- und Prozessparametern abhängen, und können zusätzlich zu prozessbedingten Fehlern wie unzureichender Stranghaftung oder Deformation führen.

Diese Arbeit adressiert diese Herausforderungen durch die Entwicklung experimenteller, analytischer und numerischer Methoden zur Verbesserung der Vorhersagegenauigkeit von MEX-Prozessen. Im Fokus stehen vier zentrale Fragestellungen: (1) die Auswirkung der Firmware-Interpretation von G-Code auf die reale Düsenbewegung und lokale Prozessbedingungen, (2) die zuverlässige Charakterisierung von Materialeigenschaften unter realen MEX-Prozessbedingungen, (3) die Berücksichtigung struktureller Anisotropie in Prozesssimulationen ganzer Bauteile zur Vorhersage prozessinduzierter Deformation, sowie (4) die Kopplung hochauflösender kleinskaliger Modelle mit Simulationen auf Bauteilebene in einem multiskaligen Framework.

Im ersten Teil wird ein Simulationsframework entwickelt, das die reale Düsenbewegung unter Berücksichtigung firmware-spezifischer Bewegungsplanung (z.B.

Beschleunigungsgrenzen) rekonstruiert. Es quantifiziert Abweichungen zwischen den im Slicer eingestellten Prozessbedingungen und den tatsächlich realisierten lokalen Bedingungen, sodass Prozesssimulationen die real implementierte Düsenbewegung berücksichtigen und Vorhersagen zu Material- und Bauteileigenschaften verbessern können.

Der zweite Teil widmet sich der mechanischen Charakterisierung PLA-basierter MEX-Bauteile. Verschiedene Probenpräparationsmethoden werden hinsichtlich Reproduzierbarkeit und Repräsentativität verglichen. Gefräste Zugproben aus gedruckten Platten liefern besonders zuverlässige Ergebnisse, die als Grundlage für Materialmodelle dienen und Inkonsistenzen in der Literatur adressieren.

Der dritte Teil der Arbeit widmet sich der Abbildung der prozesstypischen strukturellen Anisotropie in Prozesssimulationen ganzer Bauteile zur Vorhersage prozessinduzierter Deformation. Hierzu wird ein Homogenisierungsansatz entwickelt, der auf Orientierungstensoren zweiter und vierter Ordnung basiert. Die lokale Strangausrichtung wird aus dem G-Code abgeleitet und in finite Elemente überführt, wodurch lokale Steifigkeitsverteilungen realitätsnah abgebildet werden können. Experimentelle Untersuchungen und numerische Studien bestätigen die Relevanz der berücksichtigten Effekte.

Im vierten Teil wird ein multiskaliger Simulationsansatz vorgestellt, der Prozesssimulationen auf Bauteilebene mit hochauflösenden kleinskaligen Modellen koppelt. Mittels Submodellierung werden zeitabhängige Randbedingungen aus der großskaligen Simulation auf lokale Detailbereiche übertragen. Die Methode wird numerische verifiziert und experimentell validiert. Der Multiskalenansatz erlaubt die präzise Vorhersage lokaler Temperaturverläufe und Effekte wie Grenzflächenfestigkeiten innerhalb ganzer Bauteile.

Insgesamt liefert die Arbeit einen Beitrag zur physikalisch fundierten Simulation von MEX-Prozessen. Die entwickelten Methoden ermöglichen eine präzisere Abbildung prozessinduzierter Effekte und bilden die Grundlage für effiziente virtuelle Prozessketten zur Auslegung und Fertigung individualisierter Polymerbauteile.

Danksagung

Die vorliegende Arbeit entstand während meiner Tätigkeit als wissenschaftlicher Mitarbeiter am Institut für Fahrzeugsystemtechnik (FAST), Institutsteil Leichtbau, des Karlsruher Instituts für Technologie (KIT). Ohne die Unterstützung zahlreicher Personen und Institutionen wäre diese Dissertation in dieser Form nicht möglich gewesen. Ihnen allen gilt mein aufrichtiger Dank.

Mein besonderer Dank gilt meiner Referentin Frau Prof. Dr.-Ing. Luise Kärger für die vertrauensvolle Betreuung, die wertvollen Anregungen und die kontinuierliche Unterstützung während meiner Promotionszeit. Sie war jederzeit ansprechbar und hat sich immer die Zeit genommen, auch kurzfristig aufkommende Fragen zu besprechen und intensive fachliche Diskussionen zu führen, die mich inhaltlich und persönlich enorm weitergebracht haben. Ebenso danke ich Herrn Prof. Dr.-Ing. Thomas Hanemann für die Übernahme des Korreferats und seine hilfreichen Anmerkungen zur Arbeit.

Bei meinen Kolleginnen und Kollegen am FAST bedanke ich mich für die stets offene, freundschaftliche und produktive Zusammenarbeit, die mir den Alltag im Institut sehr bereichert hat. Besonders hervorheben möchte ich Florian Wittemann, Clemens Zimmerling, Constantin Krauß, Louis Schreyer und Lukas Hof, die mir jederzeit mit Rat und Expertise zur Seite standen. Ebenso gilt mein Dank Sarah Müller und Kevin Daiß, die durch ihren unermüdlichen Einsatz ein Forschen überhaupt erst möglich machen. Beide haben mit ihrer stets zuverlässigen Unterstützung viele organisatorische und technische Hürden aus dem Weg geräumt und damit wesentlich zum reibungslosen Ablauf meiner Arbeit beigetragen. Mein Dank gilt außerdem Alexander Jackstadt, der mich

bereits während meiner Masterarbeit am FAST betreute und mir so den Weg an das Institut eröffnete.

Darüber hinaus danke ich den Kolleginnen und Kollegen der Gruppe Hybride Werkstoffe und Leichtbau (HWL) des Instituts für Angewandte Materialien – Werkstoffe (IAM-WK), die entscheidend zum Gelingen dieser Arbeit beigetragen haben. Besonders möchte ich Benedikt Scheuring, Anselm Heuer und Wilfried Liebig danken, deren Unterstützung, Fachdiskussionen und Hilfsbereitschaft einen maßgeblichen Anteil am Fortschritt meiner Forschung hatten.

Ebenso möchte ich allen Studierenden danken, die mich im Rahmen ihrer Arbeiten unterstützt haben, insbesondere Jonathan Knirsch, Mario Emanuele Di Nardo und Andrea Posselt.

Für die finanzielle Unterstützung meiner Forschung danke ich der Deutschen Forschungsgemeinschaft (DFG), dem Ministerium für Wissenschaft, Forschung und Kunst Baden-Württemberg (MWK) sowie der Vector Stiftung.

Ein besonders herzlicher Dank gilt meinen Freunden, die mir über all die Jahre Rückhalt, Ausgleich und Freude gegeben haben. Vor allem meine WG und alle, mit denen ich in Karlsruhe zusammenwohnen durfte, darunter Jonas, Max, Matthias, Peter, Julia, Valentin und Armin, haben das Leben außerhalb der Arbeit geprägt und mir ein Zuhause geschaffen, in dem ich Kraft tanken konnte. Die gemeinsamen Erlebnisse, Gespräche und die enge Freundschaft haben entscheidend dazu beigetragen, dass ich diese intensive Zeit nicht nur bewältigen, sondern auch genießen konnte.

Von Herzen danken möchte ich meinen Eltern und meiner Schwester Anne. Sie haben mir nicht nur das Studium ermöglicht und mir den Weg geebnet, den ich gehen durfte, sondern mich in den vergangenen 31 Jahren als Mensch geprägt und zu dem gemacht, der ich heute bin. Ihre Liebe, ihre Geduld und ihr unerschütterlicher Rückhalt waren die Grundlage für alles, was ich erreichen konnte.

Gleichzeitig gilt mein größter Dank auch meiner Freundin Klara. Sie hat mit mir die Herausforderungen einer Fernbeziehung gemeistert und mir in allen Höhen

und Tiefen der Promotionszeit Rückhalt gegeben. Ihre Geduld, ihr Verständnis und ihre Unterstützung haben mich immer wieder aufgefangen, gerade in Phasen der Frustration. Sie hat mir nicht nur Halt gegeben, sondern auch den nötigen Ausgleich geschaffen, der es mir ermöglichte, meine Arbeit zu Ende zu führen. Ohne ihre Liebe, ihr Vertrauen und ihre unermüdliche Unterstützung wäre diese Dissertation in dieser Form nicht möglich gewesen.

Karlsruhe, September 2025 *Felix Frölich*

Contents

Acronyms and symbols

Acronyms

2D	Two-dimensional
3D	Three-dimensional
ABS	Acrylonitrile Butadiene Styrene
AM	Additive Manufacturing
ASTM	American Society for Testing and Materials
BC	Boundary Condition
CAD	Computer Aided Design
CLT	Classical Laminate Theory
CP	Center Point
CTE	Coefficient of Thermal Expansion
DC3D8	Linear isoparametric 3D element with 8 heat transfer nodes in ABAQUS
DED	Discrete Energy Deposition
DEM	Discrete Element Method
DIC	Digital Image Correlation
DOF	Degree Of Freedom
DMA	Dynamic Mechanical Analysis
DSC	Differential Scanning Calorimetry
eff	Effective

E	Element
FDM	Finite Difference Method
FEM	Finite Element Method
FE	Finite Element
FFF	Fused Filament Fabrication
FFT	Fast Fourier Transform
FVM	Finite Volume Method
G-Code	Geometric Code
H	Hypothese
hc	Homochiral
kNN	k-Nearest Neighbor
LPBF	Laser Powder Bed Fusion
MEX	Material Extrusion
MPM	Material Point Method
OT	Orientation tensor
p	Polymer
PLA	Polylactic Acid
PLLA	Poly-L-lactic
PDLA	Poly-D-lactic
PDLLA	Racemic PLA (formed when a mixture of L- and D-lactide is polymerized)
PiD	Process-Induced Deformation
R	Requirement
RMSE	Root Mean Square Error
RT	Room Temperature

RVE	Representative Volume Elements
sc	Stereo Complex
SEM	Scanning Electron Microscopy
SO	Special Orthogonal Group
SPH	Smoothed Particle Hydrodynamics
STL	Stereolithography
TMA	Thermomechanical Analysis
TRB	Thermal Reaction Bonding
TPS	Transient Plane Source
UMAT	Subroutine for user-defined material behavior in *ABAQUS/Standart*
UEXTENALDB	Pre/post-analysis data interface subroutine in *ABAQUS/Standart*
VOF	Volume-Of-Fluid Method
WJC	Waterjet Cutting

Scalars

α	Infill angle
α_{th}	Coefficient of thermal expansion (CTE)
β	Angle between the extrusion direction and the load direction
χ_{c}	Absolute crystallinity
ΔH_{m}	Absolute melting enthalpy
ΔH_{cc}	Absolute cold crystallization enthalpy
$\Delta H_{\mathrm{m}}^{\circ}$	Absolute melting enthalpy of $100\,\%$ crystalline polymer
$\Delta\varepsilon_{\beta}$	Change in length due to cold crystallization
$\Delta\varepsilon_{\gamma}$	Change in length due to entropy elasticity

δ	Junction deviation
$\tan\delta$	Loss factor
δT	Test function
ϵ	Emissivity coefficient
ϵ_{loc}	Local error
$\epsilon_{\mathrm{global,t}}$	Time averaged global error
$\epsilon_{\mathrm{global,s}}$	Spacial averaged global error
Γ_O	Boundary of a spatial domain
κ	Thermal conductivity
ν	Poisson ratio
Ω	Spatial domain
ϕ	Fraction of the material orientation under analysis
Φ	Fiber volume content
ρ	Mass density
ρ_{ref}	Reference mass density
ρ_{rel}	Relativ filling density
ρ_{specimen}	Mass density of a specimen
σ	Stephan-Boltzmann constant
Θ	Rotation angle of the global coordinate system
θ	Turning angle
ε	Engineering strain
$\varepsilon_{\mathrm{norm}}$	Normalized strain
$\varepsilon_{\mathrm{th}}$	Thermal strain
ξ	Strand orientation angle
$a_{\mathrm{fr}}^{\mathrm{pl}}$	Planar fractional anisotropy

a_{soft}	Softening coefficient
a_{N}	Nozzle acceleration
c_{p}	Specific heat capacity
$c_{\mathrm{p}}^{\mathrm{eff}}$	Effective specific heat capacity
d_{edge}	Additional distance at the edges of the plate due to the cutting method
d_{N}	Nozzle diameter
e_{width}	Extrusion width
E	Young's modulus
E'	Storage modulus
E''	Loss modulus
$E_{\mathrm{res}}^{\mathrm{direct}}$	Resulting Young's Modulus of a printed specimen
$E_{\mathrm{ori}}^{\mathrm{plate}}$	Measured Young's Modulus of a cut test specimen with strand orientation ori relative to the direction of loading
E_{0}^{plate}	Measured Young's Modulus of a cut specimen with strand orientation of 0° relative to the direction of loading
F_{tensile}	Tensile load
$f(\boldsymbol{x}, \boldsymbol{p})$	Orientation distribution function (ODF)
G	Shear modulus
h_{conv}	Convection coefficient
k	Extrusion multiplier
l_{height}	Layer height
m	Mass
n_{peri}	Number of perimeters
$n_{t_{\mathrm{inc}}}$	Time increment number
p_{mh}	Milling head velocity
Q	Heat

$\dot{q}$	Specific heat flow
$\dot{q}_{\mathrm{n}}$	Normalized specific heat flow
R	Theoretical curve radius
R_{contact}	Contact resistance
R_{m}	Tensile strength
T	Temperature
T_{amb}	Ambient temperature
T_{bp}	Build platform temperature
T_{c}	Crystallization temperature
T_{cc}	Cold crystallization temperature
T_{G}	Glass transition temperature
T_{m}	Melting temperature
T_{N}	Nozzle temperature
T_{poly}	Temperature in the surrounding polymer
T_{proc}	Processing temperature
T_{vitr}	Vitrification temperature
t	Time
t_{inc}	Time increment
$t_{\mathrm{inc}}^{\mathrm{out}}$	Time increment outside the submodel
$t_{\mathrm{inc}}^{\mathrm{sub}}$	Time increment inside the submodel
t_{layer}	Time required for printing one layer
t_{move}	Movement duration
t_{p}	Printing duration
s	Surface flux
s_{conv}	Heat flux caused by free convection

s_{rad}	Heat flux by radiation
s_{hp}	Heat flux into the component due to the heat of the print plate
s_{move}	Movement distance
$s_{\mathrm{poly}}^{\mathrm{cond}}$	Heat flux across Γ_O in surrounding polymer
s_{width}	Strand width
v_0	Initial velocity
v_1	Final velocity
v_{fr}	Feed rate
v_{infill}	Infill printing velocity
v_{junc}	Junction velocity
v_{nozzle}	Nozzle velocity
v_{p}	Printing velocity
v_{peri}	Perimeter printing velocity
$v_{\mathrm{t},m}$	Target printing velocity from segment m
$\dot{V}_{\mathrm{extrusion}}$	Extrusion rate (Slicer)
$\dot{V}_{\mathrm{poly}}$	Flow rate (Slicer)
$W(\boldsymbol{n})$	Directional strain energy response
w	Strain energy potential

Vectors

$\boldsymbol{a}_{\mathrm{max}}$	Maximum acceleration
$\boldsymbol{j}$	Jerk vector
$\boldsymbol{j}_{\mathrm{max}}$	Axis specific jerk limits
$\boldsymbol{p}$	Orientation vector
$\boldsymbol{u}$	Displacement vector

$\boldsymbol{v}$	Velocity vector
$\boldsymbol{v}_{\mathrm{junc},m}^{in/out}$	Entry/exit junction velocity vector from segment m
$\boldsymbol{x}$	spatial position

Tensors (second-order and fourth-order)

$\boldsymbol{\varepsilon}$	Logarithmic strain tensor
$\boldsymbol{\kappa}$	Thermal conductivity tensor
$\boldsymbol{\sigma}$	Cauchy stress tensor
$\boldsymbol{\sigma}_{\mathrm{el}}$	Elastic part of the cauchy stress tensor
$\boldsymbol{\sigma}_{\mathrm{ve}}$	Pseudo-viscoelastic part of the cauchy stress tensor
$\boldsymbol{A}$	Second-order orientation tensor
$\boldsymbol{I}$	Second-order identity tensor
$\boldsymbol{Q}$	Second-order rotation tensor
$\mathbb{A}$	Four-order orientation tensor
$\mathbb{A}_{\mathrm{pl}}$	Planar four-order orientation tensor
$\mathbb{C}$	Stiffness tensor
$\mathbb{C}_0$	Stiffness tensor below T_{vitr}
$\mathbb{C}_{\mathrm{inf}}$	Stiffness tensor above T_{vitr}
$\mathbb{C}_{\mathrm{iso}}$	Isotropic stiffness tensor
$\mathbb{C}_{\mathrm{ortho}}$	Orthotropic stiffness tensor
$\mathbb{I}$	Fourth-order identity tensor
$\mathbb{I}^{\mathrm{S}}$	Identity on symmetric second-order tensors
$\mathbb{P}_1, \mathbb{P}_2$	Isotropic projection operators

Operators, math symbols and additional notations

$\mathbb{A}[\boldsymbol{B}]$	Mapping of a 2nd-order tensor by a 4th-order tensor, i.e. $(\mathbb{A}[\boldsymbol{B}])_{ij} = A_{ijkl}B_{kl}$
$\mathrm{tr}(\bullet)$	Trace, e.g. $\mathrm{tr}(\boldsymbol{A}) = A_{ii}$
$\| \bullet \|$	Frobenius norm, e.g. $\|\boldsymbol{A}\| = \sqrt{\boldsymbol{A} : \boldsymbol{A}}$
$\cdot$	Scalar product, e.g. $\boldsymbol{A} \cdot \boldsymbol{B} = A_{ij}B_{ij}$
$:$	Frobenius scalar product, e.g. $\boldsymbol{A} : \boldsymbol{B} = A_{ij}B_{ij}$
$\otimes$	Dyadic product, e.g. $\boldsymbol{n} \otimes \boldsymbol{n} = n_i n_j$
$\square$	Product between second-order tensors: $(\boldsymbol{A} \square \boldsymbol{C})\boldsymbol{B} = A_{ik}B_{kl}C_{lj}$
$\star$	Rayleigh product: $\boldsymbol{Q} \star \boldsymbol{A} = \boldsymbol{Q}\boldsymbol{A}\boldsymbol{Q}^\top$ with $\boldsymbol{Q} \in \mathrm{Orth}^+$
$(\bullet)^{n\otimes}$	Dyadic product repeated n times to form an nth-order tensor
$\langle \bullet \rangle_{\mathcal{S}}$	Averaging over surface $\mathcal{S}$

Remark on attributions. Excerpts of this work have been previously published as manuscripts [1–4] with my significant personal contribution as lead author. This is indicated by footnotes with attributions to the original publication and further details in the beginning of applicable sections of this work. Reproduced paragraphs or sections are explicitly noted and have been modified only marginally due to the notation and structure of this work. Sections that are based on the original publication but where the text has been adapted are marked accordingly. The footnotes to the corresponding publications are numbered in the order in which they appear to provide a consistent reference.

1 Introduction

In an era of increasing product personalization, manufacturing systems must balance flexibility and efficiency. Customers increasingly demand tailored solutions in sectors such as medical technology, aerospace, and consumer goods. This trend is driving the shift toward mass customization, which combines the efficiency of mass production with the adaptability of individual manufacturing [5, 6] and enables companies to offer customized products economically [7, 8]. However, realizing this potential requires flexible manufacturing technologies that ensure consistent product quality. Additive Manufacturing (AM) offers promising capabilities in this regard [9, 10]. By building components layer by layer directly from digital models, AM enables the production of complex geometries, functionally integrated structures, and individualized components without the need for tool-specific setup. As such, AM is particularly suited for cost-effective manufacturing of customer-specific products in small batches, even down to single-piece production [11].

One well-established AM process is material extrusion (MEX), in which a thermoplastic polymer is deposited layer by layer along predefined paths [12]. The process stands out for its simple machine technology, low material costs, and comparable minimal safety requirements. These advantages make it highly attractive for an efficient implementation across various industries, particularly for customized components [11].

Despite these strengths, the industrial application of MEX faces significant challenges: Numerous adjustable process parameters, such as extrusion temperature, print velocity, and path strategies, directly influence component quality [13]. The complex interplay between these parameters, material behavior,

and machine-specific influences can lead to process-induced defects, such as poor strand adhesion [14] or process-induced deformation (PiD) [15], also known as warping, which may ultimately result in print failure [16, 17]. Moreover, the layer-by-layer deposition creates a characteristic mesostructure, defined by strand orientation, interlayer bonding, and voids [18, 19]. This structure induces significant anisotropy in mechanical properties, which depend heavily on material and process parameters [14, 20, 21]. To address these challenges during manufacturing, the process is often adjusted using trial and error, a method that is inefficient, especially for customer-specific tasks, and does not guarantee optimal results. This underscores the need for both experimental and simulation-based approaches across multiple scales to reliably predict process outcomes and develop robust process design methods.

Many experimental studies have investigated how different process parameters affect material properties in MEX [14, 20, 21]. However, considerable variation in the reported results complicates comparability between studies and limits the transferability of material data from coupon-level specimens to real printed components.

To predict process-related effects using simulation methods, various models have been proposed in the literature, each addressing specific aspects of the MEX process. Microscale approaches focus on polymer melt flow near the nozzle, capturing effects such as air inclusions or additives [22, 23]. On a higher level, mesoscale models explicitly represent the typical material structure, including voids and strand geometries [24–26], and are suitable for predicting local temperature profiles, crystallization, and welding processes between strands [27, 28]. Macroscale simulations represent the entire component in a homogenized form and are suited for predicting PiD [29, 30]. However, at this scale, mesostructural anisotropy, particularly the directional dependence of mechanical properties, is often simplified or neglected. As expected, locally altered mesostructures affect deformation behavior during manufacturing, highlighting a key research gap. Moreover, macroscale models cannot accurately capture local effects like interfacial strength or crystallization, which depend on local thermal history and mesostructure. These can only be adequately represented

with high-resolution mesoscale models. Yet, consistent multiscale coupling remains a major challenge. Existing approaches are typically limited to transferring effective stiffnesses from idealized mesostructures, failing to reflect the complex structural effects in real components [31].

In addition, machine-specific influences are often overlooked. Printer firmware translates the given machine code (G-Code) into actual machine movements. Parameters such as acceleration limits and motion smoothing can alter the nozzle velocity, affecting local process conditions and thus the resulting component quality [32,33]. Most current simulation approaches do not consider this aspect.

Building on the research gaps outlined above, this thesis aims to enable more accurate predictions of process-induced effects and poses the following key research questions:

1) How does the firmware's interpretation of G-Code affect the nozzle motion in the MEX process and the resulting local process conditions?

2) How can material properties be reliably characterized under realistic MEX processing conditions?

3) How can mesostructure-induced anisotropy be effectively captured in homogenized macroscopic process simulations?

4) What constitutes a suitable multiscale simulation framework that couples high-resolution mesoscale models with component-level simulations?

The following Chapter 2 provides an overview of the fundamental principles and current state of research related to the MEX process. It covers characteristic mesostructures, the material behavior of MEX-manufactured components, and simulation approaches at the micro-, meso-, and macroscale. Additionally, it addresses firmware-related influences on nozzle motion. Based on this analysis, key research gaps are identified, which form the foundation for the objectives and structural outline presented in the subsequent Chapter 3.

2 Fundamentals and state of research

2.1 Material extrusion process (MEX)

Additive Manufacturing (AM) is a group of manufacturing processes that build components directly from 3D digital models by adding material in layers. In contrast to subtractive processes, where material is removed (e.g. milling), or formative processes (e.g. injection molding), AM is based on an additive build-up principle. This allows for a high degree of design freedom, the creation of complex geometries, and resource-efficient production because only the material needed is used. [12, 34]

Material extrusion (MEX) is one of the seven main categories of additive manufacturing as defined by the American Society for Testing and Materials (ASTM) [12]. If the feedstock for MEX is a thermoplastic material, the material is joined by thermal reaction bonding (TRB) and the process is referred to as MEX-TRB/pASTM/ISO529002021. The p stands for polymer. In the further course of the work, the term MEX-TRB/p is abbreviated to MEX.

In MEX, a feedstock is selectively extruded through a nozzle or orifice and deposited layer by layer. Figure 2.1 shows a schematic illustration of a MEX system. The extrudate is deposited onto a build platform or onto previously deposited material. The previously extruded material is melted by the newly extruded material, creating a bond that forms the process-typical interfaces between adjacent extruded strands. For large overhangs, additional support structures can be added at appropriate locations. The feedstock is melted in

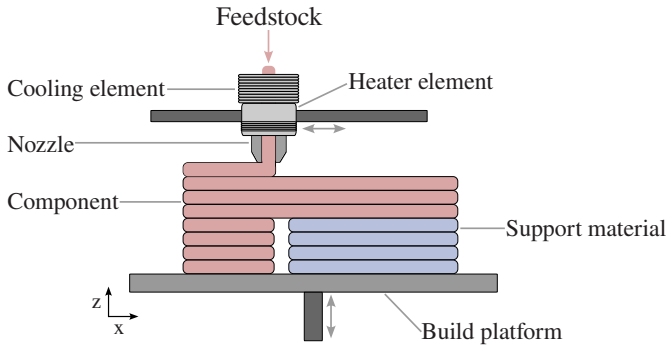

Figure 2.1: Schematic illustration of a MEX system.

a heating system. To prevent the feedstock from overheating before entering the heater, a cooling element is usually installed between the heater and the feedstock inlet. Depending on the system, the build platform may be heated or unheated, and some machines include an additional heated build chamber. Some specialized systems also provide advanced process and material handling features, such as multi-material printing or adaptive zone heating.

The feedstock can be provided as pellets or filament. When provided as thermoplastic filament, the process is called Fused Filament Fabrication (FFF) and has been commercialized under the name Fused Deposition Modeling. In addition to pure thermoplastics, composite materials can also be processed. Short fiber reinforced filaments and pellets with carbon, glass or aramid fibers are commercially available. MEX can also be used to produce structures with local continuous fiber reinforcement. The movement of the nozzle along the x and y axes and the relative movement of the build platform and the nozzle along the z axis allows the production of a component based on a given 3D digital model.

2.1.1 Process chain

A typical MEX process chain is shown in Figure 2.2.

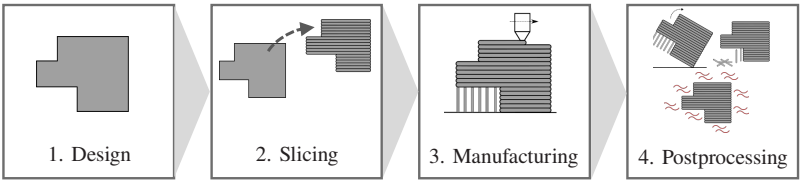

Figure 2.2: Schematic representation of the MEX process chain. Component design (1), slicing and process parameter definition (2), manufacturing (3), and various post-processing steps (4).

It can be described as follows [34]:

1. **Design:** Creation of the component design using CAD software. In most slicer programs, the component geometry is transferred in STL format, which only contains information about the outer contour of the component. However, some slicers can also transfer step files or other formats.

2. **Slicing:** The design is sliced into individual layers, the nozzle trajectory within these layers is defined using a slicer software. The information about the nozzle path and the process parameters are transmitted to the printer in the form of a G-Code. The contour is followed by any number of paths to create the shape of the component. How the inner component (infill) is constructed can be freely defined. The infill is essentially determined by its density, orientation, and general pattern shape. Figure 2.3 shows three examples of infill patterns with different infill densities. The infill angle α and perimeter are highlighted.

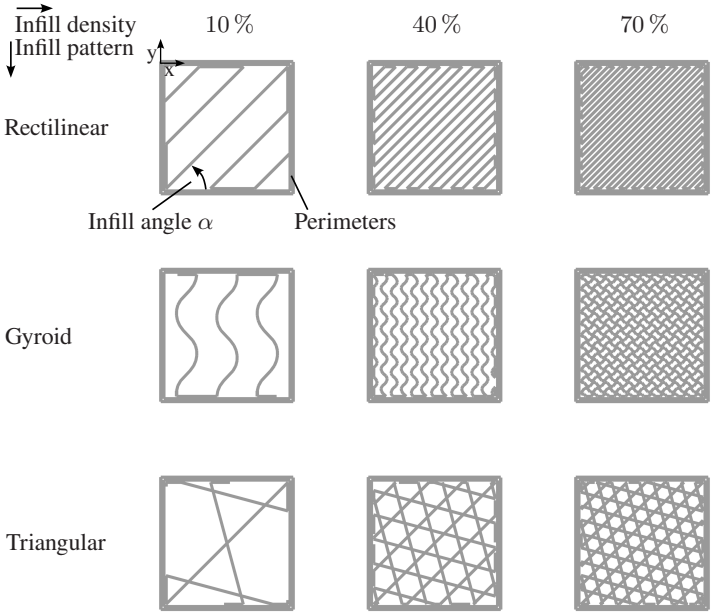

Figure 2.3: Three examples of infill patterns with different infill densities. The fill angle α and the perimeter are highlighted.

3. **Manufacturing:** The firmware interprets the G-Code according to printer-specific constraints such as possible nozzle velocity, acceleration, and cornering. The limitation of cornering is described by the so-called jerk. In physics this refers to the maximum change of acceleration per unit of time (the third derivative of position). In many 3D printer firmwares the term is used differently and usually defines the maximum allowed velocity change at a corner without requiring an intermediate deceleration. There are various firmware solutions, some of which are available as open source and some of which build on each other. Depending on the firmware used, the jerk is interpreted differently and thus influences the actual movement of the printhead in curves. The printer then builds the component according to the specifications in the G-Code.

4. **Post-Processing:** The component is detached from the build platform and the support structures are removed. The printed component can then be finished in a variety of ways. For example, it can undergo surface treatment or annealing to improve thermal stability or mechanical properties.

2.1.2 Factors affecting component quality

The resulting component quality combines not only the thermal and mechanical properties but also the dimensional accuracy [13]. This in turn determines the overall manufacturability. The quality of the manufacturing result is determined by a large number of influencing factors. The most important ones are summarized in the Ishikawa diagram in Figure 2.4 [35, 36]. The selected ma-

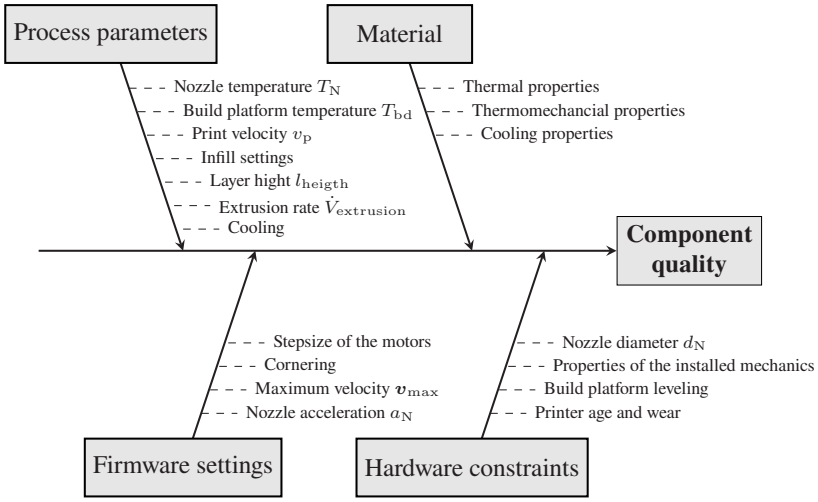

Figure 2.4: Ishikawa diagram with the most important parameters that influence the resulting quality of a MEX component [35, 36].

terial largely determines the resulting specific component properties. Thermal properties such as heat conductivity and heat capacity, as well as thermomechanical properties such as stiffness and thermal expansion, are crucial for the performance and reliability of the final component [13]. However, material- and component-specific convection and radiation effects during the process can influence the final component quality and dimensional accuracy [15]. After material definition, the process parameters set in the slicer have the most significant impact on component properties and quality. In particular, the nozzle temperature T_{N} and build platform temperature T_{bp}, the selected infill, and the layer height l_{height} should be mentioned here [13]. The infill density, infill angle α, and infill pattern have an enormous influence on the subsequent thermal and mechanical properties [14]. The printing velocity v_{p} and the settings of a cooling system (e.g. fans) can also be predefined and influence the process and the component quality. The process parameters set in the slicer are interpreted by the printer-specific firmware before printing starts. This firmware translates the G-Code, considering the firmware settings. The resulting nozzle movement is directly influenced by these settings. The maximum possible axis velocities $\boldsymbol{v}_{\mathrm{max}}$, the given nozzle acceleration a_{N}, and the possible cornering therefore have a direct influence on the process conditions and the resulting component quality [32]. Another important factor is the diameter of the nozzle d_{N} installed in the printer. This is specified as a parameter in the slicer, but can usually be changed. There are also variables that are directly related to the mechanics of the components installed in the printer, whose influence on component quality can vary depending on the printer. An example of this is the stiffness of the individual printer components. In addition, the general condition of the printer plays a role. Increasing age and mechanical wear can reduce reproducibility and lead to deviations in the dimensional accuracy of the manufactured components. Furthermore, the quality of the build platform leveling is critical, since even small misalignments between nozzle and platform can cause adhesion problems and irregularities in the first layers, which in turn propagate throughout the component. These hardware-related aspects, together with the material, process, and firmware parameters, therefore represent practical constraints that must be considered in order to ensure consistent component quality.

2.1.3 Typical process errors

Apart from the many factors that influence component quality, there are additional reasons why a printing process may not be considered successful. One key factor is process-induced deformation (PiD), often referred to as warpage. PiD arises during the MEX process due to complex thermomechanical interactions. As the molten polymer is extruded and deposited layer by layer, it undergoes rapid cooling and solidification [37]. This transition is accompanied by thermal expansion during heating and shrinkage during cooling, which leads to internal stresses. These stresses are often unevenly distributed due to temperature gradients across the component and the sequential nature of layer deposition. Additionally, anisotropic thermal conductivity of the material and the lack of uniform support during printing can exacerbate deformation. The accumulation of these effects results in warping or dimensional inaccuracies, particularly in regions with large overhangs or insufficient adhesion to the build platform. [15, 17]. This phenomenon is particularly pronounced in semi-crystalline polymers due to their crystallization behavior, but it can also occur in amorphous thermoplastics depending on the specific material.

Figure 2.5 provides a schematic representation of these mechanisms during the MEX process. As the extruded filament is deposited, the temperature distribution within the component (illustrated from blue to red) gives rise to thermal gradients. Heat is dissipated through conduction, convection, and radiation, which drive different cooling rates across the layers. As shown, thermal shrinkage (orange arrows) and solidification shrinkage (green arrows) occur during different stages of cooling and both contribute to internal stress formation. These shrinkage phenomena act together to generate residual stresses that can result in deformation. The spatial and temporal variation in shrinkage leads to complex stress distributions, particularly in the lower layers where accumulated shrinkage and restricted movement can cause PiD, as indicated by the arrows. This illustration highlights the dynamic interplay between temperature evolution and material behavior, which ultimately governs the onset and severity of PiD.

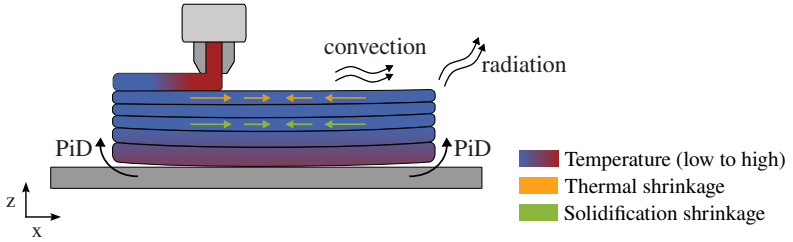

Figure 2.5: Schematic illustration of process-induced deformation (PiD) mechanisms during the MEX process. The extruded polymer experiences rapid cooling after deposition, leading to thermal gradients and uneven shrinkage across layers. Heat dissipation occurs through conduction, convection, and radiation. Thermal shrinkage (orange arrows) and solidification shrinkage (green arrows) contribute to residual stress formation and component deformation. The PiD arrows indicate typical deformation behavior due to the accumulated stresses, especially in the lower layers.

PiD can result in failure to achieve the required dimensional accuracy of the finished component, which is particularly problematic for high-precision applications. In addition, PiD can cause serious problems during the printing process. A typical problem is component detachment from the build platform (cf. Figure 2.5), causing the printing process to stop prematurely [17]. Similarly, if PiD accumulates during printing, the nozzle can collide with the component [16]. Such collisions can not only interrupt the printing process but also cause damage to the nozzle or the component itself.

Another known problem is the inadequate bonding of adjacent strands [14]. If process control is not optimized, there may be insufficient fusion between the individual strands. This results in reduced mechanical strength of the component and can significantly affect its functionality and durability in later use [14]. A more detailed discussion of the thermal and mechanical properties of MEX components and the influence of the process parameters described is given in Section 2.4.

2.1.4 Used printer systems

The printers used in this work for characterization and validation are the *Ultimaker 2+* from *Ultimaker*, the *Prusa Mini* from *Prusa3D*, and the *Composer A4* from *Anisoprint*. All are FFF systems and therefore use filament as feedstock. The printers are briefly described below. The selected process parameters are specified in the corresponding sections.

Ultimaker 2+ This printer system can process unreinforced and short fiber-reinforced thermoplastic filaments with processing temperatures ranging from $180\,^{\circ}\mathrm{C} - 260\,^{\circ}\mathrm{C}$. The build volume is $223\,\mathrm{mm} \times 223\,\mathrm{mm} \times 205\,\mathrm{mm}$. The *Ultimaker 2+* has a heated build platform and the standard glass build platform has been replaced by a *FilaPrint* build platform from *Filafarm*. The *Ultimaker 2+* firmware is based on *Marlin* with some proprietary customizations. The firmware is open source and the source code can be found on *GitHub* in the official *Ultimaker* repository [38]. The jerk parameter and motion control are configurable in the firmware. Table A.1 in Appendix A.1 lists the firmware settings that were set at the time of use.

Prusa Mini The *Prusa Mini* is a compact extrusion-based printing system capable of processing both unreinforced and short-fiber-reinforced thermoplastic filaments at temperatures up to $280\,^{\circ}\mathrm{C}$. It offers a build volume of $180\,\mathrm{mm} \times 180\,\mathrm{mm} \times 180\,\mathrm{mm}$ and includes a heated build platform equipped with a flexible spring steel sheet coated with PEI, which can be heated up to $110\,^{\circ}\mathrm{C}$. The firmware is derived from *Marlin* and has been extensively modified by *Prusa Research*. The open-source code is available in the official *Prusa3D GitHub* repository [39]. Motion control parameters, including jerk, are adjustable. Table A.2 in Appendix A.1 provides the firmware settings used.

Composer A4 In addition to unreinforced and short fiber-reinforced structures, the printer can also print locally continuous fiber-reinforced structures.

Thermoplastics with a processing temperature of up to $270\,^{\circ}\mathrm{C}$ can be processed. The build volume is $297\,\mathrm{mm} \times 210\,\mathrm{mm} \times 140\,\mathrm{mm}$. The *Anisoprint Composer A4* features a heated build platform. The standard glass build platform has been retained. The *Composer A4* uses a customized version of the *MK4duo* firmware developed specifically for the requirements of this printer. The *MK4duo* firmware is an evolution of the *Marlin* firmware and offers advanced features optimized for *Anisoprint's* Composite Fiber Coextrusion (CFC) process. The firmware source code is open source and can be found on *GitHub* [40]. Table A.3 in Appendix A.1 lists the firmware settings that were set at the time of use.

2.2 Polylactic Acid (PLA)

Polylactic Acid (PLA) is one of the most commonly used materials in MEX due to its ease of processing, biodegradability and good mechanical properties. PLA is mainly used for prototyping and modeling, but is increasingly used for functional components. In this work, PLA filament is used as an application example for the developed methods and models as well as for their validation. The chemical structure of PLA and its general thermal, mechanical and kinetic properties are described below. Finally, the material Ultrafuse PLA black from *forwardAM* used in this work is presented.

2.2.1 Chemical structure and its variants

PLA is a bio-based polymer produced by the polymerization of lactic acid (lactide). PLA consists of long macromolecules that repeat the monomers of lactic acid ($\mathrm{C_3H_6O_3}$). Lactic acid can exist in two isomeric forms: L-lactide and D-lactide. These isomers determine the structure and properties of the resulting polymer: Poly-L-lactide (PLLA) is formed by the polymerization of L-lactide, Poly-D-lactide (PDLA) by the polymerization of D-lactide. They are semi-crystalline and have comparable properties due to their enantiomerism.

In most applications, however, PLA is not used as a homopolymer because of the high cost. Instead, a copolymer PLA is produced and processed. In this case, a PDLLA copolymer is formed when a mixture of L- and D-lactide is polymerized. In this copolymer, the molecular structure is mainly based on L-lactic acid with a certain amount of D-lactic acid monomers. As the content of D-lactic acid increases, the crystallizability of PDLLA decreases [41]. PDLLA with a D-lactic acid content of more than $8\,\mathrm{mol}\%$ is considered completely amorphous, while PDLLA with a D-lactic acid content between $4\,\mathrm{mol}\%$ and $8\,\mathrm{mol}\%$ is classified as very slow crystallizing.

The properties of the PLA types depend on the molecular weight, molecular structure (e.g. linear/branched) and molecular configuration (e.g. D-lactic acid fraction) [42, 43]. All these factors influence the melting properties of PLA, crystallization kinetics, processability and mechanical properties of the material. In general, the homopolymers PLLA and PDLA have better thermal stability and strength than the copolymer PDLLA due to their higher potential crystallinity. Therfore, PDLLA is more compliant (cf. following Subsection 2.2.2).

When PLLA and PDLA are mixed in a 1:1 molar ratio to form a PLLA/PDLA blend, stereocomplex PLA (sc-PLA) can be generated [42]. In this case, the two homopolymers form stable stereochemical structures in which the enantiomeric monomers of PLLA and PDLA are incorporated into stereocomplex (sc) crystals in a highly regular, alternating arrangement. This stereocomplex structure is more thermodynamically stable than the homochiral (hc) crystals of PLLA or PDLA, resulting in higher thermal stability and improved mechanical strength. Due to these properties, sc-PLA is particularly advantageous for applications requiring high thermal and mechanical stress. However, its production is significantly more expensive than that of the copolymer PDLLA [42].

2.2.2 Properties of PLA

Homopolymers of PLA have a tensile strength of approx. $50\,\mathrm{MPa} - 70\,\mathrm{MPa}$, a tensile modulus of $2.7\,\mathrm{GPa} - 4.2\,\mathrm{GPa}$, an elongation at break of $2\,\% - 10\,\%$ [42, 44–47]. According to Perego et al. [43], the differences in the measured properties can be attributed to the molar mass and the degree of crystallinity of the test specimens. The degree of crystallinity depends heavily on the processing of the PLA. The results in [43] show that injection-molded specimens exhibit only a crystallinity of $3\,\% - 9\,\%$ depending on the molar mass. Subsequent annealing of the specimens yielded a degree of crystallinity of $70\,\%$. This shows the slow crystallization kinetics of PLA compared to other thermoplastics. PLLA and PDLA and PDLLA differ in their mechanical properties mainly due to their different crystallinities.

According to Zhang et al. [48], the glass transition temperature T_G of the homopolymer PLLA ranges from approximately $49\,^\circ\mathrm{C}$ to $68\,^\circ\mathrm{C}$, depending on the molar mass. For the copolymer PDLLA, they measured T_G slightly lower, at approximately $43\,^\circ\mathrm{C}$ to $61\,^\circ\mathrm{C}$. In both cases, T_G increases systematically with increasing molar mass. [48]

The thermomechanical properties of PLA materials depend strongly on the degree of crystallinity. Amorphous PLA exhibit a significant loss of stiffness and strength above T_G, whereas semi-crystalline specimens show enhanced heat resistance and improved mechanical performance [49]. Figure 2.6 schematically illustrates the storage modulus E' of quenched (nearly amorphous) and annealed semi-crystalline PLLA as a function of temperature. The sharp drop in the modulus of amorphous PLLA above T_G and the subsequent increase due to cold crystallization are clearly visible. In contrast, crystalline PLA shows no such increase, as crystallization has already occurred, and the modulus remains significantly higher across the entire temperature range.

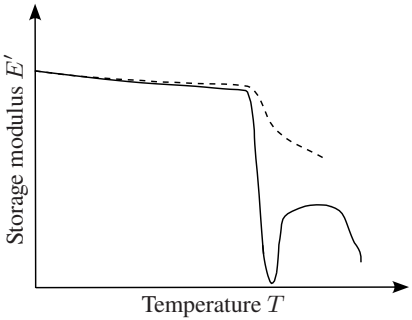

Figure 2.6: Schematic representation of the storage modulus E' over temperature for a quenched and thus almost amorphous PLLA (solid line) and an annealed PLLA (dashed line). (Adapted from [49])

2.2.3 Filament used in this work

The material used is the commercial Ultrafuse PLA filament in black from *forwardAM* [50]. The recommended processing parameters and selected material properties, shown in Table 2.1, are specified in [50]. *forwardAM* does not explicitly state which PLA types are involved. Furthermore, the manufacturer does not provide information about the molecular mass or the precise chemical composition of the PLA used, such as whether it is PLLA, PDLA, or

Table 2.1: Recommended processing parameters and selected material properties of *forwardAM* Ultrafuse PLA filament [50].

Process parameter	**Value**	**Unit**
Nozzle temperature T_N	210 - 230	$^\circ\mathrm{C}$
Build platform temperature T_bp	50 - 70	$^\circ\mathrm{C}$
Nozzle diameter d_N	≥ 0.4	mm
Printing velocity v_p	40 - 80	$\mathrm{mm/s}$
Density ρ	1248	$\mathrm{kg/m^3}$
Glass transition temperature T_G	61	$^\circ\mathrm{C}$
Melting temperature T_m	151	$^\circ\mathrm{C}$

PDLLA with a specific D-lactide content. This lack of detail makes correlating mechanical and thermal material properties with values found in the literature difficult, as these values can vary significantly depending on the polymer structure, molecular mass, and the presence of additives such as pigments (cf. Section 2.2.2), since pure PLA is typically whitish in appearance.

2.3 MEX typical material structure

Components manufactured by MEX consist of layers divided into an outer perimeter and an inner infill area. The orientation and arrangement of the strands differ depending on the type of area. In the perimeter, the strands follow the component surface because they determine the component's outer geometry and volume [51]. In contrast, the infill can be designed flexibly. The orientation of the printing paths can be adjusted by selecting specific process parameters. While the perimeter is printed with a filling degree of almost $100\,\%$, a lower density is often used inside to reduce weight or production time [52]. This creates defined cavities inside the component that influence its mechanical and thermal properties. The material structure is characterized by interfaces between adjacent strands and cavities. These lead to the overall porosity of the structure typical for this process [14, 52, 53].

The resulting material structure is significantly influenced by the selected strand orientation, the layer thickness, and other process-specific parameters such as temperature and printing velocity. Figure 2.7 shows a typical MEX material structure for a unidirectional trajectory along the x-axis with a nominal infill density of $100\,\%$. Figure 2.7a shows a schematic structure and Figure 2.7b a microscopic image of the cross-section in the y-z plane. The process parameters used influence not only the shape of the strands themselves, but also their relative arrangement. Insufficient fusion can lead to interfaces between adjacent strands, which represent potential weak points [14]. A distinction is made between interfaces within the same layer (intralayer, IV) and those between layers lying on top of each other (interlayer, III), as shown in Figure 2.7b. Since the degree

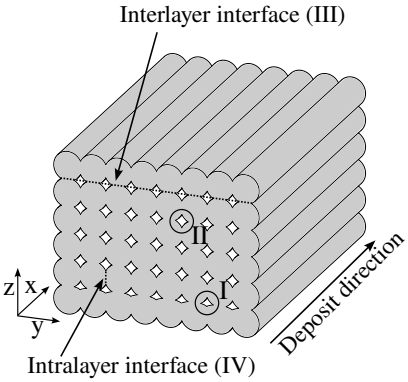

(a) The illustration highlights various structural elements and their positions within the layered arrangement. It depicts triangular (I) and diamond-shaped (II) voids located between the layers, as well as the interfaces that exist between the layers (III) and those found within the layers themselves (IV)

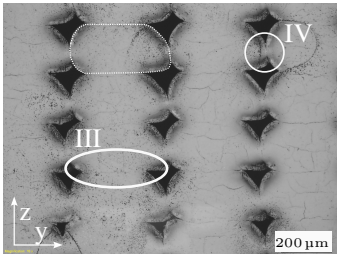

(b) Microscopic view of the MEX structure analyzed in this study. A pronounced neck formation is visible between the layers at the interlayer bonding interfaces (III), while a smaller neck formation can be observed between adjacent strands within the layers at the intralayer bonding interfaces (IV).

Figure 2.7: Typical MEX material structure for a unidirectional trajectory along the y-axis. (Reproduced from [1])

of fusion and the contact area differ in both cases, the strength and stiffness also vary locally. Another key aspect is the voids between the strands, which are also marked in Figure 2.7a (I and II). Depending on the filling strategy, these voids can have different geometries, which affects the local stress peaks and thus the failure behavior.

In addition to the geometric arrangement, the process control also affects the material behavior within the strands. For example, it influences the crystallinity of the polymer and, in the processing of fiber-reinforced filaments, also the fiber orientation [54, 55]. In continuously reinforced systems, the infiltration of the fibers also depends heavily on the process used [56].

The process-typical material structure described above leads to the well-known anisotropy of the mechanical properties [14], which has been described in many publications (cf. Section 2.4.2). Due to the large number of process parameters and the complex interaction between trajectory, material properties and cooling

conditions, there is a wide range of possible material structures, which makes the mechanical evaluation of printed components difficult.

As discussed, the material structure is influenced by the process control on different length scales. The resulting properties can therefore also be observed on different size scales. For example, the influence of the process control on the resulting interface strength between two adjacent strands or on the resulting strength of the entire component can be examined. In the following, a scale separation is introduced in order to be able to classify the size scales considered in the further course of the work. Figure 2.8 illustrates the three characteristic scales introduced for this thesis, which will be used in the following:

Microscale: Resolving a single deposited strand, whereby the polymer and all fibers or other inclusions are individually observed.

Mesoscale: Description of the material structure of the individual strand geometry and voids. The effective contact areas between the strands are explicitly represented. Polymer and any fibers or inclusions in the single strand are considered as homogenized.

Macroscale: Description of the material structure as a homogenized continuum. Voids and strand geometry are not resolved individually.

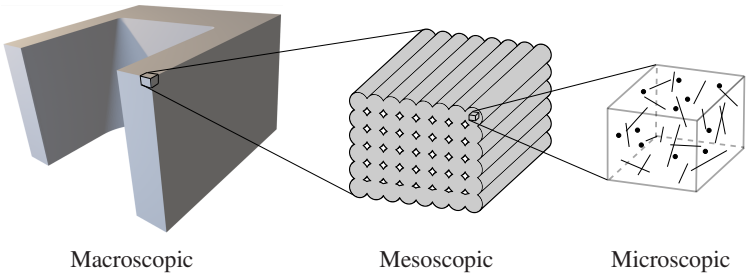

Figure 2.8: Schematic illustration of the scale separation introduced into macro-, meso- and microscale.

2.4 MEX characteristic material behavior

2.4.1 Thermal behavior

The thermal behavior of MEX-printed components, particularly their thermal conductivity and heat capacity, is strongly influenced by their anisotropic and porous structure. Commonly used methods for characterizing these properties are described below, together with a summary of key studies on thermal conductivity in MEX structures and heat capacity in MEX materials.

2.4.1.1 Experimental methods

Measurement of thermal conductivity To characterize thermal conductivity κ, the measurement methods can be devided into two main categories: steady-state methods and transient methods. [57, 58]

Steady-state methods, such as the guarded hot plate and the heat flow meter, are based on Fourier's law [57]. These methods determine thermal conductivity by measuring the temperature gradient under a steady heat flow through the specimen [58]. They are particularly well suited for materials and composites with low thermal conductivity. A key advantage of steady-state methods is that they allow the direct determination of thermal conductivity in each direction, making them especially suitable for anisotropic materials. However, these methods typically require relatively large specimen dimensions, longer measurement durations, and are sensitive to heat losses and contact resistances at the temperature sensors, which can affect measurement accuracy [57].

Transient methods, such as the Transient Plane Source (TPS), Laser Flash, Transient Hot Wire, or modulated Differential Scanning Calorimetry (DSC) use a time-dependent supply of heat [57]. The heat is applied either as a pulse or periodically, causing the temperature in the material to change over time. These methods measure the thermal diffusivity and calculate the thermal conductivity from the density and heat capacity of the material. A major advantage of

transient methods is the short measurement time (within a few minutes) and the ability to work at high temperatures and pressures [58]. However, the accuracy of transient methods is lower than that of steady-state methods, and calculation of thermal conductivity requires additional measurements of density and heat capacity. [57]

Measurement of specific heat capacity The specific heat capacity describes the amount of heat required to raise the temperature of a substance. DSC (cf. Section 2.4.3.1) and Drop Calorimetry are the main methods used to measure the specific heat capacity in the temperature range of 25°C to 400 °C, which is of interest for the MEX process. DSC is particularly suitable for this temperature range because it offers both high temperature resolution and short measurement times. The difference in heat flow between the specimen and the reference is recorded during a defined temperature program. The specific heat capacity can then be determined as a function of temperature. [59–61]

The DSC measurement of heat capacity is standardized in DIN EN ISO 11357-4 [62], which describes the determination by comparison with a calibration sample. Commonly used reference materials are sapphire or synthetic calcium fluoride, whose heat capacities are well known. The standard also specifies requirements for heating rate, sample size, and calibration.

2.4.1.2 Thermal conductivity

Thermal conductivity κ in MEX structures is influenced by the polymer's intrinsic properties and the printed component's specific mesostructure [63–67]. Typically, polymers have a low thermal conductivity compared to metals [68]. In MEX structures, thermal conductivity can also be anisotropic, i.e. it varies depending on the global direction within the material [64, 65]. This anisotropy results from the mesostructure formed by the extrusion process, in which the thermal conductivity along the extrusion direction is higher than perpendicular to it. On the one hand, this is controlled by the strand geometry

and volume fraction of voids [64]. On the other hand, thermal contact resistance between layers and strands due to incomplete fusion or air inclusions can lead to a reduction in conductivity perpendicular to the extrusion direction [65]. The thermal conductivity is thus determined by the underlying trajectory, the associated material structure, and the total internal interface area of the strands. This weld quality is in turn determined by the factors that influence the local temperature profile at the interface. The longer the interface is exposed to higher temperatures, the better the weld will be. Such factors are listed in Section 2.1.2 and include print velocity, print temperature, heating plate temperature, and firmware settings.

Figure 2.9 schematically shows the description of the thermal conductivity of a MEX structure for the finer-resolved mesoscale and the homogenized macroscale. To consider the characteristic influence of the MEX structure in models at the mesoscale, a conductivity κ must be assigned to the polymer and the air, and the contact resistance R_{contact} at the interfaces must also be taken into account. For macroscale models, a homogenized effective thermal conductivity κ_{eff} is used, which takes into account the material structure and contact resistances R. To account for the anisotropic character, the thermal conductivity can be written as a second-order tensor $\boldsymbol{\kappa}_{\mathbf{eff}}$, whose trace entries are written as the effective thermal conductivities $\kappa_{\mathrm{eff}}^{\mathrm{xx}}$, $\kappa_{\mathrm{eff}}^{\mathrm{yy}}$, $\kappa_{\mathrm{eff}}^{\mathrm{zz}}$ in the direction of the corresponding global axis.

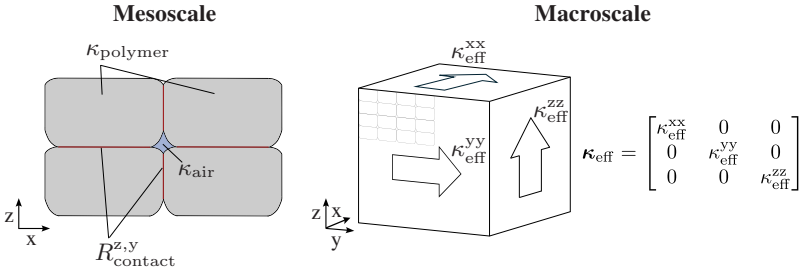

Figure 2.9: Schematic description of the thermal conductivity of a MEX structure for the fine-grained mesoscale and the homogenized macroscale.

There are several publications dealing with the thermal conductivity of MEX structures. Since unreinforced PLA is used as an example in this work, some publications on thermal conductivity characterization are presented below, which provide information on the thermal conductivity of unreinforced PLA structures and the influence of the mesostructure. Regarding the influence of fibers or other fillers on the resulting thermal properties, Shanmugam et al. [69] provide a detailed overview of published work in their review article.

Laureto et al. [70] used the guarded heat flow method of ASTM F433 using a Holometrix TCA300 Through-Plane Thermal Conductivity Tester to quantify the thermal conductivity in PLA-metal composites. They used printed specimens. For pure PLA, they measure a thermal conductivity of $\kappa = 0.185\,\mathrm{W/(m \cdot K)}$ at $50\,^{\circ}\mathrm{C}$. An influence of the material structure on this conductivity was not measured or discussed.

Flaata et al. [71] published a test setup specifically designed to characterize specimens with very low thermal conductivity. They used the steady-state method and examined specimens made of Acrylonitrile butadiene styrene (ABS), neat PLA and PLA with different fillers, which were produced with MEX. The cold plate was maintained at $20\,^{\circ}\mathrm{C}$, and the samples were allowed to reach steady-state conditions before measurements were taken. No information is given about the trajectory used, so the measured values cannot be interpreted in terms of material structure. For the ABS specimens the mean value is $0.433\,\mathrm{W/(m \cdot K)}$ and for PLA $0.435\,\mathrm{W/(m \cdot K)}$. These values are very high compared to the rest of the literature and also compared to the values expected from the bulk material conductivities.

Elkholy et al. [64] experimentally and numerically investigated the influence of layer height and grid spacing to characterize the effective thermal conductivity of 3D printed components and to analyze the thermal anisotropy of unidirectionally printed components. For this purpose, a special test apparatus was developed based on a modified guarded hot plate technique as described in ASTM C177, which is based on the steady-state method. The thermal conductivity measurements were conducted at room temperature. The results show

that increasing the layer height and grid spacing leads to a decrease in the effective thermal conductivity of up to 65% compared to the pure polymer. In addition, the thermal conductivity was measured for different PLA compounds. It was found that the anisotropic ratio can reach a value of 2. Finally, the effective thermal conductivity of several commercially available PLA composite filaments was experimentally determined. Elkholy et al. [64] provide the thermal conductivities of pure PLA for all three global spatial directions. At room temperature these are $\kappa^{\mathrm{xx}} = 0.195\,\mathrm{W/(m \cdot K)}$, $\kappa^{\mathrm{yy}} = 0.135\,\mathrm{W/(m \cdot K)}$ and $\kappa^{\mathrm{zz}} = 0.181\,\mathrm{W/(m \cdot K)}$. Here, the x-direction corresponds to the extrusion direction of the strands, y is the in-plane direction perpendicular to it, and z denotes the build direction. The higher conductivity in z compared to y can be explained by the larger overall interfacial area in build direction, which facilitates heat transport across adjacent layers.

Bute et al. [72] investigated the thermal conductivity of a total of 14 different commercially available filament materials, including three different unreinforced PLA filaments. They measured the conductivities to determine the three-dimensional thermal conductivity tensor using a self-developed method that combines the TPS method with numerical simulation and inverse solution. All measurements were conducted at room temperature. The conductivities $\kappa^{\mathrm{xx}} = 0.229 - 0.247\mathrm{W/(m \cdot K)}$, $\kappa^{\mathrm{yy}} = 0.189 - 0.231\mathrm{W/(m \cdot K)}$, and $\kappa^{\mathrm{zz}} = 0.206 - 0.229\mathrm{W/(m \cdot K)}$ were measured for the three PLAs.

Lendvai et al. [73] investigated the influence of the extrusion multiplier k on the thermal conductivity of printed PLA structures, where k is a process parameter in MEX printing that controls the material feed rate relative to the nominal value. Adjusting k changes the deposited volume, where values below 1 reduce the amount of extruded material and increase porosity, while values above 1 lead to higher deposition, which may reduce voids but can also cause dimensional inaccuracies. In their study the conductivity in the build-up direction was measured using the flash diffusion test on a Netzsch LFA467 Hyperflash, a transient test method, at a temperature of $25\,^{\circ}\mathrm{C}$ under an inert $\mathrm{N_2}$ atmosphere. A range of $97-105\,\%$ ($k = 0.97-1.05$) was examined. The investigations show that, as

the number of defects decreases, the thermal conductivity of the components increases from $\kappa^{zz} = 0.157\,\mathrm{W/(m \cdot K)}$ to $\kappa^{zz} = 0.188\,\mathrm{W/(m \cdot K)}$.

The presented works show that the characteristic mesostructure influences the resulting thesrmal conductivity. It is expected to be different from the bulk material [73]. The process-typical voids and the contact resistance of the interfaces between the strands and layers lead additionally to an anisotropic thermal conductivity. The papers dealing with the thermal conductivity of PLA all show a comparable value in the direction of build-up, with the exception of Flaata et al. [71] who greatly overestimate it, also in comparison to the typical value for the bulk material. Elkholy et al. [64] and Bute et al. [72] are the only ones to report the conductivities in the extrusion direction and transverse to it in one layer.

Table 2.2 provides an overview of publications on the thermal conductivity of unreinforced MEX structures.

Table 2.2: Overview of publications on the thermal conductivity of unreinforced PLA MEX structures. In addition to the measured values, the materials investigated and the general test methodology are listed.

Publication	**Testing method**	**Results** $(\mathrm{W/(m \cdot K)})$
Bute et al. [72]	Transient	$\kappa^{xx} = 0.229 - 0.247$
		$\kappa^{yy} = 0.189 - 0.231$
		$\kappa^{zz} = 0.206 - 0.229$
Elkholy et al. [64]	Steady state	$\kappa^{xx} = 0.195$
		$\kappa^{yy} = 0.135$
		$\kappa^{zz} = 0.181$
Flaata et al. [71]	Steady state	$\kappa = 0.45$
Laureto et al. [70]	Steady state	$\kappa = 0.185$
Lendvai et al. [73]	Transient	$\kappa^{zz} = 0.157 - 0.188$

2.4.1.3 Specific heat capacity

In the mesoscopic view of a MEX structure, the polymer is assigned a separate specific heat capacity $c_{\mathrm{p,polymer}}$ and the air is assigned a specific heat capacity $c_{\mathrm{p,air}}$.

For macroscopic descriptions, however, the MEX structure is often considered a homogenized, continuous medium with effective material parameters. This requires an effective specific heat capacity $c_{\mathrm{p}}^{\mathrm{eff}}$ to model the thermal behavior of the structure as a whole.

The effective heat capacity $c_{\mathrm{p}}^{\mathrm{eff}}$ of a mixture based on mass fractions is derived from the principle of heat balance [74]. When two substances are mixed and heat is added or removed, the total heat exchanged is the sum of the heat exchanged by each substance. Thus, $c_{\mathrm{p}}^{\mathrm{eff}}$ of the mixture is a weighted average of the heat capacities of the individual components. In the case of MEX structures, consider two substances: Polymer and Air, with masses m_{polymer} and m_{air}, and specific heat capacities $c_{\mathrm{p,polymer}}$ and $c_{\mathrm{p,air}}$, respectively. The heat Q exchanged by each substance is therefore given by:

$$Q_{\mathrm{polymer}} = m_{\mathrm{polymer}} c_{\mathrm{p,polymer}} \Delta T \quad \text{and} \quad Q_{\mathrm{air}} = m_{\mathrm{air}} c_{\mathrm{p,air}} \Delta T, \tag{2.1}$$

where ΔT is the temperature change. The total heat exchanged by the system is

$$Q_{\mathrm{total}} = Q_{\mathrm{polymer}} + Q_{\mathrm{air}} = (m_{\mathrm{polymer}} c_{\mathrm{p,polymer}} + m_{\mathrm{air}} c_{\mathrm{p,air}}) \Delta T. \tag{2.2}$$

The total heat Q_{total} can also be written in terms of the effective specific heat capacity $c_{\mathrm{p}}^{\mathrm{eff}}$ of the mixture as

$$Q_{\mathrm{total}} = (m_{\mathrm{polymer}} + m_{\mathrm{air}}) c_{\mathrm{p}}^{\mathrm{eff}} \Delta T. \tag{2.3}$$

Equating the two expressions for Q_{total} yields

$$(m_{\mathrm{polymer}} + m_{\mathrm{air}}) c_{\mathrm{p}}^{\mathrm{eff}} = m_{\mathrm{polymer}} c_{\mathrm{p,polymer}} + m_{\mathrm{air}} c_{\mathrm{p,air}}. \tag{2.4}$$

By resolving according to $c_{\mathrm{p}}^{\mathrm{eff}}$, the formula for the effective specific heat capacity $c_{\mathrm{p}}^{\mathrm{eff}}$ of the mixture is obtained with:

$$c_{\mathrm{p}}^{\mathrm{eff}} = \frac{m_{\mathrm{polymer}} c_{\mathrm{p,polymer}} + m_{\mathrm{air}} c_{\mathrm{p,air}}}{m_{\mathrm{polymer}} + m_{\mathrm{air}}}. \tag{2.5}$$

Due to the low density of air and its low specific heat capacity compared to the polymer, its influence on the effective heat capacity is very low. Even with high porosities, air only contributes a small proportion of the mass and has a minimal influence on the effective heat capacity of the overall system. Thus, assuming that the mass of air is negligible,

$$c_{\mathrm{p}}^{\mathrm{eff}} \approx \frac{m_{\mathrm{polymer}} c_{\mathrm{p,polymer}}}{m_{\mathrm{polymer}}} = c_{\mathrm{p,polymer}} \tag{2.6}$$

follows. This simplification is permissible, especially at low porosities, such as those found with a nominal infill density of 100%.

It is important to note that the specific heat capacity of thermoplastics is temperature-dependent and typically increases with temperature [75]. According to Pyda et al. [75], the specific heat capacity c_{p} of PLA at room temperature is approximately $1.2\,\mathrm{J/(g \cdot K)}$, rising to approximately $2.1\,\mathrm{J/(g \cdot K)}$ at the melting temperature. However, it is important to note that the specific heat capacity can vary depending on the molar mass and composition of the PLA (cf. Section 2.2).

2.4.2 (Thermo)mechanical properties[1]

MEX components exhibit complex deformation and failure behavior, primarily due to the intrinsic heterogeneity of their material structure, as described in Section 2.3 [20, 76, 77]. This heterogeneity results from the layer-by-layer manufacturing process and the specific deposition strategy within each layer [21], which together govern the anisotropic nature of both the quasi-static and the temperature- and time-dependent mechanical behavior [14, 78].

Moreover, factors such as reduced interfacial strength between strands and layers [19, 79, 80], voids between deposited strands [18], and surface waviness caused by strand geometry significantly influence the mechanical response. These effects are closely tied to various process parameters, whose influence on mechanical properties is discussed in Section 2.1.2 and further examined here, with a focus on tensile behavior under different loading and environmental conditions.

In this section, the thermomechanical performance of MEX components is discussed based on selected literature, with particular attention given to unreinforced material systems and specifically to PLA, which is the focus material in this study. While this work emphasizes unreinforced PLA, the general trends and parameter dependencies can also be extended to MEX structures incorporating discontinuously reinforced strands. A comprehensive overview of the mechanical behavior of fiber-reinforced MEX components can be found in the review by Penumakala et al. [77].

The subsequent sections present the methodology used for specimen preparation and mechanical testing, followed by a discussion of quasi-static tensile properties, temperature- and time-dependent behavior, and thermal expansion.

[1] Extracts from Section 2.4.2 have been previously published in [1], © CC BY 4.0, i.e. Felix Frölich, Lennart Bechtloff. Benedikt M. Scheuring, Anselm L. Heuer, Florian Wittemann, Luise Kärger, Wilfried V. Liebig. Evaluation of mechanical properties characterization of additively manufactured components. *Progress in Additive Manufacturing*, 10(2):1217-1229, 2025 - Reproduced sections and paragraphs are marked with [1].

Finally, procedures for deriving engineering material constants relevant for design and simulation purposes are introduced.

2.4.2.1 Specimen Preparation[1]

The study of the various influences of structural features requires an appropriate characterization method. Cuan-Urquizo et al. [78] even defines the selected characterization method itself as an influencing parameter. First, different specimen geometries can be distinguished. For example, both a dogbone and a rectangle shape allow the investigation of mechanical parameters. For characterization in the injection molding process, standards such as DIN EN ISO 527-2 [81] for testing tensile properties by using dogbone specimens are available. However, these standards do not define how the specimens should be produced in polymer-based AM. Cuan-Urquizo et al. [78] show, for example, that if the specimens are printed directly in the corresponding geometry, the perimeter and turning points of the nozzle trajectory influence the effective orientation in the measuring range of the specimen. For small specimens, this can lead to the methodological error that, despite the desired $90°$ orientation of the strands to the loading direction, there is no pure $90°$ orientation. In addition, pores formed at the turning points between the perimeter and the filling lead to an additional internal notch effect [18]. If the ratio of specimen width to strand width is not an integer, other geometrically induced pores and notch effects may occur. These influences may explain the different tensile strengths of two specimen shapes (ASTM D638 [82] Type I and Type IV) that Laureto et al. [83] observed in a large-scale measurement campaign. When the specimens are examined after specimen post-processing, further differences become apparent. Zhang et al. [84] used waterjet cutting to cut specimens from additively manufactured plates and showed that both the stiffness and strength of the cut specimens were on average $50\,\%$ lower than those of the directly manufactured specimens. This was explained by the absence of perimeters, which have a strengthening effect

[1] Verbatim reproduced section from [1], © CC BY 4.0, cf. footnote p. 29 for details.

in the load direction. In contrast, the cut specimens failed more often within the measurement length due to the lack of process-related notches in the conical area. This increase in validity was also observed from Park et al. [85], where the validity increased from about 27 % to 62 %. Validity was also assessed based on the crack initiation point. Park et al. [85] uses a laser cutter for specimen preparation.

2.4.2.2 Experimental Methods

Tensile test Tensile tests are used to determine quasi-static properties such as Young's modulus, tensile strength, and elongation at break. Tensile testing is typically performed in a universal testing machine. Test actuators (hydraulic or electric) apply a controlled tensile force to the specimen while clamping jaws grip the specimen at both ends. The strain of the specimen is measured by an extensometer and the tensile force is measured by a load cell.

In addition, Digital Image Correlation (DIC) can be used to optically monitor the strain and deformation of the specimen during the test. This involves applying special markers to the surface of the specimen. Cameras capture high-resolution images during the tensile test, which are then analyzed by software. This analysis provides precise information about deformation, strain patterns, and even local material defects. The results include detailed stress-strain diagrams that visualize mechanical properties such as Young's modulus, elongation at break, and even local strains, which is particularly useful for more complex materials and components.

Both DIN and ASTM standards exist for tensile testing and provide specific guidelines. ASTM D638 [82] describes the procedure for determining the tensile properties of reinforced and unreinforced plastics. The standard also defines specimen shapes and dimensions, the test procedure including environmental conditions, and requirements for testing machines and extensometers. ASTM D3039/D3039M [86] is specifically used for tensile testing of fiber-reinforced composites. It allows the determination of elastic properties such as

tensile modulus and Poisson's ratio, as well as the tensile strength of composites, including unidirectional and multidirectional fiber-reinforced laminates. DIN EN ISO 527-1 [87] defines the general principles for determining the tensile properties of plastics, DIN EN ISO 527-2 [88] defines the special test conditions for molded and extruded materials, DIN EN ISO 527-4 [89] defines the test conditions for isotropic and anisotropic fiber-reinforced plastics, and DIN EN ISO 527-5 [90] defines the test conditions for unidirectional fiber-reinforced plastics.

Although ASTM D638 [82] and DIN EN ISO 527 [87–90] have similar objectives, there are differences in specimen dimensions, test velocitys, and strain measurement requirements. For example, ASTM D638 uses Type I specimens that are $3.1\,\mathrm{mm}$ thick and $50\,\mathrm{mm}$ long, while ISO 527-2 uses Type 1A specimens that are $4\,\mathrm{mm}$ thick and $75\,\mathrm{mm}$ long. In addition, the test and strain rates specified in the standards may vary.

Dynamic mechniacal analysis (DMA) DMA is used to study temperature and frequency dependent behavior. It helps to understand material transitions such as the glass transition temperature T_G. DMA characterizes the viscoelastic properties of materials such as storage modulus E', loss modulus E'', and damping behavior as a function of temperature T, and frequency f. DMA is typically performed using a dynamic mechanical analyzer that applies a sinusoidal stress or strain to the specimen and measures the response. Depending on the material and application, an average load is applied to test the specimen in either tension or compression. Depending on the type of DMA measurement (e.g., tensile, bending, or shear), the specimen is typically clamped between two jaws or placed on a cantilever.

The storage modulus (elastic response) and loss modulus (viscous response) of the material are determined from both the amplitude and the phase difference between the applied stress or strain and the resulting strain or stress. Other properties can be derived from these measurements, such as the damping factor ($\tan\delta$), which provides information about the energy dissipation of the material.

DMA testing is guided by the ASTM D4065 [91] standard for determining the dynamic mechanical properties of polymers. This standard describes the test procedures, specimen dimensions, and equipment requirements for measuring storage and loss moduli. In addition, DIN EN ISO 6721 [92–94] provides guidelines for measuring viscoelastic properties and is widely used to test polymers and polymer-based composite materials.

Thermomechanical analysis (TMA) TMA is a technique used to measure the dimensional changes of a material as a function of temperature, time, and applied force. In a typical TMA experiment, a constant force is applied to the specimen and the resulting dimensional changes are monitored as the temperature is varied. This allows the determination of thermomechanical properties, such as the coefficients of thermal expansion and the glass transition temperature T_{G}. The change in length, width, or height of the test specimen is measured under controlled application of force at increasing or decreasing temperature. TMA can be performed in various modes, such as compression, tension, or penetration, depending on the specific test configuration and the material being analyzed. Dimensional changes are plotted against temperature and provide valuable information about the thermal behavior of the material. TMA can also be used to evaluate the effects of additives, fillers, or processing conditions on material behavior.

TMA testing is guided by several standards, including ASTM E831 [95], which provides procedures for measuring the coefficient of thermal expansion and other thermomechanical properties of materials. It should be noted that the T_{G} determined by TMA can differ from that obtained by DSC. This is because TMA measures the macroscopic dimensional response of the material under a small applied force, whereas DSC detects changes in heat flow associated with molecular mobility.

Creep and Stress Relaxation Testing Creep and stress relaxation experiments are techniques to study the time-dependent deformation of materials

under constant load or constant strain. For thermoplastics, such tests are typically carried out on universal testing machines, often with temperature- and humidity-controlled chambers. In creep testing, a constant stress is applied and the resulting strain is measured over time, while in stress relaxation experiments a constant strain is imposed and the decay of stress is recorded. These methods provide important information on the viscoelastic behavior and dimensional stability of thermoplastic components. Creep and relaxation tests are guided by standards such as ASTM D2990-17 [86].

2.4.2.3 Quasistatic tensile properties

The structure–property relationships of MEX structures, have been investigated extensively since the early 2000s. Bertoldi et al. [96], Es-Said et al. [21], and Ahn et al. [97] were among the first to explore the dependence of mechanical properties, such as strength and stiffness, on the orientation of printed strands. The infill angle and thus the strand orientation, the infill pattern, and the infill density significantly determine the resulting mesostructure and therefore the mechanical properties. For this reason, the influence of the infill geometry on the quasi-static tensile properties of MEX structures is first examined below. Subsequently, further process settings such as layer height, temperature conditions, nozzle diameter, and printing velocity are investigated.

Influence of the infill geometry The choice of infill pattern has a direct influence on the resulting mechanical properties and their anisotropy. While aligned infill exhibits the most pronounced anisotropy, more isotropic infill patterns such as triangular or gyroidal infill show comparatively low anisotropy and more homogeneous mechanical properties [98]. Increasing the infill density enhances mechanical properties, particularly stiffness and tensile strength [98, 99]. In the case of an aligned infill, it has been demonstrated that components with unidirectional strand orientation and $100\,\%$ infill density are generally orthotropic in nature [96, 98, 100–107]. It should be noted that a 100% infill density is only achievable with aligned infill patterns. While aligned infill

with alternating angles between layers can provide more balanced mechanical properties across different directions, the highest stiffness and strength in a specific loading direction is typically achieved with a unidirectional $0\,^{\circ}$-aligned infill.

The outcome of the main published work on the orientation-dependent properties of aligned mesostructures using PLA filament is summarized below:

- **Stiffness**: For unidirectionally printed, orthotropic mesostructures, stiffness in the extrusion direction ($\alpha = 0\,^{\circ}$) typically ranges from $1.0\,\mathrm{GPa}$ to $4.0\,\mathrm{GPa}$ [98, 108–115]. In the transverse direction, the stiffness is reduced by $2\,\%$ to $23\,\%$ [108, 110–113], and by up to $42\,\%$ in the build direction [98, 109, 114, 115].
- **Tensile strength**: Tensile strength also follows an anisotropic pattern, with values between $36\,\mathrm{MPa}$ and $77\,\mathrm{MPa}$ in the extrusion direction [98, 99, 108–116]. Strength reductions of $10\,\%$ to $35\,\%$ are observed in the transverse direction [99, 108, 110–113, 116], and up to $90\,\%$ in the build direction [98, 109, 114, 115].
- **Elongation at break**: In the extrusion direction, elongation at break values between $4.2\,\%$ and $5.4\,\%$ are reported [98, 112–114]. In the transverse direction, elongation at break is typically reduced by $17\,\%$ to $74\,\%$ relative to these values.

Influence of further process parameters In addition, other process parameters defined in the slicer influence the mechanical properties of MEX-printed components:

- **Layer height**: Increasing the layer height l_{hight} from $1\,\mathrm{mm}$ to $2\,\mathrm{mm}$, with a correspondingly increased material flow rate, improves stiffness in extrusion direction by $1.7\,\%$ to $6.9\,\%$ [111, 112, 114, 115], though tensile strength in the same direction decreases by $1.6\,\%$ to $15.2\,\%$ [99, 111, 112, 114–117]. Further increases to $3\,\mathrm{mm}$ result in additional stiffness

gains of up to $4.6\,\%$ [110, 118], but strength declines by $4.1\,\%$ to $24.2\,\%$ [99, 110, 117, 118].

- **Build platform and nozzle temperature**: Higher build platform temperatures (T_{bp}) and nozzle temperatures (T_{N}) are generally associated with enhanced mechanical properties, including increased stiffness and strength [111, 113, 114].

- **Nozzle diameter**: Increasing the nozzle diameter d_{N} from $0.4\,\mathrm{mm}$ to $0.8\,\mathrm{mm}$ can result in an increase in strength due to the reduction in the relative interface area between the strands [117]. For the same l_{hight}, the volumetric flow rate must be reduced accordingly to prevent over-extrusion, since a larger nozzle naturally deposits more material per unit time at the same printing velocity.

- **Print velocity**: Most studies report little to no significant effect on stiffness or strength with varying print velocitys [109, 112, 113]. However, Pachauri et al. [112] observed an $8\,\%$ increase in strength when print velocity was increased from $20\,\mathrm{mm/s}$ to $60\,\mathrm{mm/s}$ at $80\,\%$ infill density. Heuer et al. [80] demonstrated that interfacial strength, which is crucial for the overall strength of a component, only improves once a critical print velocity threshold is exceeded. At low velocitys, excessive cooling between strand deposition negatively impacts bonding quality. This threshold velocity depends on the component size and geometry as well as the chosen trajectory.
  It should be noted that there is also a practical upper limit for print velocity. If the velocity exceeds the extruder's capacity to supply material at the required volumetric flow, the extruded strand may become thinner, leading to under-extrusion and reduced bonding. This maximum velocity depends on nozzle diameter, filament properties, and printer heating performance.

Summary In summary, the infill pattern and layer height are critical factors that determine the quasistatic tensile properties of MEX-printed components.

Process parameters such as nozzle and build platform temperatures, as well as increased infill density, contribute to enhanced stiffness and tensile strength. However, the mechanical properties reported in the literature are highly variable, which highlights the complexity of the MEX process and the interconnected nature of its influencing factors. Discrepancies in experimental methodologies and inconsistent documentation also impede the comparability of results across studies.

2.4.2.4 Determination of engineering material constants

To describe the orthotropic behavior of MEX structures with an aligned infill pattern numerically, nine independent engineering constants must be identified. A common approach involves mechanical testing on specimens with varying orientations, in which both the infill angle and the build direction relative to the loading axis are systematically modified [100, 104, 106]. This enables the determination of direction-dependent Young's Modulus E_{ii} and Poisson's ratios ν_{ij}. The shear moduli G_{ij} are typically identified through specialized shear tests [98, 106].

Tröger et al. [106] conducted a comprehensive study comparing different strategies for the identification of orthotropic material parameters for MEX-manufactured structures. These include conventional analytical methods based on tensile and shear tests, as well as numerical approaches using full-field measurement techniques like DIC in combination with FE simulations within a nonlinear least-squares framework (NLS-FEM-DIC). While all methods provided plausible results, the study highlighted limitations of numerical procedures due to parameter correlations and uncertainties in the evaluation. Based on their findings, Tröger et al. [106] recommend a purely experimental approach [104, 105], in which the elastic moduli E_{ii} and Poisson's ratios ν_{ij} are derived from tensile tests in different orientations. The shear moduli G_{ij} can then be obtained analytically by considering the rotation of the orthotropic

compliance matrix within the layers, as commonly formulated in Classical Laminate Theory (CLT), by

$$G_{ij} = \left(\frac{4}{\hat{E}^{45,\mathrm{ij-plane}}} - \frac{1}{E_{ii}} - \frac{1}{E_{jj}} + \frac{2\nu_{ij}}{E_{ii}} \right)^{-1}, \tag{2.7}$$

where $\hat{E}^{45,\mathrm{ij-plane}}$ is the Young's modulus of specimens rotated in the i-j plane by $45\,^{\circ}$ relative to the load direction. In this approach, the specimens are interpreted as laminate-like layered structures, which allows a simplified but accurate determination of G_{ij}. This approach originates from the description of fiber reinforced composites and shows according to the investigations of Tröger et al. a high degree of agreement with experimental reference data and proves to be particularly robust and practical for the calibration of orthotropic material models in additively manufactured structures.

2.4.2.5 Temperature- and time-dependent behavior

The temperature- and time-dependent behavior of polymers is typically characterized by quasi-static tests at varying strain rates or temperatures [119–124], DMA [102,114,125–133], or creep and stress relaxation tests [134–136]. TMA can also be employed to study creep behavior, although it is generally applied for determining thermal expansion, which will be discussed separately (cf. Section 2.4.2.6).

Strain rate sensitivity Numerous studies consistently report a strain rate sensitivity in MEX-printed structures [119–124]. With increasing strain rate, both stiffness and strength tend to rise significantly, which is attributed to the limited time available for molecular relaxation and polymer chain mobility. Luo et al. [120] confirmed this behavior through uniaxial tensile testing, demonstrating a distinct increase in mechanical performance at higher strain rates. Similar findings are reported by Vidakis et al. [123] and Slavković et al. [122], who conducted extensive mechanical testing specifically on PLA-based MEX-structures.

Their results likewise show a strong dependence of stiffness and strength on the applied strain rate, further validating the viscoelastic nature of PLA and its sensitivity to time-dependent loading conditions.

Frequency-dependent behavior and damping In addition to quasi-static tests at varying strain rates, DMA is widely used to assess the viscoelastic behavior of polymers. A substantial number of studies have applied DMA to characterize the mechanical response of MEX-printed structures. However, these investigations predominantly focus on the influence of process parameters on the storage modulus E', often without considering variations in excitation frequency. While E' characterizes the elastic stiffness of the material, it provides only limited insight into how process parameters influence the time-dependent viscoelastic behavior. This aspect is more accurately captured by analyzing the loss factor $\tan\delta$ and the frequency dependence of the material response. Consequently, the following discussion is limited to studies investigating the influence of process parameters on damping behavior (quantified via $\tan\delta$) and its frequency dependence. Overall, such investigations remain scarce.

The viscoelastic behavior of MEX-printed structures is primarily governed by the intrinsic rheological and viscoelastic properties of the polymer. However, processing parameters can modulate the extent to which these effects manifest in the printed component. Among the most influential parameters are the printing trajectory, including the number of perimeters, infill angle, and air gap, as well as the nozzle temperature, all of which have been shown to affect the loss factor $\tan\delta$. The impact of these parameters on the frequency-dependent viscoelastic response has, however, been explored only in a few studies: Dhanapal et al. [125] conducted DMA tests on PEEK specimens with different infill patterns across multiple frequencies. For the storage modulus E', they reported only marginal variations in the glass transition temperature between infill patterns and no significant influence of the pattern on the frequency dependence. In contrast, the loss modulus E'' and the loss factor $\tan\delta$ showed a clear sensitivity to the infill geometry: line and grid patterns exhibited higher energy dissipation and tanδ values compared to cubic and hexagon patterns, which demonstrated

lower damping due to their more uniform stress distribution. Domingo-Espin et al. [102] evaluated the frequency response of MEX-printed specimens without modifying processing parameters and reported an overall low sensitivity to frequency. In contrast, Huang et al. [127] performed a more comprehensive study, combining process parameter variations, such as raster angle and raster width, with frequency sweeps. Their findings revealed a frequency dependence of both storage and loss moduli and indicated that these properties can be influenced by processing conditions. However, the individual contributions of specific parameters to this dependence were not quantitatively isolated.

Temperature-dependent behavior Similarly, the temperature-dependent mechanical behavior of MEX structures essentially follows the thermal properties of the polymer. At the glass transition temperature T_G, most thermoplastics exhibit a significant drop in stiffness and strength [132]. This effect is particularly pronounced in amorphous and weakly crystalline polymers such as PLA (cf. Figure 2.6). The low crystallinity leads to a pronounced softening around the T_G, resulting in strong relaxation processes and a significant drop in mechanical properties. In dynamic mechanical analysis, this is indicated by a rapid drop in the storage modulus E' and a pronounced peak in the loss modulus E'' and loss factor $\tan\delta$ [126, 127, 132, 133, 137].

In contrast, semi-crystalline polymers such as PEEK show less temperature sensitivity because the crystalline phase above the T_G contributes to mechanical stabilization [125]. The extent of these effects depends strongly on the printing parameters: higher nozzle temperatures and suitable cooling conditions promote crystallization within the filaments, while the interlaminar bonding zones often remain amorphous [131]. Thus, both the polymer structure and the process control influence the temperature dependence of the mechanical behavior of MEX-printed components made of semi-crystalline polymers.

Numerous studies have shown that PLA has a pronounced temperature- and time-dependent mechanical behavior . In the T_G range (about $55\,^\circ\mathrm{C}$ to $65\,^\circ\mathrm{C}$), PLA shows a significant softening (cf. Figure 2.6). At temperatures above

$70\,^{\circ}\mathrm{C}$, a slight increase in the storage modulus has been observed in some cases, which is attributed to restructuring in the polymer and the onset of cold crystallization. To date, only limited data are available on the high-temperature behavior of MEX-printed PLA structures. However, conventionally produced PLA specimens have shown comparable behavior, such as significant softening near T_{G} and, in some cases, a slight increase in storage modulus at higher temperatures due to polymer restructuring and the onset of cold crystallization. For completeness, the melting temperature of PLA is typically around $150\,^{\circ}\mathrm{C}$ to $180\,^{\circ}\mathrm{C}$ for partially crystalline specimens, depending on the isomer composition and processing conditions [126].

2.4.2.6 Thermal expansion

One of the key properties of polymers, that significantly affects PiD is thermal expansion [126, 138–140] (cf. Section 2.1.3). It is specified by the coefficient of thermal expansion (CTE) α_{th}. This describes the relative change in length of a material as a function of temperature and can typically be characterized using TMA (cf. Section 2.4.2.2) or alternatively with a dilatometer.

Several studies have investigated the CTE of MEX printed structures, with the choice of material and the microstructure of the components having a significant influence [69, 72, 141]. When using unreinforced filaments, the CTE of printed structures can usually be considered nearly isotropic [126, 138, 141]. This means that the CTE in different spatial directions differs only slightly, due to the relatively homogeneous material distribution and the lack of directional reinforcements.

In contrast, fiber-reinforced structures show a distinctly anisotropic expansion behavior. For example, embedding glass fibers, carbon fibers, or carbon nanotubes reduces the CTE in the extrusion direction because the fibers have higher stiffness and lower thermal expansion than the polymer matrix [126, 142, 143]. At the same time, the aligned orientation of the fibers, a direct result of

the MEX process, leads to strong directional dependence of thermal expansion [69, 141, 144]. The influence of the fibers is comparatively small in the build-up direction, which is why higher CTE values are often observed here.

The literature consistently shows that CTE increases above the glass transition temperature T_G [72, 138, 142]. Below T_G, thermoplastics are in an energy-elastic state in which the molecular chains are severely restricted in their movement. This results in comparatively low CTE values. However, when the T_G is exceeded, the polymers enter an entropy-elastic state in which the macromolecules have significantly more freedom of movement. This results in a significant increase in thermal expansion. This effect has been observed in numerous studies and is independent of the polymer or fiber reinforcement used. Accurate determination of the CTE in both temperature ranges is therefore crucial, especially when MEX components are subjected to thermal stresses near or above T_G.

Several studies report typical CTE values for unreinforced PLA of approximately $\alpha_\mathrm{th} = 63 \cdot 10^{-6} - 100 \cdot 10^{-6}\,1/\mathrm{K}$ below T_G and significantly higher values of up to $\alpha_\mathrm{th} = 217 \cdot 10^{-6}\,1/\mathrm{K}$ above T_G [72, 126, 138].

2.4.3 Thermal phase transitions and crystallization

During the MEX process, polymers undergo thermal transitions. These transitions influence the polymers' thermomechanical properties, such as elasticity and viscosity, during processing. Understanding these varying properties is essential for adjusting process parameters optimally, particularly to prevent PiD or achieve the best possible bonding of adjacent strands. Additionally, heat management during processing affects the crystallization behavior of semi-crystalline polymers. Because the resulting degree of crystallinity directly affects the material's thermomechanical behavior, a comprehensive understanding of the relevant thermal transitions and crystallization kinetics is essential for robust process control and precise numerical modeling.

2.4.3.1 Experimental methods

A thermal analysis technique commonly used to study thermal phase transition phenomena and crystallization kinetics is called DSC. A DSC measures the flow of heat into or out of a material as a function of temperature or time. It is primarily used to study phase transitions such as glass transition temperature T_{G}, melting temperature T_{m}, crystallization behavior, and, and thermal properties such as heat capacity. DSC is widely used to analyze polymers, composites, and other materials, providing information on their thermal stability and behavior during heating and cooling cycles.

In a typical DSC experiment, a small specimen is placed in a specimen pan and subjected to a controlled temperature program. The temperature of the specimen is compared to that of a reference material, and the difference in heat flow between the specimen and the reference is measured. The resulting heat flow is plotted against temperature and reveals endothermic or exothermic transitions such as melting, crystallization, or decomposition. These transitions can be used to identify important thermal properties, including glass transition temperature, melting point, and heat of fusion. Figure 2.10 shows a schematic DSC curve illustrating typical thermal transitions during heating and cooling, including glass transition, cold crystallization, melting, and crystallization peaks.

DSC can also be used to determine the degree of crystallization present within a specimen (absolute crystallinity) and thus to examine the thermal history of the polymer. The absolute crystallinity of a specimen χ_{c} can be calculated by:

$$\chi_{\mathrm{c}} = \frac{\Delta H_{\mathrm{m}} - \Delta H_{\mathrm{cc}}}{\Delta H_{\mathrm{m}}^{\circ}} \times 100\,\% \tag{2.8}$$

where ΔH_{m} is the absolute melting enthalpy, ΔH_{cc} is the absolute cold crystallization enthalpy (both of them are illustrated in Figure 2.10), and $\Delta H_{\mathrm{m}}^{\circ}$ is the absolute melting enthalpy of $100\,\%$ crystalline polymer.
DSC testing is guided by several standards, including ASTM D3418 [146], which provides procedures for determining T_{G} and other thermal properties

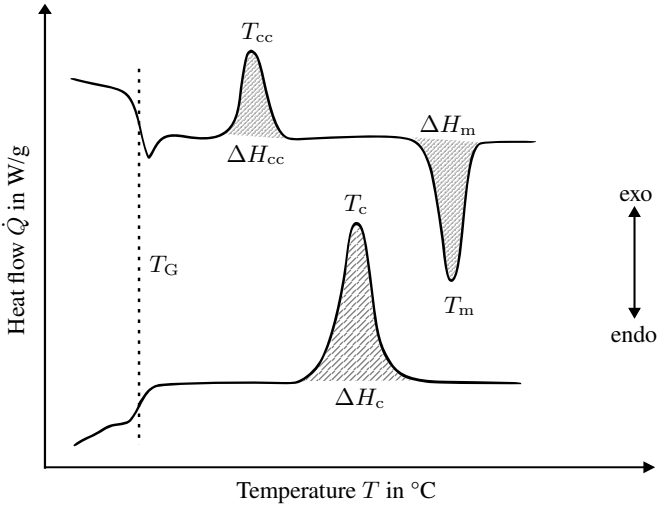

Figure 2.10: Schematic representation of a typical DSC thermogram of a semi-crystalline polymer during heating and cooling. The heating segment (upper curve) shows the glass transition temperature T_G as a step change in the baseline, followed by an exothermic cold crystallization peak with its maximum at the cold crystallization temperature T_{cc} and corresponding enthalpy ΔH_{cc}, as well as an endothermic melting peak with its maximum at the melting temperature T_m and associated enthalpy ΔH_m. The cooling segment (lower curve) reveals the crystallization peak with a maximum at the crystallization temperature T_c and corresponding enthalpy ΔH_c. (Adapted from [145])

of materials using DSC. In addition, DIN EN ISO 11357 [147–149] provides guidelines for performing DSC tests, specifying requirements for specimen size, heating rates, and test conditions. Both ASTM D3418 [146] and DIN EN ISO 11357 [147–149] ensure reproducible results by defining test parameters such as temperature range, calibration, and choice of reference material.

2.4.3.2 Thermal transitions

Various thermal transitions can be determined using a DSC measurement. The most relevant ones for the temperature range prevailing in the MEX are:

- **Melting temperature** (T_m): The melting temperature for PLA generally ranges from $150\,^\circ\mathrm{C}$ to $180\,^\circ\mathrm{C}$, reflecting the point at which crystalline regions melt [126].
- **Crystallization temperature** (T_c): The crystallization temperature, typically ranging from $90\,^\circ\mathrm{C}$ to $130\,^\circ\mathrm{C}$ for PLA [43], is a critical point at which the polymer begins to crystallize. This temperature, and in the case of non-isothermal processes, the cooling rate, plays an important role in controlling the degree of crystallization during the cooling phase in the MEX process.
- **Glass transition temperature** (T_G): For PLA, the glass transition temperature is typically observed between $55\,^\circ\mathrm{C}$ and $65\,^\circ\mathrm{C}$, marking the transition from a rigid, glassy state to a more flexible, rubbery state [43].
- **Cold crystallization temperature** (T_cc): In PLA, this transition occurs at temperatures between $90\,^\circ\mathrm{C}$ and $130\,^\circ\mathrm{C}$, indicating when crystallization begins during heating [43].

2.4.3.3 Degree of crystallization

The degree of crystallization of MEX structures is determined by the crystallization kinetics of the polymer used. Both the achievable degree of crystallization and the rate of crystallite formation during cooling are material dependent and vary with process conditions. DSC can be used to characterize these properties (cf. Section 2.4.3.1). The degree of crystallization can be determined from the initial heating process, while the crystallization kinetics can be analyzed from cooling curves at different cooling rates. In this way, the influence of thermal

processes on the structure development and the resulting material properties can be studied in detail.

Due to the small strand dimensions in the MEX process, high cooling rates occur throughout the volume compared to other manufacturing processes. For fast-crystallizing thermoplastics, a flash DSC measurement must be performed. However, in thermoplastics with slow crystallization kinetics, the high cooling rates lead to incomplete crystallization during the printing process. This results in limited mechanical properties and lower heat resistance. Subsequent heat treatment (annealing) can counteract this effect. PLA is one of the slowly crystallizing polymers. Perego et al. [43], for example, have demonstrated a degree of crystallinity of up to $9\,\%$ [43] in injection-molded PLA components. Giani et al. [126] investigated the crystallization kinetics of PLA filaments and also found a degree of crystallinity of approximately $3\,\%$ in additively manufactured PLA structures.

2.5 Process simulation[2]

As illustrated in Figure 2.8, the simulation approaches reported in the literature can be classified according to different length scales. In the following, these methods are discussed starting with the microscopic approaches.

2.5.1 Microscopic approaches

Microscale numerical methods that consider the polymer melt and the fibers or other reinforcing elements within the extruded strands separately are found

[2] Extracts from this Section have been previously published in [2], i.e. F. Frölich, M. E. Di Nardo, C. Krauß, A. Heuer, W. V. Liebig, F. Wittemann, P. Carlone, L. Kärger. An orientation-based homogenization approach for predicting process-induced deformations in extrusion-based additive manufacturing. *Additive Manufacturing*, 113:105023, 2025 - Adapted sections and paragraphs are marked with [2].

only sporadically in the literature, and are limited to the polymer melt within the nozzle and the region immediately after the nozzle exit. Coupled methods are usually used, where either finite volume method (FVM) [150] or smoothed particle hydrodynamics (SPH) [22, 23] is combined with discrete element method (DEM) to map the multiphase interactions between the matrix and the reinforcing fibers [151].

Yang et al. [151] present a coupled SPH-DEM model, where the viscous polymer matrix is modeled with SPH and the fibers are modeled as DEM particles. The model allows for the representation of fiber motion, deformation, and interaction, but is currently limited to 2D and does not yet account for thermal effects.

Zhang et al. [22] developed a three-dimensional FVM-DEM model to simulate the flow of rigid short fibers in polymer melts. The model is experimentally validated and shows that fiber length and fiber content contribute significantly to nozzle clogging, while low-viscosity matrix materials can mitigate this effect for short fibers.

Guo et al. [23] extended Zhang's model to flexible fibers. The study shows that flexible fibers adapt much more to geometric changes in the nozzle and therefore tend to form fiber bridges. This extension leads to a more realistic description of the microstructure evolution, but is associated with an increased numerical effort.

2.5.2 Mesoscopic approaches

Mesoscale models that represent the extruded strands as homogeneous units or explicitly map the resulting mesostructure allow the prediction of important properties of printed structures. These include strand geometry and the resulting material structure, interfacial strength, and the degree of crystallinity within the strands. The models range from numerical predictions of the extrusion of a single strand to simulations of larger-scale mesostructures representing the

deposition of multiple adjacent strands. These approaches can be broadly divided into fluid mechanical models, such as those based on FVM or SPH, and solid mechanical models, typically employing the finite element method (FEM). While fluid mechanical models are well-suited for simulating the flow behavior of molten polymer during single-strand extrusion, their high computational cost limits their scalability. In contrast, solid mechanical models enable the simulation of larger mesostructures involving multiple deposited paths. In these cases, extrusion is modeled by progressive activation of initially inactive elements along a predefined trajectory that closely replicates the actual deposition path of the material.

While mesoscale models provide important insights into the formation of local material properties, they are inherently limited in their applicability to full component behavior. In particular, fluid-mechanical approaches that resolve the extrusion of single strands deliver highly detailed results, but their computational expense restricts them to very small domains and prevents direct upscaling to entire components. Solid-mechanical models based on FEM with element activation are more efficient and, in principle, allow a link to the component scale by representing the deposition of several adjacent strands. However, in the existing literature these models have so far only been applied to relatively small, idealized sections due to computational restrictions, and not in the context of the process conditions encountered during the printing of full components. For the purpose of this work, detailed simulations of isolated strands are not further pursued, as the main objective is the prediction of process-induced effects at the component level. However, for completeness within the state of the art, the most relevant mesoscale models and their main capabilities are briefly summarized in the following sections.

Since this work focuses on unreinforced PLA, models for predicting fiber orientation are not discussed in detail. Such approaches are mainly found in studies that combine flow simulations with orientation tensors [152,153] to predict fiber orientation within extruded strands during the MEX process [24,154–158]. Furthermore, only publications dealing with the numerical prediction of MEX from the moment the polymer exits the nozzle are considered. Models dealing with

polymer flow within the nozzle are not discussed here. The main models in the literature that predict the above MEX characteristics are presented below.

2.5.2.1 Strand deposition and the resulting material structure

There are several mesoscale modeling approaches to predict the deposition of a single strand, its resulting shape, and the resulting material structure. In most cases, these approaches use numerical methods such as the FVM [24–26, 159, 160], SPH [158, 161, 162] and FEM [27, 28, 163, 164], each of which takes into account different physical aspects of the process such as flow, heat transfer, and material solidification.

The FVM is commonly used for detailed prediction of the extrusion of individual strands. Xia et al. [25] combine the FVM with the front tracking method to simulate the flow, temperature distribution, and viscosity in the polymer flow. Mollah et al. [159] use the volume-of-fluid method (VOF) to analyze the behavior of polymer flow in corners with different angles and to investigate differences between different extruder types. Galloway et al. [26] couple the VOF method with overset meshing to explicitly model nozzle motion and simulate complex pressure scenarios such as inclined surfaces. Pricci et al. [160] use FVM to optimize the ironing process to reduce porosity and improve the mechanical properties in the surface layer of printed PLA structures. Serdeczny et al. [24] also use FVM in combination with the volume-of-fluid and level-set methods to simulate the flow of molten polymer at the free surface during strand deposition. The resulting material structure is derived from the geometry of the individual strands. The model allows detailed predictions of strand shape, porosity, weld line density, and surface roughness and shows good agreement with experimental observations.

SPH is also used to simulate strand extrusion. Makino et al. [161] use it to analyze strand formation and identify viscosity and volume flow from the nozzle as important influencing factors. Ouyang et al. [162] use a SPH model to study the thermomechanical behavior of fiber-reinforced materials and their anisotropic

thermal conductivity during printing. Pibulchinda et al. [158] implement an anisotropic viscous flow model using SPH in *Abaqus* to investigate the influence of process parameters such as nozzle height, velocity ratio, and strand overlap on strand geometry, fiber orientation, and strand-to-strand contact. The model is validated against experimental strand shapes and provides insight into the effect of flow conditions on the internal structure of printed strands. However, the approach does not solve for temperature, and therefore cannot capture thermally induced effects such as crystallization or residual stresses.

Agassant et al. [163] first used FEM simulations to model the propagation of the polymer melt. Based on these numerical results, they developed an analytical approximation to estimate the influence of process parameters such as layer thickness and nozzle pressure. In addition, FEM is used in combination with element activation to simulate strand extrusion and the resulting mesostructure. Studies such as those by Barocio et al. [27], Lepoivre et al. [28], and Pibulchinda et al. [164] demonstrate the application of this method to simulate the extrusion of individual strands into a mesostructure and to predict the resulting interfacial strength between the individual strands. In this case of mesoscopic modeling, the geometry of each individual strand is fixed. Within a strand the geometry is discretized into multiple elements across its width and height, allowing for a highly accurate representation of the temperature distribution within the strand.

In addition to the frequently used numerical methods, however, other approaches are also used in the literature: The material point method (MPM) is used in the work of Yildizah et al. [165] to represent viscous material flow with phase change. The model allows the influence of parameters such as nozzle distance, cooling rate, and nozzle movement on the print quality to be investigated. Meng et al. [166] applies a reduced thermo-viscoelastic filament model based on discrete differential geometry and solves the resulting dynamic system using a Newmark implicit time integration method. The approach models filament kinematics, thermal transport and deformation during and after extrusion. A collision detection and response strategy is integrated, and the influence of printing parameters such as print velocity, layer height and nozzle temperature on filament sagging and temperature distribution is investigated. Elmoghazy et

al. [167] used the multiphase field method in combination with a finite difference method (FDM) to investigate the influence of process parameters such as nozzle and bed temperature, viscosity, and layer height on the porosity and Young's modulus of PLA structures. It was found that at higher temperatures, the porosity decreased, resulting in a linear increase in the elastic modulus.

Although these approaches provide detailed insights into strand geometry and mesostructure formation, they are computationally intensive and limited to isolated strands or small representative sections, preventing direct application at the component scale.

2.5.2.2 Predicting interfacial strength

The published methods for predicting the resulting interface strength are mainly based on the non-isothermal healing model of Yang and Pitchumani [150], which is based on polymer reptation process and examines the effects of temperature changes on interface strength. The published papers generally use FEM in combination with element activation [27, 28, 164, 168, 169], finite difference method (FDM) [170] or FVM [171].

Barocio et al. [27] developed a non-isothermal FE model for fiber-reinforced semi-crystalline polymers based on Yang and Pitchumani's healing model, which simulates the interactions between polymer chain diffusion and crystallization during cooling. Benarbia et al. [168] also published a multiphysical FEM model based on Yang and Pitchumani [150] that takes into account the effects of crystallization on bonding. Mahmoud et al. [169] used a combination of heat transfer simulations in *Abaqus* and statistical modeling to analyze layer bonding as a function of various process parameters. Lepoivre et al. [28] complemented these approaches with a transient 2D heat transfer model to determine heat fluxes and the evolution of bonding at interfaces. Coogan et al. [170], on the other hand, used the FDM to simulate interlayer bonding, incorporating real-time melt pressure and temperature data to calculate interlayer strength through contact and diffusion.

While the above work focused on interlayer bonding, i.e., bonding between individual layers, the work of Pibulchinda et al. [164] focuses on bonding between strands, i.e., intralayer bonding. Pibulchinda et al. [164] build on the work of Barocio et al. [27] and use FEM-based heat transfer analyses as well as geometric models to investigate the influence of layer geometry and layer times.

Oskolkov et al. [171] developed a real-time control system for the heating cycle in the FFF printing process based on the FVM. Through segmented heating control, he was able to optimize weld quality, reduce thermal stresses, and improve process stability.

All models highlight the importance of temperature, time and process parameters on the quality of the bond and provide valuable approaches for optimizing bonding in MEX. However, because each strand and interface must be explicitly resolved, the high spatial resolution required for accuracy prevents these models from being directly applied to coarser, component-scale simulations while maintaining the same level of predictive fidelity.

2.5.2.3 Stress formation in the printed strand

Several numerical studies deal with the analysis of stress formation in printed strands during the MEX process. In two consecutive studies, Xia et al. [172, 173] use FVM in combination with the front tracking method to simulate the flow, cooling, solidification, and resulting residual stresses in extruded polymer filaments. While the first study extends the modeling approach of Xia et al. [25] to include shrinkage and solid-state stresses, the second publication focuses on viscoelastic effects that have a decisive influence on the shape and recovery behavior of the filaments. Both models allow detailed prediction of temperature distributions, filament shapes and residual stresses, but are computationally intensive and therefore limited to simple and small structures. An FEM-based stress analysis method is presented by Lukhi et al. [174]. They simulate the material flow using the arbitrary Lagrangian-Eulerian technique and analyze the influence of printing parameters such as velocity and nozzle temperature

on the stress distribution in the strand. Using viscoelastic material models, it is shown that non-uniform stresses build up during cooling, which can lead to deformation. Experimental validations with PLA show that higher printing velocities lead to higher internal stresses and larger bending deformations.

As with other mesoscale approaches, these models are restricted to single strands or small geometrical domains and cannot be applied directly to entire printed components.

2.5.2.4 Crystallinity within the strands

Methods based on numerical techniques have been developed and published for predicting crystallinity within a deposited strand during the MEX process: Brenken et al. [175] used the FEM to simulate both the temperature profile and the crystallization behavior of a fiber-reinforced, semi-crystalline thermoplastic. By coupling a transient heat transfer model with a non-isothermal crystallization model, they were able to predict the temperature and crystallinity distribution during the printing process and predict the evolution of residual stresses as a function of thermal and crystalline history. Elmoghazy et al. [167] used the Nakamura model [176–178] in combination with the multiphase field method to simulate crystallization in PLA during the MEX process. McIlroy et al. [179] extended an existing model using the finite difference method (FDM) and the Rolie-Poly equation [180] to simulate crystallization kinetics in semi-crystalline polymers, such as PLA. They showed that at low printing temperatures, so-called "flow-enhanced crystallization" occurs, in which strain at the filament surface leads to accelerated crystallization, while the interior of the filament crystallizes more slowly.

Although crystallization can be predicted in detail within individual filaments, such predictions cannot be directly extended to full components. The strong dependence of crystallization on local thermal history means that both a much finer discretization and consideration of the different process conditions in an entire component would be required for accurate component-scale predictions.

2.5.2.5 Summary

Published work on numerical prediction of single strand extrusion allows prediction of strand geometry, the resulting degree of crystallinity, or stress formation within the strand. To predict the influence of process parameters on the resulting material structure, individual strands are combined into a MEX structure. However, this influence can only be studied on a small scale and not at the component level.

Overall, mesoscale models provide valuable insights into local mechanisms but are computationally limited and therefore restricted to small geometrical sections. Fluid-mechanical models, while very detailed, are not suitable for representing process conditions at the component scale due to their prohibitive computational cost. In contrast, FEM-based approaches with element activation are more efficient and, in principle, offer a route to link mesoscale phenomena with the component scale. However, in the literature they have so far only been applied to representative volume elements or very small components, rather than under real process conditions of full component printing.

2.5.3 Macroscopic approaches[2]

In recent years, several numerical approaches have been developed to simulate and predict thermo-mechanical phenomena such as PiD or resulting residual stresses during the MEX process at the component level. The FEM is the most widely used approach for simulating additive manufacturing processes. The basic MEX process simulation approach was first introduced by Zhang and Chou [181, 182]. As mentioned above, it is based on the progressive activation of initially inactive elements along a predefined trajectory. Figure 2.11 illustrates the schematic structure of this simulation framework.[2]

[2] Adapted and revised from [2], © CC BY 4.0, cf. footnote p. 46 for details.
[2] Adapted and revised from [2], © CC BY 4.0, cf. footnote p. 46 for details.

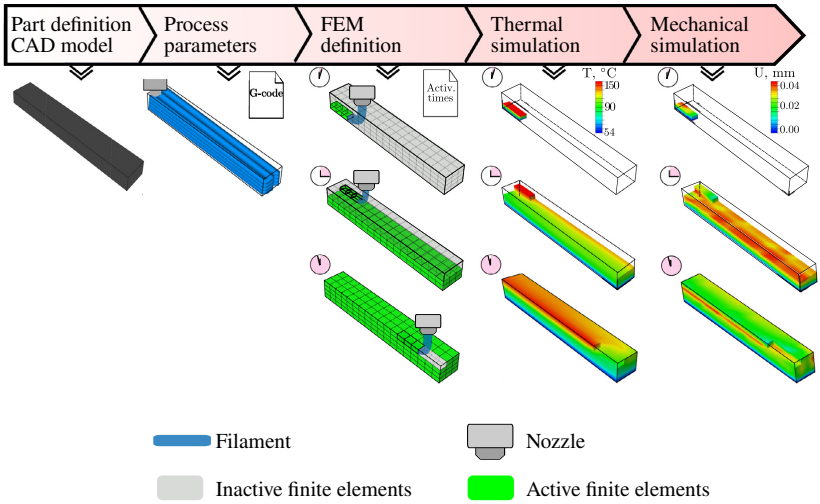

Figure 2.11: Schematic representation of the FE-based simulation framework for MEX process simulation on macro scale. The approach based on the progressive activation of elements that are initially inactive along the deposition path defined by the G-Code. The simulation incorporates process parameters, the material deposition strategy, and temporal activation in order to predict PiD and residual stresses at the component level. (Adapted from Trofimov et al. [30])

The simulation begins with defining the component to be printed and its corresponding G-Code, which specifies the deposition strategy and other adjustable process parameters. In a preprocessing step, the component is discretized using hexahedral or tetrahedral finite elements. These elements are initially inactive and activated step by step according to the deposition path defined in the G-Code. The activation schedule is also determined during preprocessing. This element activation approach is implemented, for example, in *Abaqus* (provided through the so-called AM Modeler [183, 184]), but also in other simulation platforms, such as *Digimat-AM* [185] and *Ansys Additive* [186]. The specific implementation of the activation step varies depending on the commercial FE

software used. Since *Abaqus* is used in this thesis, please refer to the official *Abaqus* documentation for detailed information on element activation [183].[2]

Abaqus uses a so-called *event series* to control the deposition strategy, specifying the timing, path and extrusion status. Inactive elements do not contribute to the global solution of the FE model. However, they can be included in the solution process and adapt to the deformation of the already printed structure during the PiD simulation. This approach helps to prevent excessive deformation of inactive elements and improves numerical stability. Furthermore, *Abaqus* supports partial element activation, allowing multiple strands or layers to be represented within a single element. In such cases, the element mass is scaled proportionally to the actual printed volume, enabling a more accurate representation of the material distribution. Moreover, this simulation strategy is not limited to MEX processes. Similar element activation-based approaches are employed in the simulation of other additive manufacturing technologies, such as Laser powder bed fusion (LPBF) and Directed energy deposition (DED) [183, 186]. In these processes, the PiD is also computed by activating elements in accordance with the energy input and material consolidation path.[2]

In addition to thermal modeling, the material model used to describe the polymer's mechanical behavior plays a crucial role in the accuracy of PiD predictions. Consequently, published simulation approaches primarily differ in their choice of material model and its complexity. Most studies employ a linear elastic model with either temperature-independent stiffness [181, 182, 187–191] or temperature-dependent stiffness [192–195].

More advanced approaches incorporate viscoelastic behavior [29, 196, 197] or elastoplastic effects [30, 198–200]. Notably, Corvi et al. [199] and Trofimov et al. [30] build upon the modeling framework proposed by Cattenone et al. [198]. Brenken et al. [201] demonstrated that viscoelasticity and stress relaxation significantly influence the accuracy of PiD predictions. Additionally, several

[2] Adapted and revised from [2], © CC BY 4.0, cf. footnote p. 46 for details.

studies have examined the crystallization behavior of semi-crystalline polymers because it can affect the deformation of printed components [190,192,196,197].

The influence of the developing mesostructure on stiffness and anisotropic structural properties has been discussed in the previous sections. Nevertheless, in most simulations the material is still modeled as temperature-dependent but isotropic. For example, Zhou et al. [195] employ a thermoelastic isotropic polymer model, while Cattenone et al. [198] use a thermoelastoplastic model without accounting for process-induced anisotropy. *Abaqus*-based studies (e.g., Brenken et al. [29,201] and Trofimov et al. [30]) rely on the ORIENT subroutine to assign an orientation vector along the deposition path. In the implementation provided by the *Abaqus AM Modeler* [183], the orientation vector is defined once based on the initially deposited volume fraction and is not updated when additional material with different orientations is added to the same element. As a consequence, a component with alternating $0\,°/90\,°$ infill and an element height that is an even multiple of the layer height may be represented as having effectively unidirectional material properties (e.g., entirely $0\,°$). The actual mixture of orientations within the element is therefore neglected. This simplification can introduce significant errors in predicting stiffness and deformation behavior. Furthermore, the approach is inherently limited, as it considers only a single orientation vector rather than a full orientation tensor, thereby restricting the representation of more complex orientation states.[2]

2.5.4 Multiscale MEX-simulation

As discussed in detail in the previous sections, numerous simulation approaches have been developed to describe the MEX process at individual size scales (micro, meso, and macro). The challenge in this context is how to effectively link these scales to accurately predict local component-level properties, such as

[2] Adapted and revised from [2], © CC BY 4.0, cf. footnote p. 46 for details.

degree of crystallization or interfacial strength between strands, under realistic process conditions.

In the context of multiscale simulation of the MEX process, modeling approaches at different scales have mostly been linked sequentially. Microscale or mesoscale information (e.g., mesostructure) is used as input data for component simulations (macrosimulation). These approaches are commonly used to homogenize stiffness tensors with representative volume elements (RVEs) and are typically utilized in structural simulations (cf. Section 2.6). Castello-Pedro et al. [31], however, transferred this principle to process simulation using the commercial software *Digimat-AM*. Using RVE models with explicitly mapped fiber orientation, they generated material data for component simulations to predict residual stresses and PiD. Besides this work, the author is not aware of any other publication on other sequentially coupled multiscale approaches for predicting local properties, such as degree of crystallization or interfacial strength, at the component level.

Xia et al. [202] addressed the consistent coupling of different scales in their research. They developed a multiscale, multiphysics model for MEX that considers temperature gradients, crystallization effects, and process parameters. The model enables the numerical simulation of temperature distributions and shape changes at the macroscale, filament formation at the mesoscale, and thermal stresses and crystallization processes at the microscale. For the numerical implementation of the multiscale approach across the different scales, the model uses the pressure correction method in combination with a parallel Poisson solver and fast fourier transformation (FFT) to calculate temperature and phase changes at the macroscale. The system is solved in a decoupled elliptical framework, where temperature and phase fields are treated separately. At the microscale, the invariant energy quadratization method is employed, which linearizes the system and ensures unconditional energy conservation, enabling larger time steps with stable computation. However, integrating existing numerical methods into the multiscale approach poses significant challenges. The mathematical and numerical methods typically employed at the macro, meso,

and micro scales (e.g., FEM, FVM, or SPH) differ in their underlying characteristics, making seamless coupling and the direct application of previously published approaches difficult. These challenges are particularly due to the varying requirements of each method in terms of time and spatial resolution.

In summary, coupling different scales is essential for quantitatively predicting local properties, such as the degree of crystallization or interfacial strength, at the component level.

2.6 Structural simulation[2]

Since the local mesostructure determines final component performance, studies have examined typical mesostructures in structural simulations of MEX components using sequentially coupled multiscale approaches to formulate stiffness. The selected overarching approaches in this area are therefore summarized and evaluated with regard to their applicability in process simulations for predicting PiD. Published work in this area aims to capture the anisotropic stiffness properties and mechanical characteristics of MEX components, typically through multiscale modeling techniques. These approaches include homogenization based on classical laminate theory (CLT) [101, 203–205], representative volume elements (RVEs) [206–208], coupled RVE and CLT approaches [209], and fast fourier transform homogenization [210].[2]

CLT estimates the effective elastic properties of MEX components by modeling a laminate composed of multiple layers with different infill angles and combining the stiffness contributions of each layer. This approach efficiently captures the variation of material properties across the laminate thickness and is suitable for simulating the overall structural behavior at the laminate scale. However, in process simulations at the component level, where elements are activated

[2] Adapted and revised from [2], © CC BY 4.0, cf. footnote p. 46 for details.

successively and the material structure evolves over time, CLT cannot directly account for these dynamic changes during the manufacturing process.[2]

Homogenized models based on RVEs provide a more detailed mesoscale description, making it possible to capture evolving material structures and temperature-dependent properties throughout the process. Despite this advantage, RVE simulations in FEM-based process models face significant computational challenges: for each element and time increment where the local mesostructure or temperature differs, a separate RVE calculation would be required. Continuous recalculation of RVEs throughout the simulation is highly demanding, which severely limits their practical applicability for real-time process simulations with element activation.[2]

FFT-based homogenization methods are a promising approach for efficiently calculating effective material properties in heterogeneous systems, such as MEX structures. These methods are particularly effective for modeling material behavior in complex microstructures because they can accurately capture material distribution and spatial variations. FFT-based homogenization rapidly and accurately accounts for structural variations through Fourier transformations, allowing for the calculation of material properties at the mesoscale. Liu et al. [210] developed an FFT-based homogenization approach that accurately captures the anisotropic material properties of MEX components. Their model uses a coupled geometry-material description in which the anisotropic properties of materials along the extrusion paths are represented by a rotation-transformed transversely isotropic material model. For macro-homogenization, the researchers applied a Green's functional approach and an FFT-based solution to the Lippmann-Schwinger equation to determine effective material stiffness. However, this approach is limited for real-time process simulations with element activation because it requires recalculating the material properties at each time step to account for temperature variations and changes in the mesostructure. The resulting high computational demand complicates integration into

[2] Adapted and revised from [2], © CC BY 4.0, cf. footnote p. 46 for details.

commercial FE software, such as *Abaqus*, and renders its practical application in real-time process simulations virtually impossible.[2]

In summary, various approaches exist for accounting for the influence of mesostructure on anisotropic stiffness. However, these methods are primarily designed for the final, static stiffness of components. Consequently, they are either unsuitable or extremely computationally costly when applied to process simulations with element activation, wherein mesostructures and temperature distributions change continuously.[2]

2.7 G-Code interpretation

The G-Code contains instructions for the movement of the print nozzle, extrusion rates, nozzle velocity, and other process parameters, such as temperature and layer height. These parameters are crucial for printing the component step by step. Additionally, the G-Code is interpreted by printer-specific firmware, which considers hardware-related restrictions, such as acceleration and cornering, as well as other physical limitations depending on the installed hardware. During this motion planning, the nozzle velocity and trajectory are adjusted according to these constraints, which can lead to deviations from the originally specified path. Figure 2.12 illustrates this typical workflow from a CAD model to an extruded polymer. As shown in the figure on the right, the discrepancy between the planned and actual nozzle position can lead to local over-extrusion, potentially impairing the functionality of the final component.

Although G-Code is the standard programming language, only little research has been conducted on how printer firmware interprets G-Code and its influence on the printing result. Yadav et al. [32] demonstrate that parameters in the firmware, such as velocity, acceleration, and jerk (the rate of change of acceleration, which in firmware settings controls curve behavior and smoothness), can impact the

[2] Adapted and revised from [2], © CC BY 4.0, cf. footnote p. 46 for details.

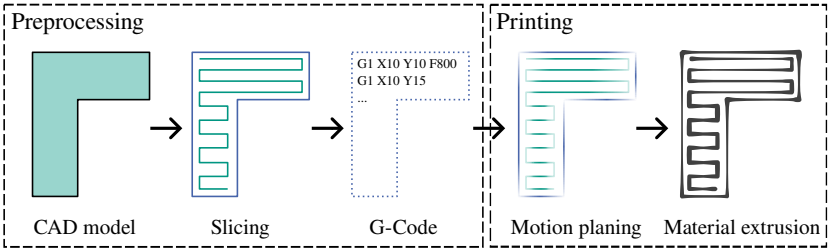

Figure 2.12: Typical workflow from CAD model to extruded polymer. The interpretation of the G-Code through motion planning, including variations of the nozzle velocity along the trajectory (indicated by the color gradient), results in a different nozzle position compared to the trajectory specified in the slicing. As illustrated in the figure on the right, this discrepancy can lead to local over-extrusion, impairing the functionality of the final component.

surface roughness of components. However, only the influence on surface quality was considered, while other possible effects on mechanical properties or process conditions were not taken into account. Propst and Mueller [33] also highlight the limitations of G-Code. They demonstrate that G-Code's sequential line interpretation makes integrating complex control commands difficult and can potentially lead to defects. These findings illustrate that, while G-Code provides basic path information, it must be translated into motion sequences by printer firmware. This, in turn, can influence the manufacturing process. A systematic investigation of this effect in relation to the MEX of thermoplastic filaments is still lacking.

Since the nozzle movement affects both the effective material flow and the temperature distribution within the component during the process, it also has a direct impact on the development of internal stresses and PiD. Therefore, it is essential to account for nozzle movement in process simulations. Commercial simulation software for additive manufacturing adopts different strategies to incorporate nozzle motion as a boundary condition. Some solutions, such as *Digimat-AM* and *Ansys Additive*, allow direct import of G-Code files [185,186], while others, such as *Abaqus*, require trajectory information to be provided in a software-specific format [183].

Digimat-AM first converts the G-Code into layer-by-layer path segments, which are then prepared for thermomechanical simulations. The motion paths are segmented and the process parameters are extracted and converted into a form suitable for simulation. However, the *Digimat-AM* user manual does not detail how the G-Code is interpreted internally. Nor does it explicitly state whether hardware restrictions are taken into account. Therefore, it can be assumed that the software derives the nozzle movement for each path segment from the positions and feed rates defined in the G-Code and uses this information to determine layer activation for the simulation. [185]

Ansys Additive, a software for simulating metal-based additive manufacturing processes (e.g. DED), also allows users to import G-Code files directly. The G-Code is read by the software, which translates motion and laser commands into clusters that are used for thermal and mechanical simulation of the weld seams. These clusters then serve as the basis for layer-by-layer simulation of material application and component development. However, there is no detailed information available on how the G-Code is interpreted with regard to intervening firmware. Alternatively, machine paths and other relevant information that are typically included in the G-Code can also be manually specified. [186]

In contrast, *Abaqus* requires an *event series* for process simulation that describes the temporal activation of individual component segments. For the material extrusion process (MEX), this means that information on position, time, and extrusion status must be specified for each linear motion segment. Users are responsible for generating this *event series* from the G-Code, which requires additional preprocessing steps. Currently, there are no standardized interfaces for this within *Abaqus*. [183]

Since *Abaqus* is used in this work, the following section explains the extent to which information from the G-Code was extracted and interpreted for the *event series* in previously published studies, provided that such details were specified. In literature, the process of generating the required *event series* from nozzle movement is rarely described explicitly. Barocio [211] records nozzle movement directly during the printing process and converts it into an

event series . Cattenone et al. [198], on the other hand, generate the necessary information line by line from the G-Code using a *Matlab* script, without considering additional influencing factors or making any further interpretations of the firmware-specific implementation. One advantage of the approach by Barocio [211] is that it includes firmware effects, such as acceleration profiles or cornering, in the recorded motion data. However, this method requires the component to be physically printed before simulation can begin.

In summary, a systematic interpretation of the G-Code that takes relevant firmware limitations into account has not been performed to achieve the most realistic representation of nozzle movement possible. Additionally, the impact of firmware settings on nozzle movement, process conditions, and final component behavior has not been extensively studied.

2.8 Literature summary and research gap

Summary MEX is a widely used additive manufacturing process. It is characterized by simple handling, low cost, and a high degree of design freedom. During the process, a thermoplastic filament is melted in a heated nozzle and built up layer by layer to form a component. The quality of the resulting component is determined by the interaction of material properties, process parameters, and printer-specific influences. To ensure reliable dimensional accuracy and reproducible component properties, all process steps and their interactions must be thoroughly understood, from filament feeding and melt cooling to process-induced deformation behavior of the entire component.

PLA is one of the most commonly used materials in the MEX process. It is biodegradable and easily processed. However, its thermal and mechanical properties vary widely due to differences in its chemical composition, particularly with regard to the stereochemical form used (PLLA, PDLA, or racemic PDLLA), as well as additives, molecular weight, and crystallinity. The thermomechanical behavior of PLA is highly temperature-dependent. Several studies

have shown that PLA crystallizes poorly under typical cooling conditions in the MEX process, as well as in other processes such as injection molding. rapid cooling prevents the formation of an ordered crystal structure, resulting in PLA predominantly being present in an amorphous form in these applications. This affects its strength, stiffness, and thermal stability.

The layered, strand-based arrangement resulting from the MEX process creates a characteristic mesostructure. It is defined by inter-strand bonding, pores, and deposition-induced interfaces. These features significantly influence the component's mechanical properties, particularly its anisotropy in stiffness and strength. The orientation and cross-linking of filament strands cause substantial variation in mechanical behavior depending on the measurement direction. For instance, components with unidirectionally aligned strands tend to be stronger and stiffer along the printing direction, whereas transverse directions demonstrate reduced performance. Thus, the anisotropic properties are strongly influenced by the printing parameters and the chosen deposition path. Many studies have examined these effects, but the results vary considerably due to differences in specimen preparation and processing conditions. This variability, together with the lack of standardized guidelines for specimen preparation and testing, makes it difficult to compare mechanical properties across studies in a consistent and reliable manner.

Several process simulation approaches have been published for predicting process-induced effects such as fiber orientation, strand geometry, interfacial strength, crystallization, or residual stresses and PiD. Microscopic models capture polymer dynamics and flow behavior in the nozzle area, explicitly resolving individual fibers. However, due to the level of detail required, these models are limited to small geometries and are computationally intensive. Mesoscopic approaches consider the local strand geometry and voids within the mesostructure. This enables the detailed prediction of temperature profiles and local phenomena, such as interfacial strength and crystallization. However, they are usually only applicable to smaller components or representative volume elements, making it difficult to simulate normal-sized components. Macroscopic

models homogenize the complex mesostructure, enabling the simulation of entire components. They are therefore useful for predicting residual stresses and PiD. These models usually follow a basic FE approach of element activation. The approaches differ mainly in the material model chosen. Due to computing time requirements, the complex mesostructure and its effects are often combined into a single element. However, the influence of these mesostructures on the simulation results is often not adequately considered, which can affect the accuracy of the predictions. To predict local component properties, such as degree of crystallization or interfacial strength, under realistic process conditions, the different scales must be linked. Most multiscale approaches in process simulation sequentially couple these scales, using micro- or mesoscale information (usually the mesostructure) as input for macroscopic component simulations. However, only stiffness information is typically transferred. Moreover, in macroscopic simulations with stepwise element activation, the local mesostructure evolves continuously during the process, which makes an efficient and accurate transfer of mesoscale information particularly challenging. Currently, there is no multiscale approach that connects mesoscale methods for predicting local properties with FE simulations at the component level.

In the field of structural simulation, multiscale modeling approaches have been developed to capture the anisotropic stiffness and mechanical properties of MEX components. These methods aim to understand how the complex mesostructure of the material influences the overall mechanical behavior of the component across different scales. These include classical laminate theory (CLT)-based homogenization, representative volume elements (RVEs), coupled RVE and CLT methods, and fast Fourier transform (FFT)-based homogenization. CLT and RVE models provide insight into material behavior but have limitations in real-time process simulations due to difficulties in accurately modeling temperature and mesostructure changes. FFT-based homogenization is a more efficient approach for complex microstructures but still struggles with the high computational requirements necessary for element activation in process simulations.

The so called G-Code contains instructions for nozzle motion and other parameters of the MEX process. The printer's firmware then interprets these

instructions. However, due to hardware limitations, such as acceleration and cornering capabilities, the firmware may modify these instructions. This affects the actual motion of the nozzle and, consequently, the properties of the final component. While some simulation programs allow G-Code import, it is often unclear how firmware limitations are considered. Little research has been conducted on integrating firmware effects into nozzle motion and their influence on surface quality. Consequently, the complete effect of firmware on MEX simulations and component behavior remains unclear.

Research gap and challenges Despite substantial progress in the field of MEX, several critical challenges remain that limit the accurate prediction and control of process-induced effects. The interpretation of G-Code by printer firmware can modify nominal commands due to hardware constraints, leading to deviations in nozzle motion, local deposition rates, and thermal histories. These deviations influence strand bonding, crystallization, and process-induced deformations (PiD), yet no systematic study has quantified these effects or investigated their impact on component properties. A thorough analysis of firmware-induced deviations is therefore essential to understand and predict local process conditions accurately.

Mechanical property data for MEX structures often exhibit considerable variability, resulting not only from differences in filament chemistry but also from variations in specimen preparation. Without standardized, process-representative characterization methods, simulations cannot reliably reproduce component behavior. Establishing methodologies for characterizing material properties under realistic MEX process conditions is thus crucial to provide consistent and reliable input data for both experiments and computational analyses.

The strand-based mesostructure of MEX components evolves dynamically during printing, strongly affecting anisotropic stiffness and and the resulting PiD. Current macroscopic models for predicting PiD largely neglect these evolving mesostructures, limiting their predictive accuracy. Homogenization frameworks

that account for mesostructural evolution are therefore required to capture global deformations while remaining computationally efficient.

Although high-resolution mesoscale models can resolve local phenomena such as interfacial strength and crystallization, these models are rarely coupled consistently with component-level simulations. Existing multiscale approaches typically transfer only stiffness information, failing to capture how local variations influence overall component performance. Developing multiscale modeling strategies that integrate detailed mesoscale simulations with macroscopic models is necessary to enable accurate prediction of local material behavior under realistic process conditions.

Overall, there is a pressing need to systematically capture and model the effects of firmware interpretation, process-representative material properties, evolving mesostructures, and multiscale interactions to enable reliable prediction of process-induced effects in MEX components.

3 Objectives and outline

3.1 Objectives

A thorough evaluation of the relevant research in the field of MEX reveals that, despite substantial progress, there are still key research gaps. Significant advances have been made in understanding the underlying manufacturing processes, the effects of process-specific mesostructures on structural properties, and the development of simulation approaches across different scales. However, several open questions still hinder the accurate prediction of process-induced effects in MEX-manufactured components. These include systematically investigating G-Code interpretation by printer firmware, ensuring representativeness in experimental characterizations, and considering dynamically evolving mesostructures when predicting PiD. Additionally, consistent multi-scale modeling approaches that effectively link small-scale system models with component-level representations are lacking.

This thesis addresses these challenges by developing novel methodological approaches and numerical models that accurately represent process conditions, with the aim of improving the understanding of the underlying physical mechanisms and enhancing the prediction accuracy of process-induced effects. Based on the identified research gaps, the following four main objectives have been derived for this thesis:

Objective O-1. Systematic investigation of the influence of firmware interpretation of G-Code on nozzle motion during the MEX process, including quantification of deviations from theoretical motion paths and analysis of their impact on local process conditions.

Objective O-2. Development and evaluation of methodologies for characterizing material properties under real process conditions, specifically for PLA-based MEX components. This aims to ensure that the measured mechanical properties accurately reflect those of actual components, providing reliable data for both experimental studies and computational analyses of MEX structures.

Objective O-3. Development of a homogenization framework for MEX process simulations that incorporates the dynamically evolving local mesostructures and anisotropic stiffness characteristics at the macro scale. This enables efficient prediction of process-induced deformations at the component level, accounting for mesostructural effects without requiring full-resolution mesoscale simulations.

Objective O-4. Development of a multiscale simulation approach that couples high-resolution mesoscale FE models with macroscopic component-level models. This approach enables accurate prediction of local material behavior under component-specific process conditions, capturing phenomena that homogenized macro models cannot resolve.

Delimitation This thesis focuses on the MEX process, addressing research gaps related to the effects of firmware, the characterization of representative materials, the homogenized consideration of evolving MEX mesostructures in component simulations, and the coupling of detailed mesoscale models with

macroscopic simulations to predict local material behavior under realistic process conditions. The methods and numerical approaches are developed and validated using PLA filaments. More complex material systems, such as multi-material prints or materials with additives or fiber reinforcements, are not considered. Post-processing effects, such as annealing or heat treatments, which can influence final material properties, are also neglected. These aspects require further investigation and lie beyond the scope of this thesis.

3.2 Outline

This thesis is structured according to its objectives into four main chapters (Chapters 4–7), followed by a conclusion and recommendations for future research in Chapter 8.

Chapter 4 deals with the discrepancy between the nominal and actual nozzle motion during the MEX process, addressing objective O-1. First, Section 4.1 introduces a methodology for predicting motion deviations. Next, the methodology is validated using experimental printing data (Section 4.2). Then, metrics to quantify deviations are presented (Section 4.3), and the influence of firmware settings on final process conditions is investigated (Section 4.4).

Chapter 5 examines the representativeness of mechanical characterization in MEX structures, addressing objective O-2. Requirements for suitable specimen preparation are defined and translated into hypothesis that can be validated experimentally (Section 5.1). These hypotheses are verified through tensile tests and SEM analysis (Sections 5.2–5.4). Based on these results, guidelines for specimen preparation are derived (Section 5.5).

Chapter 6 addresses the influence of the process-typical mesostructure on the numerical prediction of PiD, focusing on objective O-3. After outlining the general modeling procedure (Section 6.1), experimental studies are conducted to identify the relevant thermomechanical and kinetic effects of the PLA

mesostructure (Section 6.2). Subsequently, the PLA material modeling is described (Section 6.3), and typical mesostructures are categorized (Section 6.4). Section 6.5 presents homogenization approaches, including an isotropic method and a technique that accounts for the development of local mesostructures and the resulting anisotropic stiffness. The corresponding implementation workflow is outlined and verified, and subsequent numerical studies investigate material orientation, its evolution, and element size effects. Finally, the anisotropic homogenization method is validated experimentally and compared to the isotropic approach (Section 6.6).

Chapter 7 addresses objective O-4 by coupling macroscale process simulations with finely resolved mesoscale FE models using a submodeling approach. The necessary modeling steps to apply the methodology to the MEX process are outlined in Section 7.1. The considerations used for PLA as an example material are described in Section 7.2. Section 7.3 presents a sensitivity analysis of mesh size and time increment for the most accurate prediction of the temperature history. The approach is then verified numerically in Section 7.4 and validated experimentally in Section 7.5.

4 Prediction and evaluation of accurate nozzle motion using G-Code simulation

Outline

The following chapter presents a methodology for G-Code simulation to analyze the discrepancy between the nominal nozzle motion defined by the slicer and the actual nozzle motion during manufacturing. As part of this work, a simulation framework named *pyGCodeDecode* (*pyGCD*) was developed and published as open-source software [212, 213]. The methodology replicates the printer-specific firmware's interpretation, taking into account the different procedures used by different firmware versions. First, the methodology for analyzing deviations in nozzle motion is presented in Section 4.1 considering firmeware settings like maximum velocity, acceleration sequences, and cornering. Second, the methodology is validated using experimentally measured printing times in Section 4.2. Section 4.3 presents metrics for quantifying deviations between defined and actual process conditions within the printed component. Finally, Section 4.4 shows the influence of firmware settings on the final process conditions using the introduced metrics with simple component geometries and different infills. The main objective of G-Code simulation is to provide information on the current nozzle motion for process simulations, as well as a methodology for predicting how firmware settings influence current process conditions. Section 4.5 summarizes the results and discusses possible applications of the methodology.

4.1 G-Code simulation

The goal is to translate the G-Code generated by the slicing software into the actual nozzle motion [212] in order to reconstruct the event series for process simulation, and to subsequently analyze the influence of the firmware settings on the realized nozzle motion compared to the specified target motion. The final nozzle motion is determined by the target nozzle position and velocity specified in the slicing software and stored in the G-Code. This is done in conjunction with accelerations sequences and maximum possible velocities for each axis, as well as any curve motion algorithms implemented in the printer's firmware. In most applications, each nozzle motion represents a straight-line movement between two specified coordinates in the build space. Therefore, a curve is defined by the turning angle θ of the direction vectors of two consecutive movement sections. As part of this work, a simulation framework named *pyGCodeDecode* (*pyGCD*) was developed and published as open-source software [212, 213]. The basic concept and implementation of *pyGCD* were first published in [212]. *pyGCD* interprets G-Code similarly to firmware and predicts resulting nozzle motion while accounting for printer-specific hardware restrictions and firmware behavior. The following sections describe the general modeling framework and how to calculate the resulting velocity profiles. This involves comparing various common firmware versions.

4.1.1 Trajectory modeling framework

For each motion m, the nozzle positions and relevant motion parameters are extracted from the G-Code. These include the scalar target velocity $v_{\mathrm{t},m}$ in the G-Code, which specifies the magnitude of the desired feedrate along the planned motion path, as well as the nozzle acceleration $a_{\mathrm{N},m}$.

A continuous motion path is reconstructed by linking the nozzle positions as defined in the G-Code. Each movement is associated with its own real velocity profile $v_m(t)$ [212] (hereinafter referred to as v_m), which is influenced by $v_{\mathrm{t},m}$ of

the G-Code as well as the kinematic constraints from preceding and subsequent motions.

The printer-specific firmware optimizes v_m by considering the accelerations $a_{\mathrm{N},m}$, the maximum allowable velocities $\boldsymbol{v}_{\max}$ for each axis, and limitations on direction changes (corners), often characterized by the maximum permissible jerk $\boldsymbol{j}_{\max}$ [38–40, 214, 215]. The entry and exit velocity vectors $\boldsymbol{v}^{\mathrm{in}}_{\mathrm{junc},m}$ and $\boldsymbol{v}^{\mathrm{out}}_{\mathrm{junc},m}$ of each motion m are computed using firmware-specific cornering methods. These methods take into account the preceding and following movement sequences to ensure smooth transitions and optimal performance. To realistically simulate the execution of the G-Code, this behavior is replicated virtually within the presented framework and described in detail in Section 4.1.3.

To determine the axis-specific velocities, the scalar velocity v_m is projected onto the direction of the current motion m and a normalized extrusion component. The motion direction is defined by the normalized displacement vector of motion m, i.e., scaled to unit path length. Similarly, the extrusion value represents the amount of material to be deposited during motion m, also normalized by the path length of that motion. This projection yields a velocity vector $\boldsymbol{v}_m \in \mathbb{R}^4$ at each time, with the first three entries corresponding to the velocities along the X-, Y-, and Z-axes, and the fourth entry representing the extrusion rate v_E:

$$\boldsymbol{v}_m = (v_X, v_Y, v_Z, v_E)^\top. \tag{4.1}$$

The projection approach is based on the assumption that all axes involved must move proportionally to one another in order to produce a linear trajectory in cartesian space. By projecting v_m onto the normalized motion and extrusion value, it is ensured that both the axis velocities and the extrusion rate remain consistently coupled to the actual nozzle velocity. This guarantees uniform material deposition along the intended linear path.

Each successive motion in the G-Code is represented as a so-called *planner block* with an individual velocity profile v_m, which comprises segments with constant acceleration [212]. The firmware-specific cornering algorithm defines

how adjacent *planner blocks* interact with each other. A detailed description of the modeling approach of these velocity profiles follows in Subsection 4.1.2.

4.1.2 Velocity profile

A velocity profile within a *planner block* describes the velocity profile v_m as a function of time. The scalar target velocity $v_{\mathrm{t},m}$ is specified for each movement via the G-Code. v_m in each motion starts from the initial velocity $\|\boldsymbol{v}^{\mathrm{in}}_{\mathrm{junc},m}\|$ with a given acceleration $a_{\mathrm{N},m}$ until $v_{\mathrm{t},m}$ is reached. This defines the acceleration phase (ap). This is followed by a uniform phase with constant velocity ($v_{\mathrm{t},m}$). To reduce v_m to the exit velocity $\|\boldsymbol{v}^{\mathrm{out}}_{\mathrm{junc},m}\|$, a deceleration is applied, which defines the braking phase (bp). Figure 4.1 shows four different types of velocity profiles. If a movement starts and ends at standstill and the target velocity $v_{\mathrm{t},m}$ can be reached, a trapezoidal profile is produced (Figure 4.1 top left). If multiple movements are linked together, the initial and final velocities $\|\boldsymbol{v}^{\mathrm{in}}_{\mathrm{junc},m}\|$ and $\|\boldsymbol{v}^{\mathrm{out}}_{\mathrm{junc},m}\|$ may be non-zero. Provided the available distance is still sufficient, the target velocity $v_{\mathrm{t},m}$ can still be reached, as illustrated in the top right of Figure 4.1. However, if the available distance is too short to reach $v_{\mathrm{t},m}$ using the maximum acceleration and deceleration, a triangular profile results (Figure 4.1 bottom left). In extreme cases, the movement is limited to a single acceleration or braking phase, resulting in a linear velocity profile without a constant-velocity segment (Figure 4.1 bottom right).

Since a change in the path orientation occurs between segment m and $m{+}1$ (i.e., at the corner), the two velocity vectors $\boldsymbol{v}^{\mathrm{out}}_{\mathrm{junc},m}$ and $\boldsymbol{v}^{\mathrm{in}}_{\mathrm{junc},m+1}$ generally differ in direction, even if their magnitudes are identical. While the G-Code specifies $v_{\mathrm{t},m}$, the firmware calculates these transition velocities using special curve algorithms. This behavior has been replicated in the simulation, which is explained in more detail in the following Subsection 4.1.3.

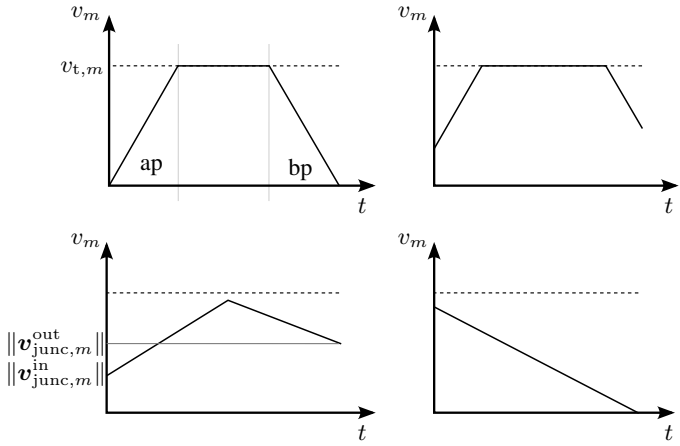

Figure 4.1: A variety of representative velocity profiles within a *planner block* are shown, with the target velocity $v_{\mathrm{t},m}$ indicated by a dotted line. *Upper left:* A profile that starts and ends at rest and reaches the target velocity during motion. *Upper right:* A planning block with non-zero initial and final velocities due to adjacent motion segments that allow the target velocity to be reached. *Lower left:* A scenario with non-zero initial and final velocities where the target velocity is not attained. *Lower right:* A planning block that terminates at rest. The entire distance is required for deceleration, and the target velocity remains unattained.

4.1.3 Cornering method

At the transition between two linear motion segments with different orientation, the movement is governed by a continuous change in the velocity vector. The key quantities are the exit velocity $\boldsymbol{v}^{\mathrm{out}}_{\mathrm{junc},m}$ from segment m, and the entry velocity $\boldsymbol{v}^{\mathrm{in}}_{\mathrm{junc},m+1}$ into the subsequent segment $m+1$. To ensure a smooth and dynamically consistent transition, both vectors must have the same magnitude, denoted by v_{junc}.

The goal is to calculate v_{junc} so that the transition time between consecutive segments is as short as possible. However, this must be done within the limits imposed by the system's dynamic capabilities, particularly the lateral forces resulting from directional changes, to avoid vibrations or instability. Figure 4.2

illustrates the motion across multiple segments, including the translational target velocities $\boldsymbol{v}_{\mathrm{t},m-1}$, $\boldsymbol{v}_{\mathrm{t},m}$, and $\boldsymbol{v}_{\mathrm{t},m+1}$, as well as the corresponding junction velocities. The directional change between segments is quantified by the turning angle θ, defined between $\boldsymbol{v}^{\mathrm{out}}_{\mathrm{junc},m}$ and $\boldsymbol{v}^{\mathrm{in}}_{\mathrm{junc},m+1}$. Larger angles θ generally require lower values of v_{junc}, as higher accelerations are needed to redirect the motion within physical constraints.

There are two commonly used approaches to compute the junction velocity v_{junc} when a change in movement direction occurs. In both methods, the scalar magnitude of the junction velocity v_{junc} is determined first. By projecting this scalar value onto the direction of motion, i.e., onto the direction of the current motions m and $m+1$, the resulting vectorial junction velocities $\boldsymbol{v}^{\mathrm{out}}_{\mathrm{junc},m}$ and $\boldsymbol{v}^{\mathrm{in}}_{\mathrm{junc},m+1}$ are obtained.

The first approach is the *Classic jerk* method. In this method, v_{junc} is determined by scaling the target velocity vectors $\boldsymbol{v}_{\mathrm{t},m}$ and $\boldsymbol{v}_{\mathrm{t},m+1}$ such that the maximum instantaneous change in their individual axis components does not exceed a predefined limit.

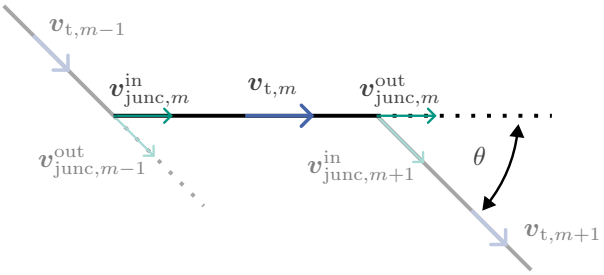

Figure 4.2: Visualization of successive linear motion segments and their associated velocity vectors. The transition between segments is characterized by the turning angle θ, defined between the exit velocity $\boldsymbol{v}^{\mathrm{out}}_{\mathrm{junc},m}$ and the entry velocity $\boldsymbol{v}^{\mathrm{in}}_{\mathrm{junc},m+1}$. The diagram illustrates how θ describes the directional change in motion and serves as a key parameter for determining admissible cornering velocities.

The second approach, called *Junction deviation*, models direction changes as virtual circular arcs. The velocity at the junction is limited to ensure that the resulting centripetal acceleration does not exceed the maximum acceleration specified in the firmware. The following provides a basic introduction to both approaches.

Classic jerk In the Classic jerk method, the velocity change at the junction between two consecutive motion segments is evaluated based on the instantaneous difference between the corresponding velocity vectors. The resulting jerk vector $\boldsymbol{j}$ is defined as a function of the incoming and outgoing target velocities $\boldsymbol{v}_{\mathrm{t},m}$ and $\boldsymbol{v}_{\mathrm{t},m+1}$, each in $\mathbb{R}^4$ including all relevant axes (commonly X, Y, Z, and E):

$$\boldsymbol{j} = F(\boldsymbol{v}_{\mathrm{t},m}, \boldsymbol{v}_{\mathrm{t},m+1}), \quad F : \mathbb{R}^4 \times \mathbb{R}^4 \to \mathbb{R}^4 \tag{4.2}$$

The function F typically computes the element-wise difference between the velocity components of the motions, i.e., $\boldsymbol{j} = \boldsymbol{v}_{\mathrm{t},m+1} - \boldsymbol{v}_{\mathrm{t},m}$. If the magnitude of $\boldsymbol{j}$ exceeds the magnitude of the predefined axis-specific jerk limit vector $\boldsymbol{j}_{\max} = (j_{x,\max}, j_{y,\max}, j_{z,\max}, j_{e,\max})^\top$, the velocity must be reduced to comply with these constraints.

Accordingly, a scalar junction velocity v_{junc} is computed as a function of the actual jerk vector $\boldsymbol{j}$ and the maximum allowable jerk $\boldsymbol{j}_{\max}$:

$$v_{\mathrm{junc}} = V(\boldsymbol{j}_{\max}, \boldsymbol{j}), \quad \boldsymbol{j}_{\max}, \boldsymbol{j} \in \mathbb{R}^4, \quad V : \mathbb{R}^4 \times \mathbb{R}^4 \to \mathbb{R} \tag{4.3}$$

The function V effectively scales down the velocity until the jerk remains within the allowed thresholds. Due to differences in segment orientation, the projection of v_{junc} onto the direction of motion produces varying axis-wise velocity components before and after the junction. The resulting discontinuities, so-called axis jumps, are an inherent consequence of this projection step. However, they are explicitly limited by the *Classic jerk* formulation: since v_{junc} is computed

under the constraint that the resulting jerk vector must remain within axis-specific bounds, the magnitude of these discontinuities is kept within physically acceptable limits.

Various firmware implementations define their own specific realizations of the functions F and V based on the *Classic jerk* principle [216–219]. While the general concept remains the same, the actual computation of the permitted junction velocity differs across systems. For the printers used in the scope of this work, the behavior of the respective firmwares has been implemented in the simulation framework: the *Prusa* firmware (for *Prusa* machines) [216], the *MKA* firmware (for the *Anisoprint Composer A* series) [218], and the *Ultimaker* firmware (*Marlin Ultimaker* edition) [217]. The corresponding algorithms are described in Appendix A.2. Notably, *Prusa* and *MKA* firmwares apply a similar jerk limitation in an axis-wise manner. In contrast, the *Ultimaker* firmware uses a vector-based evaluation that constrains the overall change in velocity for the XY-plane, rather than evaluating each axis separately.

Junction deviation The *Junction deviation* method is based on a geometric interpretation of direction changes between consecutive motion segments [220, 221]. Instead of assuming an instantaneous change in direction, the transition is modeled as a virtual circular arc connecting the two linear motion segments. This arc introduces a defined lateral deviation from the nominal corner, referred to as the *Junction deviation* and denoted as δ. It represents a user-defined tolerance and indirectly determines the radius R of the virtual arc [220, 221]. Figure 4.3 illustrates the geometric principle behind this approach. The two linear target velocity vectors $\boldsymbol{v}_{\mathrm{t},m}$ and $\boldsymbol{v}_{\mathrm{t},m+1}$ enclose an angle ω, and a circular arc with radius R is inserted to smooth the corner transition. The virtual deviation δ represents the distance from the ideal corner to the centerline of the circular segment. To ensure that the physical acceleration limit $\boldsymbol{a}_{\max}$ (defined in the firmware) is not exceeded during the curved transition between two linear segments, the junction velocity v_{junc} is limited by the centripetal acceleration condition:

$$v_{\mathrm{junc}} = \sqrt{\|\boldsymbol{a}_{\max}\| \cdot R}. \tag{4.4}$$

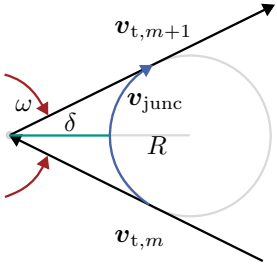

Figure 4.3: Geometric interpretation of the *Junction deviation* method. The velocity transition is modeled as a circular arc with radius R and lateral deviation δ. (Adapted from [221])

The radius R of the virtual arc is defined by the user-specified junction deviation δ and the half-angle $\omega/2$ between the motion directions:

$$R = \delta \cdot \frac{\sin(\omega/2)}{1 - \sin(\omega/2)}. \tag{4.5}$$

The angle ω between the velocity vectors $\boldsymbol{v}_m$ and $\boldsymbol{v}_{m+1}$ is determined via the cosine formula:

$$\cos(\omega) = \frac{\boldsymbol{v}_{\mathrm{t},m} \cdot \boldsymbol{v}_{\mathrm{t},m+1}}{\|\boldsymbol{v}_{\mathrm{t},m}\| \, \|\boldsymbol{v}_{\mathrm{t},m+1}\|}. \tag{4.6}$$

To avoid evaluating trigonometric functions numerically, the sine of the half-angle is rewritten using the identity:

$$\sin\left(\frac{\omega}{2}\right) = \sqrt{\frac{1 - \cos(\omega)}{2}}. \tag{4.7}$$

By substituting Equations 4.6 and 4.7 into Equation 4.5, and inserting the result into the expression for v_{junc} in Equation. 4.4, the final formula becomes:

$$v_{\mathrm{junc}} = \sqrt{\|\boldsymbol{a}_{\max}\| \cdot \delta \cdot \frac{\sqrt{\frac{1 - \frac{\boldsymbol{v}_{\mathrm{t},m} \cdot \boldsymbol{v}_{\mathrm{t},m+1}}{\|\boldsymbol{v}_{\mathrm{t},m}\| \, \|\boldsymbol{v}_{\mathrm{t},m+1}\|}}{2}}}{1 - \sqrt{\frac{1 - \frac{\boldsymbol{v}_{\mathrm{t},m} \cdot \boldsymbol{v}_{\mathrm{t},m+1}}{\|\boldsymbol{v}_{\mathrm{t},m}\| \, \|\boldsymbol{v}_{\mathrm{t},m+1}\|}}{2}}}}. \tag{4.8}$$

This expression allows for computing the maximum admissible junction velocity using only vector operations and basic arithmetic, without explicit trigonometric function evaluation, which improves computational efficiency on embedded systems with limited processing capabilities, such as typical printer controllers.

To determine the maximum allowable velocity at the junction, the following expression is applied:

$$v_{\mathrm{junc,final}} = \min\left(v_{\mathrm{junc}},\, \min\left(\|\boldsymbol{v}_{\mathrm{t},m}\|, \|\boldsymbol{v}_{\mathrm{t},m+1}\|\right)\right), \tag{4.9}$$

which ensures that the junction velocity does not exceed the target velocities at either the entry or exit segments, thereby preserving continuity. This method yields smooth and continuous velocity profiles while ensuring that the machine's mechanical limits, especially $\boldsymbol{a}_{\max}$, are respected. For small direction changes (i.e., large ω), higher junction velocities are allowed; whereas for sharp transitions, velocity is reduced accordingly.

The tuning parameter of the Junction Deviation, δ, can generally be described by $\boldsymbol{j}_{\max}$ used in the *Classic jerk* approach. This relationship is expressed as follows:

$$\delta = 0.414 \cdot \frac{\|\boldsymbol{j}_{\max}\|}{\|\boldsymbol{a}_{\max}\|}, \tag{4.10}$$

where the value of 0.414 may vary slightly depending on the firmware used. This reference was chosen such that, for a turning angle of $\theta = 90\,^{\circ}$, where the velocity vectors $\boldsymbol{v}_{\mathrm{t},m}$ and $\boldsymbol{v}_{\mathrm{t},m+1}$ are aligned exactly along the X and Y axes of the global coordinate system, the junction velocity v_{junc} is identical in both the *Classic jerk* and *Junction deviation* approaches. This ensures a level of interoperability across different motion planning methods and allows user-defined printer profiles to remain somewhat compatible between firmwares.

Comparing cornering methods Figure 4.4 presents a comparison of different cornering methods and their impact on the junction velocity v_{junc} as a function of the turning angle θ. The graph illustrates how v_{junc} decreases as θ

increases, highlighting the different behaviors of several widely used firmware approaches, including the *Junction deviation* approach and four common implementations based on the *Classic jerk* approach (*Marlin*, *Prusa/MKA*, and *Ultimaker* firmware). The curves clearly show the different velocity profiles,

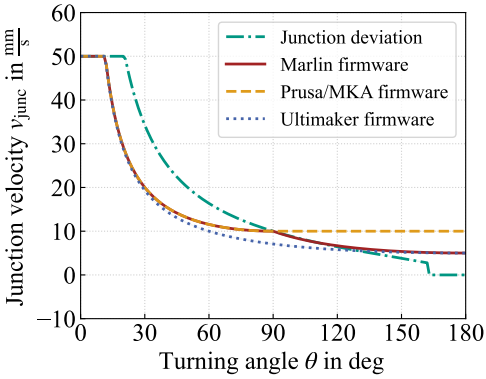

Figure 4.4: Comparison of firmware with regard to their implemented cornering method for a range of turning angles θ from $0°$ to $180°$. Target velocity is $v_{\text{t},m} = 50\,\text{mm/s}$, the acceleration $a_{\text{N},m} = 1000\,\text{mm/s}^2$ and jerk $10\,\text{mm/s}$ for all entries in $\boldsymbol{j}_{\max}$.

with the most notable differences occurring at higher turning angles. Specifically, the *Junction deviation* approach reduces v_{junc} to zero not exactly at a direction change of $\theta = 180\,°$, but already at a firmware-dependent threshold angle (here about $162\,°$), in order to avoid undershooting a minimal permissible velocity. In contrast, the *Classic jerk*-based firmwares allow a velocity jump, with the *Prusa/MKA* firmware exhibiting the highest jump.

The *Junction deviation* approach maintains higher v_{junc} at smaller θ, which progressively decrease as the turning angle increases. Compared to *Marlin* firmware, the *Junction deviation* approach and the Ultimaker firmware show a more continuous decrease in v_{junc}. The observed discontinuity in v_{junc} is a result of the axis-dependent calculation in *Marlin*, where v_{junc} for a given turning angle depends on the position of the direction change in the global

coordinate system. This dependency is visible in Figure 4.5, which shows v_{junc} at a $90\,^{\circ}$ turning angle with a rotating global coordinate system, where the global coordinate system is rotated by the angle Θ.

Since the *Prusa/MKA* firmware follows a similar axis-dependent implementation, its calculations are also affected by the global coordinate system, leading to a similar discontinuity, as seen in Figure 4.5. In Figure 4.4, the discontinuity is not directly apparent, due to a $45\,^{\circ}$ shift compared to *Marlin* firmware. Figure A.1 in Appendix A.2 shows v_{junc} as a function θ for rotated global coordinate systems, based on Figure 4.4.

Under certain conditions, the dependence of v_{junc} on the position of the curve in the global coordinate system can lead to undesired effects, since a simple rotation of the component on the building plate may change relevant properties of the printed component, such as surface quality or layer adhesion. This limitation does not apply to approaches such as *Junction Deviation* or the *Ultimaker* implementation, which determine v_{junc} independently of the orientation in the global coordinate system.

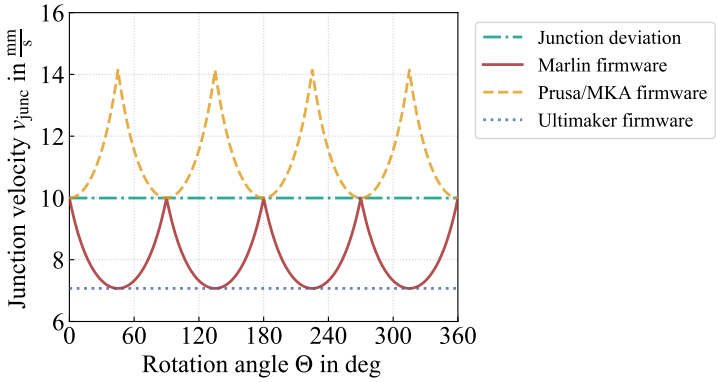

Figure 4.5: Comparison of the firmware with regard to the implemented cornering method for a turning angle of $\theta = 90°$ and a rotating global coordinate system by the angle Θ. Target velocity is $v_{\mathrm{t},m} = 50\,\mathrm{mm/s}$, the acceleration $a_{\mathrm{N},m} = 1000\,\mathrm{mm/s^2}$ and jerk $10\,\mathrm{mm/s}$ for all entries in $\boldsymbol{j}_{\max}$.

Velocity coupling The velocity magnitudes of adjacent junction vectors, $\|\boldsymbol{v}^{\text{out}}_{\text{junc},m}\|$ and $\|\boldsymbol{v}^{\text{in}}_{\text{junc},m+1}\|$, must be continuous (equal to the scalar v_{junc} defined in Equation. 4.3 or Equation 4.9), while their directions can exhibit discontinuities, which are limited by the curve-motion approaches presented above. Therefore, chaining *planner blocks* can cause reduced velocity to spread to adjacent movements. This is particularly true with limited acceleration capabilities and short movements. A segment may be too short to reach the target or interface velocity. This results in discrepancies between the target and actual process parameters. If the final velocity $\|\boldsymbol{v}^{\text{out}}_{\text{junc},m}\|$ is less than the initial velocity $\|\boldsymbol{v}^{\text{in}}_{\text{junc},m}\|$ and the segment is too short to brake in time, then the initial velocity $\|\boldsymbol{v}^{\text{in}}_{\text{junc},m}\|$ must be reduced. This has a retroactive effect on previous segments. After forward planning the velocity profiles, the simulation performs a correction step in reverse order, based on the firmwares implementation of forward and reverse passes within the motion planning.

4.2 Validation

Two validation cases were designed to evaluate the accuracy of the simulation, focusing solely on the nozzle movement without material extrusion. Each test consisted of repeated motion cycles, returning the nozzle to its starting point.

1) **Influence of turning angle θ**:
   This case aimed to validate the influence of the turning angle θ on the nozzle velocity and, consequently, the required manufacturing time. To achieve this, a nozzle movement that included a corner with a defined θ was executed. Figure 4.6a illustrates this validation case. The layer included a variable turning angle as well as acceleration and deceleration phases related to a $\theta = 180\,^\circ$.

2) **Influence of jerk parameter $\boldsymbol{j}_{\max}$**:
   To evaluate the effect of the maximum jerk value firmware parameter

$\boldsymbol{j}_{\max}$, and thus the cornering algorithm implemented, a symmetric triangle was printed. Figure 4.6b illustrates this validation case. The test was repeated across different $\boldsymbol{j}_{\max}$ configurations. $\boldsymbol{j}_{\max}$ was adjusted identically for all axes. This validation experiment was already presented in [212].

The total printing duration of ten repetitions was used as the validation metric. The validation tests were performed on the *Prusa Mini*, using the corresponding *Prusa* firmware and cornering method (*Prusa* jerk junction velocity algorithm (cf. Appendix A.2)). The process and firmware parameters applied are summarized in Table 4.1.

Figure 4.7 shows the results of Validation Case 1, illustrating the printing duration t_{p} as a function of the turning angle θ. The experimentally measured t_{p} were accurately predicted using the simulation framework presented in this chapter. For small θ, v_m is highest, resulting in the shortest t_{p}. As θ increases,

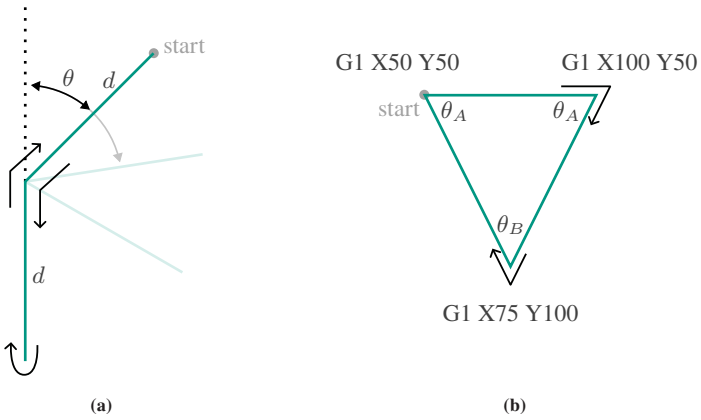

Figure 4.6: Experiments designed to validate the time-accurate simulation of nozzle motion. (a): Path with varying turning angle θ to evaluate its influence on nozzle velocity and printing time. For this study, $d = 30\,\mathrm{mm}$ was chosen. (b): Symmetric triangular path used to investigate the effect of the maximum jerk parameter $\boldsymbol{j}_{\max}$ on cornering behavior and layer duration. The coordinates of the corner points are specified in the form of a G-Code excerpt.

Table 4.1: The process and firmware settings used for validation.

Setting	Case 1	Case 2	Unit
$v_{\mathrm{t},m}$	30	30	mm/s
$\boldsymbol{j}_{\max}$	8	$\{1, 5, 7, 10, 15, 20, 30\}$	$\mathbf{1}_4 \cdot$ mm/s
$a_{\mathrm{N},m}$	50	50	mm/s^2

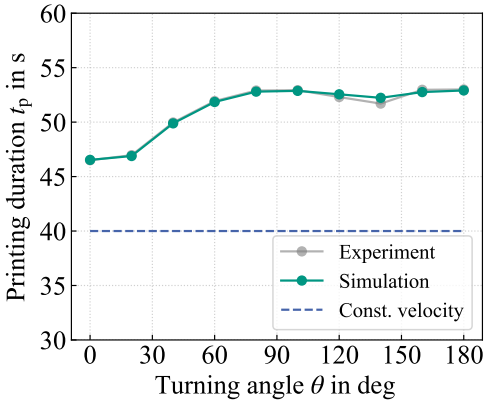

Figure 4.7: Validation of the simulation by measuring the printing duration t_p with different turning angles θ at a constant jerk setting with $j_{\max,i} = 8\,\mathrm{mm/s}$ for all axes. The underlying validation geometry is shown in Figure 4.6a. In addition, t_p for a constant velocity $v_{\mathrm{t},m}$ is plotted, which would result if the G-Code was not interpreted by the firmware.

v_m decreases, leading to an increase in t_p, which then converges at higher θ. This trend corresponds well with v_m profiles shown in Figure 4.4. Between approximately $\theta = 120\,^\circ$ and $\theta = 140\,^\circ$, a slight decrease in t_p can be observed before it rises again for larger θ. This behavior is attributed to the axis-wise jerk limitation in the *Prusa* firmware. Within this θ range, the resultant motion is distributed evenly across the involved axes, which reduces the effective velocity change per axis. This effect arises from the dependence of the *Classic jerk* formulation on the global coordinate system (see Fig. 4.5). Consequently, the jerk constraint is less restrictive, enabling higher v_m. However, for larger θ, the direction change increasingly concentrates on individual axes. This causes

the jerk limits to be reached more quickly, necessitating a stronger reduction in velocity. The comparison with the hypothetically required printing duration for an unlimited curve movement ($v_m = v_{\mathrm{t},m}$) emphasizes the necessity of taking the firmware interpretation of the G-Code into account in the process simulation.

Figure 4.8 shows the results of Validation Case 2 and presents the printing duration t_p plotted as a function of jerk values ranging from $1\,\mathrm{mm/s}$ to $30\,\mathrm{mm/s}$ [212]. The upper value matched the target velocity specified in the test G-Code. In the considered scenario, t_p is significantly affected by the selected jerk setting.

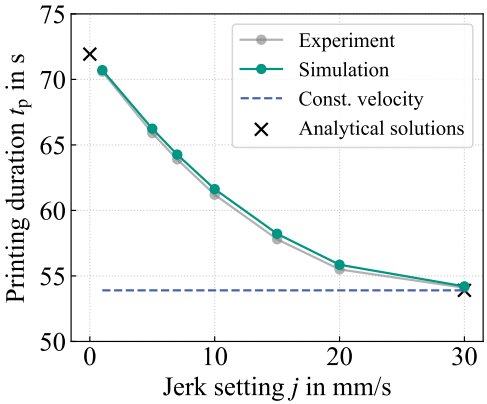

Figure 4.8: Validation of the simulation by measuring the printing duration t_p with different jerk settings at constant turning angles θ as shown in Figure 4.6b. The jerk settings are the same for each axis. In addition, t_p for a constant velocity is plotted, which would result if the G-Code was not interpreted by the firmware. (Reproduced from [212])

When the jerk value equals the target printing velocity, the expected t_p closely aligns with the constant velocity solution determined by analysis. In this case, the acceleration and cornering algorithms do not impact the overall t_p. This reflects current standard practice, in which no additional modeling is performed. Conversely, when the jerk value is close to zero, the printer decelerates almost completely at every corner of the path. This behavior resembles the simplest

case of a velocity trapezoid, where the entry and exit velocities are both zero. Analytical calculations confirmed the printing time t_p for this limiting case. Comparing this with experimental data for jerk values between these extremes shows that the implemented algorithm accurately replicates the behavior of the *Prusa* firmware.

4.3 Error measures

To evaluate the difference between the target process velocity $v_{\mathrm{t},m}$ specified in the G-Code and the velocity actually achieved, an error metric has been introduced. Due to the modeled acceleration processes (cf. Section 4.1), the desired velocity is not immediately reached when a movement begins or ends. The resulting error describes the transient deviation between the target velocity $v_{\mathrm{t},m}$ and the actual velocity v_m. Figure 4.9 shows the resulting nozzle velocity when printing a c-shaped component using the proposed framework. The component was sliced in *Prusa Slicer 2.5.1* using the settings listed in Table 4.2. As can be seen, $v_{\mathrm{t},m}$ is only achieved in the perimeter and locally in the infill due to the acceleration and deceleration processes.

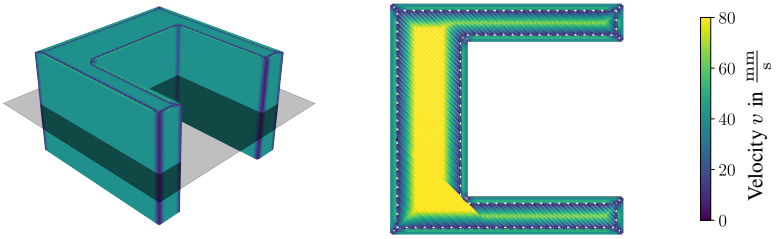

Figure 4.9: The nozzle velocity, mapped onto the trajectory, is displayed for a C-shaped component. The highlighted layer indicates the position within the component. It was sliced using the settings from Table 4.2 in *Prusa Slicer 2.5.1*.

Table 4.2: Printing & slicer settings for example component.

Setting	Value	Unit
Perimeter Count	2	–
Infill density	100	%
Perimeter target velocity	50	$\mathrm{mm/s}$
Infill target velocity	80	$\mathrm{mm/s}$
$a_{\mathrm{N},m}$	1000	$\mathrm{mm/s^2}$
$\boldsymbol{j}_{\max}$	10	$\mathbf{1}_4 \cdot \mathrm{mm/s}$
Cornering Method	*Prusa* firmware	–

A local and a global error measure are introduced. The local error is calculated at all locations in the component, while the global error provides an overall value per segment or component, describing a general deviation.

4.3.1 Local error measure

The local error ϵ_{loc} is defined as the relative difference between the target velocity $v_{\mathrm{t},m}$ and the current velocity v_m at each location in the component by

$$\epsilon_{\mathrm{loc}} = \frac{v_{\mathrm{t},m} - v_m}{v_{\mathrm{t},m}}. \tag{4.11}$$

This error value can be mapped onto the component to identify areas with different process velocities. Unwanted artifacts can particularly easily occur at these positions. Figure 4.10 illustrates a visualization of local error ϵ_{loc} for the c-shaped test component. Overall, the outer contours (perimeter) are printed efficiently, as evidenced by the few areas with increased errors. The infill, on the other hand, shows significantly larger areas with severe velocity errors ϵ_{loc}. The narrow geometry and short movement paths make it difficult to achieve the target velocity $v_{\mathrm{t},m}$. The increased target velocity for the infill exacerbates this effect.

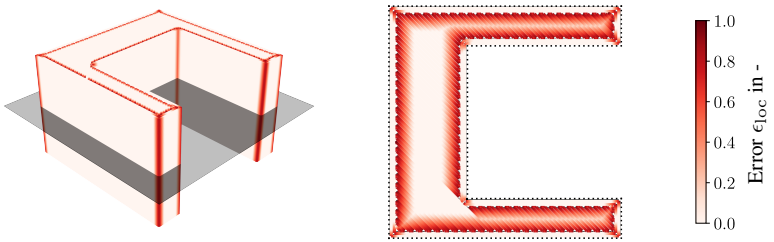

Figure 4.10: The local error ϵ_{loc}, mapped onto the trajectory, is displayed for a C-shaped component. The highlighted layer indicates the position under investigation. It was sliced using the settings from Table 4.2 in *Prusa Slicer 2.5.1*.

4.3.2 Global error measures

The local deviation from the actual velocity can be aggregated to form a global error measure ϵ_{glob}. This measure quantifies how strongly the actual process deviated from the conditions set in the slicer during production. As aggregation, an averaging method is proposed to estimate inefficiencies over the course of production, or spatially, to evaluate the uniformity of material application.

4.3.2.1 Time-averaged global error measure

When averaged over time, the time-averaged global error $\epsilon_{\mathrm{glob,t}}$ is formulated as

$$\epsilon_{\mathrm{glob,t}} = \frac{1}{t_{\mathrm{move}}} \int_0^{t_{\mathrm{move}}} \epsilon_{\mathrm{loc}} \mathrm{dt}, \tag{4.12}$$

with the movement duration t_{move}. This measure can be interpreted as an indicator of the time efficiency of the planned trajectory with respect to the specified process parameters.

As shown in Figure 4.11, this integral weights the deviation according to the dwell time in a particular operating state, making it particularly suitable for analyzing and optimizing production time. For instance, a time-averaged global

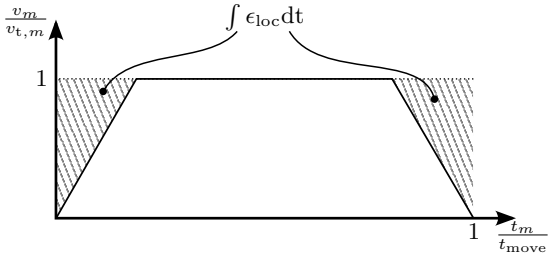

Figure 4.11: Normalized velocity over normalized time with time-averaged error $\epsilon_{\mathrm{glob,t}}$ as marked area.

error of $\epsilon_{\mathrm{glob,t}} = 25\,\%$ indicates that, on average, only $1 - \epsilon_{\mathrm{glob,t}} = 75\%$ of the target velocity is achieved. Accordingly, for a distance of s_{move}, the effective printing duration is

$$t_{\mathrm{move}} = \frac{s_{\mathrm{move}}}{v_{\mathrm{t}_m}(1 - \epsilon_{\mathrm{glob,t}})}. \tag{4.13}$$

4.3.2.2 Space-averaged global error measure

Alternatively, the local velocity error can be averaged along the path length to obtain a distance-based measure, where the space-averaged global error $\epsilon_{\mathrm{glob,s}}$ is expressed as

$$\epsilon_{\mathrm{glob,s}} = \frac{1}{s_{\mathrm{move}}} \int_0^{s_{\mathrm{move}}} \epsilon_{\mathrm{loc}} \mathrm{ds}, \tag{4.14}$$

with s_{move} representing the total distance traveled.
As illustrated in Figure 4.12, this formulation weights the error by the actual distance covered, acknowledging the correlation between travel distance and the amount of extruded material in the MEX process. When this error is evaluated specifically for extrusion segments, it effectively captures the average deviation in process velocity relative to the extrusion amount, providing a valuable metric

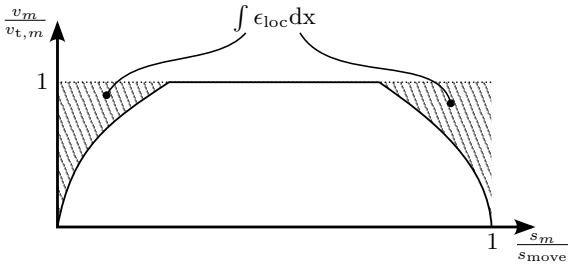

Figure 4.12: Normalized velocity over normalized space with space averaged error $\epsilon_{\mathrm{glob,s}}$.

for assessing component uniformity and compliance with process specifications.

For instance, a space-averaged global error $\epsilon_{\mathrm{glob,s}} = 25\,\%$ indicates that, relative to a specific amount of extruded material, the material is, on average, extruded at only $1 - \epsilon_{\mathrm{glob,s}} = 75\,\%$ of the target extrusion velocity. In principle, the extrusion velocity is continuously adapted to the commanded v_m, which would ensure correct material flow in the case of an ideal, inertia-free extruder. In practice, however, effects such as slip, compliance, and actuator inertia lead to deviations during dynamic phases, so that changes in extrusion rate can cause temporary over- or under-extrusion (cf. Fig. 4.13). Consequently, the goal is to maintain stationary operating conditions as much as possible to minimize such unpredictable effects.

4.3.2.3 Averaging Differences

To emphasize the differences between the two definitions, the space-averaged error $\epsilon_{\mathrm{glob,s}}$ shown in Figure 4.12 can be compared with the time-averaged error $\epsilon_{\mathrm{glob,t}}$ presented in Figure 4.11. Initially, the large gap between $v_{\mathrm{t},m}$ and the actual velocity v_m quickly diminishes in the case of the space-averaged error $\epsilon_{\mathrm{glob,s}}$ as the motion accelerates. By contrast, in the time-averaged global error $\epsilon_{\mathrm{glob,t}}$, this gap decreases linearly as time progresses. Consequently, the time-averaging approach tends to overweight slower movements because they

persist for longer durations, while the space-averaged approach assigns equal importance to all extruded material, regardless of how long it takes.

Figure 4.13 illustrates an initial extruded move, highlighting the non-linear relationship between space and time. It can be observed that after $0.7\,\mathrm{s}$ only half of the total distance has been covered, even though the entire distance is completed in just $1\,\mathrm{s}$. At the start or end of an extrusion move, issues such

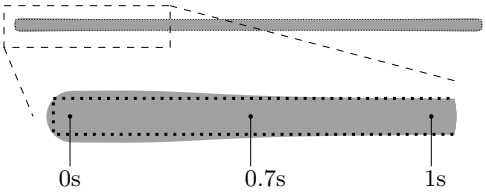

Figure 4.13: The process times at the start of an accelerated move are shown, with overextrusion at the beginning indicated by the dark grey area. This area exceeds the dotted target region, where material is intended to be deposited.

as overextrusion or underextrusion may arise, caused by various factors related to the extruder and nozzle system. These effects can be minimized through careful parameter tuning. Figure 4.13 also depicts an example of overextrusion. By refining the trajectory to achieve the shortest possible distance or time for acceleration and deceleration, the uniformity of the printed component can be improved, as well as the time efficiency of the manufacturing process.

4.4 Influence of firmware settings on process conditions for different component sizes and infill patterns

The introduced error metrics (cf. Section 4.3) allow for a detailed analysis of how firmware settings impact actual process conditions. As shown in Figure 4.10, this analysis can be performed locally on the component using the

local error ϵ_{loc} introduced in Section 4.3.1. In contrast, the global error metrics allow, described in Section 4.3.2, allows for the comparative visualization of different firmware configurations via heat maps.

Figure 4.14 presents a heat map of the spatially averaged global error $\epsilon_{\mathrm{global,s}}$ for the component depicted in Figure 4.10, using the process parameters and firmware settings listed in Table 4.2. Figure 4.14 illustrates $\epsilon_{\mathrm{global,s}}$ for various

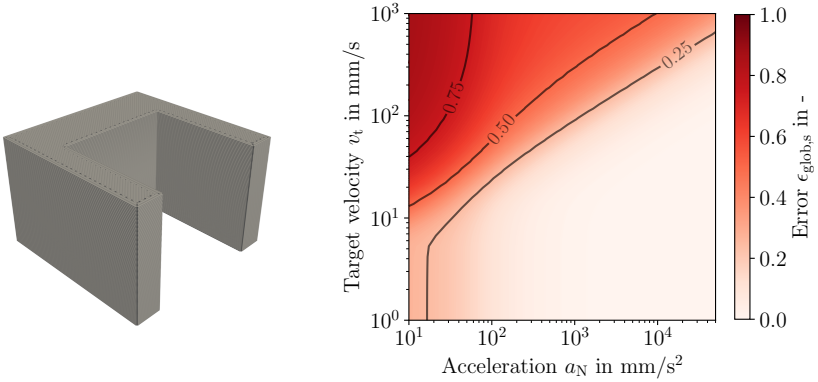

Figure 4.14: Heat map of the spatially averaged global error $\epsilon_{\mathrm{global,s}}$ for the component shown on the left, based on the process parameters and firmware settings provided in Table 4.2. It illustrates $\epsilon_{\mathrm{global,s}}$ for various target velocities $v_{\mathrm{t},m}$ (equal for all motions) and different accelerations a_{N} (equal for all motions).

target velocities $v_{\mathrm{t},m}$ (equal for all motions in the component), which can be set in the slicer, and for different accelerations a_{N} (equal for all motions in the component). It is evident that a significant high $\epsilon_{\mathrm{global,s}}$ may occur at low values of a_{N}. Notably, $\epsilon_{\mathrm{global,s}}$ increases with higher $v_{\mathrm{t},m}$ and can approach a value of $\epsilon_{\mathrm{global,s}} = 1$ in extreme cases, which is especially relevant for big size printer systems with large, heavy print heads. Additionally, $\epsilon_{\mathrm{global,s}}$ decreases with increasing a_{N}. This underscores the importance of printer systems with the capability to achieve high accelerations to ensure process accuracy and economic potential. However, it should be noted that the heat map varies depending on

the component and is directly influenced by the length of the single segments of the trajectory. Therefore, it depends not only on the component's geometry, but also on its overall size. Due to the significant impact of segment length, the selected infill pattern affects the resulting process conditions as well.

Figure 4.15 illustrates this with heat maps of a single layer of a rectangular component sliced with three different infill patterns, each with the same infill density of 50 %. Variations in component size are also shown. As can be seen, the choice of infill pattern directly affects how the firmware settings influence the process conditions. While component size plays a role, its impact is less pronounced.

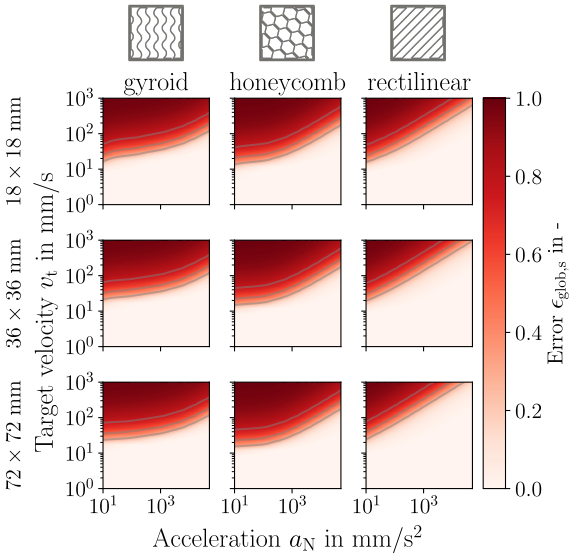

Figure 4.15: Heat maps illustrating the spatially averaged global error $\epsilon_{\mathrm{global,s}}$ as a function of v_t (equal for all motions) and a_N (equal for all motions), evaluated for a single layer of a rectangular component with varying dimensions. The jerk setting is $8\,\mathrm{mm/s}$ for all axes and motions. Results are shown for three different infill patterns at an infill density of 50 %.

Figure 4.16 shows that with constant $v_{\mathrm{t},m}$, variations in the jerk setting affect the impact of component size on the actual process condition more strongly than comparable variations in $v_{\mathrm{t},m}$, as shown above (cf. Figure 4.15). Nevertheless, the effect of the infill pattern remains dominant.

The studies demonstrate that both the firmware settings such as acceleration and jerk and the selected infill pattern influence nozzle motion and thus process conditions, component behavior, and printing time. Inappropriate combinations can lead to local fluctuations in polymer flow, causing over- or under-extrusion and resulting in inhomogeneous material properties, including features like seam lines in highly stressed areas. For more complex geometries, such as the component shown in Figure 4.10, the infill angle affects segment lengths,

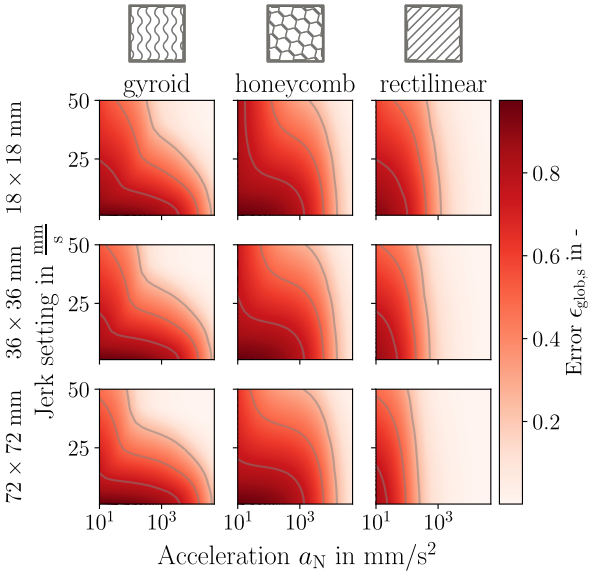

Figure 4.16: Heat maps illustrating the spatially averaged global error $\epsilon_{\mathrm{global,s}}$ for various jerk settings (equal for all axes and motions) and a_{N} values (equal for all motions), for a single layer of a rectangular component with varying dimensions and three different infill patterns, an infill density of 50 %, and $v_{\mathrm{t}} = 100\,\mathrm{mm/s^2}$ (equal for all motions).

which further influences required printing time. Choosing an appropriate infill pattern can reduce the extent of such inhomogeneities relative to component volume, improving both local material uniformity and production throughput. The global error metric $\epsilon_{\mathrm{global,s}}$ introduced in this work provides a quantitative measure of these deviations, allowing assessment of their potential impact on local mechanical properties and overall component quality.

4.5 Summary and conclusion

This chapter introduces a comprehensive methodology for simulating and evaluating nozzle motion in MEX through G-Code interpretation. The simulation framework replicates printer firmware behavior by accounting for hardware-specific constraints, such as maximum acceleration, maximum velocity, and cornering algorithms (e.g., *Classic jerk* and *Junction deviation*). It reconstructs actual nozzle trajectories and velocity profiles, which often deviate from the nominal G-Code due to physical limitations. The open-source software *pyGCodeDecode* (*pyGCD*), developed in this work, further facilitates integration into both research and industrial workflows.

The methodology was validated experimentally using a *Prusa Mini* printer, demonstrating high agreement between the simulated and measured printing durations across different turning angles and jerk settings. To quantify deviations between the target and actual process conditions, local and global error metrics were introduced. These metrics enable spatial and temporal analyses of velocity discrepancies, providing insight into potential quality issues, such as over- or under-extrusion, as well as their impact on actual process times and overall manufacturing efficiency.

The effects of firmware parameters on process accuracy were systematically analyzed using the introduced metrics as a function of infill patterns and component size. Heat maps of global errors revealed that low accelerations combined with high target velocities can result in substantial deviations. It became clear that

parameters such as acceleration and velocity must always be evaluated relative to component or segment size. For instance, a large-format printer combined with G-Code and large segment lengths can execute motion with sufficient process accuracy despite comparatively low acceleration because the acceleration is sufficient relative to the segment length. Additionally, it became evident that the choice of infill pattern, along with other slicing parameters that affect the straight-segment length of the toolpath, has a dominant influence on the resulting process conditions and overall printing time.

The presented G-Code simulation framework is a tool for predicting and analyzing actual nozzle motion in MEX processes. By incorporating firmware-specific motion planning and physical constraints, the framework bridges the gap between nominal slicing parameters and real-world execution. The introduced error metrics provide a quantitative basis for evaluating process fidelity and identifying regions of potential quality degradation.

The results show that firmware settings, especially acceleration and jerk, greatly affect the achievable process conditions. Additionally, the infill pattern and component geometry are crucial in determining the uniformity and efficiency of material deposition. These findings underscore the importance of considering machine capabilities and slicing strategies when optimizing print quality and production throughput.

Ultimately, this methodology enables more accurate process simulations and supports the development of adaptive slicing and control strategies that account for machine dynamics. This paves the way for improved reliability and economic efficiency in additive manufacturing.

5 Evaluation of mechanical properties characterization to accurately reflect the printed mesoscopic structure[1]

Outline

This chapter examines the representativeness of the mechanical characterization of MEX structures. Section 5.1 defines requirements to ensure test specimens reflect the process conditions. Hypotheses meeting these requirements are formulated and verified through tensile tests and scanning electron microscopy in Sections 5.2–5.4. Section 5.2 details specimen manufacturing, while Section 5.3 describes the characterization methods. The results are analyzed in terms of representativeness and repeatability. Initial experimental work and results were developed in the context of a Bachelor's thesis [222, 223] guided within the course of this dissertation. Finally, Section 5.5 formulates practical guidelines for specimen preparation, and Section 5.6 summarizes the findings and discusses further research possibilities.

[1] Extracts from Chapter 5 have been previously published in [1], © CC BY 4.0, i.e. Felix Frölich, Lennart Bechtloff. Benedikt M. Scheuring, Anselm L. Heuer, Florian Wittemann, Luise Kärger, Wilfried V. Liebig. Evaluation of mechanical properties characterization of additively manufactured components. *Progress in Additive Manufacturing*, 10(2):1217-1229, 2025 - Reproduced sections are marked with [1].

5.1 Requirements and hypotheses[1]

This chapter investigates the manufacturing of test specimens to represent the resulting structures within additively manufactured components accurately. This ensures that the structural properties of the component can be effectively characterized at the specimen level. To guarantee that the specimens faithfully reflect the structure to be tested and that no additional process-specific properties distort the structural properties, the following requirements for a representative specimen are defined and briefly explained:

R 1. The process-related material orientation must be accurately replicated within the specimen according to the structure intended for investigation.

As demonstrated in numerous publications [14, 18–21, 76–80], material orientation significantly influences the resulting mechanical properties. Therefore, when characterizing these properties, it is crucial to ensure that specimen preparation does not distort the material orientation.

R 2. A constant process velocity must be maintained within the specimen test area to account for the influence of process velocity fluctuations and the associated time interval between two deposited strands.

Hardware velocity and acceleration limitations can lead to deviations from the nozzle velocity specified in the slicer. Additionally, the time interval between the deposition of two adjacent strands can influence the degree of welding and, consequently, the resulting strength [19, 80].

R 3. The uncertainty in specimen preparation with notable influence on characterization results should be minimized.

[1] Verbatim reproduced section from [1], © CC BY 4.0, cf. footnote p. 101 for details.

The resulting mechanical properties of additively manufactured structures can be sensitive to changing process conditions and external influences [78, 224]. Thus, uncertainties in printing and further processing of specimens may lead to fluctuating resultant properties that are not representative of the actual properties being tested.

In the following, hypotheses are formulated, and their validity is tested and evaluated within the scope of this publication to fulfill the above-mentioned requirements for a test specimen:

H 1. Directly additively manufactured specimens involve non-constant process velocity due to the printer-specific lower curve velocity and acceleration after changes in trajectory direction.

H 2. Directly additively manufactured specimens may exhibit an additional, unrepresentative material orientation due to the perimeter and the turning points of the deposited strands.

H 3. By separating the specimens from a printed plate, the areas of turning points and lower printing velocity are not present in the specimens. Thus, the effects formulated in H 1 and H 1 can be avoided.

H 4. A dogbone specimen geometry results in more valid characterization tests compared to a rectangular geometry.

H 5. The size of the printed plate used to produce the test specimens influences the mechanical properties and their uncertainty.

The hypotheses were investigated and evaluated based on tensile tests to assess the influence of process-related material orientation on mechanical properties, along with SEM images of fracture surfaces and cut edges.

5.2 Specimen manufacturing

5.2.1 Material[2]

For the experiments, commercially available Ultrafuse polylactic acid (PLA) filament from BASF [50] was employed, as described in Section 2.2.3. PLA is particularly suitable for additive manufacturing due to its low melting and glass transition temperatures, minimal warping tendency, and relatively high surface hardness [225]. Its good printability makes it an ideal choice for demonstrating the processes examined in this work.

5.2.2 Process parameters

The test specimens for this study were manufactured using the *Ultimaker 2+* from the company *Ultimaker* (refer to Section 2.1.4). The slicer and printer settings detailed in Table 5.1 were chosen based on prior printing studies to ensure a uniform and repeatable microstructure. The cooling fan was activated starting from the second layer.

5.2.3 Specimen geometries[1]

In this study, experimental investigations were conducted on test specimens with a dogbone geometry and rectangular shape, following DIN EN ISO 527-2 [81] standards as illustrated in Figure 5.1.

[2] Adapted and revised from [1], © CC BY 4.0, cf. footnote p. 101 for details.
[1] Verbatim reproduced section from [1], © CC BY 4.0, cf. footnote p. 101 for details.

Table 5.1: Slicer and process parameters selected for the manufacturing of all specimens. [1]

Process parameter	Value	Unit
Nozzle temperature T_{N}	210	$^{\circ}\mathrm{C}$
Build platform temperature T_{bp}	60	$^{\circ}\mathrm{C}$
Layer height l_{height}	0.2	mm
Extrusion width e_{width}	0.4	mm
Infill printing velocity v_{infill}	50	$\mathrm{mm/s}$
Perimeter printing velocity v_{peri}	40	$\mathrm{mm/s}$
Flow rate (Slicer) $\dot{\mathrm{V}}_{\mathrm{poly}}$	95	$\%$
Maximum acceleration a_{max}	750	$\mathrm{mm/s^2}$

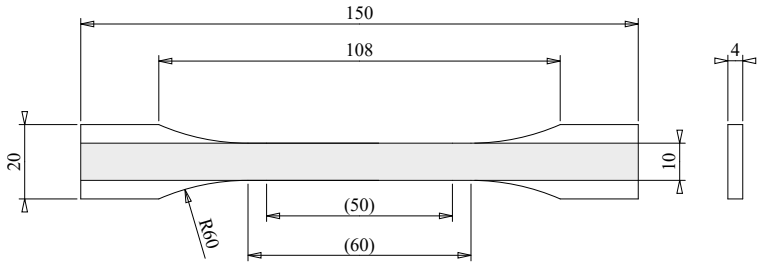

Figure 5.1: Dimensions for a dogbone and rectangular specimen shape in mm according to DIN EN ISO 527-2 [81]. (Reproduced from [1])

5.2.4 Specimen preparation[1]

PLA structures with 100% fill density and varying intralayer material orientations are printed. This includes unidirectional structures oriented along the load direction (0°), structures oriented transverse to the load direction (90°), and structures with alternating material orientations of ±45°. Each preparation configuration undergoes a minimum of five valid tests for evaluation. To investigate the mechanical properties and failure behavior of direct printed specimens, both dogbone and rectangular specimens are fabricated using the process parameters detailed in Table 5.1. All direct printed specimens are printed with a perimeter. To compare directly additively manufactured test specimens with

specimens cut from additively manufactured plates, large square plates were utilized. Five specimens were cut from each square plate by waterjet cutting. Additionally, small rectangular plates were produced to accommodate exactly one dogbone specimen, allowing for an assessment of the effect of plate size. Figure 5.2 provides an overview of the specimen variants. Finally, specimens were cut from the smaller plates using various cutting methods to quantify the influence of the cutting method on the mechanical properties.

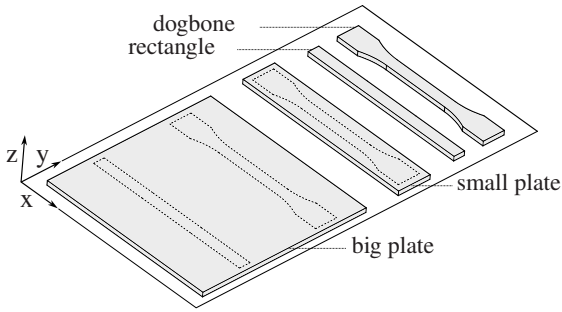

Figure 5.2: Illustration of the different approaches of preparing the specimens to be tested. Directly printed and cut from plates of different sizes. (Reproduced from [1])

5.2.4.1 Plate dimensions[1]

In addition to the material allowance due to the cutting method, an additional distance d_{edge} at the edges of the plate (see Figure 5.3) must be considered when dimensioning the plates. This is crucial due to the printer-specific acceleration after changing the extrusion direction and the perimeter. It ensures that the resulting print velocity in the test area of the specimen matches the velocity set in the slicer, as illustrated in Figure 5.3 and previously discussed in [223],

[1] Verbatim reproduced section from [1], © CC BY 4.0, cf. footnote p. 101 for details.

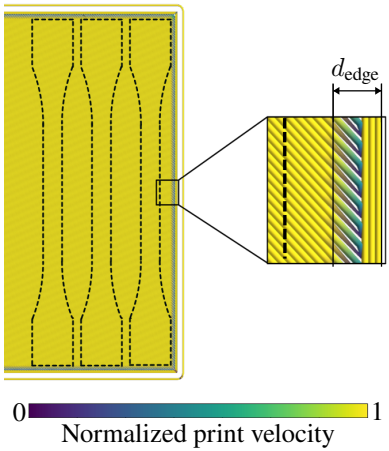

Figure 5.3: Resulting nozzle velocity v_{nozzle}, normalized to the specified infill velocity v_{infill}, considers hardware limitations such as acceleration and possible curve velocities. This calculation and visualization are performed using the Python package *pyGCD* [212, 213]. The additional required width d_{edge} is indicated in the visualization. (Reproduced from [1])

confirming hypothesis H 1. The additional distance d_{edge} on each edge of the plate can be estimated by

$$d_{\text{edge}} = n_{\text{peri}} d_{\text{N}} + \frac{v_{\text{infill}}^2 \sin(\beta \frac{\pi}{180})}{2\|\boldsymbol{a}_{\max}\|}. \tag{5.1}$$

Here n_{peri} represents the number of specified perimeters, d_{N} denotes the nozzle diameter, v_{infill} signifies the print velocity under investigation, β stands for the angle between the extrusion direction and the load direction, and $\boldsymbol{a}_{\max}$ represents the maximum possible acceleration of the printer. It is assumed that the nozzle velocity v_{nozzle} at the edge of the specimen, i.e., at the turning point, is $v_{\text{nozzle}} = 0\,\text{mm/s}$, which is considered conservative. Equation 5.1, alongside the process parameters detailed in Table 5.1, the specified specimen dimensions, the number of specimens, and the cutting width for cutting, results in the minimum plate sizes listed in Table 5.2. Five specimens were cut from

Table 5.2: Minimum plate sizes, dimensioned using Eq. 5.1, the process parameters listed in Table 5.1, the specified specimen dimensions, the number of specimens and the cutting width for cutting. [1]

Plate type	**Dimensions x-y in mm**		
	$\beta = 0\,^\circ$	$\beta = 90\,^\circ$	$\beta = \pm 45\,^\circ$
Large	155×122	152×125	154×124
Small	155×22	152×25	154×24

the large plates. $5\,\mathrm{mm}$ of material was provided between each specimen for the separation process.

5.2.4.2 Cutting methods[1]

Waterjet cutting (WJC) was selected for the initial investigations due to its capability to produce specimens of any geometry within the required tolerances. The potential influence of moisture on the mechanical properties of PLA resulting from the cutting process can be disregarded based on the short WJC process time and the findings of Banjo et al. [226]. To assess the impact of different cutting processes, laser cutting and milling were chosen in addition to WJC, as they can introduce additional influences on the specimens. Laser cutting subjects the specimens to direct thermal stress, whereas milling subjects them to mechanical stress.

Waterjet cutting (WJC) The *iCUT water smart* WJC system from *imesicore* was utilized for the experiments. The manufacturer specifies a positioning accuracy of $80\,\mathrm{\mu m/m}$ and a repeatability of less than $40\,\mathrm{\mu m/m}$. Cutting sand, specifically *Classic Cut 120 garnet* from *GMA*, was employed as the cutting medium. The parameters employed for processing additively manufactured PLA structures are detailed in Table 5.3.

[1] Verbatim reproduced section from [1], © CC BY 4.0, cf. footnote p. 101 for details.

Table 5.3: Parameters for waterjet processing of additively manufactured PLA structures. [1]

Process parameter	Value	Unit
WJC-nozzle velocity	5	$\mathrm{mm/s}$
Pressure	1450	bar
Flow rate of cutting sand	250	$\mathrm{g/min}$

Laser cutting The *Trotec speedy 400* was used. A cutting study was performed to determine the lowest possible temperature effect on the specimens. The study resulted in process parameters corresponding to $100\,\%$ of the adjustable power and $0.4\,\%$ of the adjustable traverse velocity.

Milling A customized holder tailored to the specimen geometry was designed and manufactured for fixation in the milling machine. The milling process was executed in a total of six steps:

1. Milling the outer contour with a tolerance of $+0.15\,\mathrm{mm}$ to the nominal dimension in four steps, removing $1\,\mathrm{mm}$ of material at each step.
2. Precisely milling the contour to nominal dimensions over the full height of the specimen.
3. Sawing to the nominal length.

To prevent the specimen from heating up and the cutting edge from melting, water cooling was employed throughout all milling operations.

Table 5.4: Parameters for milling of additively manufactured PLA structures. [1]

Process parameter	Value	Unit
Feed rate	8	$\mathrm{mm/s}$
Milling head speed	13000	$\mathrm{R/min}$
Milling infeed	1	mm

5.3 Characterization Methods[1]

5.3.1 Tensile test[1]

The tensile test was selected to achieve a uniaxial stress state, allowing for a clear interpretation of individual effects such as material orientation or failure mechanisms. A *Zmart.Pro 200 kN* universal testing machine from *ZWICK/Roell*, equipped with a $20\,\mathrm{kN}$ load cell, was employed for testing. The specimens were clamped using hydraulic jaws featuring a finely ribbed surface. For precise strain evaluation using virtual extensometers, the commercial DIC system *ARAMIS Adjustable* from *GOM Metrology GmbH*, with a recording frequency of $2\,\mathrm{Hz}$, was utilized. The force signal from the testing machine was simultaneously integrated into the system. All experiments were performed at a room temperature of $RT = 23\,^{\circ}\mathrm{C}$.

5.3.2 Microstructure characterization[1]

In various studies, both non-destructive methods like computer tomography [80, 227] or X-ray tomography [228, 229] and destructive methods are employed for microstructure characterization. In this work, the destructive method scanning electron microscopy (SEM) [18, 80, 84] was chosen as the preferred method. This decision was driven by the necessity to examine fracture surfaces in greater detail, in addition to assessing the influence of cutting methods on the microstructure. The SEM analysis was conducted using a *LEO EVO 50* and a *LEO 1530* microscope from *Carl Zeiss AG*. The specimens were first cut to size, attached to a slide using conductive tape, and then sputtered with gold for $25\,\mathrm{s}$ at a voltage of $20\,\mathrm{mV}$. To ensure sufficient conduction from the surface to the slide, a thin layer of conductive varnish was applied. The *LEO EVO 50*

[1] Verbatim reproduced section from [1], © CC BY 4.0, cf. footnote p. 101 for details.

operated with an accelerating voltage of 20 kV, while the *LEO 1530* operated with an accelerating voltage of 5 kV.

5.4 Results and discussion[1]

5.4.1 Validity of the experiments[1]

To evaluate which specimen geometry and specimen preparation are more likely to result in valid tests and thus more effective characterization, the validity of the tests is recorded in addition to the mechanical properties, thereby checking H 4. This is achieved by verifying if the failure location is within the valid gauge length of the specimen. The validity refers to minimum 10 tests performed. The results are depicted in Figure 5.4, which has been partially presented in preliminary investigations in [223]. It is evident that only the dogbone geometry

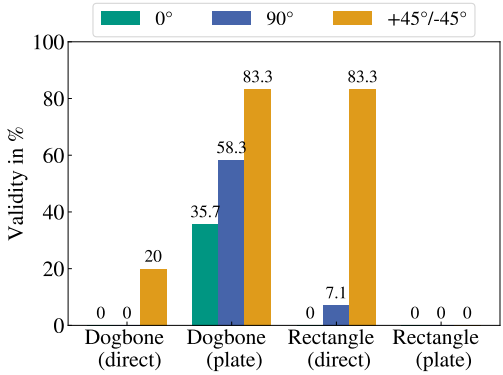

Figure 5.4: Validity of the tensile tests on rectangular and dogbone specimens directly printed (direct) and separated from the plates (plate). At least 10 tests were performed for each intralayer material orientation of 0°, 90° and ±45° to the loading direction. (Reproduced from [1])

[1] Verbatim reproduced section from [1], © CC BY 4.0, cf. footnote p. 101 for details.

separated from the plate exhibits a clear majority of valid specimens for all tested material orientations. The rectangular specimens fail outside the gauge length due to the stress jump at the clamps. The lower number of valid tests for the directly printed dogbone specimens can be attributed to the process-related notch in the area of the taper of the specimen width. Figure 5.5a) illustrates the resulting notches and the local increase in strain during the tensile test. In

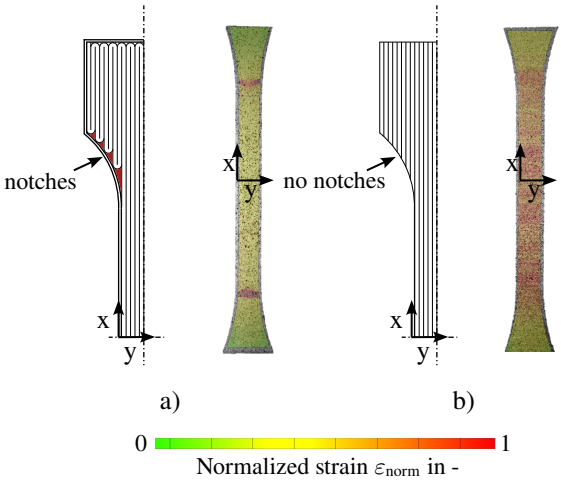

Figure 5.5: Directly printed specimen with notches (a) and cut specimen (b) with corresponding strain distributions during tensile test. (Reproduced from [1])

comparison, Figure 5.5b) shows a homogeneous strain field during the test on a cut specimen. These findings are consistent with the observations of Park et al. [85]. Thus, the study demonstrates that a dogbone geometry increases the probability of valid tests, confirming H 4.

5.4.2 Fracture surface[1]

Figure 5.6 displays SEM images of fracture surfaces of failed specimens with a material orientation of 90° as an example. The fracture surfaces of a directly printed specimen (a) and a cut specimen (b) are depicted. In the case of directly printed specimens, the material orientation of the perimeter is also tested rather than the actual material orientation intended for characterization. With an infill orientation of ±45°, the influence of the perimeter on the resulting fracture surface is similar. However, with a 0° orientation, the perimeter has no significant influence. These investigations thus confirm R 3. They demonstrate that this approach is essential for identifying potential failure mechanisms of an additively manufactured component structure without confounding effects from the perimeter or other edge effects.

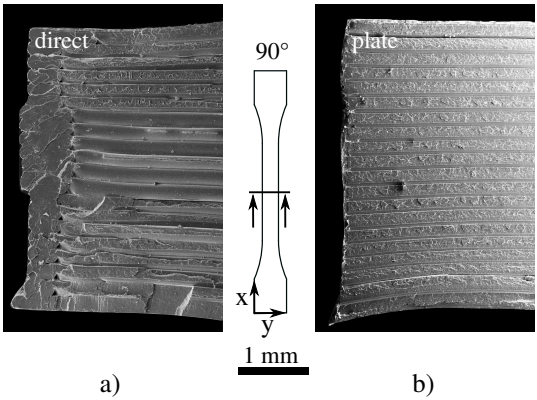

Figure 5.6: SEM images of the fracture surface of specimens with 90° material orientation. Shown is a directly printed specimen (a) and a specimen cut from a plate (b). (Reproduced from [1])

[1] Verbatim reproduced section from [1], © CC BY 4.0, cf. footnote p. 101 for details.

5.4.3 Mechanical properties[1]

The tensile tests exhibit linear elastic behavior. Figure 5.7 displays the mean tensile strength and mean stiffness resulting from the tensile tests initially presented in [223]. These tests were conducted on directly printed specimens and specimens cut from a large plate by WJC. Both valid and invalid tests were included to facilitate comparison between manufacturing methods. Overall, the influence of the preparation method on tensile strength is more pronounced than the influence on stiffness, particularly when the material orientation deviates from 0°.

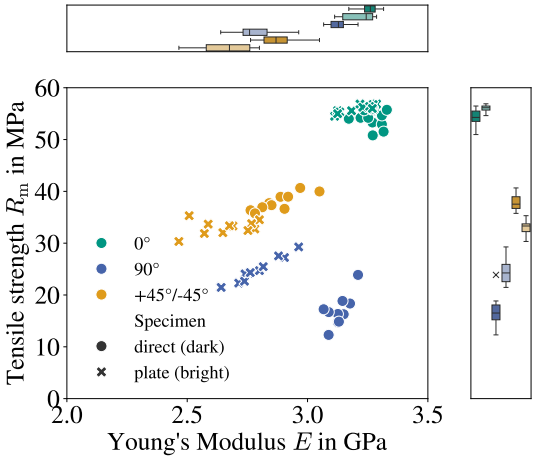

Figure 5.7: Results of tensile tests on directly printed (●) and waterjet-cut dogbone specimens from a large plate (×) with intralayer material orientations 0°, 90° and ±45°. The measured values of each test and the standard deviation for the stiffness and strength of each configuration are shown. Initially presented in [223]. (Reproduced from [1])

[1] Verbatim reproduced section from [1], © CC BY 4.0, cf. footnote p. 101 for details.

Tensile strength The comparable tensile strength of the 0° specimens can be attributed to the non-critical influence of both the resulting notches (II in Figure 5.8) and the additional 0° material orientations introduced by the perimeter (I in Figure 5.8), turning points (III in Figure 5.8), or blurred microstructure in the initial layers (Figure 5.9).

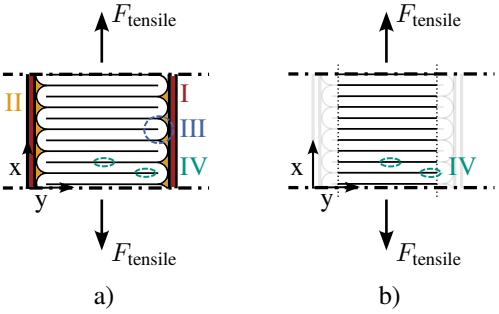

Figure 5.8: Schematic representation of the trajectory in the test area for a printed specimen (a) and a specimen cut from a plate (b). Colored highlighting and numbering of the expected effects based on the trajectory: The perimeter (I) introduces an additional material orientation. Notches (II) are formed by the turning points of the trajectory. Turning points (III) result in an additional material orientation along the load direction. Varying degrees of welding (IV) occur due to different times between the deposition of two adjacent strands at the turning point and in the center of the specimen. (Reproduced from [1])

The lower strength of the directly printed specimen with a 90° material orientation is due to the process-related notches (Section 5.4.1). Therefore, it can be expected that the strength-reducing effect of these notches is greater than the strength-increasing effect of the additional 0° orientation. For this reason, the study did not include tests on directly printed specimens without a perimeter, as an even greater decrease in strength would be expected. For structures with a material orientation of ±45°, the strength of the directly printed specimens is higher. Because the shape of the dogbone specimen is more filled by the alternating +45° and -45° layers, the notches are less pronounced than with a 90° orientation. Therefore, the strength-reducing effect of the notches is less

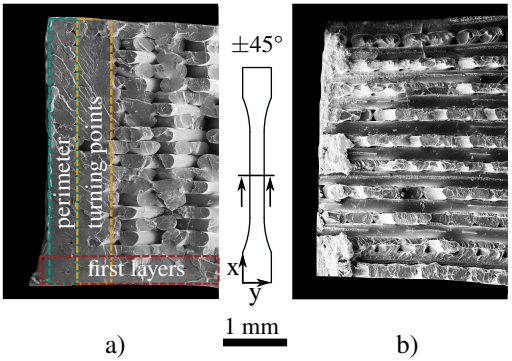

Figure 5.9: SEM images of the fracture surface of specimens with ±45° material orientation. Shown is a directly printed specimen (a) and a specimen cut from a plate (b). (Reproduced from [1], © CC BY 4.0)

pronounced than the strength-enhancing effect of the additional 0° material orientations.

Stiffness The stiffness of the 0°-oriented structure is similar for both preparation types since the perimeter has the same material orientation as the orientation being tested. The higher stiffness of the ±45°- and 90°-oriented structures with direct printing is attributed to the perimeter, as well as the turning points and thus the additionally integrated 0° orientation (I and III in Figure 5.8). For ±45° structures, the introduction of a 0° orientation has less influence on the resulting stiffness. Therefore, the difference in stiffness between the two preparation methods is less pronounced for ±45° structures.

To validate the influence of the perimeter on the resulting stiffness of a printed specimen, the resulting stiffness $E_{\mathrm{res}}^{\mathrm{direct}}$ can be estimated from the measured stiffnesses of the cut 0° specimens E_0^{plate} and the corresponding orientation $E_{\mathrm{ori}}^{\mathrm{plate}}$ using the mixing rule

$$E_{\mathrm{res}}^{\mathrm{direct}} = \phi E_{\mathrm{ori}}^{\mathrm{plate}} + (1-\phi) E_0^{\mathrm{plate}}. \tag{5.2}$$

Where ϕ denotes the fraction of the material orientation under analysis. The SEM image of the fracture surface of a directly printed $\pm 45°$ specimen in Figure 5.9a) illustrates the additional 0° orientation due to the perimeter, the turning points, and a blurring of the structure in the first layers. Conversely, Figure 5.9 b) indicates that this blurring of the first layers is less pronounced in cut specimens. Assuming these areas possess the properties of a 0° oriented structure, ϕ can be approximated as 0.635. This yields a modulus of elasticity of $E_{\mathrm{res}}^{\mathrm{direct}} = 2.86\,\mathrm{GPa}$. Consequently, the plausibility check confirms that the perimeter, the turning points, and the blurring of the microstructure in the area of the first layers impact the measured stiffness. Consequently, the measurement is not representative. These investigations confirm H 2.

Scatter The scattering is more pronounced in the cut specimens than in the directly printed specimens. Scattering can be caused by the effect labeled IV in Figure 5.8. Owing to the turning point of the deposited strand, different times elapse between the deposition of two adjacent strands. In the area of the turning point, the times are shorter than in the center of the specimen or plate, which allows a higher degree of welding. This results in an inhomogeneous degree of welding across the cross section. In the case of directly printed specimens, the degree of welding is therefore not homogeneous across the cross section and does not represent the structural property being tested. However, the inhomogeneity is the same for all specimens, so the scatter is less pronounced. Although the use of plates avoids the effect of turning point acceleration described in Section 5.2.4.1, inhomogeneity of the degree of welding across the plate cross section remains. When multiple specimens are cut from a plate, this inhomogeneity is transferred to the specimens in the case of $\pm 45°$ and 90° structures. This can lead to a scattering of the measurement results. Therefore, in Section 5.4.4 the influence of the plate size and thus the influence of the preparation method on the measurement uncertainty is investigated.

5.4.4 Plate size[1]

The influence of plate size is evaluated using the measured tensile strengths, stiffnesses, and their scatter as depicted in Figure 5.10 and Figure 5.11.

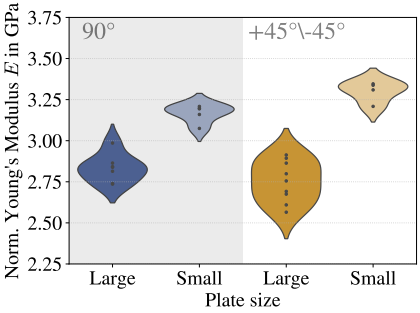

Figure 5.10: Young's modulus E normalized to the relative filling density ρ_{rel} for specimens cut from large plates and for specimens cut from plates from which exactly one specimen can be taken. Displayed as a violin plot. (Reproduced from [1])

As explained in Section 5.4.3, the plate size does not affect the mechanical properties of the 0° structure. Therefore, only the 90° and ±45° material orientations will be discussed in this section. For this purpose, specimens are cut from two different plate sizes (Section 5.2.4.1). Since the same orientations are being compared, only the influence on the degree of welding and its distribution over the cross-section of a specimen is considered. Therefore, the results are normalized to the relative filling density

$$\rho_{\mathrm{rel}} = \frac{\rho_{\mathrm{specimen}}}{\rho_{\mathrm{ref}}}. \tag{5.3}$$

This eliminates the influence of the printing process on the filling density. Density measurements were performed according to the Archimedean principle

[1] Verbatim reproduced section from [1], © CC BY 4.0, cf. footnote p. 101 for details.

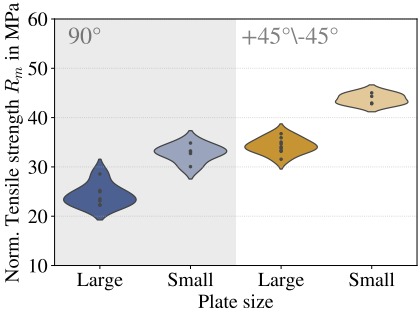

Figure 5.11: Tensile strength R_m normalized to the relative filling density ρ_rel for specimens cut from large plates and for specimens cut from plates from which exactly one specimen can be taken. Displayed as a violin plot. (Reproduced from [1])

using the ME-DNY-43 density meter and the ME204T/00 analytical balance from Mettler Toledo. The density of the untreated filament, which was also measured, was used as a reference density. This eliminates the influence of the printing process on the filling density. Density measurements were performed according to the Archimedean principle using the *ME-DNY-43* density meter and the *ME204T/00* analytical balance from *Mettler Toledo*. The density of the untreated filament, which was also measured, served as a reference density.

Both stiffness and tensile strength are greater and less scattered when the small plate is used. In particular, the stiffness scatter decreases significantly. The scatter arises from the heterogeneous interface properties across the width of the plate, as explained in Section 5.4.3. When only one specimen is cut from each plate, there is a consistent interface property among all specimens compared to the situation when multiple specimens are cut from a larger plate. An explanation for the higher measured mechanical properties is provided by Zhang et al. [84] and Vaes et al. [230]: For smaller specimens, less time elapses between the deposition of the individual strands adjacent to each other if the process parameters are kept constant. This further promotes the welding of the strands and increases the load-carrying capacity. This effect is depicted in Figure 5.12. Consequently, the choice of plate size influences the measured

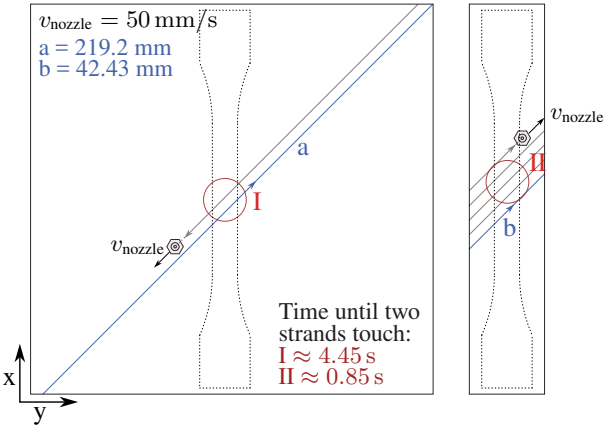

Figure 5.12: Schematic representation of the additively manufactured large and small plates for preparing a dogbone specimen and the nozzle trajectory for a ±45° material orientation. The time interval between the placement of two neighboring strands is indicated in red. (Reproduced from [1])

values and their uncertainty. Hypothesis H 5 stated in Section 5.1 is thus confirmed. To reproduce the actual structure to be tested independent of the plate size and thus meet Requirement R 1, it is necessary to set the time between the deposition of two adjacent strands according to the process conditions during component manufacture. This can be achieved by adjusting the G-Code.

5.4.5 Influence of cutting methods[1]

Dogbone specimens were cut from small plates by laser cutting, milling, and water jet cutting (WJC) and compared based on their mechanical properties using the 90° material orientation as an example. Figure 5.13 illustrates the stiffness normalized to the relative filling density ρ_{rel}, and Figure 5.14 depicts the normalized tensile strength of these specimens.

[1] Verbatim reproduced section from [1], © CC BY 4.0, cf. footnote p. 101 for details.

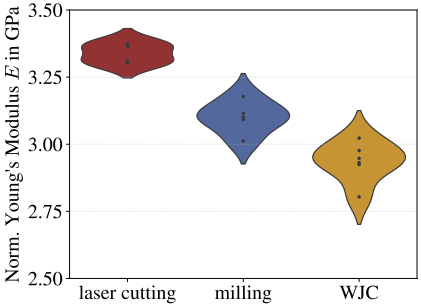

Figure 5.13: Young's Modulus E normalized to the relative filling density ρ_{rel} for specimens cut from small plates by WJC, milling, and laser cutting. Displayed as a violin plot. (Reproduced from [1])

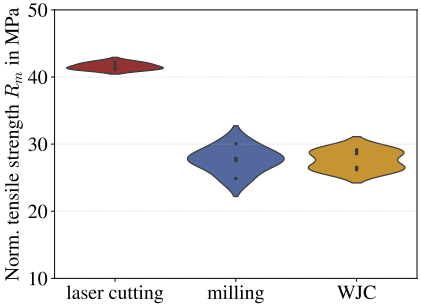

Figure 5.14: Tensile strength R_{m} normalized to the relative filling density ρ_{rel} for specimens cut from small plates by WJC, milling, and laser cutting. Displayed as a violin plot. (Reproduced from [1])

Both the stiffness and tensile strength of the laser-cut specimens are higher than those of the waterjet-cut and milled specimens. This can be explained by the SEM images of the cutting edge and fracture surface shown in Figure 5.15 and Figure 5.16. As the cutting edges show, the edge zone melts during laser cutting. In particular, the laser focus in the center of the cutting edge leaves a characteristic surface structure. The fracture surface of a laser-cut specimen

shows a layer-thick melted edge zone (marked in yellow in Figure 5.16). This influence of the cutting method on the surface layer area is not visible in milling and WJC and explains the increased mechanical properties. The slightly lower stiffness of the WJC specimens can be explained by the increasing width of the water jet. As a result, the cross-sectional shape is trapezoidal rather than rectangular and therefore slightly smaller than specified and more difficult to measure. In addition, WJC results in a much rougher surface with defects compared to laser cutting. The cut edge of a milled specimen has no significant effect on the edge area. The individual strands are visible (marked in yellow in Figure 5.15). However, the defective surface of the WJC specimens has no significant effect on the measured tensile strength.

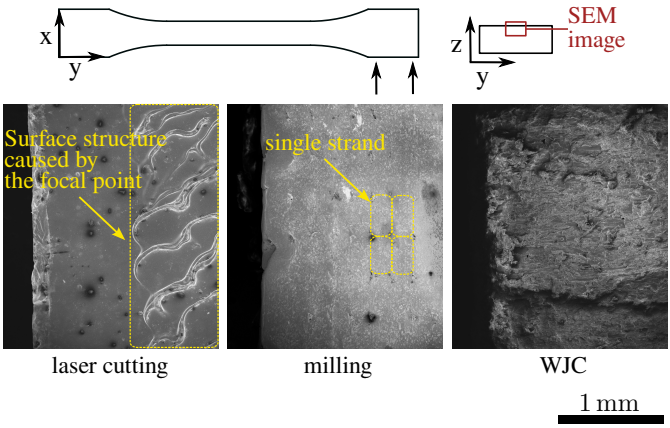

Figure 5.15: SEM images of the cut surface of laser cut, milled, and waterjet cut specimens with a material orientation of 90°. The typical microstructure can be seen in the milled specimens (marked in yellow). (Reproduced from [1])

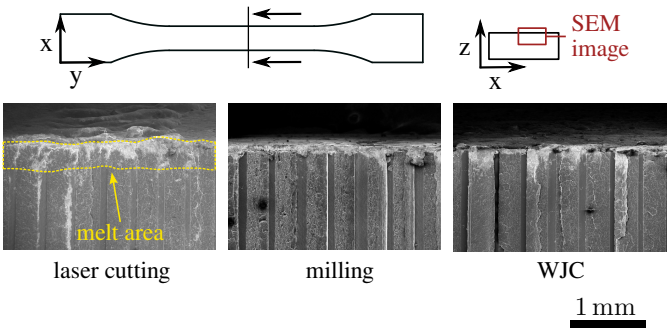

Figure 5.16: SEM images of the fracture surface of laser cut, milled and waterjet cut specimens with a material orientation of 90°. The melt area created during laser cutting is highlighted in yellow. (Reproduced from [1])

5.5 Guidelines for specimen preparation[1]

Based on the presented results, the following recommendations are made for test specimens to meet the requirements specified in Section 5.1:

Specimen geometry

- The investigations (Section 5.4.1) demonstrate that the specimen geometry significantly impacts the probability of valid tests, confirming hypothesis H 4. As a result, the dogbone geometry is recommended for test specimens.

Transferring the component structure to coupon level

- To ensure that the material orientation is accurately tested as intended (R 1), the specimen preparation must avoid introducing any deviating

[1] Verbatim reproduced section from [1], © CC BY 4.0, cf. footnote p. 101 for details.

material orientation caused by the perimeter or turning points of the trajectory. Cutting the specimen from an additively manufactured plate prevents such deviations, confirming hypotheses H 2 and H 3. Therefore, this method is recommended.

- To avoid acceleration paths within the measuring range (R 2), the time interval between the deposition of two adjacent strands must be constant over the entire specimen. This can be achieved by cutting the specimens from additively manufactured plates. Equation 5.1 can be utilized to ensure that there are no acceleration paths in the cut specimens.
- The time interval between two deposited strands must be transferred according to the process conditions during the manufacture of the component. This can be achieved by specifying a waiting time in the G-Code before printing a strand.

Cutting Method

- Milling preserves the typical MEX microstructure, avoids deviation from the specified cross-sectional shape, and is thus recommended as a cutting method. This ensures compliance with R 3. The procedure outlined in Section 5.2.4.2 can be employed for this purpose.

Reproducibility

- The preparation method must remain consistent throughout a test series.
- All process parameters must be specified as shown in Table 5.1.
- To minimize the influence of the preparation method on measurement uncertainty, it is advisable to cut each specimen from a single plate. This approach ensures that the degree of welding is consistent across the cross-section of each specimen, thereby fulfilling R 3.

- It should be noted that the hardware and firmware installed in a printer can impact the printing outcome. Therefore, it is recommended to use the same printer consistently within a test series.

5.6 Summary and conclusion[1]

The present work addresses the characterization of mechanical properties in components manufactured through AM via MEX, focusing on the challenge of achieving consistent and reproducible results. Specifically, the research aims to identify the requirements for specimen preparation to accurately represent the distinctive structure of additively manufactured components at the coupon level. To address this challenge, the study formulates requirements for test specimens and hypotheses regarding their fulfillment. Various experimental investigations are conducted, evaluating preparation methods based on tensile strength, stiffness, intralayer material orientations (0°, 90°, and ±45°), and SEM imaging of fracture surfaces and cut edges.

In conclusion, the main findings are:

- The comparison between directly printed dogbone specimens and those cut from a printed plate with rectangular geometry reveals that the cut dogbone specimens yield a higher number of valid tests.
- For material orientation in the direction of loading (0°), there are no significant differences in tensile strength and stiffness between directly printed and cut dogbone specimens.
- For specimens with material orientation transverse to the loading direction (90°), direct printing of the specimen results in higher stiffness due to the perimeter. However, the process-induced notches result in lower tensile strength.

[1] Verbatim reproduced section from [1], © CC BY 4.0, cf. footnote p. 101 for details.

- For specimens with ±45° material orientation, direct printing of the specimen results in higher stiffness and strength. The perimeter has a greater influence than the resulting notches.
- Especially for material orientations ±45° and 90°, different plate sizes have an influence on the measured stiffness and strength as well as their scatter. An equation for dimensioning the plates is presented in this paper.
- Laser cutting as a cutting method leads to a fusion of the edge area and thus to an increase in stiffness and strength.
- Compared to milling, WJC results in an uneven surface with defects at the cut edge. However, this does not significantly affect the tensile strength. In addition, WJC results in a trapezoidal cross-section of the specimen, which makes it difficult to measure the cross-sectional area.

Finally, a guideline for the preparation of representative specimens is recommended: Dogbone specimens according to DIN EN ISO 527-2 should be used and milled from one plate. The plate size should be such that exactly one specimen can be taken. To ensure that the structure on the coupon level corresponds to the structure on a printed part, the time between the deposition of two adjacent strands must also be considered. Consistent definition of the process parameters leads to increased comparability and reproducibility of the results obtained. In further work, this preparation method can be further validated by producing a component with different local processing parameters and comparing the mechanical properties of corresponding specimens.

6 MEX process simulation and prediction of process-induced deformation considering the process-characteristic mesostructure[2,3]

Outline

This chapter addresses process-specific mesostructures in process-induced deformation (PiD) prediction. Section 6.1 outlines the process modeling. Section 6.2 presents thermomechanical and kinetic PLA properties influenced by mesostructure. Section 6.3 introduces the material model used for PLA. Section 6.4 categorizes typical MEX mesostructures. Section 6.5 presents homogenization approaches considering local mesostructures. Numerical studies within Section 6.5 examine material orientation, its evolution, and element size effects. Section 6.6 validates the approaches experimentally, including sensitivity analyses. Section 6.7 summarizes findings and conclusions.

[2] Extracts from this Chapter have been previously published in [2], i.e. F. Frölich, M. E. Di Nardo, C. Krauß, A. Heuer, W. V. Liebig, F. Wittemann, P. Carlone, L. Kärger. An orientation-based homogenization approach for predicting process-induced deformations in extrusion-based additive manufacturing. *Additive Manufacturing*, 113:105023, 2025 - Reproduced sections and paragraphs are marked with [2].

[3] Extracts from this Chapter have been previously published in [3], © CC BY 3.0, i.e. F. Frölich, D. Dörr, A. Jackstadt, F. Wittemann, L. Kärger. Mechanical and kinetic characterization of additively manufactured PLA structures for improved process and W modeling. *Materials Research Proceedings*, 54:2281-2290, 2025 - Reproduced sections are marked with [3].

6.1 Process modeling approach[2]

In this work, the entire process chain leading to the final component is numerically represented using the AM-Modeler in *Abaqus* [183]. The simulation framework comprises the following steps:

1) Simulation of the additive manufacturing process via a sequentially coupled thermomechanical approach.

2) Cooling of the printed component using a predefined thermal profile of the build plate.

3) Detachment of the component from the build plate.

The construction of the simulation model is performed fully automatically. A dedicated automation framework was developed for this purpose as part of a Bachelor's thesis [231] guided within the broader scope of this doctoral research. The individual stages of the process simulation workflow are illustrated in Figure 6.1. To initiate the simulation, a bounding cube encompassing the maximum dimensions of the component is defined within the global coordinate system and discretized using hexahedral finite elements. Linear hexahedral elements are employed for thermal analyses, whereas thermomechanical simulations utilize quadratic hexahedral elements with reduced integration. Based on a sensitivity analysis (cf. Section 6.6.3.1), the temporal and spatial discretization is selected to balance computational efficiency with prediction accuracy. Specifically, a time increment of $t_{\mathrm{inc}} = 5\,\mathrm{s}$ and an element size of $1\,\mathrm{mm} \times 1\,\mathrm{mm} \times 0.4\,\mathrm{mm}$ are used.

Element activation follows a defined event sequence to ensure that only material corresponding to deposited regions is activated. This event sequence is automatically derived from the G-Code by means of the open-source tool, *pyGCD* [212, 213]. The initial temperature of each activated element is set to the extrusion temperature of $220\,^{\circ}\mathrm{C}$.

[2] Adapted and revised from [2], © CC BY 4.0, cf. footnote p. 127 for details.

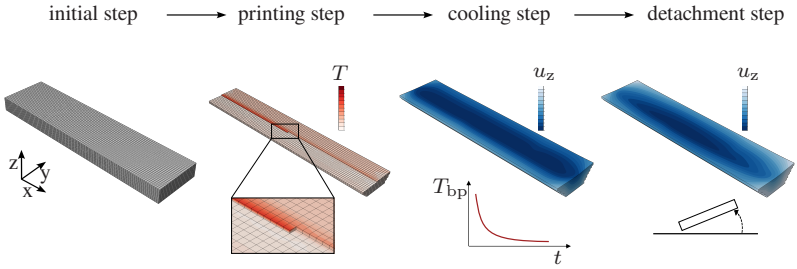

Figure 6.1: Sequential steps of the MEX process chain simulated to predict PiD. During the "initial step", domains with inactive elements are prepared. In the "printing step", the MEX process is modeled using a sequential thermomechanical simulation with a fixed build plate temperature of $T_{\mathrm{bp}} = 40\,^{\circ}\mathrm{C}$. In the "cooling step", this temperature gradually decreases to ambient conditions. Finally, in the "detachment step", the component is released from the build plate. (Reproduced from [2])

Within the thermal analysis, the temperature of the build plate is applied as a Dirichlet boundary condition to the nodes at the base of the component. In the subsequent mechanical simulation, these nodes are constrained accordingly to represent the mechanical fixation of the component to the build plate. This constraint remains active until the simulated detachment step, at which point the boundary condition is removed. The definition of boundary conditions is carried out in accordance with the guidelines for static determinacy outlined in [30].

Heat exchange with the environment is represented by convection and radiation, using a convection coefficient of $h_{\mathrm{conv}} = 8\,\mathrm{W/m^2{\cdot}K}$ and an emissivity of $\epsilon = 0.97$ as reported in [196].

6.2 Experimental characterization of additively manufactured PLA structures

This section focuses on the experimental characterization of printed structures, building on the guidelines and methodological insights established in Chapter 5. The goal is to determine which thermomechanical and kinetic properties are affected by the process-specific mesostructure, and which properties ultimately need to be considered in material modeling.

6.2.1 Specimen preparation[3]

The *Ultimaker 2+* was used to produce the test specimens. The standard glass print bed has been replaced by a FilaPrint print bed from Filafarm. The nozzle used has a diameter of $0.4\,\mathrm{mm}$ and was specified with a print resolution of $200\,\mu\mathrm{m}$ to $20\,\mu\mathrm{m}$. The slicer and printer settings, listed in Table 6.1, were selected based on printing studies to achieve a consistent and reproducible microstructure. The fan was switched on from the second layer on. To exclude manufacturing influences, such as the perimeter or the turning points, previous investigations on suitable mechanical properties characterization (cf. Chapter 5) were utilized. The specimens were cut from an additively manufactured plate

Table 6.1: Slicer and process parameters selected for the manufacturing of all specimens. [3]

Process parameter	Value	Unit
Nozzle temperature T_N	210	$^\circ\mathrm{C}$
Bed temperature T_bp	60	$^\circ\mathrm{C}$
Layer height l_height	0.2	mm
Extrusion width e_width	0.4	mm
Printing velocity v_p	50	$\mathrm{mm/s}$

[3] Verbatim reproduced section from [3], © CC BY 3.0, cf. footnote p. 127 for details.

according to the specifications in Chapter 5. The dimensions of the specimens are described in the respective subsections of the individual characterization tests.

6.2.2 Experimental methods

6.2.2.1 Tensile tests

To describe the MEX typical orthotropic stiffness tensor $\mathbb{C}_{\mathrm{ortho}}$ as described in the literature (cf. Section 2.4), the required nine engineering constants were determined according to the recommendation of Tröger et al. [106] (cf. Section 2.4.2.4). Tensile moduli (E_{11}, E_{22}, E_{33}) and Poisson's ratios (ν_{12}, ν_{13}, ν_{23}) are determined from tensile tests on specimens with three different orientations: $0\,^{\circ}$, $90\,^{\circ}$, and $90\,^{\circ}\mathrm{z}$. The $0\,^{\circ}$ and $90\,^{\circ}$ specimens lie in the x-y plane, with $0\,^{\circ}$ aligned along the extrusion direction and $90\,^{\circ}$ perpendicular to it. The $90\,^{\circ}\mathrm{z}$ specimens capture the behavior along the build direction (z-direction). For these, square towers are printed, from which plates are cut and prepared into specimens as described in Section 6.2.1. The shear moduli (G_{12}, G_{13}, G_{23}) are determined using Equation 2.7.

The same test setup and the same specimen geometry (dogbone) were used as in Chapter 5, please refer to the explanations in Section 5.3.1 on the test setup and the explanations in Section 5.2.3 on the geometry. All experiments were performed at a room temperature of $RT = 23\,^{\circ}\mathrm{C}$. The specimens were vacuum-dried at $25\,^{\circ}\mathrm{C}$ for 24 hours before testing. At least eight tests were carried out for each configuration.

6.2.2.2 Dynamic Mechanical Analysis (DMA)[3]

A DMA was performed at 1 Hz to determine the relative influence of temperature on stiffness. In the context of this work, this was carried out on a specimen with a structure oriented in the direction of loading (0 °). The influence of the strand orientation is not considered in this work. This is based on the assumption that the influence of orientation on the temperature dependence of the stiffness of PLA is comparatively small and can therefore be neglected, which has been confirmed in preliminary experiments. An Instron E3000 ElectroPuls™ with a nominal force of 3 kN and a load cell capacity of 5 kN was used. The machine was equipped with an Instron liquid nitrogen-cooled temperature chamber. To protect the load cell from overheating during the test, a water-cooling system was used to ensure accurate force measurement. Rectangular specimens with a length of 160 mm, a width of 10 mm, and a thickness of 3 mm were used. The clamping on both sides was 50 mm, resulting in a free specimen length of 60 mm. A temperature range of 25 °C to 145 °C was measured with isothermal steps of 2.5 °C. The specimens were loaded with a mean strain of 0.25 % and a strain amplitude of 0.125 %. This loading is within the linear viscoelastic region.

6.2.2.3 Thermomechanical Analysis (TMA)[3]

The key factor for PiD mechanisms in the process chain is the volume change due to temperature changes. The solid mechanics modeling of the printing process and the study of the reheating during the annealing process make it necessary to determine the volume change of the printed structures and not of raw material. Therefore, a TMA was performed to characterize the changes in length. The TMA/SS-6000 from Seiko Instruments was used. The investigations were carried out on cubic specimens with a uniform edge length of 6 mm. Specimens were prepared with unidirectional orientation of the

[3] Verbatim reproduced section from [3], © CC BY 3.0, cf. footnote p. 127 for details.

deposited strands to examine the change in length along ($0\,^\circ$) and across ($90\,^\circ$) the extrusion direction. The specimens were printed with a nozzle diameter (d_N) of $d_\mathrm{N1} = 0.4\,\mathrm{mm}$ and $d_\mathrm{N1} = 0.8\,\mathrm{mm}$, respectively. Furthermore, the specimens were annealed to separate the irreversible effects during this process step. The heating rate was $1\,\mathrm{K/mm}$, and the applied preload was $20\,\mathrm{mN}$.

6.2.2.4 Differential Scanning Calorimetry (DSC)[3]

Material-specific crystallization kinetics are an important factor in the formation of PiD in the process chain. Crystallization effects lead to volume changes and the degree of crystallinity influences the stiffness of the material. DSC measurements are used to characterize the kinetics and to determine which crystallization effects occur at which stages of the process. To account for the full history of the PLA, the crystallization behavior during cooling from the melt (extrusion from the nozzle) and during heating of the additive manufactured structures (annealing) is performed.

For cooling from the melt, cooling rates of $5\,\mathrm{K/min}$, $10\,\mathrm{K/min}$, $20\,\mathrm{K/min}$, $30\,\mathrm{K/min}$, $40\,\mathrm{K/min}$, and $50\,\mathrm{K/min}$ were investigated. It should be noted that much higher cooling rates can occur during the printing process. To assess the absolute crystallinity χ_c of the specimens after cooling, they were reheated at a rate of $10\,\mathrm{K/min}$. The absolute crystallinity χ_c in different specimens can be calculated by Equation 2.8. The absolute melting enthalpy of $100\,\%$ crystalline PLA is $93\,\mathrm{J/g}$ according to [232]. To increase the validity of the data, two measurements were made for each cooling rate.

To investigate the kinetics of additively manufactured structures, specimens are taken from printed plates and heated at $0.5\,\mathrm{K/min}$, $1\,\mathrm{K/min}$, $5\,\mathrm{K/min}$, $10\,\mathrm{K/min}$, and $20\,\mathrm{K/min}$. To determine the absolute crystallinity χ_c of the printed plate, the initial absolute crystallinity was determined based on the enthalpy changes during the heating process.

[3] Verbatim reproduced section from [3], © CC BY 3.0, cf. footnote p. 127 for details.

As part of these investigations, two measurement campaigns were carried out. The first with cooling rates of $1\,\mathrm{K/min}$ - $10\,\mathrm{K/min}$ with two measurements each. A second was performed at $0.5\,\mathrm{K/min}$ and $20\,\mathrm{K/min}$ with three measurements each to cover a wider range of heating rates occurring during annealing. To ensure comparability of the two sets of measurements, an additional measurement at $1\,\mathrm{K/min}$ was made during the second campaign and compared with those of the first campaign. The enthalpy change during cold crystallization and melting was used as a comparative measure. The first set of measurements gave an average enthalpy change of $\Delta H_{\mathrm{cc}} = 21.21\,\mathrm{J/g}$ during cold crystallization and $\Delta H_{\mathrm{m}} = 23.01\,\mathrm{J/g}$ during melting. The second set of measurements gave an average enthalpy change of $\Delta H_{\mathrm{cc}} = 20.90\,\mathrm{J/g}$ during cold crystallization and $\Delta H_{\mathrm{m}} = 23.61\,\mathrm{J/g}$ during melting. The comparison shows that the two sets of measurements are comparable and can be combined for investigation.

To investigate the influence of the typical mesostructure on the crystallization behavior, the enthalpy changes were compared when heating a printed structure and a previously melted and resolidified structure (unstructured) at a heating rate of $1\,\mathrm{K/min}$. The comparison is made within a single measurement on a specimen with multiple heating and cooling phases. This ensures that the measurements are not subject to scatter between different series of measurements.

6.2.3 Characterization results

6.2.3.1 Tensile tests[2]

The tensile tests performed as part of this work resulted in the material properties listed in Table 6.2. The corresponding stress-strain diagrams can be found in the A.3.

The resulting orthotropic stiffness tensor $\mathbb{C}_{\mathrm{ortho}}$ for a unidirectional infill pattern at $100\,\%$ infill density was determined from the tensile test results shown in

[2] adapted and revised from [2], © CC BY 4.0, cf. footnote p. 127 for details.

Table 6.2. The tests performed enabled to characterize the required nine material constants to describe $\mathbb{C}_{\mathrm{ortho}}$ at room temperature, except ν_{23}, $\hat{E}^{45,13-\mathrm{plane}}$, and $\hat{E}^{45,23-\mathrm{plane}}$. The remaining constants, the experimentally determined material properties of Tröger et al. [106] were used, since the experiments in [106] led to similar results. The resulting nine engineering constants to describe $\mathbb{C}_{\mathrm{ortho}}$ are shown in Table 6.3, which were previously published in [2].

Table 6.2: Material properties from tensile tests on specimens with 0 °, 90 °, 90 °z and 45° orientation.

E^0 (MPa)	E^{90} (MPa)	E^{90z} (MPa)	$\hat{E}^{45,12-\mathrm{plane}}$ (MPa)	ν_{12} –	ν_{13} –
3257 ± 94	2469 ± 177	2667 ± 189	2590 ± 233	0.35 ± 0.02	0.27 ± 0.04

Table 6.3: Engineering constants used to determine the orthotropic stiffness $\mathbb{C}_{\mathrm{ortho}}$ of a unidirectional MEX structure. [2]

E_{11} (MPa)	E_{22} (MPa)	E_{33} (MPa)	ν_{12} –	ν_{13} –	ν_{23} –	G_{12} (MPa)	G_{13} (MPa)	G_{23} (MPa)
3257	2469	2667	0.35	0.27	0.31 [106]	953	1029	803

6.2.3.2 Dynamic Mechanical Analysis (DMA)[3]

Figure 6.2 shows the storage modulus E' as a function of temperature T. E' is significantly higher below the glass transition temperature $T_{\mathrm{G}} = 62.4 \pm 0.3\,^{\circ}\mathrm{C}$. At a temperature of $25\,^{\circ}\mathrm{C}$, the module is $E' = 2910\,\mathrm{MPa}$, and just above T_{G} it is $E' = 20\,\mathrm{MPa}$. From around $70\,^{\circ}\mathrm{C}$ the stiffness increases to $E' = 150\,\mathrm{MPa}$ before decreasing with increasing temperature. The 99.28% decrease

[3] Verbatim reproduced section from [3], © CC BY 3.0, cf. footnote p. 127 for details.

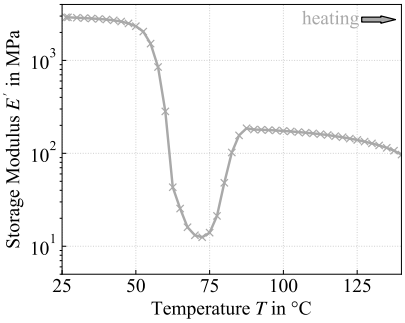

Figure 6.2: Storage modulus E' as a function of temperature T, measured by DMA at a frequency of 1 Hz. (Reproduced from [3])

in modulus shows the strong softening of PLA when T_{G} is exceeded. The increase of E' at higher temperatures is due to cold crystallization effects during the experiment. The visible cold crystallization effects also indicate that the initial absolute degree of crystallinity of the specimens was low. This may be due to the high cooling rates during the manufacturing process combined with PLA-specific slow crystallization kinetics. These hypotheses will be addressed in the discussion of the DSC experiments later in this work. For material modeling of PLA over the entire process chain, these results imply that during the printing process for $T > T_{\mathrm{G}}$, the stiffness of PLA corresponds to the stiffness of a low degree of crystallinity.

6.2.3.3 Thermomechanical Analysis (TMA)[3]

Figure 6.3 shows the change in length as a function of temperature as strain ε in %. The minimum and maximum values at each measurement point are shown in shaded colors. The blue line shows the change in length for specimens with a nozzle diameter of $d_{\mathrm{N1}} = 0.4\,\mathrm{mm}$. The yellow line shows data for a nozzle

[3] Verbatim reproduced section from [3], © CC BY 3.0, cf. footnote p. 127 for details.

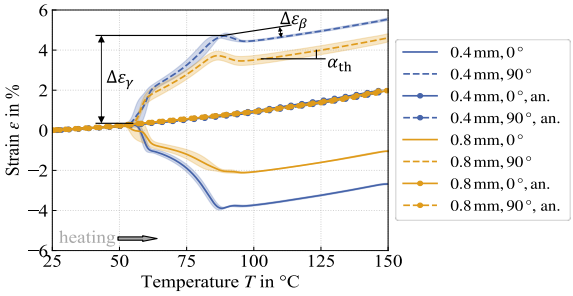

Figure 6.3: The change in length due to temperature increase as strain ε in % in extrusion direction (0 °) and transverse to extrusion direction (90 °). (Reproduced from [3])

diameter of $d_{\mathrm{N2}} = 0.8\,\mathrm{mm}$. The solid lines illustrate the measurements in the extrusion direction (0 °), and the dashed lines transverse to the extrusion direction (90 °). The lines with dots at the measuring points show the measurements on annealed specimens. When the temperature exceeds T_{G} there is a negative change in length in the extrusion direction and a positive change in length in the transverse direction for unannealed specimens. The behavior is affected by the nozzle diameter used, indicating that the effect is related to the shear strain in the polymer, which is affected by the nozzle diameter. The shear strain in the polymer stretches the molecular chains as they exit the nozzle. Due to the high cooling rates and nozzle motion, the chains do not reorient completely after exiting the nozzle and remain in an aligned state. When reheated above the glass transition temperature, the chains reorient to their energetically most favorable state, which is a ball-like form. This phenomenon is also referred to as entropic elasticity and results in the deposited strands becoming shorter on reheating but wider transverse to the extrusion direction. This change in length is irreversible and is labeled $\Delta\varepsilon_\gamma$ in Figure 6.3. The slope below T_{G} and after the change in length due to entropic elasticity $\Delta\varepsilon_\gamma$ represents the thermal expansion coefficient α_{th}. This expansion is reversible, as shown by the same slope for the annealed specimens. In addition, a change in length due to cold crystallization effects can be observed. This is labeled $\Delta\varepsilon_\beta$ in Figure 6.3. DSC tests confirm the temperature range in which this effect occurs. The changes

in length with increasing temperature of the annealed specimens show no significant dependence on the strand orientation. This allows the assumption that α_{th}can be modeled isotropically. In contrast, $\Delta\varepsilon_{\mathrm{y}}$ and $\Delta\varepsilon_{\beta}$ should be modeled anisotropically.

6.2.3.4 Differential Scanning Calorimetry (DSC)[3]

Cooling from the melt stage Figure 6.4a shows the specific heat flow $\dot{q}$ of PLA during cooling at rates of $-5\,\mathrm{K/min}$, $-10\,\mathrm{K/min}$, $-20\,\mathrm{K/min}$, $-30\,\mathrm{K/min}$, $-40\,\mathrm{K/min}$ and $-50\,\mathrm{K/min}$. The figure shows the mean of two measurements, with the minimum and maximum values for each measurement point shown in shaded form. The crystallization peaks are less pronounced compared to the measured $\dot{q}$, which is a first indication that no significant crystallization effects occur at these cooling rates during the MEX process. In Figure 6.4b the mean $\dot{q}_{\mathrm{n}}$ normalized to the cooling rate is plotted for the measured rates. The crystallization peak region is shown without the heat flow

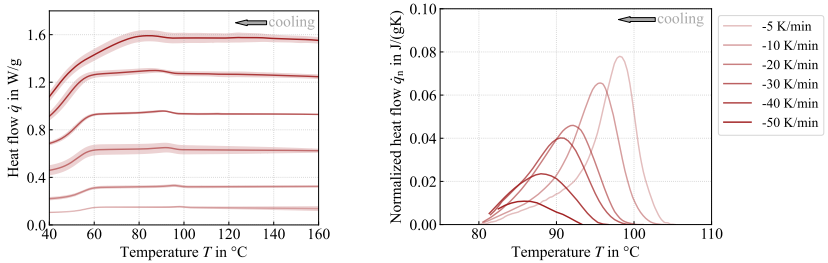

Figure 6.4: a) Specific heat flow $\dot{q}$ of PLA Ultrafuse during cooling at cooling rates of $-5\,\mathrm{K/min}$, $-10\,\mathrm{K/min}$, $-20\,\mathrm{K/min}$, $-30\,\mathrm{K/min}$, $-40\,\mathrm{K/min}$, and $-50\,\mathrm{K/min}$. b) Mean heat flow $\dot{q}_{\mathrm{n}}$ normalized to the cooling rate for the measured rates. The area of the crystallization peak minus the baseline is shown. (Reproduced from [3])

[3] Verbatim reproduced section from [3], © CC BY 3.0, cf. footnote p. 127 for details.

baseline. In defining the crystallization temperature range, it was assumed that no crystallization effects occur below $80\,^{\circ}\mathrm{C}$ at the cooling rates used here. This is based on previous isothermal DSC measurements. The enthalpy change is small, especially at the higher cooling rates. Since much higher cooling rates occur in the MEX process, this is another indication that the absolute degree of crystallinity after the printing process is low.

To further confirm this hypothesis, the measured specimens were reheated at a rate of $10\,\mathrm{K/min}$ and the changes in enthalpy during cold crystallization ΔH_{cc} and melting ΔH_{m} were measured. Figure 6.5 shows the specific heat flow $\dot{q}$ in the respective temperature ranges for cold crystallization (Figure 6.5a) and melting (Figure 6.5b). The enthalpy changes are much larger than for crystallization during cooling (Figure 6.4b) and are not significantly different for all specimens. The initial degrees of crystallization in the specimens are therefore comparable, and it can be assumed that the initial degree of crystallinity must have been low.

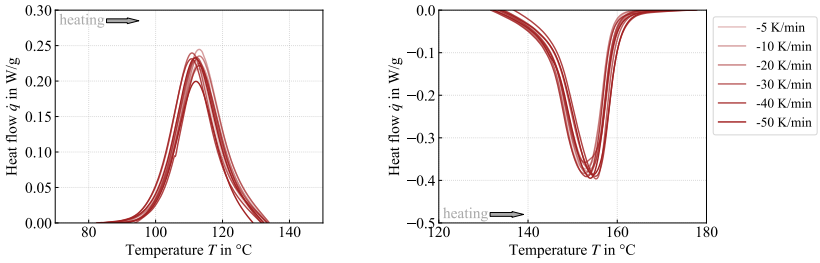

Figure 6.5: a) Specific heat flow $\dot{q}$ in the respective temperature ranges for cold crystallization and b) melting, resulting from heating the specimens previously cooled at different rates. The heating rate was 10 K/min for all measurements. (Reproduced from [3])

Heating additively manufactured structures Figure 6.6a shows the specific heat flow $\dot{q}$ of printed PLA structures during heating at rates of $0.5\,\mathrm{K/min}$, $1\,\mathrm{K/min}$, $5\,\mathrm{K/min}$, $10\,\mathrm{K/min}$, and $20\,\mathrm{K/min}$. The mean of two measurements per heating rate is shown, with the minimum and maximum values for each measurement point shown in shaded form. T_G appears as a peak in the range of $60\,^\circ\mathrm{C}$ to $70\,^\circ\mathrm{C}$ due to macromolecular organization and associated stress relaxation. Compared to cooling, the dependence of crystallization kinetics on the underlying heating rate is more pronounced during heating. Figure 6.6b illustrates the mean heat flow $\dot{q}_\mathrm{n}$ normalized to the heating rate. The crystallization peak region is shown without the heat flow baseline. The measurements show the effect of the heating rate on the crystallization behavior of the printed structures. The enthalpy changes are higher compared to the cooling of the raw material. Hence, when modeling PLA in the annealing process step, crystallization effects and their influence on stiffness during heating must be considered. The measurements can also be used to determine the initial absolute degree of crystallinity χ_c of the specimens using Equation 2.8. Since the underlying specimens were cut from a printed plate, their degree of crystallinity provides information on the crystallization effects during the MEX process with PLA. A total of 13 specimens were measured and a mean absolute crystallinity of $\chi_\mathrm{c} = 2.67\,\% \pm 1.28\,\%$ was determined.

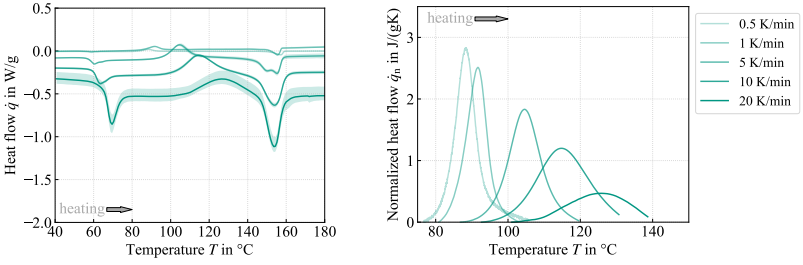

Figure 6.6: a): Specific heat flow $\dot{q}$ of PLA specimens printed with MEX during heating at rates of $0.5\,\mathrm{K/min}$, $1\,\mathrm{K/min}$, $5\,\mathrm{K/min}$, $10\,\mathrm{K/min}$, and $20\,\mathrm{K/min}$. b): Mean heat flow $\dot{q}_\mathrm{n}$ normalized to the heating rate for the measured rates. The area of the crystallization peak minus the baseline of the heat flow is shown. (Reproduced from [3])

6.2.4 Mechanisms to be modeled[3]

The thermomechanical and kinetic characterizations conducted in this section provide a detailed understanding of PLA's behavior across the stages of the MEX process chain. The goal of these investigations was to identify process-specific mechanisms arising from the mesostructure that significantly contributes to PiD, as well as to determine which mechanisms must be explicitly incorporated into material modeling to enable reliable numerical prediction.

The results show that different physical mechanisms dominate in different phases of the process. Notably, crystallization phenomena during printing and post-processing steps, such as detachment from the build plate and removal of support structures, were found to have a negligible influence on deformation behavior. Consequently, the material modeling for these stages can be unified and implemented without considering crystallization effects.

Although a possible annealing step was considered during the experimental investigations, this thesis focuses on modeling the printing, cooling on the build plate, detachment, and support structure removal phases. Accordingly, only the effects relevant for these four phases are summarized below.

- The deposition path induces a directional material orientation, which leads to anisotropic stiffness. This effect must be taken into account in the mechanical model in order to reflect the influence of the developing mesostructure.
- A significant decrease in stiffness occurs when the glass transition temperature is exceeded, as evidenced by a 99.28% drop in the storage modulus. This emphasizes the importance of including the strong temperature dependence of mechanical properties in simulations.
- Cold crystallization was observed in the additively manufactured specimens. However, the low degree of crystallinity measured after printing

[3] Adapted and revised from [3], © CC BY 3.0, cf. footnote p. 127 for details.

suggests that crystallization during the printing process is minimal and can be disregarded in the material model.

- TMA experiments revealed that thermal expansion during printing is isotropic. Only subsequent annealing revealed anisotropic volume changes due to molecular reorientation and cold crystallization. Structures that have already been annealed again exhibit isotropic thermal expansion.

6.3 Material modeling

This section presents the selected material modeling. The thermal behavior is mapped using existing material models in *Abaqus*. The thermomechanical material model is provided as an *Abaqus* user subroutine (UMAT). Viscoelasticity and temperature-dependent stiffness are simplified using a path-dependent material model. Thermal expansion is modeled as isotropic and temperature-dependent.

6.3.1 Thermal behavior

The thermal behavior of PLA was modeled using the built-in material models in *Abaqus*. The density of the PLA structure using the process parameters listed in Table 6.4 is $\rho_{\mathrm{PLA}} = 1208\,\mathrm{kg/m^3}$ [4] and was determined in accordance with Archimedes' principle using a *ME-DNY-43* meter and an *ME204T/00* analytical balance, both from *Mettler Toledo*.

The anisotropic thermal conductivity $\boldsymbol{\kappa}$ was approximated as isotropic based on a simulation study using the approach described in Chapter 7 (cf. Appendix A.5). Since heat dissipation through convection and radiation influences the cooling of the material much more than heat conduction transport does, the difference caused by material orientation can be neglected in the modeled thermal conductivity. For this reason, an effective isotropic thermal conductivity

coefficient of $\kappa_{\mathrm{eff}} \approx 0.17\,\mathrm{W/(m \cdot K)}$ was used, based on the average of the anisotropic values determined by Elkholy et al. [64].

The temperature-dependent specific heat capacity, $c_{\mathrm{p}}(T)$, was determined using differential scanning calorimetry (DSC) and is shown in Figure 6.7 [4]. In accordance with the explanations in Section 6.2.3.4, it is assumed that the material does not crystallize during the printing process or the considered post-processing steps.

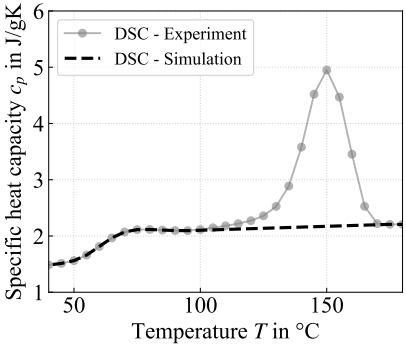

Figure 6.7: Temperature-dependent specific heat capacity $c_{\mathrm{p}}(T)$ of the PLA used, measured by DSC. (Previously published in [4])

6.3.2 Thermomechanical behavior

6.3.2.1 Thermomechanical model[2]

In the mechanical simulations, a path-dependent material formulation is applied to capture the viscoelastic response of the material [233]. The viscoelastic behavior is represented in a simplified manner by assuming that the relaxation

[2] Adapted and revised from [2], cf. footnote p. 127 for details.

time τ approaches infinity below a characteristic vitrification temperature T_{vitr} (glassy state), whereas it tends toward zero above this temperature (rubbery state). Within this framework, the Cauchy stress $\boldsymbol{\sigma}$ is additively decomposed into an elastic part $\boldsymbol{\sigma}_{\mathrm{el}}$ and a simplified pseudo-viscoelastic part $\boldsymbol{\sigma}_{\mathrm{ve}}$:

$$\boldsymbol{\sigma} = \boldsymbol{\sigma}_{\mathrm{el}} + \boldsymbol{\sigma}_{\mathrm{ve}}. \tag{6.1}$$

The elastic part of the stress at the current increment t_{i} is updated according to

$$\boldsymbol{\sigma}_{\mathrm{el}}(t_{\mathrm{i}}) \approx \boldsymbol{\sigma}_{\mathrm{el}}(t_{\mathrm{i}-1}) + \bar{\mathbb{C}}_{\infty}\big(\Delta\boldsymbol{\varepsilon}(t_{\mathrm{i}}) - \Delta\boldsymbol{\varepsilon}_{\mathrm{th}}(t_{\mathrm{i}})\big), \tag{6.2}$$

where $\boldsymbol{\sigma}_{\mathrm{el}}(t_{\mathrm{i}-1})$ denotes the elastic stress from the previous increment, and $\bar{\mathbb{C}}_{\infty}$ represents the effective stiffness above the vitrification temperature. The effective stiffness tensor $\bar{\mathbb{C}}$ can be interpreted as the local resulting stiffness that arises from the mesostructure generated by the MEX process. The strain increment $\Delta\boldsymbol{\varepsilon}$ accounts for the total strain change, whereas $\Delta\boldsymbol{\varepsilon}_{\mathrm{th}}$ corresponds to the thermal strain increment, defined as

$$\Delta\boldsymbol{\varepsilon}_{\mathrm{th}}(t_{\mathrm{i}}) = \boldsymbol{\alpha}_{\mathrm{th}}\big(T(t_{\mathrm{i}}) - T(t_{\mathrm{i}-1})\big). \tag{6.3}$$

The pseudo-viscoelastic part $\boldsymbol{\sigma}_{\mathrm{ve}}$ is expressed through two limiting cases:

$$\boldsymbol{\sigma}_{\mathrm{ve}}(t_{\mathrm{i}}) = \begin{cases} \mathbf{0}, & T \geq T_{\mathrm{vitr}} \\ \boldsymbol{\sigma}_{\mathrm{ve}}(t_{\mathrm{i}-1}) + \Delta\bar{\mathbb{C}}[\Delta\boldsymbol{\varepsilon}(t_{\mathrm{i}}) - \Delta\boldsymbol{\varepsilon}_{\mathrm{th}}(t_{\mathrm{i}})], & T < T_{\mathrm{vitr}} \end{cases}. \tag{6.4}$$

Above the vitrification temperature, the viscoelastic part vanishes due to the instantaneous relaxation ($\tau \to 0$). Below T_{vitr}, however, $\boldsymbol{\sigma}_{\mathrm{ve}}$ evolves incrementally from the previous state, accounting for the stiffness difference (between glassy and rubbery state) $\Delta\bar{\mathbb{C}}$, the applied strain increment $\Delta\boldsymbol{\varepsilon}$, and the thermal strain increment $\Delta\boldsymbol{\varepsilon}_{\mathrm{th}}$. In this way, the viscoelastic behavior is approximated by two successive elastic-type updates, independent of one another (in contrast to, for instance, the *CHILE* model [234]). This representation is particularly

relevant since the material may cross T_{vitr} multiple times, and stress relaxation upon reheating is naturally incorporated.

$\Delta\bar{\mathbb{C}}$ is defined via the relative softening coefficient a_{soft} as

$$\Delta\bar{\mathbb{C}} = \bar{\mathbb{C}}_0 - \bar{\mathbb{C}}_\infty = a_{\mathrm{soft}}\bar{\mathbb{C}}_0, \tag{6.5}$$

where $\bar{\mathbb{C}}_0$ denotes the effective stiffness tensor below the vitrification temperature.

6.3.2.2 Model parametrization

Effective stiffness tensor $\bar{\mathbb{C}}$ The parametrization of the effective stiffness $\bar{\mathbb{C}}$ is carried out on the basis of the experimentally measured orthotropic stiffness tensor $\bar{\mathbb{C}}_{\mathrm{ortho}}$ (cf. Section 6.2.3.1). To describe $\bar{\mathbb{C}}$, both an isotropic (cf. Section 6.5.1) and an anisotropic homogenization approach (cf. Section 6.5.2) are introduced, which will be discussed in detail in the following.

Softening coefficent[2] The softening coefficient a_{soft} from glassy to rubbery state is determined using the modified E' curve with

$$a_{\mathrm{soft}} = 1 - \left(\frac{\min(E')}{\max(E')}\right) = 0.991. \tag{6.6}$$

Vitrification temperature[2] The vitrification temperature T_{vitr} is determined based on DMA experiments (cf. Section 6.2.3.2) and investigations into the crystallization behavior (cf. Section 6.2.3.4) that occurs during the MEX process. For this purpose, the temperature-dependent storage modulus characteristics obtained from DMA are used. Since crystallization during the printing process is negligible, the renewed increase in storage modulus due to

[2] Adapted and revised from [2], cf. footnote p. 127 for details.
[2] Adapted and substantially extended from [2], cf. footnote p. 127 for details.

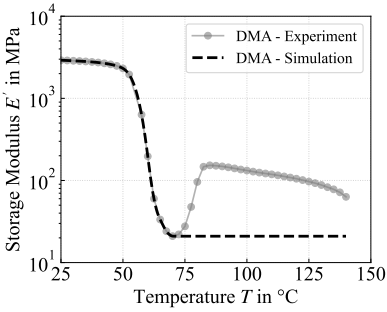

Figure 6.8: Storage modulus E' as a function of temperature obtained from DMA measurements on unidirectionally printed specimens with extrusion direction aligned with the load. The assumed curve for simulation includes the softening range, but no cold crystallization as the PLA remains amorphous during printing. (Reproduced from [2])

cold crystallization is not modeled. Thus, the lowest measured modulus is used for higher temperatures as well. Figure 6.8 shows the experimentally determined modulus in gray and the modulus assumed in the simulation in black. A further softening with rising temperatures above T_{vitr} is neglected. T_{vitr} was determined using two different approaches:

- **Approach A**: T_{vitr} is identified as the turning point in the storage modulus curve. In other words, it is the temperature at which the change in stiffness as a function of temperature ($\mathrm{d}E'/\mathrm{d}T$) is at its maximum. Figure 6.9 shows E' without cold crystallization effects above T_{vitr}, as well as the corresponding derivative with respect to temperature $\mathrm{d}E'/\mathrm{d}T$ in green.
- **Approach B**: T_{vitr} is defined as the midpoint of the softening range. Since there is no uniform definition of the softening range of thermoplastic materials based on DMA measurements, this study used a consistent and practical criterion. The upper limit of the softening range is the temperature at which the storage modulus transitions to a plateau ($\mathrm{d}E'/\mathrm{d} = 0$) and reaches its minimum. This reflects the complete softening of the material. The lower limit of the softening range is defined as the temperature corresponding to $10\,\%$, $15\,\%$, $20\,\%$, or $25\,\%$ of the maximum absolute

value of the derivative $\mathrm{d}E'/\mathrm{d}T$. Consequently, T_{vitr} is taken as the midpoint between these two limits, providing a consistent and comparable value for further analysis.

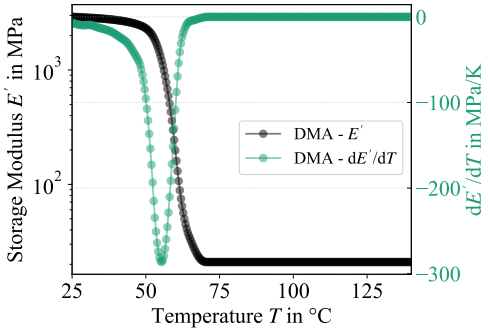

Figure 6.9: Storage modulus E' as a function of temperature, assumed in the simulation, shown in black. The corresponding derivative with respect to temperature, $\mathrm{d}E'/\mathrm{d}T$, shown in green.

During the validation phase (cf. Section 6.6.4), the two approaches were compared to evaluate their influence on the simulation results. Approach B's use of different thresholds (10%, 15%, 20%, and 25%) allowed for a sensitivity analysis of T_{vitr} determination and its effects on predicted mechanical behavior during the MEX process.

Figure 6.10 shows the path-dependent material model with different T_{vitr}, which were determined using approaches A and B as described above. The model based on approach A is shown in green. The results from approach B, which used different threshold values ($10\,\%$, $15\,\%$, $20\,\%$, and $25\,\%$), are shown in orange. For comparison, the black curve represents the experimental storage modulus E'. Additionally, the softening ranges determined using approach B are marked in different shades of gray to highlight the boundaries of the softening range and their influence on the model. This illustration demonstrates how

different approaches impact the determination of T_{vitr} and influence material behavior in process simulations.

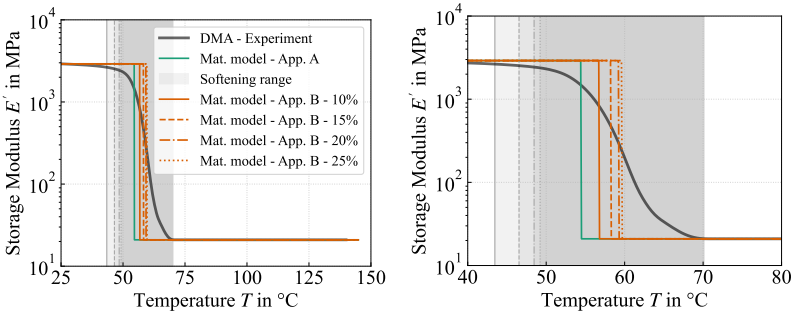

Figure 6.10: Storage modulus E', modeled using the path-dependent material model with different T_{vitr}, which were determined using approaches A and B as described above. The model based on approach A is shown in green. The results from approach B, which used different threshold values (10 %, 15 %, 20 %, and 25 %), are shown in orange. For comparison, the black curve represents the experimental storage modulus E'. Additionally, the softening ranges determined using approach B are marked in different shades of gray. a) Model in the entire test range. b) Close-up in the area of material softening.

Coefficient of thermal expansion (CTE)[2] The coefficient of thermal expansion (CTE) $\boldsymbol{\alpha}_{\mathrm{th}}$ was determined using TMA test results, as presented in Section 6.2.3.3. The experiments indicated a quasi-isotropic behavior, allowing a single scalar CTE $\alpha_{\mathrm{th}}(T)$ to be derived for all spatial directions. To obtain α_{th} as a function of temperature, the measured thermal expansion was smoothed and interpolated. Figure 6.11 shows the measured change in length in gray and the smoothed curve used for simulation in black.

[2] Adapted and revised from [2], cf. footnote p. 127 for details.

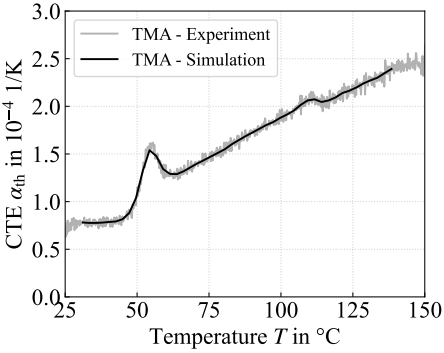

Figure 6.11: Thermal expansion behavior from TMA measurements on printed specimens, along with the assumed curve used to determine the coefficient of thermal expansion (CTE) α_{th} used in simulation. (Reproduced from [2])

6.4 Categorization of the characteristic material structure[2]

Components manufactured by using MEX can generally be divided into three distinct mesostructural regions:

1. The perimeter area, which defines the contour of the component.
2. The infill, which can be freely specified.
3. The transition zone between the perimeter and the infill, where changes in the extrusion nozzle's movement direction result in a modified mesostructure.

The infill pattern is defined by various parameters, including the infill angle, which controls the orientation of the deposited strands. Both the infill and the number of perimeters can be defined prior to fabrication, allowing for a wide range of local mesostructures within the same component geometry and material

[2] Verbatim reproduced section from [2], cf. footnote p. 127 for details.

density. Figure 6.12 schematically illustrates the three regions described. In addition to the orientation of the deposited strands, the mesostructure is also characterized by the resulting voids. Figure 6.13 shows a resulting mesostructure of an infill area for a print in which all strands are deposited in the same direction. A schematic representation (left) and a microscopic image (right) is shown. The local mesostructure strongly contributes to the stiffness of the component and thus directly controls the PiD of the manufactured component (cf. Section 2.1.3).

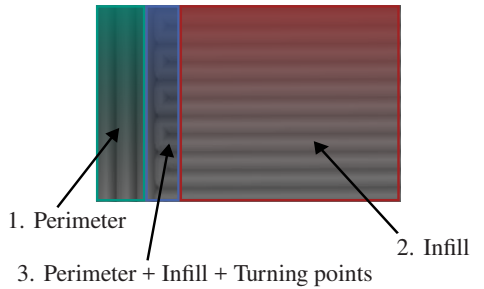

Figure 6.12: Classification of process-typical mesostructures into three different categories: perimeter (green), infill (red) and the area between perimeter and infill defined by the turning points of the extrusion and parts of the infill (blue). (Reproduced from [2])

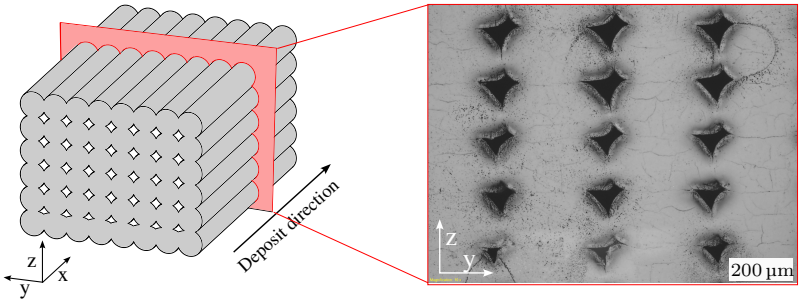

Figure 6.13: Schematic representation of a unidirectionally printed mesostructure and microscopic image of the cross-section in the y-z plane. (Reproduced from [2])

Throughout this work, the coordinate system shown in Figure 6.13 will be used. An extrusion in the x-direction is defined as an infill angle of $0\,^\circ$, and an extrusion in the y-direction is defined as an infill angle of $90\,^\circ$. It should be noted that the mesostructures within the three categories "Perimeter", "Perimeter + Infill + Turning points", and "Infill" scatter in the real process and are not exactly identical throughout the component. The approach presented in this work neglects this process scatter.

6.5 Homogenization approaches considering the mesostructure

6.5.1 Equivalent isotropic stiffness description

This section provides an equivalent isotropic description representative of the experimentally determined orthotropic stiffness $\mathbb{C}_{\mathrm{ortho}}$ (cf. Section 6.2.3.1). The implementation of this description in *Abaqus* is also explained.

6.5.1.1 Approach[2]

To obtain a representative equivalent isotropic description of an orthotropic stiffness tensor $\mathbb{C}_{\mathrm{ortho}}$ (representative of the material and its microstructure), the equivalent isotropic stiffness tensor $\bar{\mathbb{C}}_{\mathrm{iso}}$ can be calculated by integrating over all possible rotations $\boldsymbol{Q}$ in the special orthogonal group $\mathcal{SO}(3)$:

$$\bar{\mathbb{C}}_{\mathrm{iso}} = \int_{\mathcal{SO}(3)} \boldsymbol{Q} \star \mathbb{C}_{\mathrm{ortho}}, \mathrm{d}Q. \tag{6.7}$$

[2] Verbatim reproduced section from [2], cf. footnote p. 127 for details.

Using the isotropic projection operators $\mathbb{P}_1$ and $\mathbb{P}_2$, this expression can be algebraically transformed as follows:

$$\bar{\mathbb{C}}_{\mathrm{iso}} = \int_{\mathcal{SO}(3)} \boldsymbol{Q} \star \mathbb{C}_{\mathrm{ortho}}, \mathrm{d}Q = (\mathbb{C}_{\mathrm{ortho}} \cdot \mathbb{P}_1) \frac{\mathbb{P}_1}{|\mathbb{P}_1|^2} + (\mathbb{C}_{\mathrm{ortho}} \cdot \mathbb{P}_2) \frac{\mathbb{P}_2}{|\mathbb{P}_2|^2} \tag{6.8}$$

with $\mathbb{P}_1 = 1/3(\boldsymbol{I} \otimes \boldsymbol{I})$ and $\mathbb{P}_2 = \mathbb{I}^{\mathrm{S}} - \mathbb{P}_1$, where $\mathbb{I}^{\mathrm{S}}$ denotes the identity on symmetric second-order tensors. This formulation is derived from the orthogonal decomposition of $\mathbb{C}\mathrm{ortho}$ into its isotropic components. The projection coefficients are obtained by contraction with $\mathbb{P}_1$ and $\mathbb{P}_2$, ensuring that only the isotropic contributions are retained. The normalization by $|\mathbb{P}_i|^2$ guarantees the correct scaling of the projected components.

6.5.1.2 Implementation

The components of $\bar{\mathbb{C}}_{\mathrm{iso}}$ are calculated using Equation 6.8 from the experimentally determined orthotropic stiffness tensor $\mathbb{C}_{\mathrm{ortho}}$ (cf. Section 6.2.3.1) prior to process simulation. These tensor entries are then used as input variables for the path-dependent material model in the UMAT subroutine, where they correspond to the entries of $\bar{\mathbb{C}}_0$ (cf. Section 6.3.2).

The isotropic description leads to the averaged directional strain energy density $W(\mathbf{n})$, visualized in blue in Figure 6.14. The red curves show $W(\mathbf{n})$ computed from $\bar{\mathbb{C}}_{\mathrm{orth}}$, as listed in Tab. 6.3.

6.5.2 Anisotropic stiffness description

This section presents a homogenization method that accounts for the time-dependent anisotropic stiffness state when numerically predicting PiD. The goal is to accurately capture direction-dependent material properties, despite the strand- and layer-combining nature of the finite element discretization. Within this framework, the effective stiffness tensor $\bar{\mathbb{C}}$ used in the path-dependent material model (cf. Section 6.3.2) is determined. Its evaluation is based on the

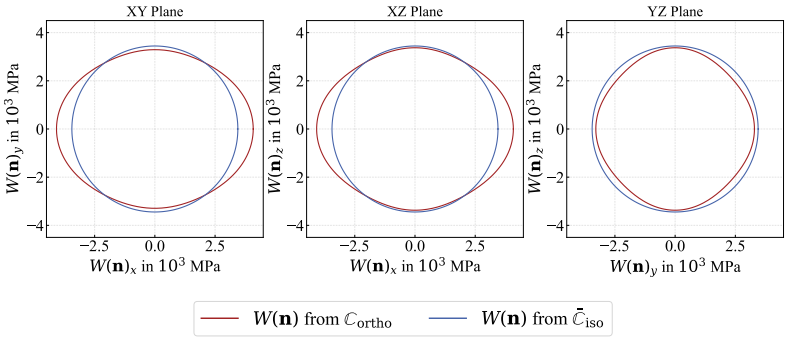

Figure 6.14: Directional strain energy density response derived from orthotropic and isotropic stiffness tensor. The plots show $W(\mathbf{n}) = \frac{1}{2}(\mathbf{n} \otimes \mathbf{n}) : \mathbb{C} : (\mathbf{n} \otimes \mathbf{n})$ evaluated for all in-plane directions $\mathbf{n}$ in the XY, XZ, and YZ planes. Units are given in MPa, corresponding to elastic strain energy density under unit strain in direction $\mathbf{n}$. (Reproduced from [2])

experimentally obtained orthotropic stiffness tensor $\bar{\mathbb{C}}_{\text{ortho}}$ (cf. Section 6.2.3.1). First, the homogenization approach is introduced. The complete workflow is then described, beginning with the analysis of the G-Code, followed by the determination of local orientation states, and concluding with the assignment of anisotropic stiffness tensors at the element level within the *Abaqus* simulation environment. Finally, the methodology is validated using suitable reference examples.

6.5.2.1 Homogenization approach[2]

To homogenize the resulting mesostructure, the orientation average scheme is used in this work [153]. It is used to determine the statistical distribution of the orientation of particles or fibers (e.g., in suspensions or composites) and to derive effective macroscopic properties.

[2] Verbatim reproduced section from [2], cf. footnote p. 127 for details.

This approach is applied to the MEX process to determine the influence of the process-typical complex and directional mesostructure on the macroscopic properties of the additively manufactured component. The orientation formulation is based on the following assumptions:

- The properties of the resulting material are considered as a function of the spatial distribution and orientation of its phases (extruded strand and air).
- Periodic mesostructures are assumed.

The orientation distribution function (ODF) $f(\boldsymbol{x}, \boldsymbol{p})$ is used to describe the resulting mesostructures statistically [153]. This function represents a probability density. Its integration yields the probability of finding an extruded strand aligned in the direction $\boldsymbol{p}$ at the spatial position $\boldsymbol{x}$. $f(\boldsymbol{x}, \boldsymbol{p})$ is characterized by the following properties:

$$f(\boldsymbol{x}, \boldsymbol{p}) \geq 0, \qquad f(\boldsymbol{x}, \boldsymbol{p}) = f(\boldsymbol{x}, -\boldsymbol{p}), \qquad \int_{\mathcal{S}^2} f(\boldsymbol{x}, \boldsymbol{p}) \mathrm{d}S = 1. \tag{6.9}$$

The surface of the unit sphere is denoted by $\mathcal{S}^2$ with the surface element dS.

In a simplified form, the value of ODF $f_s(\boldsymbol{x}, \boldsymbol{p}_s)$ represents the orientation fraction of strand s in position $\boldsymbol{x}$ with orientation $\boldsymbol{p}_s$. In the context of MEX, the orientation $\boldsymbol{p}$, the position $\boldsymbol{x}$, and the extrusion rate are given by the G-Code. The function $f_s(\boldsymbol{x}, \boldsymbol{p}_s)$ can therefore be defined as the volume fraction of strand s with orientation $\boldsymbol{p}_s$ within a volume (e.g. finite element) at postion $\boldsymbol{x}$. For a total of N extruded strands contributing to the volume, this is expressed as:

$$f_s(\boldsymbol{x}, \boldsymbol{p}_s) = \frac{V_s(\boldsymbol{x}, \boldsymbol{p}_s)}{\sum_{i=1}^{N} V_i(\boldsymbol{x}, \boldsymbol{p}_i)} \tag{6.10}$$

where V_s is the volume of strand s within the considered volume, and the denominator represents the total volume of all strands intersecting that volume.

Owing to the characteristics of the standard MEX process, the extruded strands are confined to the x-y plane, with no out-of-plane (z-direction) orientation (see

A.4 for a discussion on 3D deposition paths). For this planar orientation, each state of orientation is described by the angle ξ, as illustrated in Figure 6.15.

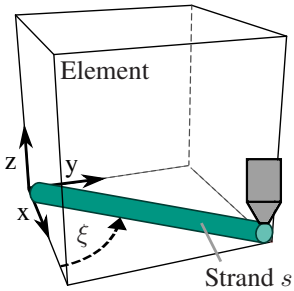

Figure 6.15: Illustration of a deposited strand s with orientation angle ξ within a finite element, considered as the control volume for homogenization. (Reproduced from [2])

Therefore, the orientation vector $\boldsymbol{p}_s$ of each strand s can be described as

$$\boldsymbol{p}_s = \begin{bmatrix} p_\mathrm{x} \\ p_\mathrm{y} \\ p_\mathrm{z} \end{bmatrix}_s = \begin{bmatrix} \cos(\xi) \\ \sin(\xi) \\ 0 \end{bmatrix}_s . \tag{6.11}$$

The orientation space is therefore not a sphere, as in the case of arbitrary spatial orientations, but rather a circle due to the restriction to the 1–2 plane.

An averaged description of the state of orientation can be obtained using orientation tensors (OT), Where the second-order tensor $\boldsymbol{A}$ and the fourth-order tensor $\mathbb{A}$ are used in practice [153]:

$$\begin{aligned} \boldsymbol{A} &= \textstyle\int_{\mathcal{S}^2} f(\boldsymbol{x},\boldsymbol{p})\boldsymbol{p}\otimes\boldsymbol{p}\,\mathrm{d}S, \\ \mathbb{A} &= \textstyle\int_{\mathcal{S}^2} f(\boldsymbol{x},\boldsymbol{p})\boldsymbol{p}\otimes\boldsymbol{p}\otimes\boldsymbol{p}\otimes\boldsymbol{p}\,\mathrm{d}S. \end{aligned} \tag{6.12}$$

The tensors must fulfill the following requirements:

$$\boldsymbol{A} = \boldsymbol{A}^\top, \qquad \mathrm{tr}\boldsymbol{A} = 1, \qquad \mathbb{A}[\boldsymbol{I}] = \boldsymbol{A} \tag{6.13}$$

Using Equation 6.10, the orientation tensors $\boldsymbol{A}$ and $\mathbb{A}$ can be approximated by the following normalized expression for a mesostructure with N strands:

$$\boldsymbol{A} = \sum_{s=1}^{N} \left(\frac{V_s}{\sum_{i=1}^{N} V_i} \right) (\boldsymbol{p} \otimes \boldsymbol{p})_s \tag{6.14}$$

$$\mathbb{A} = \sum_{s=1}^{N} \left(\frac{V_s}{\sum_{i=1}^{N} V_i} \right) (\boldsymbol{p} \otimes \boldsymbol{p} \otimes \boldsymbol{p} \otimes \boldsymbol{p})_s \tag{6.15}$$

Unlike the standard procedures used in most other process simulations (such as injection molding), this procedure allows for the explicit calculation of the 4th-order OT, rather than approximating it using a closure. This has the advantage that uncertainties associated with the closure are not transferred to the effective mechanical properties [235, 236]. As the mesostructure within a given element evolves during the printing process, the orientation tensors $\boldsymbol{A}$ (second-order) and $\mathbb{A}$ (fourth-order) become time-dependent. They are therefore computed at each time increment t_i, based on the updated strand orientation at the end of the increment.

To determine a valid macroscopic effective stiffness $\bar{\mathbb{C}}$ of the additively manufactured component, orientation averaging is performed over all strand directions in the mesostructure. This approach is based on the orientation averaging framework introduced by Advani and Tucker [153], which was originally developed for discontinuous fiber-reinforced composites. In the context of MEX printing, the framework is adapted to account for the layer by layer nature of the MEX mesostructure. A key characteristic of the MEX process is that the third orthotropic material axis, $\boldsymbol{e}_3$, is always aligned with the global build direction ($[0, 0, 1]^\top$). As a result, the orientation averaging emphasizes the in-plane variation of strand orientations, represented by the second- and fourth-order orientation tensors $\boldsymbol{A}$ and $\mathbb{A}$. The following derivation presents the orientation averaging procedure specifically tailored to this MEX-specific case.

The effective stiffness tensor $\bar{\mathbb{C}}$ is defined as a Voigt-like average:

$$\bar{\mathbb{C}} := \langle \mathbb{C} \rangle_{\mathcal{S}} = \int_{\mathcal{S}^2} \mathbb{C}(\boldsymbol{p}) f(\boldsymbol{x}, \boldsymbol{p}) \mathrm{d}S, \tag{6.16}$$

where $\mathbb{C}(\boldsymbol{p})$ is already an effective (homogenized) stiffness tensor associated with strands oriented in direction $\boldsymbol{p}$, and $f(\boldsymbol{x}, \boldsymbol{p})$ is the orientation distribution function. The goal is to express $\bar{\mathbb{C}}$ in terms of the orientation tensors and material parameters:

$$\bar{\mathbb{C}} = f\left(\mathbb{A}, \boldsymbol{A}, \boldsymbol{p}\right). \tag{6.17}$$

The derivation begins with hyperelasticity theory, where stresses $\boldsymbol{\sigma}$ are obtained as the derivative of a strain energy density function $w(\boldsymbol{\varepsilon})$. For a linear stress-strain relationship, the strain energy function $w(\boldsymbol{\varepsilon})$ must be quadratic in $\boldsymbol{\varepsilon}$:

$$\begin{aligned} w(\boldsymbol{\varepsilon}) = & \frac{a}{2}\varepsilon_{11}^2 + \frac{b}{2}\varepsilon_{22}^2 + \frac{c}{2}\varepsilon_{33}^2 + d\varepsilon_{11}\varepsilon_{22} + e\varepsilon_{11}\varepsilon_{33} \\ & + f\varepsilon_{22}\varepsilon_{33} + 2g\varepsilon_{23}^2 + 2h\varepsilon_{13}^2 + 2p\varepsilon_{12}^2 \end{aligned} \tag{6.18}$$

with nine independent material coefficients a to p.

The symmetric dyadic product is used for the strain basis tensors:

$$\boldsymbol{K}_{ij} = \frac{1}{2}\left(\boldsymbol{e}_i \otimes \boldsymbol{e}_j + \boldsymbol{e}_j \otimes \boldsymbol{e}_i\right), \tag{6.19}$$

which satisfies:

$$\boldsymbol{K}_{ij} : \boldsymbol{\varepsilon} = \varepsilon_{ij}, \quad \text{so that} \quad \boldsymbol{K}_{ij} = \frac{\partial \varepsilon_{ij}}{\partial \boldsymbol{\varepsilon}}. \tag{6.20}$$

From this, the stiffness tensor is:

$$\begin{aligned}\mathbb{C} := \frac{\partial^2 w(\boldsymbol{\varepsilon})}{\partial \boldsymbol{\varepsilon}^2} = \frac{\partial \boldsymbol{\sigma}}{\partial \boldsymbol{\varepsilon}} = a\boldsymbol{K}_{11} \otimes \boldsymbol{K}_{11} + b\boldsymbol{K}_{22} \otimes \boldsymbol{K}_{22} + c\boldsymbol{K}_{33} \otimes \boldsymbol{K}_{33} \\ + d(\boldsymbol{K}_{11} \otimes \boldsymbol{K}_{22} + \boldsymbol{K}_{22} \otimes \boldsymbol{K}_{11}) \\ + e(\boldsymbol{K}_{11} \otimes \boldsymbol{K}_{33} + \boldsymbol{K}_{33} \otimes \boldsymbol{K}_{11}) \\ + f(\boldsymbol{K}_{22} \otimes \boldsymbol{K}_{33} + \boldsymbol{K}_{33} \otimes \boldsymbol{K}_{22}) \\ + 4g\boldsymbol{K}_{23} \otimes \boldsymbol{K}_{23} + 4h\boldsymbol{K}_{13} \otimes \boldsymbol{K}_{13} \\ + 4p\boldsymbol{K}_{12} \otimes \boldsymbol{K}_{12}. \end{aligned} \tag{6.21}$$

The orthotropic basis vectors in the context of MEX, as shown in Figure 6.15, can be defined:

$$\boldsymbol{e}_1 = \begin{bmatrix} \cos(\xi) \\ \sin(\xi) \\ 0 \end{bmatrix} = \boldsymbol{p} \qquad \boldsymbol{e}_2 = \begin{bmatrix} -\sin(\xi) \\ \cos(\xi) \\ 0 \end{bmatrix} = \boldsymbol{p}_\perp \qquad \boldsymbol{e}_3 = \begin{bmatrix} 0 \\ 0 \\ 1 \end{bmatrix}. \tag{6.22}$$

With Equation 6.19, this gives

$$\boldsymbol{K}_{ij} = \operatorname{sym}\left(\begin{bmatrix} \boldsymbol{p} \otimes \boldsymbol{p} & \boldsymbol{p} \otimes \boldsymbol{p}_\perp & \boldsymbol{p} \otimes \boldsymbol{e}_3 \\ \boldsymbol{p}_\perp \otimes \boldsymbol{p} & \boldsymbol{p}_\perp \otimes \boldsymbol{p}_\perp & \boldsymbol{p}_\perp \otimes \boldsymbol{e}_3 \\ \boldsymbol{p} \otimes \boldsymbol{p} & \boldsymbol{p} \otimes \boldsymbol{p}_\perp & \boldsymbol{e}_3 \otimes \boldsymbol{e}_3 \end{bmatrix} \right). \tag{6.23}$$

From these, the $\boldsymbol{K}_{ij}$ tensors are constructed and averaged over the orientation space. The results can be expressed in terms of the orientation tensors $\boldsymbol{A}$ and $\mathbb{A}$, along with the planar identity tensor $\boldsymbol{I}^{\mathrm{pl}} = \boldsymbol{e}_1^2 + \boldsymbol{e}_2^2$, and the dyadic products involving $\boldsymbol{e}_3$. This leads to analytical expressions for the orientation-averaged components $\langle \boldsymbol{K}_{ij} \otimes \boldsymbol{K}_{kl} \rangle_{\mathcal{S}}$, as follows:

$$\langle \boldsymbol{K}_{11} \otimes \boldsymbol{K}_{11} \rangle_{\mathcal{S}} = \langle \boldsymbol{p}^{4\otimes} \rangle_{\mathcal{S}} = \mathbb{A} \tag{6.24a}$$

$$\begin{aligned}\langle \boldsymbol{K}_{22} \otimes \boldsymbol{K}_{22} \rangle_{\mathcal{S}} = &\boldsymbol{I}^{\mathrm{pl}} \otimes \boldsymbol{I}^{\mathrm{pl}} - \boldsymbol{I}^{\mathrm{pl}} \otimes \boldsymbol{A} \\ &- \boldsymbol{A} \otimes \boldsymbol{I}^{\mathrm{pl}} + \mathbb{A}\end{aligned} \tag{6.24b}$$

$$\langle \boldsymbol{K}_{33} \otimes \boldsymbol{K}_{33} \rangle_{\mathcal{S}} = \langle \boldsymbol{e}_3^{4\otimes} \rangle_{\mathcal{S}} = \boldsymbol{e}_3^{4\otimes} \tag{6.24c}$$

$$\langle \boldsymbol{K}_{11} \otimes \boldsymbol{K}_{22} + \boldsymbol{K}_{22} \otimes \boldsymbol{K}_{11} \rangle_{\mathcal{S}} = \boldsymbol{I}^{\mathrm{pl}} \otimes \boldsymbol{A} + \boldsymbol{A} \otimes \boldsymbol{I}^{\mathrm{pl}} - 2\mathbb{A} \tag{6.24d}$$

$$\langle \boldsymbol{K}_{11} \otimes \boldsymbol{K}_{33} + \boldsymbol{K}_{33} \otimes \boldsymbol{K}_{11} \rangle_{\mathcal{S}} = \boldsymbol{A} \otimes \boldsymbol{e}_3^{2\otimes} + \boldsymbol{e}_3^{2\otimes} \otimes \boldsymbol{A} \tag{6.24e}$$

$$\begin{aligned} \langle \boldsymbol{K}_{22} \otimes \boldsymbol{K}_{33} + \boldsymbol{K}_{33} \otimes \boldsymbol{K}_{22} \rangle_{\mathcal{S}} = {} & \boldsymbol{I}^{\mathrm{pl}} \otimes \boldsymbol{e}_3^{2\otimes} + \boldsymbol{e}_3^{2\otimes} \otimes \boldsymbol{I}^{\mathrm{pl}} - \\ & \boldsymbol{A} \otimes \boldsymbol{e}_3^{2\otimes} - \boldsymbol{e}_3^{2\otimes} \otimes \boldsymbol{A} \end{aligned} \tag{6.24f}$$

$$\begin{aligned} \langle \boldsymbol{K}_{13} \otimes \boldsymbol{K}_{13} \rangle_{\mathcal{S}} = {} & \frac{1}{4}\Big(\boldsymbol{A} \square \boldsymbol{e}_3^{2\otimes} + \big(\boldsymbol{A} \square \boldsymbol{e}_3^{2\otimes} \big)^{\top_R} \\ & + \boldsymbol{e}_3^{2\otimes} \square \boldsymbol{A} + \big(\boldsymbol{e}_3^{2\otimes} \square \boldsymbol{A} \big)^{\top_R} \Big) \end{aligned} \tag{6.24g}$$

$$\begin{aligned} \langle \boldsymbol{K}_{12} \otimes \boldsymbol{K}_{12} \rangle_{\mathcal{S}} = {} & \frac{1}{4}\Big(\boldsymbol{A} \square \boldsymbol{I}^{\mathrm{pl}} + \big(\boldsymbol{A} \square \boldsymbol{I}^{\mathrm{pl}} \big)^{\top_R} \\ & + \boldsymbol{I}^{\mathrm{pl}} \square \boldsymbol{A} + \big(\boldsymbol{I}^{\mathrm{pl}} \square \boldsymbol{A} \big)^{\top_R} \Big) - \mathbb{A} \end{aligned} \tag{6.24h}$$

$$\begin{aligned} \langle \boldsymbol{K}_{23} \otimes \boldsymbol{K}_{23} \rangle_{\mathcal{S}} = {} & \frac{1}{4}\Big(\boldsymbol{I}^{\mathrm{pl}} \square \boldsymbol{e}_3^{2\otimes} + \big(\boldsymbol{I}^{\mathrm{pl}} \square \boldsymbol{e}_3^{2\otimes} \big)^{\top_R} \\ & - \boldsymbol{A} \square \boldsymbol{e}_3^{2\otimes} - \big(\boldsymbol{A} \square \boldsymbol{e}_3^{2\otimes} \big)^{\top_R} \\ & + \boldsymbol{e}_3^{2\otimes} \square \boldsymbol{I}^{\mathrm{pl}} + \big(\boldsymbol{e}_3^{2\otimes} \square \boldsymbol{I}^{\mathrm{pl}} \big)^{\top_R} \\ & - \boldsymbol{e}_3^{2\otimes} \square \boldsymbol{A} - \big(\boldsymbol{e}_3^{2\otimes} \square \boldsymbol{A} \big)^{\top_R} \Big). \end{aligned} \tag{6.24j}$$

With Equation 6.14, Equation 6.15, Equation 6.21, and Equation 6.24, the effective stiffness tensor $\bar{\mathbb{C}}$ of the MEX-printed mesostructure can be expressed as a function of the second- and fourth-order orientation tensors $\boldsymbol{A}$ and $\mathbb{A}$. The material-specific coefficients a to p in Equation 6.21 are obtained directly from experimental characterization of the unidirectionally printed orthotropic material, represented by the stiffness tensor $\mathbb{C}_{\mathrm{ortho}}$.

6.5.2.2 Implementation[2]

The implementation utilizes custom-written *Python* scripts in combination with *Abaqus* user subroutines to compute the evolving effective stiffness tensor $\bar{\mathbb{C}}$ within each finite element throughout the simulated process. This calculation is informed by the local deposition of strands and their orientation vector $\boldsymbol{p}$, which changes as material is added layer by layer. The underlying input is standard G-Code, as produced by conventional slicing software for material extrusion processes. To extract the relevant sequence of deposition events, the G-Code is parsed using the methodology introduced in Chapter 4, implemented in the open-source software package *pyGCD* [213] (cf. Chapter 4).

An overview of the implemented workflow is given in Figure 6.16. Initial efforts to reconstruct and map strand orientations within individual elements, which form an essential prerequisite for calculating direction-dependent material behavior, were developed as part of a Master's thesis [237] guided in the context of this dissertation [238].

[2] Adapted and partially verbatim reproduced from [2], cf. footnote p. 127 for details.

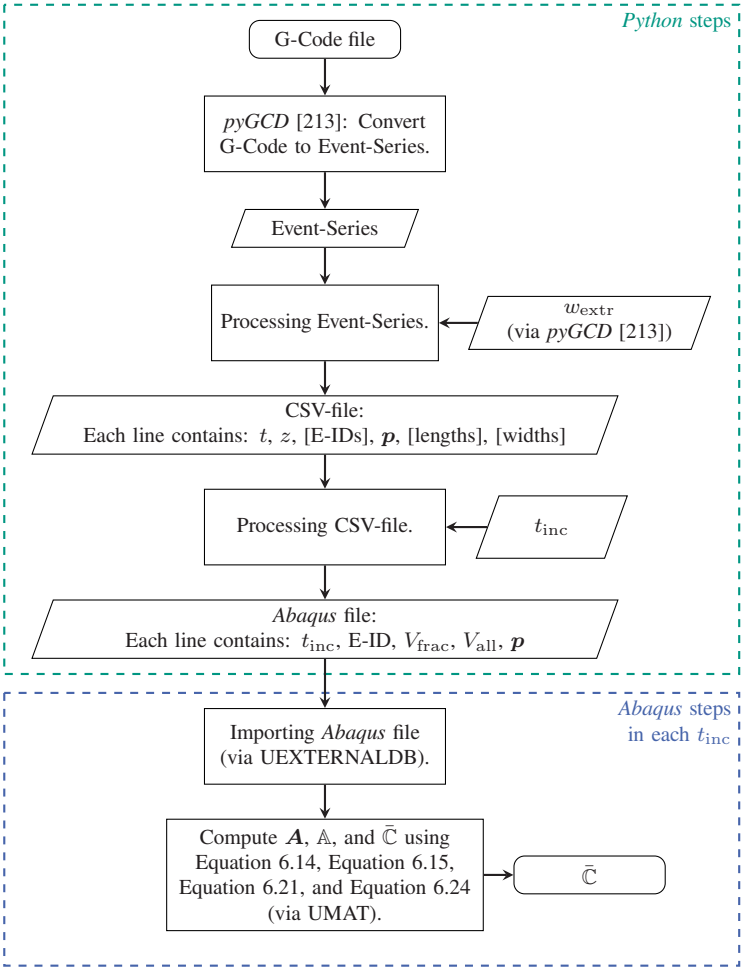

Figure 6.16: Flowchart of the implemented workflow for the computation of orientation tensors $\boldsymbol{A}$ and $\mathbb{A}$ and the corresponding effective stiffness $\bar{\mathbb{C}}$ in each element at every time increment. (Reproduced from [2])

Processing Event-Series[2] In the next step of the algorithm, the generated event series is processed line by line. For each event, it is determined which finite elements are intersected by the corresponding nozzle motion. Only movements associated with material extrusion are taken into account. To minimize computational effort, the centroids of all elements are organized in a kd-tree structure, enabling an efficient search within the current nozzle height level. This allows restricting the search to the eight elements surrounding the element currently occupied by the nozzle, thereby significantly reducing the number of intersection checks. The underlying search uses a k-nearest neighbor (kNN) approach as a practical tool to achieve this efficiency. As a result, the algorithm remains computationally efficient even for components with a large number of elements. When analyzing nozzle motion within an element, several relevant scenarios must be considered to accurately map the extrusion process onto the mesh. The scenarios are listed below and illustrated in Fig. 6.17:

a) Both the start point (1) and the end point (2) of the nozzle motion lie outside the element.

b) The start point (1) lies inside the element, while the end point (2) lies outside.

c) The start point (1) lies outside the element, while the end point (2) lies inside.

d) Both the start point (1) and the end point (2) lie inside the element.

e) The extruded strand spans across two adjacent elements.

For each element in which a strand is deposited, the respective length of the nozzle motion, the width of the deposited strand, and the orientation vector $\boldsymbol{p}$ according to Equation 6.11 are also determined. For the width of the deposited strand, *pyGCD* is used to calculate the average extrusion width from the G-Code during the analyzed nozzle motion. The orientation is defined with regard

[2] Verbatim reproduced section from [2], cf. footnote p. 127 for details.

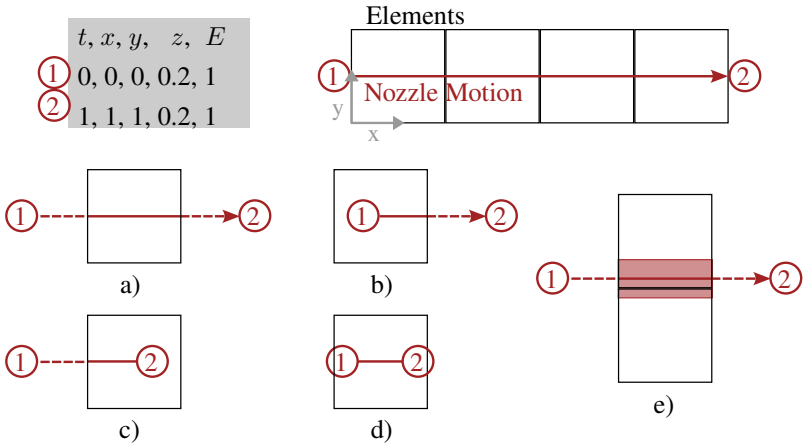

Figure 6.17: Representation of a nozzle motion ($1 \rightarrow 2$) as it passes through elements. As well as the considered scenarios for such a nozzle motion (a-e). (Reproduced from [2])

to the x-axis (1-direction). The information with the according Element-IDs (E-IDs) are stored in a CSV-file for each motion. The structure is shown in Figure 6.17. This information can then be used to calculate and interpret the resulting orientation tensors at specific times during the process.

Processing CSV-file[2] The information in the CSV-file is further interpreted for use in *Abaqus*. For a given time increment t_{inc} from the subsequent process simulation, the algorithm evaluates how many strands with a certain orientation $\boldsymbol{p}$ are deposited in which E-ID. For each time increment and each element, the strands with the same orientation are grouped. In addition, their volume fraction V_{frac} in the element and the total volume V_{all} deposited in the element up to this time increment are stored in a file.

[2] Verbatim reproduced section from [2], cf. footnote p. 127 for details.

Importing *Abaqus* file[2] At the start of the process simulation, a user subroutine UEXTERNALDB reads the file and stores the information in global arrays. In this way, the file only needs to be read once per simulation.

Compute $\boldsymbol{A}$, $\mathbb{A}$, and $\bar{\mathbb{C}}$[2] The material model used in the simulation (cf. Section 6.3) is implemented as a user subroutine UMAT. Within this UMAT, which is called for each integration point in each time increment, the information in the global arrays is accessed. For each element, the orientation tensors $\boldsymbol{A}$ and $\mathbb{A}$ are calculated here in each time increment using Equation 6.14 and Equation 6.15. Equation 6.21 and Equation 6.24 then provide $\bar{\mathbb{C}}$. If no strand is added to the element in the current time increment, $\boldsymbol{A}$, $\mathbb{A}$, and $\bar{\mathbb{C}}$ are not recalculated. $\bar{\mathbb{C}}$ is then the starting point for the further material model, which is described in Section 6.3.

6.5.2.3 Verification[2]

To verify the implemented workflow, a plate with dimensions of $27\,\mathrm{mm} \times 27\,\mathrm{mm} \times 1\,\mathrm{mm}$ and elements with dimensions of $9\,\mathrm{mm} \times 9\,\mathrm{mm} \times 1\,\mathrm{mm}$ is analyzed. Based on the G-Code generated for each case, the *Abaqus* file was created according to the procedure described in Section 6.5.2.2. The implemented *Abaqus* subroutines were then used to calculate the orientation tensors and volume fraction for the example geometry. An extrusion width of $3\,\mathrm{mm}$ and different trajectories were considered to cover different cases, as illustrated in Figure 6.18. The dimensions of the component and its discretization allow an easy comparison of the volume fractions and a direct evaluation of the results of the implemented subroutines.

[2] Verbatim reproduced section from [2], cf. footnote p. 127 for details.

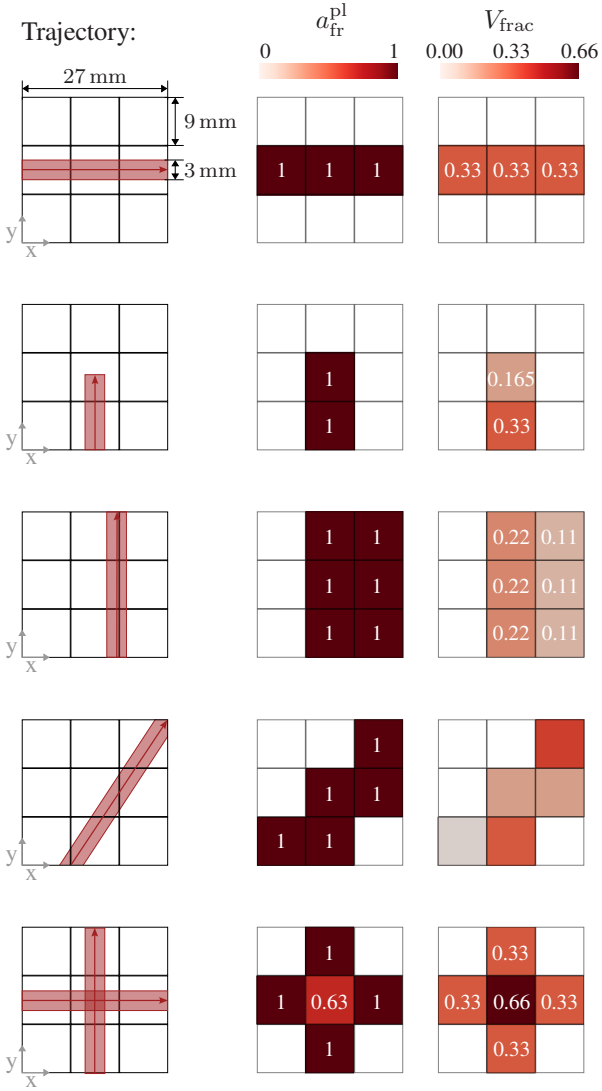

Figure 6.18: Analyzed trajectories and the corresponding planar fractional anisotropy $a_{\mathrm{fr}}^{\mathrm{pl}}$ and volume fractions V_{frac} in the nine elements of the component used to verify the implemented workflow from Figure 6.16 within *Abaqus*. (Reproduced from [2])

To verify the calculated orientation of each element, the planar fractional anisotropy given by

$$a_{\mathrm{fr}}^{\mathrm{pl}} = \sqrt{\frac{8}{5}} \frac{\|\mathbb{A}_{\mathrm{pl}} - \mathbb{A}_{\mathrm{pl}}^{\mathrm{iso}}\|}{\|\mathbb{A}_{\mathrm{pl}}\|} \tag{6.25}$$

is used. Here $\mathbb{A}_{\mathrm{pl}}$ is the planar fourth-order orientation tensor and $\mathbb{A}_{\mathrm{pl}}^{\mathrm{iso}}$ is its isotropic fraction. This provides a scalar comparison value for the orientation. Here, $a_{\mathrm{fr}}^{\mathrm{pl}} = 0$ stands for planar isotropy in the x-y plane and $a_{\mathrm{fr}}^{\mathrm{pl}} = 1$ for unidirectional orientation. Figure 6.18 shows the corresponding calculated orientations and volume fractions in the nine elements of the component with *Abaqus*. The results show that the resulting orientation and volume fraction are correctly assigned to the individual elements for all cases described in Section 6.5.2.2. The resulting volume fraction is easy to calculate, except for the fourth case, and can therefore be easily checked. Since this is not the case in the fourth case, the information on the volume fraction has been omitted here, but checked by an analytical calculation using *Python*.

6.5.2.4 Numerical studies[2]

To analyze the resulting material orientation in additively manufactured components during and at the time of completion, a plate measuring $48\,\mathrm{mm} \times 48\,\mathrm{mm} \times 2.4\,\mathrm{mm}$ was examined. The component was sliced with three perimeters and alternating $0\,^\circ$ and $90\,^\circ$ infill. The strand width was $0.4\,\mathrm{mm}$ and the height was $0.2\,\mathrm{mm}$. To demonstrate the influence of the element size, hexahedral elements with edge lengths of $0.6\,\mathrm{mm}$, $0.8\,\mathrm{mm}$, $1.2\,\mathrm{mm}$ and $2.4\,\mathrm{mm}$ in all three spatial directions were examined. The following figures in this section show the details of the plate with the respective discretization and the planar fractional anisotropy $a_{\mathrm{fr}}^{\mathrm{pl}}$ according to Equation 6.25.

Figure 6.19 shows the resulting orientation states at the end of the component production. A visualization plot of the planar fourth-order orientation tensor $\mathbb{A}_{\mathrm{pl}}$

[2] Verbatim reproduced section from [2], cf. footnote p. 127 for details.

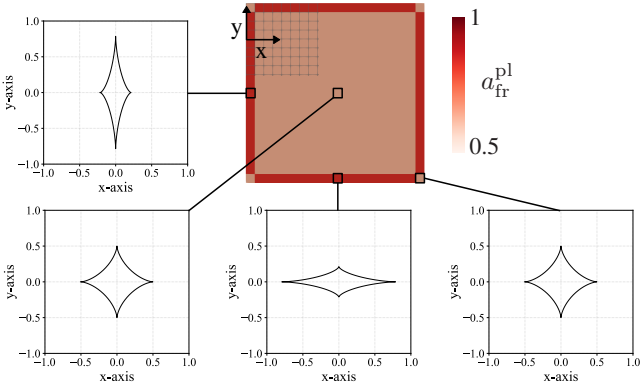

Figure 6.19: Visualization of the planar fourth-order orientation tensor $\mathbb{A}_{\mathrm{pl}}$ at different locations within the component. The component is discretized using elements with edge lengths of $2.4\,\mathrm{mm}$ in all three spatial directions. The plot illustrates the in-plane orientation of the material in the x-y plane, showing a uniform mesostructure in the center and a pronounced alignment in the outer regions due to perimeters and turning points of the extrusion. (Reproduced from [2])

using so-called HOME-glyphs [239] is shown for different locations within the component. It represents the in-plane orientation of the material in the x-y plane. The $a_{\mathrm{fr}}^{\mathrm{pl}}$ of each element shows the uniformly distributed infill mesostructure in the center of the component. Due to the element size, the "Perimeter" and "Perimeter + Infill + Turning points" mesostructures are combined. The visualization plots reveal a pronounced alignment of the material in the outer areas of the component. This is due to the perimeters and turning points. Such a prediction is plausible given the actual material orientation in the component.

Figure 6.20 shows the evolution of $a_{\mathrm{fr}}^{\mathrm{pl}}$ throughout the process time at different points in the component. The progression of the orientation after printing the first strand in the respective element is shown. It can be seen that although the same material orientation is partially reached at the end, the orientation evolves differently during the printing process. The time dependence of the material orientation is due to the alternating infill. As a result, alternating orientations

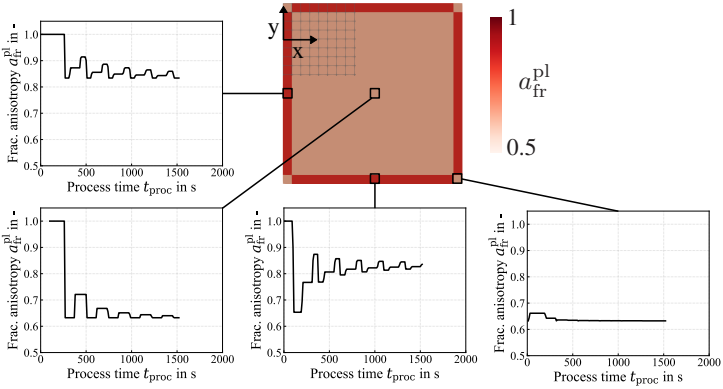

Figure 6.20: Evolution of $a_{\mathrm{fr}}^{\mathrm{pl}}$ over the process time at different points in the component. The component is discretized using elements with edge lengths of $2.4\,\mathrm{mm}$ in all three spatial directions. The plots illustrate the evolution of the material orientation, showing time-dependent variations due to alternating infill. The printing time for one layer is approximately $200\,\mathrm{s}$. (Reproduced from [2])

of the extruded material are added during the process until the element is completely filled with strands. These results show that the component has locally different stiffness during the printing process, which affects the PiD. This study demonstrates that the presented approach can capture the evolving material orientation within an individual element, thereby representing a significant advancement beyond the fixed-orientation approach currently available in *Abaqus*. To achieve an identical stiffness evolution (apart from the influence of perimeters and turning points) using the built-in method in *Abaqus*, the element height would have to correspond to the layer height, which would drastically increase the number of elements and computation time. The presented method therefore offers a practical advantage by accurately representing evolving anisotropy even with coarser meshes and, more generally, represents an advancement beyond the state of the art in computational modeling of material orientation in MEX.

Figure 6.21 shows the influence of the element size on the change in material orientation over time for the infill mesostructure. The element size affects the local stiffness evolution during the process, as it determines how many layers are

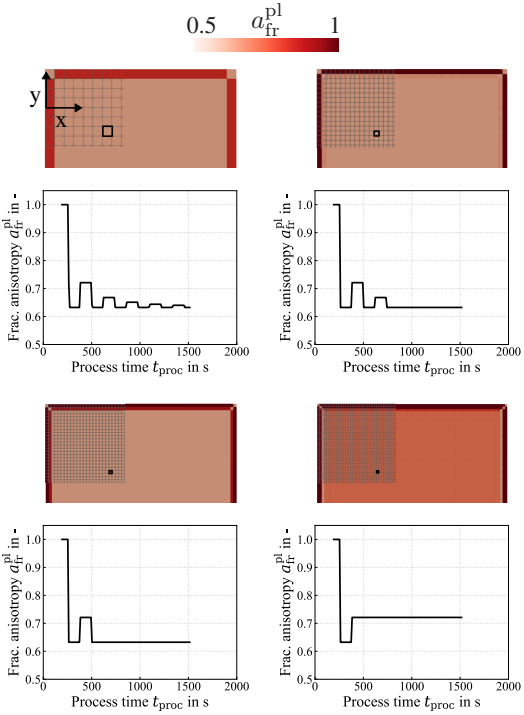

Figure 6.21: Influence of element size on the evolution of material orientation over time for the infill mesostructure. Element sizes $2.4\,\mathrm{mm}$, $1.2\,\mathrm{mm}$, $0.8\,\mathrm{mm}$ and $0.6\,\mathrm{mm}$ are shown in this order from top left to bottom right. The strand width was $0.4\,\mathrm{mm}$ and the height was $0.2\,\mathrm{mm}$. The ratio of strand height to element height is what causes $a_{\mathrm{fr}}^{\mathrm{pl}}$ to converge to a different value when the element edge length is $0.6\,\mathrm{mm}$. (Reproduced from [2])

combined within a single element. The study further reveals that the number of layers per element, specifically whether it is even or odd, has a significant impact on the resulting orientation distribution. When the element height is an even multiple of the layer height and alternating infill patterns are used, each element in the infill region tends to receive the same orientation. In contrast, for odd multiples, alternating orientations are retained within the element layers. This leads to a stepwise variation in stiffness between adjacent elements, which can

in turn cause convergence issues in the simulation. Additionally, the variation in resulting orientation decreases with increasing element size. When the infill pattern remains constant across all layers, the resulting orientation per element is unaffected by the element height.

The investigations in this section show that the presented methodology can generally be used to represent local changes in the mesostructure, such as the mesostructure categories introduced in Section 6.4. A smaller element size allows a finer resolution of the different structures, however, an even number of layers per element is recommended to avoid stiffness jumps. This is illustrated again in Figure 6.22 for the element edge length of $0.6\,\mathrm{mm}$. It can be seen that the element size and the associated uneven number of layers in the element result in different orientation states in the "Perimeter + Infill + Turning points" region.

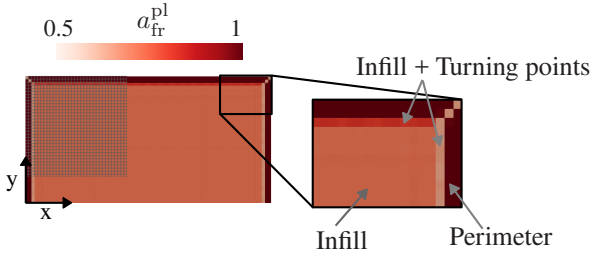

Figure 6.22: Illustration of local mesostructure changes for an element edge length of $0.6\,\mathrm{mm}$. (Reproduced from [2])

6.6 Experimental validation

6.6.1 Component design[2]

For the validation, a component geometry was chosen that leads to an expected PiD and allows for a simple evaluation. The geometry is shown in Figure 6.23. The trapezoidal cross-section, leads to residual stresses that cause the component to bend around the y-axis when removed from the build plate. This bending is the direct measure of the PiD.

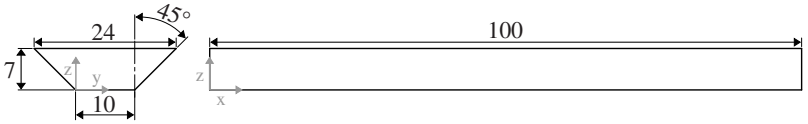

Figure 6.23: Geometry and dimensions of the validation component in mm. (Reproduced from [2])

6.6.2 Experimental tests

6.6.2.1 MEX process design[2]

The *Ultimaker 2+* from *Ultimaker* was used to produce the components in this work. The *Ultimaker* has a heated printing bed. The standard glass printing bed has been replaced with an unused FilaPrint permanent printing bed to ensure the most reproducible adhesion possible. The nozzle has a diameter of $0.4\,\mathrm{mm}$ and a print resolution of $200\,\mu\mathrm{m}$. The print bed was leveled with three adjustment screws. The slicer and printer settings listed in Tab. 6.4 were selected based on printing studies to achieve a consistent and reproducible mesostructure. To investigate the influence of the trajectory on the PiD, an infill with orientation

[2] Verbatim reproduced section from [2], cf. footnote p. 127 for details.

of $0\,^\circ$ or $90\,^\circ$ to the x-axis was selected. The components with the selected fill orientation are shown in Fig. 6.24. For each configuration, three components were printed and measured.

Table 6.4: Slicer and process parameters selected. [2]

Process parameter	Value	Unit
Nozzle temperature T_N	220	°C
Bed temperature T_bed	40	°C
Layer height l_height	0.2	mm
Extrusion width e_width	0.4	mm
Infill Density	100	%
Print speed v_print	50	mm/s

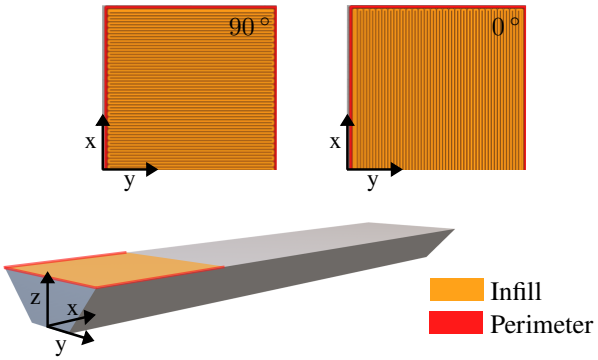

Figure 6.24: Cross section of the trajectory of the validation components with an infill density of 100 % with $0\,^\circ$ and $90\,^\circ$ orientations to the x-axis in orange and one perimeter in red. (Reproduced from [2])

6.6.2.2 X-Ray computed tomography (µCT)[2]

The validation components were scanned using a YXLON CT precision µCT system from Yxlon International CT GmbH in Hattingen, Germany. This system features a µm-focused X-ray reflection tube with a tungsten target and a high-resolution PerkinElmer Y.XRD1620 flat image detector with 2048 pixels × 2048 pixels. The scan parameters are listed in Table 6.5. The contour of

Table 6.5: Scan parameters for µCT scans of the validation components. [2]

Scan parameter	Value	Unit
Voltage	140	kV
Current	0.25	mA
Voxel size	65.84	µm
Line binning parameter	2	-
Number of projections	3000	ms
Exposure/Integration time	1000	ms

each specimen was determined from the corresponding scans and exported as an STL file.

6.6.2.3 Experimental results[2]

The measured curvature on the underside of the component was evaluated using a specially developed *Python* tool. Within this tool, the scanned 3D surface model in STL format is first loaded to analyze the deformation along a defined path on the component (red path in Figure 6.25a). An equidistant point path is generated between a start and end point in space, and the points are then projected onto the nearest points on the component surface using a k-d tree for nearest neighbor search (*cKDTree*). The projected path points obtained in

[2] Verbatim reproduced section from [2], cf. footnote p. 127 for details.

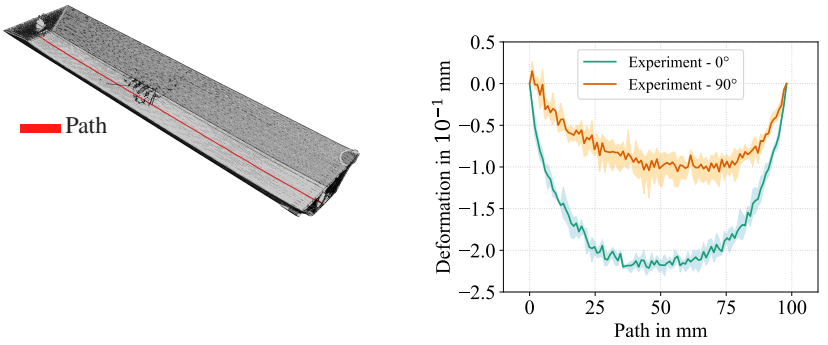

(a) (b)

Figure 6.25: (a) Validation component measured using µCT, with the evaluation path highlighted in red. (b) Mean curvature and minimum and maximum values of the underside of the component for specimens printed with 0 ° (green) and 90 ° (orange) infill angle. (Reproduced from [2])

this way form the basis for the quantitative evaluation of the local deformations along the path under consideration. The results, shown in Fig. 6.25b, include measurements at both 0 ° and 90 ° infill angles. The mean of the three measurements and their scatter are presented, revealing a reproducible PiD. A significant influence of the selected trajectory, shwon in Fig. 6.24, on the PiD can bee seen: At 90 ° infill angle, a lower PiD occurs compared to the 0 ° infill angle.

6.6.3 Sensitivity analyses for parameter identification

6.6.3.1 Time increment [2]

To evaluate the effect of the time increment t_{inc} on the resulting component deformation, the increment was varied as shown in Figure 6.26. Figure 6.26a

[2] Verbatim reproduced section from [2], cf. footnote p. 127 for details.

shows the temperature curve over the entire process chain. The initial temperature of 220 °C is followed by the period during which the material is heated and cooled during the process. After the printing process (after about 3200 s), the cooling on the printing plate follows. The time increment mainly affects

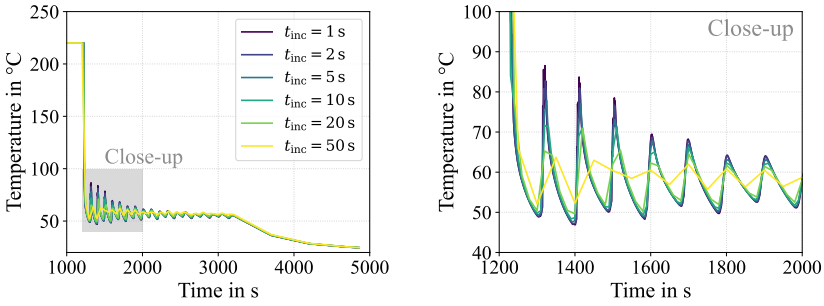

Figure 6.26: Temperature profiles over time in the center of the component for various time increments. (Reproduced from [2])

the temperature curve during printing immediately after the elements are activated. Figure 6.26b illustrates this range. Here it can be seen that the time increment influences the maximum temperature during reheating: the smaller the increment, the higher the temperature reached. As the increment increases, the process-typical temperature curve is no longer accurately represented. From a certain increment (here $t_{\mathrm{inc}} = 100\,\mathrm{s}$) the typical temperature peaks no longer occur.

The thermomechanical simulation based on the corresponding thermal simulation results in the deformations shown in Figure 6.27. The curved progression of the PiD is predicted with all selected t_{inc}, but the predicted PiD is overestimated for larger t_{inc}.

Figure 6.28 provides an overview of the influence of time increment size on the computational effort and on the deformation results to enable an efficient numerical prediction. All simulations were conducted on the same workstation

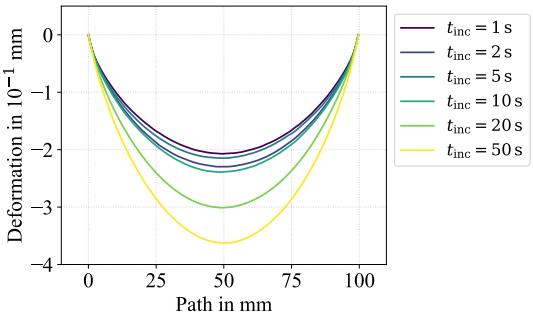

Figure 6.27: Predicted deformation in the z-direction for various time increments. (Reproduced from [2])

equipped with an AMD Ryzen Threadripper PRO 3975WX CPU @ 3.50 GHz and 32 GB of RAM. Each simulation was executed using 4 CPU cores. This setup ensures consistent computational performance across all cases. Figure 6.28a shows the total computation time required for each discretization as a function of the time increment. Figure 6.28b shows the maximum deformation versus the time increment, with the data points color-coded according to the required computation time. The predicted maximum PiD generally decreases with a smaller time increment. This trend continues down to $t_{\mathrm{inc}} = 5\,\mathrm{s}$, below which the results begin to fluctuate. At the same time, the computational cost rises significantly for smaller increments. For example, the simulation with a $t_{\mathrm{inc}} = 1\,\mathrm{s}$ required a total CPU time of 500 hours. To compare with experimentally measured deformations, a simulation with a time increment of $t_{\mathrm{inc}} = 5\,\mathrm{s}$ was selected as a compromise between numerical accuracy and computational efficiency.

6.6.3.2 Vitrification temperature T_{vitr}

As described in Section 6.3.2.2, two approaches were used to define the vitrification temperature T_{vitr}: Approach A identifies T_{vitr} as the turning point in the storage modulus curve, whereas Approach B defines it as the midpoint of the softening range. The following analyses illustrate the influence of these

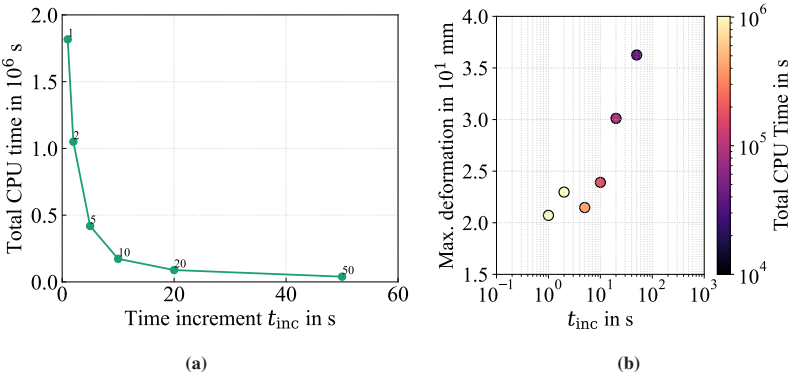

Figure 6.28: Maximum predicted deformation for different time increments. The required computation time is color-coded. a) The inactive elements follow the deformation of the active elements. b) The inactive elements do not follow the deformation of the active elements. (Reproduced from [2])

different definitions on the predicted PiD. Figure 6.29 shows the predicted PiD at an infill angle of $0\,^\circ$ for different T_{vitr} values. A clear influence of T_{vitr} on deformation is evident. A comparison with the measured PiD (shown in gray) reveals that Approach A significantly underestimates the PiD. However, Approach B can quantitatively predict deformation when the lower limit of the softening range is defined as the temperature at which $20\,\%$ of the maximum absolute value of the derivative $\mathrm{d}E'/\mathrm{d}T$ is reached.

The pronounced sensitivity of the material model to temperature can be explained using Figure 6.30. It illustrates the typical temperature curve at the center of the component throughout the process. The temperature fluctuates within the softening range around T_{vitr}. Consequently, the abrupt change in stiffness and sudden stress relaxation assumed in the model have a particularly strong effect. At a low T_{vitr}, as in approach A, the threshold value is exceeded during the final local heating, causing the viscoelastic stresses to relax completely. At higher T_{vitr}, the temperature permanently remains below the threshold value from a certain point in time, so no further stress relaxation occurs. This results in higher residual stresses in the final component and a stronger predicted PiD.

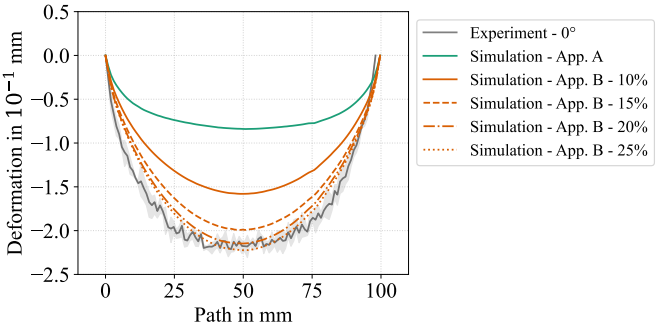

Figure 6.29: Comparison of the predicted PiD with experimental data (gray) at a fill angle of 0 ° using different definitions of the vitrification temperature T_{vitr}. T_{vitr} was determined according to Approach A (green) and Approach B (orange) as defined in Section 6.3.2.2. Approach A identifies T_{vitr} as the turning point in the storage modulus curve, whereas Approach B defines T_{vitr} as the midpoint of the softening range.

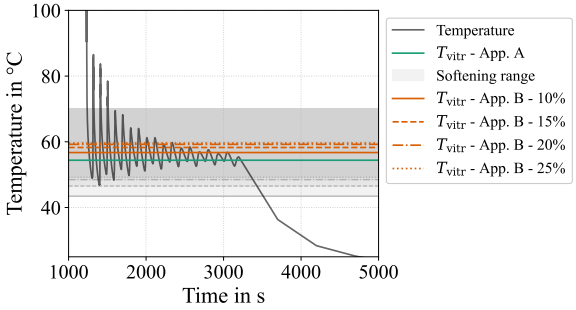

Figure 6.30: Temperature curve in the center of the component with colored softening area and T_{vitr} values plotted according to approaches A and B (cf. Section 6.3.2.2).

The investigations show that the quality of the PiD prediction using the path-dependent material model is significantly affected by the choice of the T_{vitr} parameter. This is particularly evident when the average temperature during the printing process falls within the softening range. In these cases, selecting a specific T_{vitr} value may result in an underestimation of the residual stresses and, consequently, of the PiD. Under different process conditions, such as a higher

building plate temperature, this influence may be less significant. However, a general underestimation of the resulting residual stresses is still possible.

Therefore, it should be noted that the model's assumption of full stress relaxation when T_{vitr} is exceeded is not applicable to MEX process simulations with PLA. Despite the significantly decreased stiffness and short relaxation time above T_{vitr}, numerical investigations show that viscoelastic stresses remain in the material. This could be due to the high cooling rates in the process resulting in a very short time above T_{vitr}. Thus, the stresses do not fully relax despite the short relaxation time. This explains why the simplified, path-dependent material model underestimates the resulting residual stresses in this case.

Since this work focuses on the resulting mesostructure within the process simulation rather than precisely modeling PLA's material behavior, the abovementioned simplification and its limitations are accepted. To validate the developed models, the temperature at which $20\,\%$ of the maximum absolute value of the derivative $\mathrm{d}E'/\mathrm{d}T$ is reached is used as the lower limit of the softening range for the remainder of this work. T_{vitr} is defined as the midpoint of this softening range (Approach B – $20\,\%$).

6.6.4 Validation results[2]

Figure. 6.31 shows the experimentally determined and numerically predicted PiD for infill angles of $0\,^\circ$ and $90\,^\circ$, calculated using both the anisotropic (solid line) and isotropic (dashed line) approaches. For both infill orientations, the qualitative progression of the deformation is captured accurately, with a considerably larger PiD observed for $0\,^\circ$ than for $90\,^\circ$. The anisotropic approach achieves good quantitative agreement, particularly at $0\,^\circ$. For $90\,^\circ$, the PiD is slightly overestimated. The prediction inaccuracy, especially for 90° fillings, is primarily due to the selected material model, which significantly simplifies the

[2] Verbatim reproduced section from [2], cf. footnote p. 127 for details.

relaxation processes. Note that the maximum deformation is also influenced by the selected T_{vitr}.

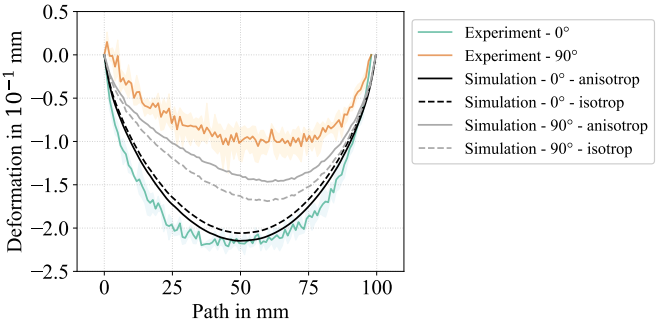

Figure 6.31: Comparison of experimentally determined and numerically predicted deformation in green using the presented anisotropic and isotropic approaches. (Reproduced from [2])

Compared to the anisotropic model, the isotropic approach underpredicts the deformation at $0\,^\circ$ by approximately $4\,\%$ and overpredicts it at $90\,^\circ$ by about $16\,\%$. This highlights the importance of incorporating orientation-dependent mechanical properties into the simulation. The differences between the two approaches can be explained as follows: The deformation observed in the isotropic model arises from variations in the timing and spatial distribution of material deposition. These differences lead to distinct thermal histories and, consequently, to infill-dependent deformation, even when mechanical anisotropy is not considered. The anisotropic model additionally accounts for the orientation-dependent stiffness introduced by the deposition path.

For an infill angle of $0\,^\circ$, the strands are aligned along the x-direction, resulting in increased stiffness in that direction. This increased stiffness is explicitly captured in the anisotropic model, whereas it is averaged out in the isotropic model. As a result, thermal expansion leads to higher residual stresses in the anisotropic model during cooling, which in turn cause larger deformations. In

contrast, for a $90\,^{\circ}$ infill, the isotropic model overestimates the stiffness in the x-direction, leading to an overprediction of deformation.

These findings highlight the importance of incorporating deposition-induced material anisotropy when aiming to reliably predict process-induced deformation, especially in materials with high thermal expansion coefficients or pronounced direction-dependent behavior.

6.7 Summary and conclusion

This chapter presents a comprehensive simulation framework for predicting PiD in MEX manufacturing. The framework focuses on the evolving mesostructure and its influence on local mechanical behavior. The approach integrates a sequentially coupled thermomechanical simulation in *Abaqus*, a path-dependent material model, and a novel orientation-based homogenization method. This method accounts for the resulting anisotropic stiffness from the deposition process.

A central contribution of this work is explicitly considering the local mesostructure and its temporal evolution during the printing process. Unlike previous approaches that often assume homogeneous or isotropic material behavior, this methodology reconstructs the nozzle's actual trajectory from G-Code and maps the orientation of the deposited strands onto the finite elements. This allows for the dynamic computation of orientation and effective stiffness tensors at each time increment, enabling the simulation to reflect the spatially and temporally varying mechanical properties of the printed component.

To identify the mesostructure-dependent mechanisms that significantly influence PiD and must therefore be considered in material modeling, extensive experimental investigations were conducted. Tensile tests, DMA, TMA, and DSC were employed to characterize the thermomechanical and kinetic behavior of MEX-manufactured PLA structures under process-relevant conditions. The results of these experiments revealed the strong temperature dependence

of stiffness near the glass transition, isotropic thermal expansion during manufacturing, anisotropic expansion due to strand orientation during annealing, and limited crystallization during printing. These findings informed the selection and parameterization of the material model, clarifying which effects could be neglected and which must be explicitly modeled.

Experimental validation of the predicted PiD, based on µCT-scanned components, confirmed the simulation framework's predictive capability. The anisotropic modeling approach exhibited significantly greater alignment with measured deformations than the isotropic assumption, especially for directional infill patterns. These results demonstrate that local variations in stiffness caused by the mesostructure have a measurable impact on the resulting PiD and must be considered for an accurate simulation.

Sensitivity analyses revealed that the accuracy of the simulation depends heavily on the time increment chosen and how T_{vitr} is defined. The path-dependent material model assumes full stress relaxation above T_{vitr}, which can result in an underestimation of residual stresses and PiD if T_{vitr} is not chosen carefully. Therefore, while the path-dependent model is practical and computationally efficient, it is not universally applicable. A more advanced viscoelastic material model that better captures time-dependent relaxation behavior would be beneficial for future work.

In conclusion, this work establishes a robust and extensible simulation framework that captures the interplay between process parameters, mesostructure evolution, and mechanical response in MEX. The methodology integrates experimentally informed material behavior and a physically motivated homogenization approach to enable more accurate, structure-aware predictions of residual stresses and deformation. This framework is a valuable foundation for process optimization and component design.

7 A submodeling approach for efficient prediction of local temperature profiles in component-scale additive manufacturing[4]

Outline

Chapter 7 addresses objective O-4 by coupling finely resolved FE-models (mesoscale) with process simulations of entire components (macroscale). The presented methodology is based on the general submodeling methodology. Section 7.1 outlines the necessary modeling steps to apply the methodology to the material extrusion process. In Section 7.1.4 the process parameters and material modeling of the PLA used as an example application are presented. These are required for numerical verification in Section 7.4 and experimental validation in Section 7.5. Section 7.3 presents a sensitivity analysis of the mesh size and time increment for the most accurate prediction of the temperature history.

[4] Extracts from Chapter 7 have been previously published in [4], © CC BY 4.0, i.e. Felix Frölich, Lukas Hof, Clemens Zimmerling, Florian Wittemann, Luise Kärger. A submodeling approach for efficient prediction of local temperature profiles in component-scale additive manufacturing. *The International Journal of Advanced Manufacturing Technology*, 136(3):1561-1576, 2025 - Reproduced sections are marked with [4].

7.1 Submodeling methodology[4]

7.1.1 Submodeling concept[4]

The FE software *Abaqus* and its plug-in for modeling additive manufacturing processes are used for simulation. Element activation according to a given trajectory enables the modeling of material extrusion. A predefined initial temperature of an element represents the extrusion temperature. In addition, the plug-in considers continuously changing surfaces with advancing element activation and the associated convection and radiation.

The high cooling rates described in the literature [37] and the comparatively low thermal conductivity of thermoplastics indicate that cooling effects such as free convection and radiation are mainly responsible for the local temperature profile during MEX. This paper presents a method based on the submodeling approach with time-dependent boundary conditions, which allows modeling only a small volume around an area of interest to predict the local temperature profile. This allows a finer spatial and temporal resolution and thus a more accurate representation of the local temperature profile. The fundamental principle behind submodeling is the Saint-Venant principle [240], according to which local effects diminish with distance. Thus, the prediction uncertainty should be sufficiently small if boundary conditions and the size of the submodel are defined appropriately.

Figure 7.1 schematically shows the submodeling approach: To predict the temperature profile at a given point on the component as accurately as possible, only a section is simulated. This section represents the submodel. While the entire component is discretized in a state-of-the-art process simulation and thus represents the domain to be solved, the submodel approach models only a smaller area around the area to be investigated. There are no elements in the region outside the submodel. The submodeling method follows the

[4] Verbatim reproduced section from [4], © CC BY 4.0, cf. footnote p. 183 for details.

approach that the modeling of the printing process for the small submodel is, in terms of the printing time and trajectory, the same as for the entire component modeled. The elements within the submodel are thus activated at the same time as the elements would be activated at the corresponding location during the simulation of the entire component. The local process conditions at the domain boundaries of the submodel are derived from an upstream simulation of the entire component with a coarser discretization. Suppose the temperature profile is to be predicted at a point near the component's boundary. In that case, these boundary effects, such as heat exchange with the air or the build platform, are also modeled within the submodel.

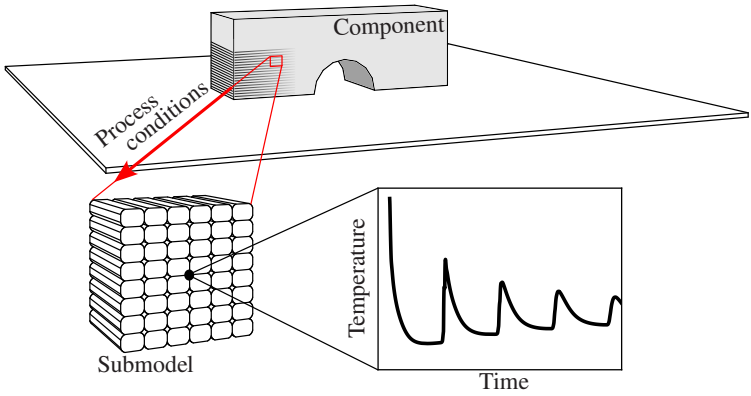

Figure 7.1: Schematic representation of the submodel approach: To predict the temperature profile at a certain point on the component as accurately as possible, only a small section is simulated. This section represents the submodel. The local process conditions are derived from an upstream process simulation of the entire component. (Reproduced from [4])

7.1.2 FE process modeling approach and gouverning equations[4]

The governing equation for thermal modeling is the heat balance equation in combination with the generalized Fourier equation [241]. It can be formulated as the weak form by multiplying a test function δT, integrating over the domain Ω, and applying the chain rule and the divergence theorem,

$$\int_{\Omega} \rho c_{\mathrm{p}} \frac{\partial T}{\partial t} \delta T \, \mathrm{d}V = -\int_{\Omega} (\boldsymbol{\kappa} \nabla T) \cdot (\nabla \delta T) \mathrm{d}V - \int_{\Gamma_O} s \delta T \, \mathrm{d}A, \tag{7.1}$$

where T is the temperature, t is the time, ρ is the material density, c_{p} is the heat capacity, $\boldsymbol{\kappa}$ is the thermal conductivity tensor, and s is a surface flux at the boundary Γ_O. The nabla operator ∇ express the gradient. The domain Ω changes continuously as the printing process progresses, resulting in a continuously changing domain boundary Γ_O. Heat flow source terms such as those caused by crystallization effects are not taken into account here.

In a process simulation of the entire component, the heat flow s can be formulated by

$$s = s_{\mathrm{conv}} + s_{\mathrm{rad}} + s_{\mathrm{hp}}. \tag{7.2}$$

s_{conv} describes the heat flux caused by free convection defined as

$$s_{\mathrm{conv}} = h_{\mathrm{conv}}(T - T_{\mathrm{amb}}), \tag{7.3}$$

with ambient temperature T_{amb} and the convection coefficient h_{conv}. s_{rad} describes the heat flux by radiation, defined as

$$s_{\mathrm{rad}} = \sigma \epsilon (T^4 - T_{\mathrm{amb}}^4), \tag{7.4}$$

with Stephan-Boltzmann constant σ, and emissivity coefficient ϵ. s_{hp} describes the heat flux into the component due to the heat of the build platform.

[4] Verbatim reproduced section from [4], © CC BY 4.0, cf. footnote p. 183 for details.

The smaller domain Ω_{sub} of the submodel implies a change in the surface flux s. The heat flux into the system through the build platform is not present in the submodel. The convection and radiation of the free surfaces at the printing front within the system are still present. In addition, there is a heat flux $s_{\mathrm{poly}}^{\mathrm{cond}}$ across Γ_O from the submodel into the surrounding printed structure. Thus, the heat fluxes across Γ_O of the submodel is given by

$$s = s_{\mathrm{conv}} + s_{\mathrm{rad}} + s_{\mathrm{poly}}^{\mathrm{cond}}. \tag{7.5}$$

7.1.3 Boundary conditions of the submodel[4]

The geometry of the submodel is defined as a cuboid volume around the area of interest (in this case the center point CP). This allows the boundary conditions to be defined individually for each surface of the submodel. In this work, different boundary conditions to represent the heat flow $s_{\mathrm{poly}}^{\mathrm{cond}}$ over each surface are compared. These methods include adiabatic conditions ($s_{\mathrm{poly}}^{\mathrm{cond}} = 0$), uniform and constant Dirichlet boundary conditions ($T_{\mathrm{poly}}^{\mathrm{const}}$), and uniform and time-dependent Dirichlet boundary conditions ($T_{\mathrm{poly}}(t)$). Figure 7.2 shows the defined boundary conditions at the domain boundaries at the CP printing time. The left side of the figure shows an additively manufactured cube modeled according to the state-of-the-art. The entire cube represents the domain and is therefore filled with elements. The cooling effects are defined by convection s_{conv} and radiation s_{rad} over all domain boundaries and the resulting free surfaces within the domain. The heat flow through the heated build platform s_{hp} is implemented by a Dirichlet boundary condition. The right side of the figure shows the modeling with the submodeling method. Here, only a certain area around the CP is filled with elements, which represents the model domain. The domain boundaries to the surrounding polymer, where the boundary conditions are defined, are shown in red. Inside the domain, heat

[4] Verbatim reproduced section from [4], © CC BY 4.0, cf. footnote p. 183 for details.

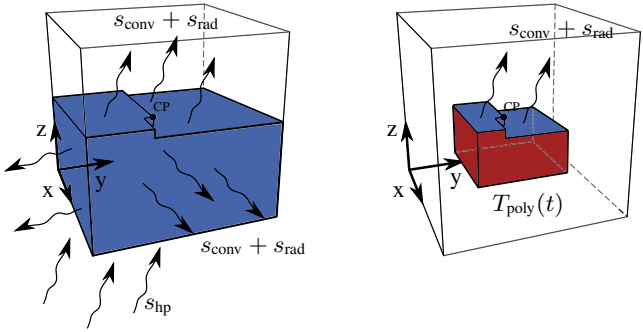

Figure 7.2: Schematic representation of the defined boundary conditions for modeling according to the state-of-the-art (left) and with the submodeling method (right). (Reproduced from [4])

flows result from convection s_{conv} and radiation s_{rad} over the free surfaces occurring during the process (shown in blue).

In the actual process, the polymer temperatures $T_{\mathrm{poly}}(t, x, y, z)$ vary with location and time along the submodel boundaries. However, this work aims for the simplest possible submodeling, so these location dependencies of the Dirichlet boundary conditions are ignored. The recommended procedure for determining these conditions involves an upstream process simulation of the entire component, which provides the temperatures for each submodel surface. A coarser discretization can be used for this simulation.

The temperatures are determined as shown in Figure 7.3 for the y and z surfaces: $T^{\mathrm{y-}}_{\mathrm{poly}}$, $T^{\mathrm{y+}}_{\mathrm{poly}}$, $T^{\mathrm{z-}}_{\mathrm{poly}}$ and $T^{\mathrm{z+}}_{\mathrm{poly}}$. The constant Dirichlet boundary condition $T^{\mathrm{const}}_{\mathrm{poly}}$ is defined as the temperature at the time of printing the layer containing the CP. These temperatures are measured at points marked in Figure 7.3, at a distance from the CP equal to half the submodel edge length. The time-dependent Dirichlet boundary condition $T_{\mathrm{poly}}(t)$ is defined as the temperature evolution at these points. For the upstream simulation, a time increment t_{inc} can be chosen so that one complete layer is activated per step. The element height equals the strand height, and the element width equals the strand width s_{width} or a multiple

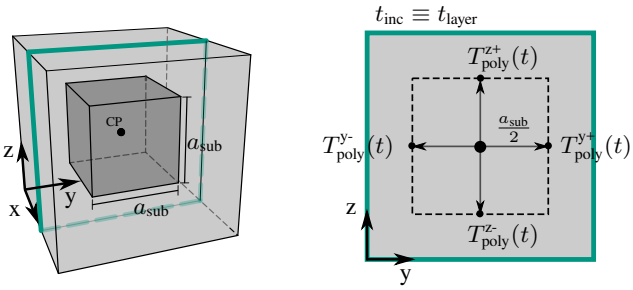

Figure 7.3: Schematic representation of the method for determining the time-dependent Dirichlet boundary condition $T_{\mathrm{poly}}(t)$ from an upstream process simulation of the entire component with low computational effort. (Reproduced from [4])

thereof, ensuring that the nodes of the component simulation and the submodel boundary overlap. Linear interpolation between the specified time-dependent temperature values is used for the submodel simulation.

7.1.4 Time discretization[4]

With the submodeling approach presented here, a high temporal resolution is only required when strands are deposited within the submodel. At times when no elements of the submodel are activated, i.e. other areas of the component are being printed, the heat input into the center is very low and the cooling rates to be recorded are smaller. Therefore at these times $t_{\mathrm{inc}}^{\mathrm{out}} >> t_{\mathrm{inc}}^{\mathrm{sub}}$ can be selected. A transition region is defined in which no elements of the submodel are activated, but small $t_{\mathrm{inc}}^{\mathrm{sub}}$ are still defined (marked orange in Figure 7.4). This allows the cooling rates immediately after leaving the virtual nozzle of the submodel to be taken into account and a single increment ($n_{t_{\mathrm{inc}}} = 1$) to be defined until the nozzle re-enters the submodel. The T_{poly} Dirichlet boundary condition ensures that when the nozzle re-enters the submodel (i.e., elements are

[4] Verbatim reproduced section from [4], © CC BY 4.0, cf. footnote p. 183 for details.

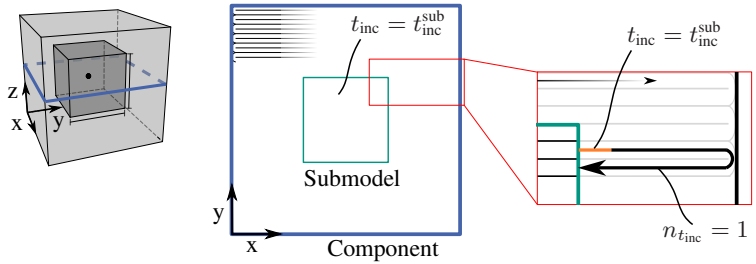

Figure 7.4: Illustration of the defined time increment t_{inc} within the submodel (green) with $t_{\mathrm{inc}} = t_{\mathrm{inc}}^{\mathrm{sub}}$ and for the time when the filament would be deposited outside the modeled domain. Here, the t_{inc} for a given time (orange) corresponds to the increment within the submodel $t_{\mathrm{inc}}^{\mathrm{out}} = t_{\mathrm{inc}}^{\mathrm{sub}}$. The remaining time (black) is defined by one increment ($n_{t_{\mathrm{inc}}} = 1$). (Reproduced from [4])

reactivated and thermal energy is introduced into the system), the temperature distribution in the real component matches the real process conditions. This makes the required computation time of the new method independent of the size of the entire component.

7.2 Process and material for method verification and validation[4]

Process The *Composer A4* made by *Anisoprint* was used to manufacture the validation components. The nozzle used has a diameter of $0.4\,\mathrm{mm}$. An extrusion width of $0.45\,\mathrm{mm}$ is specified in the slicer. The slicer-specific overlap of the individual strands, the width of the component, and the trajectory used in this work result in a strand width s_{width} of approximately $0.41\,\mathrm{mm}$, as shown in Table 7.1. The slicer and printer settings shown in Table 7.1 were chosen for the experiments as well as the simulations. The fan was switched off and the build chamber was open due to the need to insert the thermocouples. To measure the room temperature RT, a thermocouple was attached to the build platform so that the measurement point was at the height of the printed component. The average of the five measurements of the room temperature was $RT = 28.47\,^{\circ}\mathrm{C}$. The higher temperature compared to the lab temperature is due to radiant heat from the build platform.

Table 7.1: Slicer and process parameters selected for the manufacturing of all specimens. [4]

Process parameter	Value	Unit
Nozzle temperature T_{N}	212	$^{\circ}\mathrm{C}$
Bed temperature T_{bp}	55	$^{\circ}\mathrm{C}$
Layer height l_{height}	0.2	mm
Extrusion width e_{width}	0.45	mm
Strand width s_{width}	0.41	mm
Infill printing velocity v_{infill}	50	$\mathrm{mm/s}$

[4] Verbatim reproduced section from [4], © CC BY 4.0, cf. footnote p. 183 for details.

Material In this work, the mesostructure is modeled homogenized. The individual strands and the process-typical voids are therefore not explicitly modeled but combined to form a homogenized region. The given material properties thus also represent homogenized values of the process-typical mesostructure: The density $\rho_{\mathrm{PLA}} = 1208\,\mathrm{kg/m^3}$ of the PLA structure produced using the process parameters from Table 7.1 was measured according to the Archimedean principle using the *ME-DNY-43* density meter and the *ME204T/00* analytical balance from *Mettler Toledo*. The anisotropic thermal conductivity $\boldsymbol{\kappa}$ of the printed structure with unidirectional material orientation is set to $\kappa_x = 0.195\,\mathrm{W/(m \cdot K)}$, $\kappa_y = 0.135\,\mathrm{W/(m \cdot K)}$ and $\kappa_z = 0.181\,\mathrm{W/(m \cdot K)}$ according to Elkholy et al. [64]. The temperature-dependent specific heat capacity $c_{\mathrm{p}}(T)$ was determined using Differential Scanning Calorimetry (DSC) and is shown in Figure 6.7.

7.3 Mesh size and time increment[4]

To predict the temperature history as accurately as possible, the mesh size and the selected time increment t_{inc} are crucial. This section therefore presents a sensitivity analysis to identify the required mesh size and t_{inc}. The study includes the accurate prediction of the temperature gradient within a strand as well as the requirement for a steady curve of temperature history.

Mesh size. To quantify the required number of elements within a strand not only to the strand width (y-direction) and height (z-direction) but also along the extrusion direction (x-direction), a unit cell is introduced, as shown in Figure 7.5. Its width and height are equal to the strand width s_{width} and height a_{height}, and its length in the extrusion direction is equal to s_{width}. This allows a minimum number of elements to be defined for all axes. Figure 7.5 shows examples of meshing concerning the edge lengths of the unit cell. To investigate

[4] Verbatim reproduced section from [4], © CC BY 4.0, cf. footnote p. 183 for details.

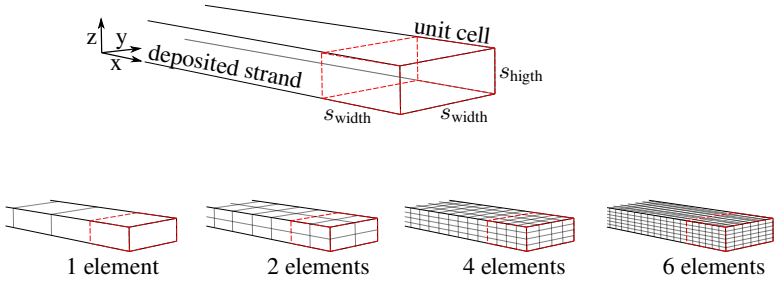

Figure 7.5: Introduced unit cell to quantify the required number of elements within a strand in terms of strand width (y-direction), strand height (z-direction), and extrusion direction (x-direction) (top). Below are examples of meshing about the edge length of the unit cell. (Reproduced from [4])

the sensitivity of the element size to the temperature gradient, a single strand deposited on the heated build platform is considered. This represents the extreme case in terms of the temperature gradient. The process parameters listed in Table 6.4 were used for the simulation studies. As shown in Figure 7.6, the temperature profile along the height of the strand (z-direction) as well as the width of the strand (y-direction) at the time of deposition (1) and at the same time $10\,\mathrm{mm}$ behind (2) are determined to evaluate the spatial discretization. In the x-direction, the temperature profile along the top of the strand is shown. The t_{inc} was chosen as a function of the element size in the extrusion direction (x-direction), resulting in one element being activated in the x-direction per t_{inc}. Figure 7.7 shows the percentage deviation of the different discretizations from the finest discretization of 10 elements per edge length of the unit cell, averaged over all nodes along the respective path. Based on the average deviations, two elements per unit cell along the extrusion direction (x-direction) are considered sufficient. However, at least four elements are required along the height and width of the strand.For the process parameters used in this work, the elements therefore have the edge lengths $l_x = 0.205\,\mathrm{mm}$, $l_y = 0.1025\,\mathrm{mm}$ and $l_z = 0.05\,\mathrm{mm}$.

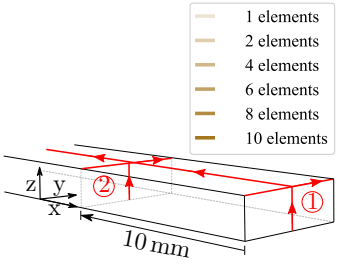

(a)

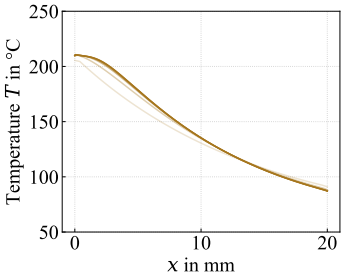

(b) X-direction.

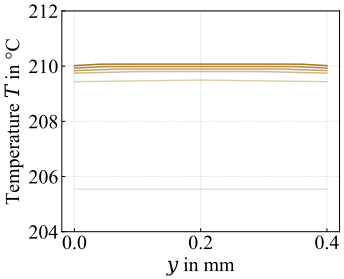

(c) Y-direction at point 1.

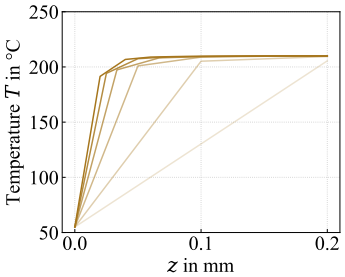

(d) Z-direction at point 1.

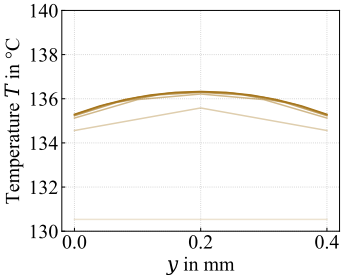

(e) Y-direction at point 2.

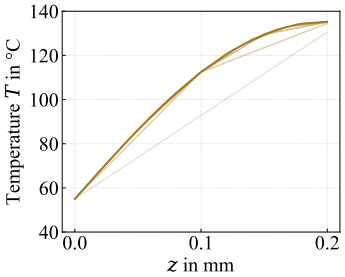

(f) Z-direction at point 2.

Figure 7.6: Results of the mesh analysis of the spatial discretization on the temperature distribution within a deposited strand. Performed with 1, 2, 4, 6, 8, and 10 elements per side length of the unit cell and evaluated immediately after element activation (point 1), shown in (c) and (d), and 10 mm afterward (point 2), shown in (e) and (f). (Reproduced from [4])

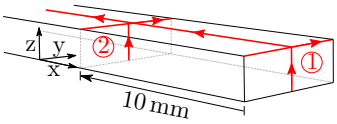

(a)

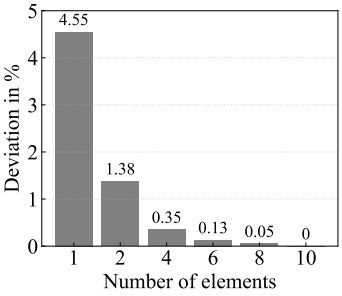

(b) X-direction.

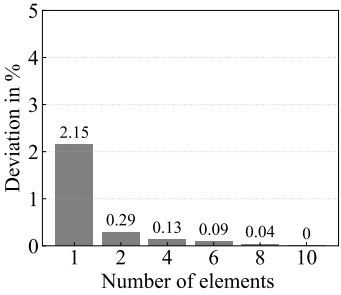

(c) Y-direction at point 1.

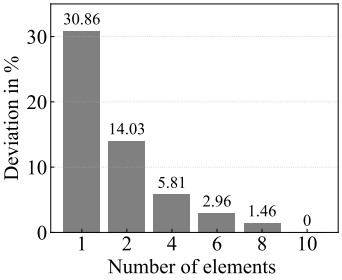

(d) Z-direction at point 1.

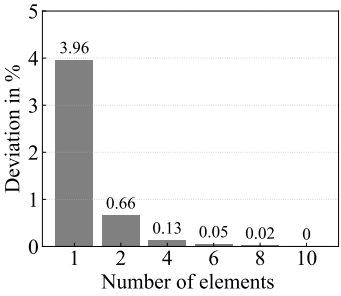

(e) Y-direction at point 2.

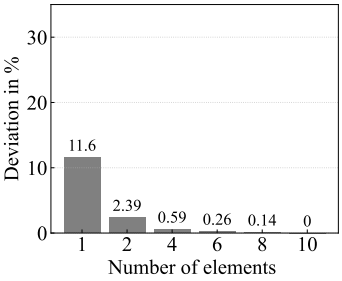

(f) Z-direction at point 2.

Figure 7.7: Percentage deviation of the different discretizations concerning the finest discretization of 10 elements per edge length of the unit cell. Averaged over all nodes along the respective path. Performed with 1, 2, 4, 6, 8, and 10 elements and evaluated immediately after element activation (point 1), shown in (c) and (d), and 10 mm later (point 2), shown in (e) and (f). (Reproduced from [4])

Time increment. To demonstrate the required t_{inc}, four 20 mm strands were placed side by side and on top of each other on a heated build platform. Four elements were selected for each edge of the unit cell. Figure 7.8 shows the temperature profile in the center of the resulting 2x2 strands component for different t_{inc}. In addition to the t_{inc} that results in the activation of one element along the extrusion direction per t_{inc} (1 element in x-direction), a smaller (1/2 element in x-direction) and a larger t_{inc} (2 elements in x-direction) were selected. Figure 7.8 b) shows that if t_{inc} is selected so that an element row is only activated every second increment, the temperature profile does not show the typical continuous curve. If several element rows are activated per t_{inc}, the temperature peak is slightly underestimated. However, the analysis shows that such larger time increments can also be selected for an accurate representation of the temperature profile. Since this work focuses on the most accurate representation of the history, a t_{inc} is selected as dependent on the element size along the extrusion direction so that one element row is activated per increment and thus the continuous extrusion process is mapped as realistically as possible.

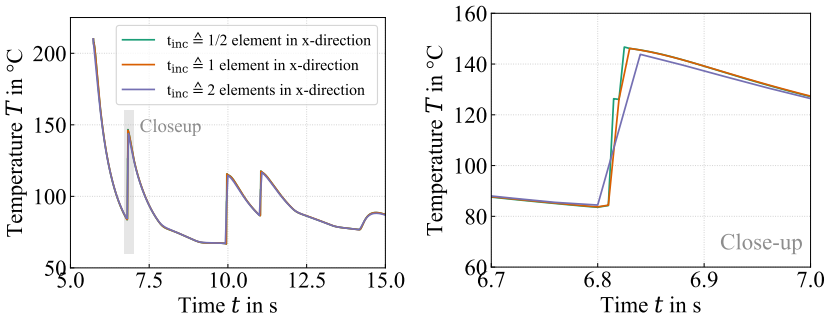

Figure 7.8: Temperature profile at a point in the filament from the time of its activation with three different time increments: t_{inc} set to activate two rows of elements per increment (t_{inc} $\widehat{=}$ 2 element in the x-direction), t_{inc} set to activate exactly one row of elements (t_{inc} $\widehat{=}$ 1 element in the x-direction), and t_{inc} set to activate one element every second increment (t_{inc} $\widehat{=}$ 1/2 element in the x-direction) (a). Close-up for a more detailed comparison of cooling rates and temperature (b). (Reproduced from [4])

7.4 Numerical verification[4]

7.4.1 Model setup[4]

To verify the numerical principle, a heat transfer analysis of the additive manufacturing of a cube, as introduced in Section 7.1, is performed as a generic component. A unidirectional trajectory as shown in Figure 7.9 is used. A

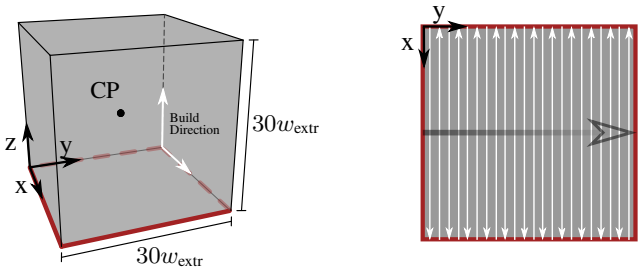

Figure 7.9: Cube as a generic component, with edge lengths (left) and the orientation of the unidirectional trajectory (right). (Reproduced from [4])

cuboid-like submodel as shown in Figure 7.2 is modeled around the center point (CP) of the component. The error can be estimated by comparing the temperature curves in the CP. Models with different edge lengths and corresponding boundary conditions are compared to evaluate the necessary size of the modeled volume of the submodel.

The small dimensions of the component allow a temporal and spatial discretization as in the submodel according to the sensitivity analysis presented in Section 7.3. This ensures that the temperature profile is predicted as accurately as possible, even in the state-of-the-art simulation of the actual component. In this way, the novel submodeling approach can be verified numerically. The

[4] Verbatim reproduced section from [4], © CC BY 4.0, cf. footnote p. 183 for details.

process parameters used for the simulation can be found in Table 6.4. The convection coefficient is set to $h_{\mathrm{conv}} = 8\,\mathrm{W/m^2{\cdot}K}$ and the emissivity coefficient is set to $\epsilon = 0.97$ according to [196]. Linear isoparametric 3D elements with 8 heat transfer nodes (DC3D8) are used.

7.4.2 Temperature prediction accuracy[4]

Figure 7.10 shows the calculated temperatures $T(t)$ at the CP for both the fine-mesh process simulation (gray) and the submodel with twelve times the extrusion width ($4.88\,\mathrm{mm}$) as length under different boundary conditions. The adiabatic boundary condition results in the green curve, the constant Dirichlet boundary condition in the blue curve, and the time-dependent Dirichlet boundary condition in the red curve. Temperature fluctuations are due to renewed heat input from nearby deposited strands. The lower part of Figure 7.10 shows the temperature deviations ΔT at the CP over time.

The adiabatic boundary condition significantly overestimates the temperature, as no heat can dissipate beyond the submodel's boundaries. The Dirichlet boundary conditions predict the temperature similarly to the simulation of the entire cube, especially immediately after the CP is printed.

The constant Dirichlet boundary condition overestimates the temperature for the later process stage. This is because the surface of the submodel cool down during the process after printing the CP, which the constant boundary condition does not account for as opposed to the time-dependent one. The initial overestimation of the temperature and the subsequent underestimation of T when using time-dependent Dirichlet boundary conditions is due to their uniformity.The boundaries of the submodel, extruded before the activation time of the CP, actually have lower temperatures than specified by the selected boundary conditions. The temperatures inside the submodel are therefore overestimated immediately after extrusion. The reverse effect at the later printed domain boundaries leads

[4] Verbatim reproduced section from [4], © CC BY 4.0, cf. footnote p. 183 for details.

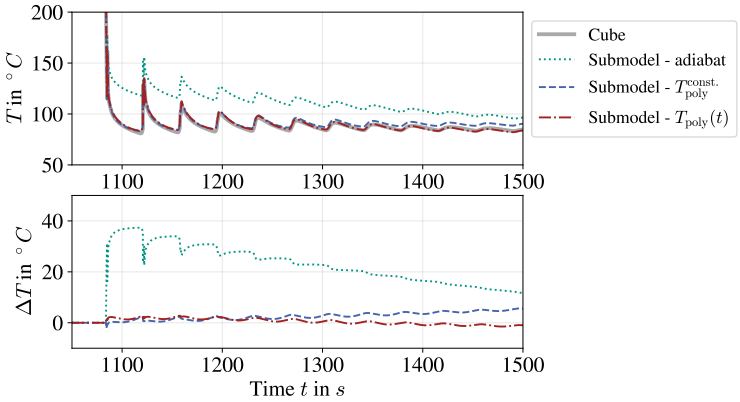

Figure 7.10: Calculated temperatures $T(t)$ at the CP of the state-of-the-art process simulation (cube) and the submodel with an edge length of $4.8\,\mathrm{mm}$ and different boundary conditions at its surfaces: Adiabatic boundary condition in green, constant Dirichlet boundary condition $T_{\mathrm{poly}}^{\mathrm{const.}}$ in blue and time-dependent boundary condition $T_{\mathrm{poly}}(t)$ in red. The lower part shows the deviation of the submodel temperatures ΔT from the calculated temperature curve. (Reproduced from [4])

to an increasing underestimation of the temperature since a location-dependent consideration of the Dirichlet boundary conditions would predict higher temperatures. However, the error does not grow infinitely but is limited by the choice of the Dirichlet boundary conditions $T_{\mathrm{poly}}(t)$.

The time-dependent Dirichlet boundary condition provides the most accurate temperature curve and is recommended and used to validate the method.

7.4.3 Required submodel size[4]

Figure 7.11 shows the ΔT of submodels of different sizes with time-dependent Dirichlet boundary conditions compared to the state-of-the-art simulation. On average, the initial overestimation and subsequent underestimation of the temperature described above can be seen for all sizes. In addition, the deviations

[4] Verbatim reproduced section from [4], © CC BY 4.0, cf. footnote p. 183 for details.

increasingly fluctuate around the mean for smaller submodel sizes. This is due to the increasing negative influence of the chosen boundary conditions on the cooling rate and the resulting temperature peaks in the CP. The comparison

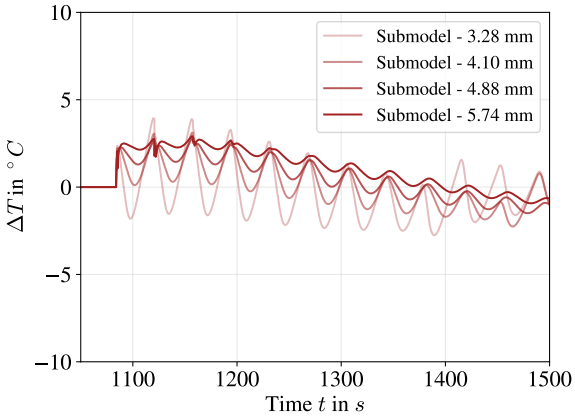

Figure 7.11: ΔT of submodels of different sizes. (Reproduced from [4])

of the computation time between the entire cube and the submodel with the upstream coarser simulation shows that the submodeling approach achieves a reduction of more than $98\,\%$. All simulations were performed on 16 cores. The time advantage increases with larger components, since the required computation time of the submodel is independent of the component size.

7.5 Experimental validation[4]

7.5.1 Experiment[4]

For experimental validation, the temperature profile during the printing of a component was measured using Type K thermocouple sensors with a diameter of $0.07\,\mathrm{mm}$. Due to the small size of the deposited strands, the exact placement of these sensors strongly influences the error of the measurements. Therefore, a component geometry was chosen that minimizes the sources of error. The selected geometry with the indicated trajectory is shown in Figure 7.12. To place the sensors, channels with the height of a layer were provided. This allows the sensor to be placed in the same position as reproducibly as possible and the nozzle to be moved over the sensor without displacing the thermocouple. The channel is in the layer with the CP. After printing the layer, the process is interrupted for $30\,\mathrm{s}$ to insert and fix the thermocouple. When printing is resumed, temperature recording begins and is evaluated from the first overprint of the sensor. From this point on, the simulation data are compared to the experimental data for validation. The extrusion direction is along the x-coordinate. An additional channel was integrated on the underside of the component to measure the temperature at the point of contact between the component and the build platform. The ambient temperature T_{amb} was measured during the process using a sensor in an area above the build platform at the height of the component. The process parameters given in Table 6.4 were used and five measurements were taken.

Figure 7.13 shows the mean values of the measurements at the middle point and the bottom of the component with the corresponding minimum and maximum values. The heat input from the deposited strands and the rapid cooling can be seen. This results in the expected temperature peaks. In Figure 7.13, a temperature peak represents a printed layer. The general increase in the

[4] Verbatim reproduced section from [4], © CC BY 4.0, cf. footnote p. 183 for details.

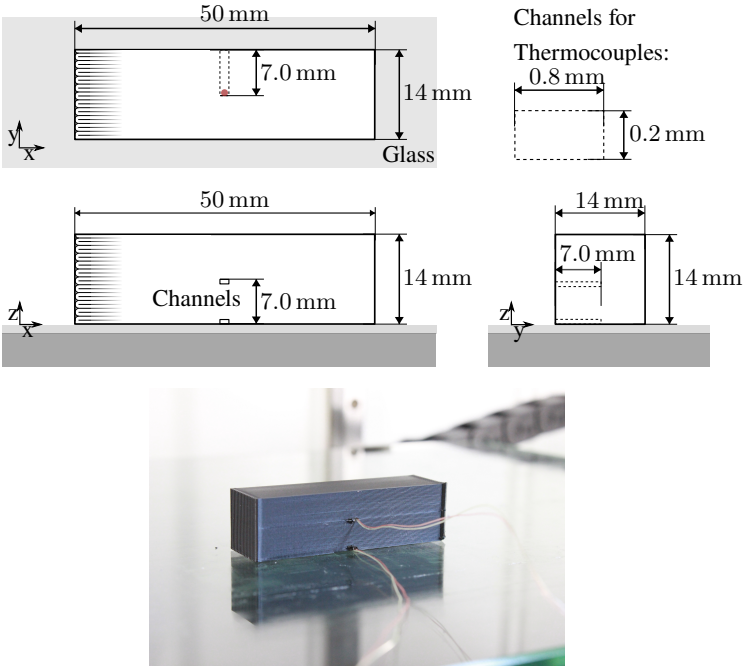

Figure 7.12: Component geometry and print setup for experimental validation with thermocouple sensors. The temperature measuring point is marked in red. (Reproduced from [4])

mean temperature at the beginning of the measurement is due to the following phenomenon: The component cools down when the sensor is inserted before the start of the measurement because printing is briefly interrupted during this time. As a result, the temperature in the component is lower at the start of the measurement than it would be during continuous printing. The heat input from the strand deposition after sensor insertion heats the component as a whole. As a result, the temperature in the entire component rises again after the sensor is inserted and the measurement begins. This effect diminishes toward the end of the measurement as the heat input moves away from the measurement point. The temperature profile at the bottom of the component shows no temperature peaks due to the deposition of the strands in the center of the component. This

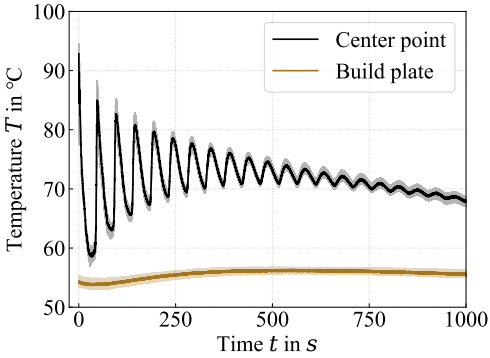

Figure 7.13: Mean value of the measured temperature profiles in the center (black) and at the bottom (brown) of the component with the corresponding minimum and maximum (lighter color) value for experimental validation. (Reproduced from [4])

proves that the local cooling rates at the measurement point are predominantly by the cooling effect of convection and radiation and not by heat conduction into the component.

7.5.2 Process simulation model[4]

For experimental validation, a submodel was modeled around the center of the validation component in Figure 7.12. Figure 7.14 shows the submodel inside the component. Ten times the extrusion width w_{extr} was chosen as the edge length of the submodel. As shown in Figure 7.11, this dimension leads to a similar peak temperature prediction as the larger submodels. The model was discretized according to the results of the analysis described in Section 7.3 with four elements in the strand height and width and two elements per unit length in the extrusion direction. The time increment at a print velocity of $v_{\mathrm{p}} = 50\,\mathrm{mm/s}$ is $t_{\mathrm{inc}} = 0.004\,12\,\mathrm{s}$. The time-dependent Dirichlet boundary conditions at the interfaces are derived from the results of the process simulation of the entire

[4] Verbatim reproduced section from [4], © CC BY 4.0, cf. footnote p. 183 for details.

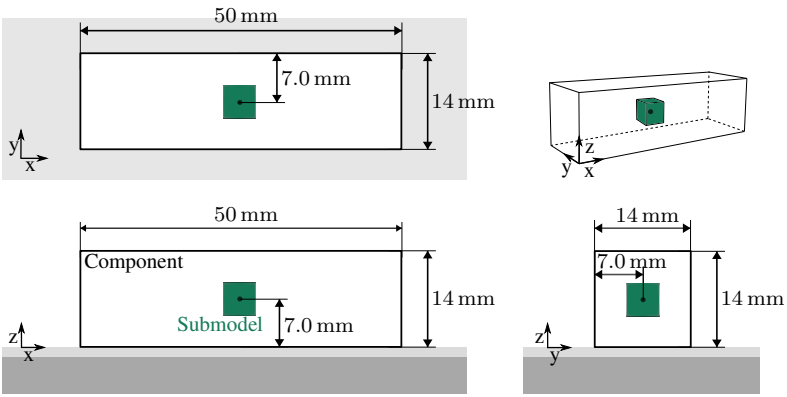

Figure 7.14: Schematic representation of the validation component with integrated submodel in green and the measuring point in black. (Reproduced from [4])

component as described in Section 7.4.3 with $t_{\mathrm{inc}} = t_{\mathrm{layer}}$. The element height was set to the layer height of $0.2\,\mathrm{mm}$. The process parameters from Table 6.4 were selected. The G-Code of the validation component was converted into actual nozzle motions using the methodology presented in Chapter 4 and the resulting open-source software *pyGCD* [213] and used as input for *Abaqus*.

7.5.3 Comparison of the local temperature profiles[4]

Figure 7.15 (a) shows the experimentally determined temperature profile in the CP and the temperature profile predicted using the submodeling approach over the same period. The temperature curve is presented starting from the point at which the CP is overprinted, as the thermocouple is capable of detecting temperature only from this moment onwards as described in Section 7.5.1. Therefore, when comparing simulated and experimental data, the temperature does not start above the melting temperature, but below it. However, it should

[4] Verbatim reproduced section from [4], © CC BY 4.0, cf. footnote p. 183 for details.

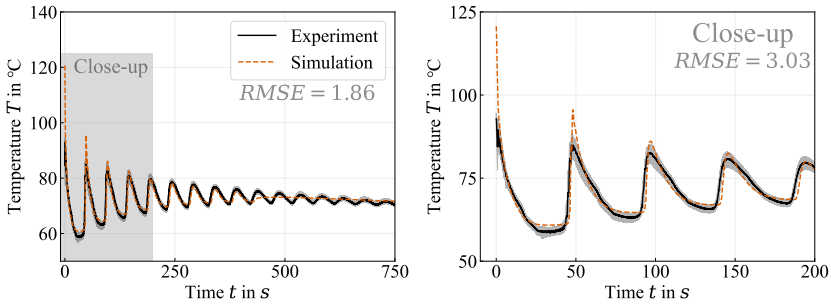

Figure 7.15: Temperature curves determined with the novel submodeling method presented in this work and measured with thermocouples sensors in experiments (a). Close-up for a more detailed comparison of cooling rates and temperature (b). The root-mean-square error ($RMSE$) is given for both sections (a) and (b). (Reproduced from [4])

be noted that in the simulation, temperature mapping is possible from the time the CP is printed ("activated" in the simulation). In this case, temperatures in the range of the nozzle temperature are predicted.

Using the submodeling approach, the fine-resolution model can reproduce the measured cooling rates and temperature peaks. Only the two initial temperature peaks are higher in the numerically calculated curve. There are two conceivable reasons for this: First, the nozzle temperature set in the slicer is assumed to be the extrusion temperature in the simulation. However, it is known from the literature [242, 243] that the actual extrusion temperature can differ from the set temperature. On the other hand, due to the thermal inertia of the thermocouple and its limited sampling rate in combination with the comparatively high nozzle velocity, the initial temperature peaks may not be recorded as they occur in the process. The constant temperature profile later in the process (after about 400 s) can be explained by the size of the submodel. At the transition from the oscillating to the constant temperature profile, the submodel is already completely printed. This means that no new elements are activated in the submodel domain and therefore no additional heat is added.

Overall, however, it can be concluded that the submodeling approach is capable of simulating the temperature history at local points of interest, using finely resolved models locally and accounting for components' geometry and process conditions globally. This is also confirmed by the corresponding root mean square error ($RMSE$). In the time range $t = 0\,\mathrm{s} - 750\,\mathrm{s}$, the $RMSE = 1.86\,^{\circ}\mathrm{C}$. In the close-up time range, where local variables such as degree of crystallization and interface strength are significantly influenced, the error is $RMSE = 3.03\,^{\circ}\mathrm{C}$.

7.6 Summary and conclusion[4]

A modeling method based on the submodeling approach is presented, which enables the coupling of high-resolution models and MEX process simulations at the component level. It thus allows the investigation of local effects and their dependence on process variables at local points of interest in a component, taking into account the component geometry as well as global and component-specific process conditions. The submodeling approach follows the Saint-Venant principle, according to which local effects decrease with increasing distance. The application of submodeling to the MEX process is based on the fact described in the literature that the high cooling rates typical for the process and the comparatively low thermal conductivity of thermoplastics indicate that cooling effects such as free convection and radiation are mainly responsible for the local temperature profile during MEX. The local process conditions in the investigated component are taken into account by time-dependent Dirichlet boundary conditions, which are determined by an upstream efficient simulation of the entire component in low resolution. In this way, the real process conditions are transferred to the submodel and enable a local prediction of the temperature profile in additively manufactured components during production. The predicted local temperature profile allows accurate prediction of local effects such as interface

[4] Verbatim reproduced section from [4], © CC BY 4.0, cf. footnote p. 183 for details.

strength and degree of crystallinity in the component. The work thus provides a modeling approach for the multiscale problem prevalent in MEX.

The required computation time is independent of the component size, which allows an efficient prediction of the temperature history. The numerical principle is verified using a state-of-the-art process simulation on the component level for unidirectional trajectories. Furthermore, different boundary conditions, and domain sizes of the submodel are compared and discussed. A sensitivity analysis provides the necessary temporal and spatial discretization for the fine-resolution model used. The presented submodeling method is validated using experimental temperature curves. The validation tests were performed with a commercial FFF printer and unreinforced PLA. The validation shows a good agreement between the temperature profiles calculated with the submodeling approach and the experimentally determined profiles. The cooling rates and the time sequence of the temperature peaks are in good agreement. The validation shows only slightly higher temperatures in the numerical determination for the first temperature peaks. This is most probably due to a lower effective extrusion temperature compared to the nominal nozzle temperature specified in the slicer and assumed in the simulation, the thermal inertia of the thermocouples, or the limited sampling rate of the sensors. These assumptions need to be investigated in subsequent work to further substantiate the prediction accuracy of the fine-resolution models and their use to predict local crystallinity and interfacial strength of adjacent strands.

The work shows that a cuboid model with an edge length of ten times the extrusion width is sufficient for the extrusion of PLA. Similar sizes are expected for other non-reinforced thermoplastics due to their low thermal conductivity. For fiber-reinforced material systems, future work will be needed to determine the required size through investigations such as those described in this article.

8 Conclusion and recommendations

The prediction of process-induced effects in components manufactured by material extrusion (MEX) has been advanced through the development of novel methodological approaches. These include numerical, analytical, and experimental methods designed to improve the accuracy and reliability of simulations under real process conditions. Based on a detailed analysis of the current state of research, four central objectives were defined to close existing research gaps related to firmware interpretation, material characterization, mesostructure-aware simulation, and multiscale modeling. The results of this thesis contribute to a deeper understanding of the underlying mechanisms and establish a methodological foundation for more robust and efficient simulation strategies in MEX. In this chapter, the main conclusions are structured according to the defined objectives (cf. Section 3.1), and recommendations are proposed to guide future research.

Conclusions

Objective O-1. Systematic investigation of the influence of firmware interpretation of G-Code on nozzle motion during the MEX process, including quantification of deviations from theoretical motion paths and analysis of their impact on local process conditions.✓

The developed simulation framework enables a detailed reconstruction of actual nozzle motion in MEX processes by incorporating firmware-specific motion planning algorithms. This includes constraints such as maximum acceleration, velocity, and cornering behavior. The framework was validated experimentally and demonstrated high accuracy in predicting layer durations and motion paths. Error metrics were introduced to quantify deviations between nominal and actual motion, revealing that firmware parameters such as acceleration and jerk significantly influence process fidelity. The study also showed that infill pattern and component geometry play a dominant role in determining local process conditions. These insights are critical for improving process simulations and developing adaptive slicing strategies that account for machine dynamics.

Objective O-2. Development and evaluation of methodologies for characterizing material properties under real process conditions, specifically for PLA-based MEX components. This aims to ensure that the measured mechanical properties accurately reflect those of actual components, providing reliable data for both experimental studies and computational analyses of MEX structures.✓

A systematic study was performed to compare different specimen preparation methods for PLA-based MEX components. Directly printed and cut specimens were analyzed across various orientations and preparation techniques. The results show that milled dogbone specimens from single-specimen plates provide the best of both representativeness and reproducibility. Furthermore, the influence of plate size, cutting method, and perimeter effects was quantified. Based on these findings, a guideline for standardized specimen preparation was derived, which enhances the reliability of mechanical property data used in simulations. This directly addresses inconsistencies in the literature and supports the development of reproducible testing protocols.

Objective O-3. Development of a homogenization framework for MEX process simulations that incorporates the dynamically evolving local mesostructures and anisotropic stiffness characteristics at the macro scale. This enables efficient prediction of process-induced deformations at the component level, accounting for mesostructural effects without requiring full-resolution mesoscale simulations.✓

A homogenization approach was developed to predict process-induced deformations (PiD) in MEX components. This approach incorporates the spatial and temporal evolution of the mesostructure into finite element simulations. Building on the orientation averaging framework of Advani and Tucker, the method uses second- and fourth-order orientation tensors to compute local anisotropic stiffnesses based on strand orientation. The presented simulation framework maps firmware-interpreted G-code trajectories onto spatially resolved orientation fields, enabling the representation of mesostructural features, such as perimeter regions, turning points, and orientation mixtures, within individual elements at component scale.

Experimental investigations using tensile tests, DMA, TMA, and DSC identified key thermomechanical effects relevant to PiD. These effects include strong temperature dependency of stiffness and isotropic thermal expansion. Furthermore, negligible crystallization occurs during these process steps. These findings informed the selection of mechanisms to be included in the material model and guided its parameterization.

Numerical studies demonstrated the evolution of orientation states during printing and their dependence on element size and trajectory geometry. Experimental validation using µCT-scanned PLA components confirmed the predictive capability of the approach, with good agreement between simulated and measured PiD. Comparative simulations with an isotropic stiffness formulation demonstrate the significant impact of considering mesostructural anisotropy, highlighting improvements over conventional approaches.

Objective O-4. Development of a multiscale simulation approach that couples high-resolution mesoscale FE models with macroscopic component-level models. This approach enables accurate prediction of local material behavior under component-specific process conditions, capturing phenomena that homogenized macro models cannot resolve.✓

A multiscale simulation approach was developed and implemented to connect macroscale MEX process simulations with mesoscale, high-resolution FE models. This method employs a submodeling technique based on the Saint-Venant principle to transfer time-dependent Dirichlet boundary conditions from a coarse global model to a fine-resolution local model. This allows for the precise prediction of local temperature histories during the additive manufacturing process while accounting for component-specific geometries and process conditions. The approach was validated using experimental measurements with thermocouples embedded in PLA MEX components during manufacturing. Comparing the simulated and measured temperature profiles revealed good agreement, particularly with regard to cooling rates and the timing of temperature peaks. Minor discrepancies in the initial temperature peaks were attributed to uncertainties in the effective extrusion temperature and sensor limitations. These factors should be the subject of further investigation. The computational effort of the method is independent of the size of the component, making the approach scalable for larger components. The predicted local thermal histories enable reliable estimation of critical effects, such as interfacial strength and crystallinity, that are essential to the mechanical performance of MEX components.

Recommendations for future research

Based on the work presented in this thesis, the following recommendations are offered to guide future research and development efforts. The recommendations are structured according to the four central objectives and highlight methodological extensions and potential application scenarios.

G-Code simulation and firmware optimization The developed G-Code simulation framework allows for a thorough analysis of machine-specific trajectory planning and its impact on local process conditions. Based on this, two future directions are recommended.

- **Trajectory optimization:** The developed tool can be used to optimize toolpaths in terms of printing time and process stability. Intelligent trajectory design minimizes frequent acceleration and deceleration phases, achieving more uniform extrusion conditions. This results in more consistent local thermal and mechanical properties, thus improving overall component quality.
- **Systematic firmware development:** The framework provides a basis for systematically testing and comparing new approaches to firmware, motion planning strategies, and their implementation. This allows for targeted firmware optimization, improving process fidelity across different machines and geometries.

Specimen preparation and material characterization The material characterization approach developed in this work provides a reliable basis for determining mechanical properties of MEX-printed PLA. However, further refinement is necessary to increase its representativeness under actual process conditions:

- **Influence of printing orientation:** The present study focused on plates manufactured flat on the build platform. Future work should systematically investigate the influence of the vertical position of the MEX structure under investigation on the resulting mesostructure and mechanical properties. This is particularly relevant because the vertical position can affect cooling rates, layer adhesion, and internal stresses, which in turn influence both the mesostructure and mechanical performance, and should be taken into account when planning future characterization studies.
- **In-situ specimen extraction:** To ensure maximum realism, mechanical test specimens could be taken directly from functional components. Their mechanical properties should then be compared with those of specimens designed and produced using the methodology developed in this work to replicate comparable process conditions.

Homogenization and material modeling The developed homogenization framework successfully incorporates evolving mesostructures into macroscopic process simulations. To increase its applicability and accuracy, the following steps are recommended:

- **Rate-dependent material modeling:** The path-dependent material model used in this work is not time-rate sensitive. Due to the high cooling rates in MEX, the accuracy of the PiD prediction is limited. Future work should investigate thermoviscoelastic or thermoviscoelasto-plastic formulations to more accurately capture stress relaxation and time-dependent PiD. Suitable models could include generalized, temperature-dependent Maxwell-like viscoelasticity. Calibrating such models requires stress relaxation, creep, or DMA tests over relevant temperature and strain rate ranges. These tests should be performed on MEX-manufactured specimens to reflect realistic mesostructures and thermal histories. Including rate-dependent effects would improve simulation of the deformation behavior and increase the model's predictive accuracy.

- **Extension to annealing processes:** The presented process simulation chain can be extended to include the annealing post-processing step. The cold crystallization effects triggered during annealing induce additional deformation of the components due to shrinkage related to crystallization. Incorporating this post-treatment into the simulation framework would allow for a thorough evaluation of various thermal annealing strategies, enabling assessment of their impact on final component deformation and overall mechanical performance. To do so, the existing material model must account for crystallization phenomena, particularly cold crystallization, and the associated shrinkage effects.

Multiscale submodeling and local property prediction The multiscale submodeling approach developed in this work enables the prediction of high-resolution temperature histories at critical locations within printed components. To exploit this capability for local property prediction and design validation, the following next steps are recommended:

- **Integration of mesoscale property models:** The submodeling framework should be extended by integrating existing mesoscale models, such as those for crystallization kinetics and interfacial strength. This will allow for the prediction of local mesostructural evolution and resulting mechanical properties as a function of component- and process-specific thermal histories.
- **Component-level validation of mechanical properties prediction:** The predictive accuracy of the integrated submodels should be validated on functional components. For instance, applying the submodel to a printed tensile specimen would allow for the local prediction of strength or stiffness, which can then be compared with experimental test results.
- **Process-aware property mapping:** To predict overall component strength as efficiently as possible, the presented methods (e.g. *pyGCD*), can be

extended to identify areas within a component with similar process conditions. In such cases, submodels only need to be calculated once per process-equivalent area. This enables an efficient, spatially resolved estimation of the mechanical properties across the entire component.

A Appendix

A.1 Default firmware settings for used printer systems

Appendix A.1 contains tables with the firmware settings of the printer systems used in this thesis. These settings were applied consistently throughout the experiments, except in Chapter 4, where they were partially varied in order to investigate their influence on the actual nozzle movement and, consequently, on the real process conditions. Please note that the configurations shown correspond to the status at the time of use. Manufacturer changes due to firmware updates may result in deviations.

Table A.1: Firmware settings of the *Ultimaker 2+*, read out in December 2024. The listed settings correspond to the firmware version that was current at that time.

Firmeware parameter	**Value**	**Unit**
Maximum X-speed $v_{\mathrm{p,max}}^{X}$	300	$\mathrm{mm/s}$
Maximum Y-speed $v_{\mathrm{p,max}}^{Y}$	300	$\mathrm{mm/s}$
Maximum Z-speed $v_{\mathrm{p,max}}^{Z}$	40	$\mathrm{mm/s}$
Maximum X-acceleration $a_{\mathrm{p,max}}^{X}$	9000	$\mathrm{mm/s^2}$
Maximum Y-acceleration $a_{\mathrm{p,max}}^{Y}$	9000	$\mathrm{mm/s^2}$
Maximum Z-acceleration $a_{\mathrm{p,max}}^{Z}$	100	$\mathrm{mm/s^2}$
XY-jerk $j_{\mathrm{max},x,y}$	20.0	$\mathrm{mm/s}$
Z-jerk $j_{\mathrm{max},z}$	0.40	$\mathrm{mm/s}$

Table A.2: Firmware settings of the *Prusa Mini*, read out in January 2024. The listed settings correspond to the firmware version that was current at that time.

Firmware parameter	Value	Unit
Maximum X-speed $v^X_{\text{p,max}}$	180	mm/s
Maximum Y-speed $v^Y_{\text{p,max}}$	180	mm/s
Maximum Z-speed $v^Z_{\text{p,max}}$	12	mm/s
Maximum X-acceleration $a^X_{\text{p,max}}$	1250	mm/s^2
Maximum Y-acceleration $a^Y_{\text{p,max}}$	1250	mm/s^2
Maximum Z-acceleration $a^Z_{\text{p,max}}$	400	mm/s^2
XY-jerk $j_{\max,x,y}$	8.0	mm/s
Z-jerk $j_{\max,z}$	2.0	mm/s

Table A.3: Firmware settings of the *Composer A4*, read out in January 2024. The listed settings correspond to the firmware version that was current at that time.

Firmware parameter	Value	Unit
Maximum X-speed $v^X_{\text{p,max}}$	180	mm/s
Maximum Y-speed $v^Y_{\text{p,max}}$	180	mm/s
Maximum Z-speed $v^Z_{\text{p,max}}$	30	mm/s
Maximum X-acceleration $a^X_{\text{p,max}}$	1000	mm/s^2
Maximum Y-acceleration $a^Y_{\text{p,max}}$	1000	mm/s^2
Maximum Z-acceleration $a^Z_{\text{p,max}}$	45	mm/s^2
XY-jerk $j_{\max,x,y}$	10.0	mm/s
Z-jerk $j_{\max,z}$	0.40	mm/s

A.2 Implementation and comparison of jerk strategies

Appendix A.2 contains the cornering algorithms implemented in this thesis, as discussed in Section 4.1.3 regarding the G-Code interpretation framework, presented in Chapter 4. The cornering algorithms of the firmware versions used for the printer systems in this thesis were replicated: *Prusa* [216], *MKA*

(*Anisoprint A4*), and *Ultimaker* [217]. The *Prusa* and *MKA* firmware implementations of the cornering strategy are identical. The approaches (*Prusa*/*MKA* and *Ultimaker*) represent their own interpretation of the *Classic jerk* approach. Additionally, the widely used *Marlin* implementation of the *Classic jerk* approach [219] was implemented and documented in this appendix.

Algorithm 1 *Prusa*/*MKA* jerk junction velocity algorithm [216, 218]

Require: $\boldsymbol{v_0}$: Current block velocity vector $\boldsymbol{v_1}$: Next block velocity vector $\boldsymbol{j}_{\max}$: Vector of maximum allowed jerk
Ensure: v_{junc}: Junction velocity magnitude

$f_v \leftarrow 1$ ▷ Initialize the velocity factor
for each axis $a \in \{X, Y, Z, E\}$ **do**
  $v'_{0,\text{a}} \leftarrow \boldsymbol{v_0}[a] \times f_v$
  $v'_{1,\text{a}} \leftarrow \boldsymbol{v_1}[a] \times f_v$
  ▷ Calculate axis jerk based on effective velocities
  $$j \leftarrow \begin{cases} v'_{0,\text{a}} - v'_{1,\text{a}} & \text{if } v'_{0,\text{a}} > v'_{1,\text{a}} \wedge (v'_{1,\text{a}} > 0 \vee v'_{0,\text{a}} < 0) \\ \max(v'_{0,\text{a}}, -v'_{1,\text{a}}) & \text{if } v'_{0,\text{a}} > v'_{1,\text{a}} \wedge (v'_{1,\text{a}} \leq 0 \wedge v'_{0,\text{a}} \geq 0) \\ v'_{1,\text{a}} - v'_{0,\text{a}} & \text{if } v'_{0,\text{a}} \leq v'_{1,\text{a}} \wedge (v'_{1,\text{a}} < 0 \vee v'_{0,\text{a}} > 0) \\ \max(-v'_{0,\text{a}}, v'_{1,\text{a}}) & \text{if } v'_{0,\text{a}} \leq v'_{1,\text{a}} \wedge (v'_{1,\text{a}} \geq 0 \wedge v'_{0,\text{a}} \leq 0) \end{cases}$$
  $j_{\max,a} \leftarrow \boldsymbol{j}_{\max}[a]$
  if $j > j_{\max,a}$ **then**
    $f_v \leftarrow f_v \times \frac{j_{\max,a}}{j}$
  end if
end for
$v_{\text{junc}} \leftarrow \|\boldsymbol{v_0} \times f_v\|$
return v_{junc}

Algorithm 2 *Ultimaker* firmware junction velocity calculation [217]

Require: $\boldsymbol{v_0}$: Current block velocity vector $\boldsymbol{v_1}$: Next block velocity vector $j_{\max,xy}$: Maximum allowed XY jerk
Ensure: v_{junc}: Junction velocity magnitude

$f_{\text{v}} \leftarrow 1$ ▷ Initialize the velocity factor
$j_{xy} \leftarrow \sqrt{(\boldsymbol{v}_{1,x} - \boldsymbol{v}_{0,x})^2 + (\boldsymbol{v}_{1,y} - \boldsymbol{v}_{0,y})^2}$ ▷ Euclidean norm as XY jerk
if $j_{xy} > j_{\max,xy}$ **then**
    $f_v \leftarrow j_{\max,xy}/j_{xy}$
end if
$v_{\text{junc}} \leftarrow \|\boldsymbol{v_0} \times f_v\|$
return v_{junc}

Algorithm 3 *Marlin Classic jerk* junction velocity algorithm [219]

Require: $\boldsymbol{v_0}$: Current block velocity vector $\boldsymbol{v_1}$: Next block velocity vector $\boldsymbol{j}_{\max}$: Vector of maximum allowed jerk
Ensure: v_{junc}: Junction velocity magnitude

$\boldsymbol{v}_{\text{diff}} \leftarrow \boldsymbol{v_0} - \boldsymbol{v_1}$
$f_v \leftarrow 1$ ▷ Initialize the velocity factor
for each axis $a \in \{X, Y, Z, E\}$ **do**
    $j_a \leftarrow |\boldsymbol{v}_{\text{diff}}[a]|$ ▷ Axis jerk per vector component
    $j_{\max,a} \leftarrow \boldsymbol{j}_{\max}[a]$
    if $j_a \times f_v > j_{\max,a}$ **then**
        $f_v \leftarrow j_{\max,a}/j_a$
    end if
end for
$v_{\text{junc}} \leftarrow \|\boldsymbol{v_0} \times f_v\|$
return v_{junc}

Figure A.1, based on Figure 4.4, shows the calculated junction velocity v_{junc} as a function of the turning angle θ with variable global coordinate system rotation Θ. The Figure shows all cornering approaches discussed in Section 4.1.3, including all variants based on the *Classic jerk* approach and the *Junction deviation* method. As illustrated by the figure, the calculated v_{junc} does not depend solely on the turning angle when using *Prusa/MKA* or *Marlin* firmware. Rather, it is also influenced by the position in the global coordinate system.

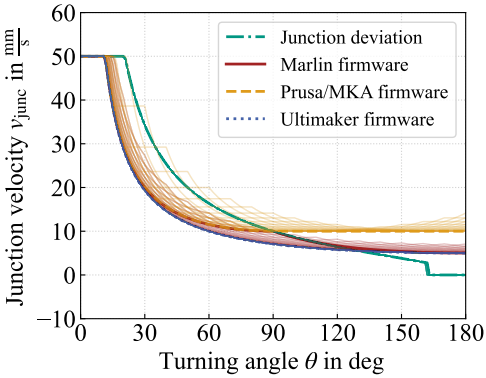

Figure A.1: Comparison of firmware with regard to their implemented cornering method for a range of turning angles from 0° to 180° with variable global coordinate system rotation Θ. Target velocity is 40 $\frac{\mathrm{mm}}{\mathrm{s}}$, acceleration 50 $\frac{\mathrm{mm}}{\mathrm{s}^2}$ and jerk 10 $\frac{\mathrm{mm}}{\mathrm{s}}$.

A.3 Additional tensile test results

Appendix A.3 presents additional stress-strain curves from tensile tests on printed specimens with various material orientations. These curves were recorded as part of the experimental characterization of nine engineering constants that describe the orthotropic stiffness tensor of a unidirectionally structured PLA MEX structure, which was carried out within the scope of Chapter 6. These results supplement the explanations in Section 6.2.2.1. Figure A.2 shows

the influence of the anisotropic mesostructure on mechanical properties. Figure A.2b confirms that linear elastic behavior occurs within a strain range of up to $0.25\,\%$. This justifies the boundary conditions used in the DMA tests to characterize temperature-dependent stiffness (cf. Section 6.2.2.2). Figure A.3

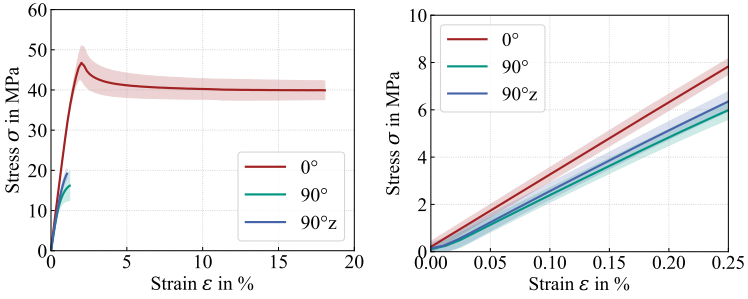

Figure A.2: Additional stress-strain curves from tensile tests on printed PLA specimens with different strand orientations. (a) Overall representation illustrating the influence of the anisotropic mesostructure on the mechanical behavior. (b) Enlarged section in the low-strain range to identify the linear-elastic behavior up to a strain of approximately $0.25\,\%$, which supports the assumptions for the boundary conditions in the DMA tests.

shows the stress-strain diagrams for each tested material orientation grouped by direction. This allows for a more accurate statement about the scatter of the test results to be made. In addition to the $0\,°$, $90\,°$, and $90\,°$z orientations, the diagram includes the $45\,°$ orientation, which was examined as part of the shear stiffness characterization in Section 6.2.3.1.

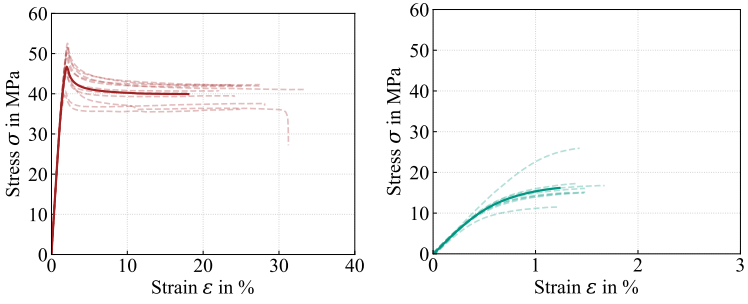

(a) 0 ° orientation (direction of extrusion)

(b) 90 ° orientation (transverse to the extrusion direction)

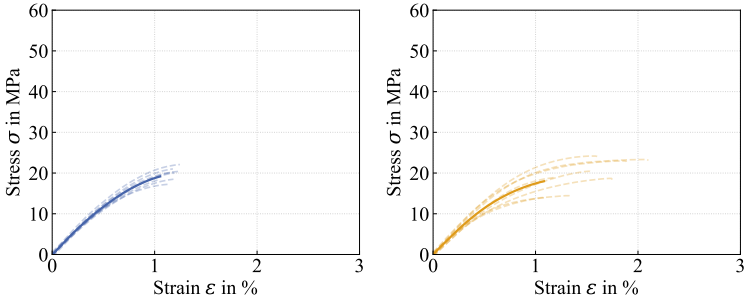

(c) 90 °z orientation along the z-axis (build direction)

(d) 45 ° orientation

Figure A.3: Individual representations of the stress-strain curves for the tested material orientations. The individual test results are shown to illustrate the scatter.

A.4 Note on out-of-plane orientations and sparse structures[2]

This work [Section 6.5.2] is based on the planar (x-y) deposition that is typical of MEX processes. However, the orientation tensor formulation presented here can be extended to three-dimensional (3D) deposition paths by including a non-zero z-component in the orientation vector, $\boldsymbol{p}$. The tensor formulation remains valid in this case. However, to convert the material orientation into a stiffness formulation for 3D additive manufacturing, the orientation averaging would need to be revised. This is because the presented approach exploits the fact that the third orthotropic material axis, $\boldsymbol{e}_3$, is always aligned with the global build direction. Furthermore, since the method requires complete filling, stiffness predictions for sparse or lattice-like structures must consider the local material volume fraction.

A.5 Influence of the anisotropy of thermal conductivity

Appendix A.5 presents a study investigating the influence of thermal conductivity $\boldsymbol{\kappa}$ on the prediction of a local temperature profile within a component. The multiscale approach introduced in Chapter 7 was applied for this purpose. The experiment described in Section 7.5, which served to validate the multiscale model, was used as the basis for the investigation.
In the process simulation, thermal conductivity was modeled both anisotropically (as in the validation study in Section 7.3) and isotropically. For the

[2] This Section has been previously published in [2], i.e. F. Frölich, M. E. di Nardo, C. Krauß, A. Heuer, W. V. Liebig, F. Wittemann, P. Carlone, L. Kärger. An orientation-based homogenization approach for predicting process-induced deformations in extrusion-based additive manufacturing. *Additive Manufacturing [re-submitted after major revision]*

isotropic case, two extreme values of the thermal conductivities used in the anisotropic scenario were selected based on the measurements reported in [64]:

- A lower bound of $\kappa = 0.135\,\mathrm{W/(m \cdot K)}$
- An upper bound of $\kappa = 0.195\,\mathrm{W/(m \cdot K)}$

This ensures that the full range of measured values is represented in [64].
The results are shown in Figure A.4 and Figure A.5. The lower isotropic κ leads to higher temperatures during the cooling phase, while the higher κ results in lower temperatures. The simulation with anisotropic thermal conductivity $\boldsymbol{\kappa}$ yields intermediate values. These results confirm the plausibility and consistency of the simulation. Nevertheless, the differences between the scenarios

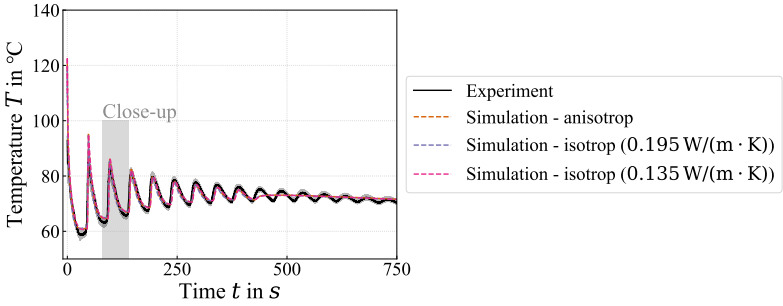

Figure A.4: Comparison of the experimentally measured local temperature profile with simulation results using anisotropic and isotropic thermal conductivities. For the isotropic case, two limiting values measured in [64] were used ($\kappa = 0.135\,\mathrm{W/(m \cdot K)}$ and $\kappa = 0.195\,\mathrm{W/(m \cdot K)}$). The shaded area indicates the zoomed-in region shown in Figure A.5.

are small. It can therefore be concluded that the anisotropy of thermal conductivity has no significant impact on the prediction of local temperature profiles. The reason for this is the low strand dimensions compared to the entire component, the low thermal conductivity of the polymer, and the fact that convection and radiation effects contribute the most to the rapid cooling behavior of the deposited strand. For the simulation of entire components, where multiple

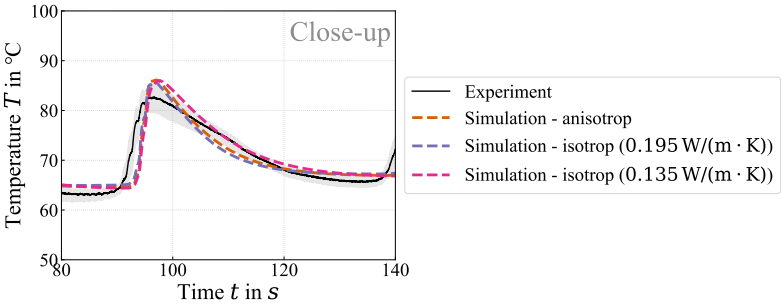

Figure A.5: Enlarged view of the highlighted region from Figure A.4, providing a detailed comparison between anisotropic and isotropic modeling of thermal conductivity. The anisotropic simulation yields temperatures between the two isotropic limit cases.

strands are aggregated within a single finite element and larger time increments are used, it is therefore reasonable to assume an isotropic thermal conductivity, using the average of the values reported in [64].

List of Figures

List of Tables

Bibliography

[1] F. Frölich, L. Bechtloff, B. M. Scheuring, A. L. Heuer, F. Wittemann, L. Kärger, and W. V. Liebig. Evaluation of mechanical properties characterization of additively manufactured components. *Progress in Additive Manufacturing*, 10(2):1217–1229, 2025.

[2] F. Frölich, M. E. Di Nardo, C. Krauß, A. Heuer, W. V. Liebig, F. Wittemann, P. Carlone, and L. Kärger. An orientation-based homogenization approach for predicting process-induced deformations in extrusion-based additive manufacturing. *Additive Manufacturing*, 113:105023, 2025.

[3] F. Frölich, D. Dörr, A. Jackstadt, F. Wittemann, and L. Kärger. Mechanical and kinetic characterization of additively manufactured PLA structures for improved process and warpage modeling. *Materials Research Proceedings*, 54:2281–2290, 2025.

[4] F. Frölich, L. Hof, C. Zimmerling, F. Wittemann, and L. Kärger. A submodeling approach for efficient prediction of local temperature profiles in component-scale additive manufacturing. *The International Journal of Advanced Manufacturing Technology*, 136(3):1561–1576, 2025.

[5] B. J. Pine. *Mass customization: the new frontier in business competition*. Harvard Business School Press, 1993.

[6] F. T. Piller. *Mass Customization: ein wettbewerbsstrategisches Konzept im Informationszeitalter*. Gabler Edition Wissenschaft Markt- und Unternehmensentwicklung. Dt. Univ.-Verl, 4., überarb. und erw. Aufl., Nachdr edition, 2008.

[7] F. Salvador, P. M. d. Holan, and F. T. Piller. Cracking the code of mass customization. *MIT Sloan Management Review*, 50(3):71–78, 2009.

[8] F. S. Fogliatto, G. J. Da Silveira, and D. Borenstein. The mass customization decade: An updated review of the literature. *International Journal of Production Economics*, 138(1):14–25, 2012.

[9] I. Paoletti. Mass Customization with Additive Manufacturing: New Perspectives for Multi Performative Building Components in Architecture. *Procedia Engineering*, 180:1150–1159, 2017.

[10] J. Savolainen and M. Collan. How Additive Manufacturing Technology Changes Business Models? – Review of Literature. *Additive Manufacturing*, 32:101070, 2020.

[11] R. Lacroix, R. W. Seifert, and A. Timonina-Farkas. Benefiting from additive manufacturing for mass customization across the product life cycle. *Operations Research Perspectives*, 8:100201, 2021.

[12] ASTM/ISO 52900. ASTM/ISO 52900:2021 - Additive Manufacturing - General Principles - Fundamentals and vocabulary. *ASTM International*, 2021(II):1–14, 2021.

[13] A. Yadav, P. Rohru, A. Babbar, R. Kumar, N. Ranjan, J. S. Chohan, R. Kumar, and M. Gupta. Fused filament fabrication: A state-of-the-art review of the technology, materials, properties and defects. *International Journal on Interactive Design and Manufacturing (IJIDeM)*, 17(6):2867–2889, 2023.

[14] X. Gao, S. Qi, X. Kuang, Y. Su, J. Li, and D. Wang. Fused filament fabrication of polymer materials: A review of interlayer bond. *Additive Manufacturing*, 37(2):101658, 2021.

[15] M. Coca-Gonzalez and M. Jimenez-Martinez. Warpage: Causes, manufacturing processes and future challenges: A review. *Proceedings of the Institution of Mechanical Engineers, Part L: Journal of Materials: Design and Applications*, 239(6):1201–1217, 2025.

[16] M. Moretti and N. Senin. In-process monitoring of part warpage in fused filament fabrication through the analysis of the repulsive force acting on the extruder. *Additive Manufacturing*, 49:102505, 2022.

[17] E. R. Fitzharris, N. Watanabe, D. W. Rosen, and M. L. Shofner. Effects of material properties on warpage in fused deposition modeling parts. *The International Journal of Advanced Manufacturing Technology*, 95(5):2059–2070, 2018.

[18] Y. Tao, F. Kong, Z. Li, J. Zhang, X. Zhao, Q. Yin, D. Xing, and P. Li. A review on voids of 3D printed parts by fused filament fabrication. *Journal of Materials Research and Technology*, 15:4860–4879, 2021.

[19] Q. Sun, G. M. Rizvi, C. T. Bellehumeur, and P. Gu. Effect of processing conditions on the bonding quality of FDM polymer filaments. *Rapid Prototyping Journal*, 14(2):72–80, 2008.

[20] N. G. Tanikella, B. Wittbrodt, and J. M. Pearce. Tensile strength of commercial polymer materials for fused filament fabrication 3D printing. *Additive Manufacturing*, 15:40–47, 2017.

[21] O. S. Es-Said, J. Foyos, R. Noorani, M. Mendelson, R. Marloth, and B. A. Pregger. Effect of layer orientation on mechanical properties of rapid prototyped samples. *Materials and Manufacturing Processes*, 15(1):107–122, 2000.

[22] H. Zhang, L. Zhang, H. Zhang, J. Wu, X. An, and D. Yang. Fibre bridging and nozzle clogging in 3D printing of discontinuous carbon fibre-reinforced polymer composites: coupled CFD-DEM modelling. *The International Journal of Advanced Manufacturing Technology*, 117(11):3549–3562, 2021.

[23] P. Guo, H. Zhang, Y. Wu, X. An, S. Jiang, K. Wu, J. Wu, and D. Yang. CFD-DEM Investigation on Effects of Fiber Deformation during 3D Printing Process Based on Fused Deposition. *Industrial & Engineering Chemistry Research*, 62(42):17052–17067, 2023.

[24] M. P. Serdeczny, R. Comminal, D. B. Pedersen, and J. Spangenberg. Numerical simulations of the mesostructure formation in material extrusion additive manufacturing. *Additive Manufacturing*, 28:419–429, 2019.

[25] H. Xia, J. Lu, S. Dabiri, and G. Tryggvason. Fully resolved numerical simulations of fused deposition modeling. Part I: fluid flow. *Rapid Prototyping Journal*, 24(2):463–476, 2018.

[26] M. Galloway, S. Hin Lam, H. Amel, R. Richardson, R. Kay, and M. Jabbari. Implementation of nozzle motion for material extrusion additive manufacturing in Ansys Fluent. *Virtual and Physical Prototyping*, 19(1):1–19, 2024.

[27] E. Barocio, B. Brenken, A. Favaloro, and R. B. Pipes. Interlayer Fusion Bonding of Semi-Crystalline Polymer Composites in Extrusion Deposition Additive Manufacturing. *Composites Science and Technology*, 230(Part 2):109334, 2022.

[28] A. Lepoivre, N. Boyard, A. Levy, and V. Sobotka. Methodology to assess interlayer quality in the material extrusion process: A temperature and adhesion prediction on a high performance polymer. *Additive Manufacturing*, 60:103167, 2022.

[29] B. Brenken, E. Barocio, A. Favaloro, V. Kunc, and R. B. Pipes. Development and validation of extrusion deposition additive manufacturing process simulations. *Additive Manufacturing*, 25:218–226, 2019.

[30] A. Trofimov, J. Le Pavic, S. Pautard, D. Therriault, and M. Lévesque. Experimentally validated modeling of the temperature distribution and the distortion during the Fused Filament Fabrication process. *Additive Manufacturing*, 54:102693, 2022.

[31] P. Castelló-Pedrero, C. García-Gascón, and J. A. García-Manrique. Multiscale numerical modeling of large-format additive manufacturing processes using carbon fiber reinforced polymer for digital twin applications. *International Journal of Material Forming*, 17(2):15, 2024.

[32] K. Yadav, S. Rohilla, A. Ali, M. Yadav, and D. Chhabra. Effect of Speed, Acceleration, and Jerk on Surface Roughness of FDM-Fabricated Parts. *Journal of Materials Engineering and Performance*, 33(14):6998–7007, 2024.

[33] S. Propst and J. Mueller. Time Code for multifunctional 3D printhead controls. *Nature Communications*, 16(1):1035, 2025.

[34] I. Gibson, D. Rosen, B. Stucker, and M. Khorasani. *Additive Manufacturing Technologies*. Springer International Publishing, Cham, 2021.

[35] S. Wenzel, E. Slomski-Vetter, and T. Melz. Optimizing System Reliability in Additive Manufacturing Using Physics-Informed Machine Learning. *Machines*, 10(7):525, 2022.

[36] Y. Zhang and S. K. Moon. Data-driven design strategy in fused filament fabrication: status and opportunities. *Journal of Computational Design and Engineering*, 8(2):489–509, 2021.

[37] E. Ferraris, J. Zhang, and B. Van Hooreweder. Thermography based in-process monitoring of Fused Filament Fabrication of polymeric parts. *CIRP Annals*, 68(1):213–216, 2019.

[38] Ultimaker. Ultimaker 2.1 Firmware. `https://github.com/Ultimaker/UM2.1-Firmware`, 2025. Accessed on August 4, 2025.

[39] Prusa Research. Prusa Firmware Buddy. `https://github.com/prusa3d/Prusa-Firmware-Buddy`, 2025. Accessed on August 4, 2025.

[40] Anisoprint. MKA Firmware. `https://github.com/anisoprint/MKA-firmware`, 2025. Accessed on August 4, 2025.

[41] M. Nofar, A. Ameli, and C. B. Park. The Thermal Behavior of Polylactide with Different D-Lactide Content in the Presence of Dissolved CO2. *Macromolecular Materials and Engineering*, 299(10):1232–1239, 2014.

[42] D. Garlotta. A Literature Review of Poly(Lactic Acid). *Journal of Polymers and the Environment*, 9(2):63–84, 2001.

[43] G. Perego, G. D. Cella, and C. Bastioli. Effect of molecular weight and crystallinity on poly(lactic acid) mechanical properties. *Journal of Applied Polymer Science*, 59(1):37–43, 1996.

[44] M. Ajioka, K. Enomoto, K. Suzuki, and A. Yamaguchi. The basic properties of poly(lactic acid) produced by the direct condensation polymerization of lactic acid. *Journal of Environmental Polymer Degradation*, 3(4):225–234, 1995.

[45] F. Carrasco, P. Pagès, J. Gámez-Pérez, O. O. Santana, and M. L. Maspoch. Processing of poly(lactic acid): Characterization of chemical structure, thermal stability and mechanical properties. *Polymer Degradation and Stability*, 95(2):116–125, 2010.

[46] S. Farah, D. G. Anderson, and R. Langer. Physical and mechanical properties of PLA, and their functions in widespread applications — A comprehensive review. *Advanced Drug Delivery Reviews*, 107:367–392, 2016.

[47] S. Jacobsen and H. G. Fritz. Plasticizing polylactide—the effect of different plasticizers on the mechanical properties. *Polymer Engineering & Science*, 39(7):1303–1310, 1999.

[48] R. Zhang, F. Du, K. Jariyavidyanont, E. Zhuravlev, C. Schick, and R. Androsch. Glass transition temperature of poly(d,l-lactic acid) of different molar mass. *Thermochimica Acta*, 718:179387, 2022.

[49] A. Celli and M. Scandola. Thermal properties and physical ageing of poly (l-lactic acid). *Polymer*, 33(13):2699–2703, 1992.

[50] Forward AM. Technical Data Sheet Ultrafuse PLA. Technical report, Mass Additive Manufacturing GmbH (a Stratasys company), 2024.

[51] J. Kechagias and S. Zaoutsos. Effects of 3D-printing processing parameters on FFF parts' porosity: outlook and trends. *Materials and Manufacturing Processes*, 39(6):804–814, 2024.

[52] Y. Tao, F. Kong, Z. Li, J. Zhang, X. Zhao, Q. Yin, D. Xing, and P. Li. A review on voids of 3D printed parts by fused filament fabrication. *Journal of Materials Research and Technology*, 15:4860–4879, 2021.

[53] X. Sun, M. Mazur, and C.-T. Cheng. A review of void reduction strategies in material extrusion-based additive manufacturing. *Additive Manufacturing*, 67:103463, 2023.

[54] J. Butt and R. Bhaskar. Investigating the effects of annealing on the mechanical properties of FFF-printed thermoplastics. *Journal of Manufacturing and Materials Processing*, 4(2):1–20, 2020.

[55] I. Ferreira, M. Machado, F. Alves, and A. Torres Marques. A review on fibre reinforced composite printing via FFF. *Rapid Prototyping Journal*, 25(6):972–988, 2019.

[56] M. Ahmadifar, K. Benfriha, M. Shirinbayan, and A. Tcharkhtchi. Additive Manufacturing of Polymer-Based Composites Using Fused Filament Fabrication (FFF): a Review. *Applied Composite Materials*, 28(5):1335–1380, 2021.

[57] A. Palacios, L. Cong, M. Navarro, Y. Ding, and C. Barreneche. Thermal conductivity measurement techniques for characterizing thermal energy storage materials – A review. *Renewable and Sustainable Energy Reviews*, 108:32–52, 2019.

[58] D. Zhao, X. Qian, X. Gu, S. A. Jajja, and R. Yang. Measurement techniques for thermal conductivity and interfacial thermal conductance of bulk and thin film materials. *Journal of Electronic Packaging*, 138(4), 2016.

[59] G. W. H. Höhne, W. F. Hemminger, and H.-J. Flammersheim. *Differential Scanning Calorimetry*. Springer Berlin Heidelberg, Berlin, Heidelberg, 2003.

[60] G. Pei, J. Xiang, G. Li, S. Wu, F. Pan, and X. Lv. A Literature Review of Heat Capacity Measurement Methods. In *10th International Symposium on High-Temperature Metallurgical Processing*, pages 569–577. Springer International Publishing, 2019.

[61] B. Wunderlich. *Thermal Analysis of Polymeric Materials*. Springer-Verlag, Berlin/Heidelberg, 2005.

[62] Deutsches Institut für Normung. DIN EN ISO 11357-4 Plastics – Differential scanning calorimetry (DSC) – Part 4: Determination of specific heat capacity. *Beuth Verlag GmbH*, 2021.

[63] S. Y. Chung, D. Stephan, M. A. Elrahman, and T. S. Han. Effects of anisotropic voids on thermal properties of insulating media investigated using 3D printed samples. *Construction and Building Materials*, 111:529–542, 2016.

[64] A. Elkholy, M. Rouby, and R. Kempers. Characterization of the anisotropic thermal conductivity of additively manufactured components by fused filament fabrication. *Progress in Additive Manufacturing*, 4(4):497–515, 2019.

[65] H. Prajapati, D. Ravoori, R. L. Woods, and A. Jain. Measurement of anisotropic thermal conductivity and inter-layer thermal contact resistance in polymer fused deposition modeling (FDM). *Additive Manufacturing*, 21:84–90, 2018.

[66] T. J. Quill, M. K. Smith, T. Zhou, M. G. S. Baioumy, J. P. Berenguer, B. A. Cola, K. Kalaitzidou, and T. L. Bougher. Thermal and mechanical properties of 3D printed boron nitride – ABS composites. *Applied Composite Materials*, 25(5):1205–1217, 2018.

[67] C. Shemelya, A. De La Rosa, A. R. Torrado, K. Yu, J. Domanowski, P. J. Bonacuse, R. E. Martin, M. Juhasz, F. Hurwitz, R. B. Wicker, B. Conner, E. MacDonald, and D. A. Roberson. Anisotropy of thermal conductivity in 3D printed polymer matrix composites for space based cube satellites. *Additive Manufacturing*, 16:186–196, 2017.

[68] L. Wang, C. Yang, X. Wang, J. Shen, W. Sun, J. Wang, G. Yang, Y. Cheng, and Z. Wang. Advances in polymers and composite dielectrics for thermal transport and high-temperature applications. *Composites Part A: Applied Science and Manufacturing*, 164:107320, 2023.

[69] V. Shanmugam, K. Babu, G. Kannan, R. A. Mensah, S. K. Samantaray, and O. Das. The thermal properties of FDM printed polymeric materials: A review. *Polymer Degradation and Stability*, 228:110902, 2024.

[70] J. Laureto, J. Tomasi, J. A. King, and J. M. Pearce. Thermal properties of 3-D printed polylactic acid-metal composites. *Progress in Additive Manufacturing*, 2(1-2):57–71, 2017.

[71] T. Flaata, G. J. Michna, and T. Letcher. Thermal Conductivity Testing Apparatus for 3D Printed Materials. In *ASME 2017 Heat Transfer Summer Conference*, Volume 2, page V002T15A006, 2017.

[72] I. Bute, S. Tarasovs, S. Vidinejevs, L. Vevere, J. Sevcenko, and A. Aniskevich. Thermal properties of 3D printed products from the most common polymers. *International Journal of Advanced Manufacturing Technology*, 124(7-8):2739–2753, 2023.

[73] L. Lendvai, I. Fekete, D. Rigotti, and A. Pegoretti. Experimental study on the effect of filament-extrusion rate on the structural, mechanical and thermal properties of material extrusion 3D-printed polylactic acid (PLA) products. *Progress in Additive Manufacturing*, 10(1):619–629, 2024.

[74] F. P. Incropera, D. P. DeWitt, T. L. Bergman, and A. S. Lavine, editors. *Fundamentals of heat and mass transfer*. Wiley, 6. ed edition, 2007.

[75] M. Pyda, R. Bopp, and B. Wunderlich. Heat capacity of poly(lactic acid). *The Journal of Chemical Thermodynamics*, 36(9):731–742, 2004.

[76] N. Hill and M. Haghi. Deposition direction-dependent failure criteria for fused deposition modeling polycarbonate. *Rapid Prototyping Journal*, 20(3):221–227, 2014.

[77] P. K. Penumakala, J. Santo, and A. Thomas. A critical review on the fused deposition modeling of thermoplastic polymer composites. *Composites Part B: Engineering*, 201, 2020.

[78] E. Cuan-Urquizo, E. Barocio, V. Tejada-Ortigoza, R. B. Pipes, C. A. Rodriguez, and A. Roman-Flores. Characterization of the mechanical properties of FFF structures and materials: A review on the experimental, computational and theoretical approaches. *Materials*, 12(6), 2019.

[79] J. Allum, A. Gleadall, and V. V. Silberschmidt. Fracture of 3D-printed microtensile specimens: Filament-scale geometry-induced anisotropy. *Procedia Structural Integrity*, 28(2019):591–601, 2020.

[80] A. Heuer, J. Huether, W. V. Liebig, and P. Elsner. Fused filament fabrication: comparison of methods for determining the interfacial strength of single welded tracks. *Manufacturing Review*, 8:32, 2021.

[81] Deutsches Institut für Normung. DIN EN ISO 527-2 Plastics –Determination of tensile properties – Part 2: Test conditions for moulding and extrusion plastics. *Beuth Verlag GmbH*, page 14, 2012.

[82] ASTM International. ASTM D638 Standard Test Method for Tensile Properties of Plastics. *Annual Book of ASTM Standards*, page 16, 2022.

[83] J. J. Laureto and J. M. Pearce. Anisotropic mechanical property variance between ASTM D638-14 type I and type IV fused filament fabricated specimens. *Polymer Testing*, 68:294–301, 2018.

[84] Y. Zhang, J. P. Choi, and S. K. Moon. Effect of geometry on the mechanical response of additively manufactured polymer. *Polymer Testing*, 100:107245, 2021.

[85] S. J. Park, J. E. Lee, S. C. Jin, N.-K. Lee, K. Choi, S.-H. Park, and Y. Son. Tensile test of additively manufactured specimens with external notch removed via laser cutting in material extrusion. *Polymer Testing*, 110:107581, 2022.

[86] ASTM International. ASTM D2990-17 Test Methods for Tensile, Compressive, and Flexural Creep and Creep-Rupture of Plastics. *Annual Book of ASTM Standards*, pages 1–21, 2017.

[87] Deutsches Institut für Normung. DIN EN ISO 527-1 Plastics – Determination of tensile properties – Part 1: General principles. *Beuth Verlag GmbH*, page 33, 2012.

[88] Deutsches Institut für Normung. DIN EN ISO 527-2 Plastics – Determination of tensile properties – Part 2: Test conditions for moulding and extrusion plastics. *Beuth Verlag GmbH*, page 14, 2012.

[89] Deutsches Institut für Normung. DIN EN ISO 527-4 Plastics – Determination of tensile properties – Part 4: Test conditions for isotropic and orthotropic fibre-reinforced plastic composites. *Beuth Verlag GmbH*, page 34, 2023.

[90] Deutsches Institut für Normung. DIN EN ISO 527-5 Plastics – Determination of tensile properties – Part 5: Test conditions for unidirectional fibre-reinforced plastic composites. *Beuth Verlag GmbH*, page 22, 2022.

[91] ASTM International. ASTM D4065 Standard Practice for Plastics : Dynamic Mechanical Properties : Determination and. *Annual Book of ASTM Standards*, pages 1–7, 2020.

[92] Deutsches Institut für Normung. DIN EN ISO 6721-1 Plastics – Determination of dynamic mechanical properties – Part 1: General principles. *Beuth Verlag GmbH*, page 30, 2019.

[93] Deutsches Institut für Normung. DIN EN ISO 6721-2 Plastics – Determination of dynamic mechanical properties – Part 2: Torsion-pendulum method. *Beuth Verlag GmbH*, page 17, 2019.

[94] Deutsches Institut für Normung. DIN EN ISO 6721-3 Plastics – Determination of dynamic mechanical properties – Part 3: Flexural vibration – Resonance curve method. *Beuth Verlag GmbH*, page 18, 2021.

[95] ASTM International. ASTM E831 Standard Test Method for Linear Thermal Expansion of Solid Materials by Thermomechanical Analysis. *Annual Book of ASTM Standards*, page 5, 2024.

[96] M. Bertoldi, M. a. Yardimci, C. M. Pistor, S. I. Guceri, and G. Sala. Mechanical characterization of parts processed via fused deposition. *Solid Freeform Fabrication Proceedings*, pages 557–565, 1998.

[97] S. H. Ahn, M. Montero, D. Odell, S. Roundy, and P. K. Wright. Anisotropic material properties of fused deposition modeling ABS. *Rapid Prototyping Journal*, 8(4):248–257, 2002.

[98] H. Gonabadi, A. Yadav, and S. J. Bull. The effect of processing parameters on the mechanical characteristics of PLA produced by a 3D FFF printer. *International Journal of Advanced Manufacturing Technology*, 111(3-4):695–709, 2020.

[99] A. Hasan, M. Fahad, and M. A. Khan. Effect of print parameters on the tensile strength and built time of FDM-printed PLA parts. *International Journal of Advanced Manufacturing Technology*, 132(5-6):3047–3065, 2024.

[100] A. Bellini and S. Güçeri. Mechanical characterization of parts fabricated using fused deposition modeling. *Rapid Prototyping Journal*, 9(4):252–264, 2003.

[101] C. Casavola, A. Cazzato, V. Moramarco, and C. Pappalettere. Orthotropic mechanical properties of fused deposition modelling parts described by classical laminate theory. *Materials & Design*, 90:453–458, 2016.

[102] M. Domingo-Espin, S. Borros, N. Agullo, A. A. Garcia-Granada, and G. Reyes. Influence of Building Parameters on the Dynamic Mechanical Properties of Polycarbonate Fused Deposition Modeling Parts. *3D Printing and Additive Manufacturing*, 1(2):70–77, 2014.

[103] R. T. L. Ferreira, I. C. Amatte, T. A. Dutra, and D. Bürger. Experimental characterization and micrography of 3D printed PLA and PLA reinforced with short carbon fibers. *Composites Part B: Engineering*, 124:88–100, 2017.

[104] S. Dai, Z. C. Deng, Y. J. Yu, K. Zhang, S. H. Wang, and J. Ye. Orthotropic elastic behaviors and yield strength of fused deposition modeling materials: Theory and experiments. *Polymer Testing*, 87:106520, 2020.

[105] R. Torre and S. Brischetto. Experimental characterization and finite element validation of orthotropic 3D-printed polymeric parts. *International Journal of Mechanical Sciences*, 219:107095, 2022.

[106] J.-A. Tröger, C. Steinweller, and S. Hartmann. Identification, uncertainty quantification and validation of orthotropic material properties for additively manufactured polymers. *Mechanics of Materials*, 197:105100, 2024.

[107] M. Somireddy and A. Czekanski. Anisotropic material behavior of 3D printed composite structures – Material extrusion additive manufacturing. *Materials and Design*, 195:108953, 2020.

[108] M. F. Afrose, S. H. Masood, M. Nikzad, and P. Iovenitti. Effects of build orientations on tensile properties of PLA material processed by FDM. *Advanced Materials Research*, 1044-1045:31–34, 2014.

[109] J. M. Chacón, M. A. Caminero, E. García-Plaza, and P. J. Núñez. Additive manufacturing of PLA structures using fused deposition modelling: Effect of process parameters on mechanical properties and their optimal selection. *Materials and Design*, 124:143–157, 2017.

[110] T. Gajjar, R. C. Yang, L. Ye, and Y. X. Zhang. Effects of key process parameters on tensile properties and interlayer bonding behavior of 3D printed PLA using fused filament fabrication. *Progress in Additive Manufacturing*, 10(2):1261–1280, 2025.

[111] A. Lanzotti, M. Grasso, G. Staiano, and M. Martorelli. The impact of process parameters on mechanical properties of parts fabricated in PLA with an open-source 3-D printer. *Rapid Prototyping Journal*, 21(5):604–617, 2015.

[112] S. Pachauri, N. K. Gupta, and A. Gupta. Influence of 3D printing process parameters on the mechanical properties of polylactic acid (PLA) printed with fused filament fabrication: experimental and statistical analysis. *International Journal on Interactive Design and Manufacturing (IJIDeM)*, 19(2):1159–1177, 2025.

[113] W. M. Verbeeten, M. Lorenzo-Bañuelos, and P. J. Arribas-Subiñas. Anisotropic rate-dependent mechanical behavior of Poly(Lactic Acid) processed by Material Extrusion Additive Manufacturing. *Additive Manufacturing*, 31:100968, 2020.

[114] S. Wang, Y. Ma, Z. Deng, S. Zhang, and J. Cai. Effects of fused deposition modeling process parameters on tensile, dynamic mechanical properties of 3D printed polylactic acid materials. *Polymer Testing*, 86:106483, 2020.

[115] Y. Zhao, Y. Chen, and Y. Zhou. Novel mechanical models of tensile strength and elastic property of FDM AM PLA materials: Experimental and theoretical analyses. *Materials and Design*, 181:108089, 2019.

[116] R. R. Shilpesh and D. K. Harshit. Effect of process parameters on tensile strength of FDM printed PLA part. *Rapid Prototyping Journal*, 24(8):1317–1324, 2018.

[117] V. E. Kuznetsov, A. N. Solonin, O. D. Urzhumtsev, R. Schilling, and A. G. Tavitov. Strength of PLA components fabricated with fused deposition technology using a desktop 3D printer as a function of geometrical parameters of the process. *Polymers*, 10(3), 2018.

[118] B. M. Tymrak, M. Kreiger, and J. M. Pearce. Mechanical properties of components fabricated with open-source 3-D printers under realistic environmental conditions. *Materials and Design*, 58:242–246, 2014.

[119] T. Fisher, J. H. S. Almeida, B. G. Falzon, and Z. Kazancı. Tension and Compression Properties of 3D-Printed Composites: Print Orientation and Strain Rate Effects. *Polymers*, 15(7):1–15, 2023.

[120] J. Luo, Q. Luo, G. Zhang, Q. Li, and G. Sun. On strain rate and temperature dependent mechanical properties and constitutive models for additively manufactured polylactic acid (PLA) materials. *Thin-Walled Structures*, 179:109624, 2022.

[121] M. Petousis, I. Ntintakis, C. David, D. Sagris, N. K. Nasikas, A. Korlos, A. Moutsopoulou, and N. Vidakis. A Coherent Assessment of the Compressive Strain Rate Response of PC, PETG, PMMA, and TPU Thermoplastics in MEX Additive Manufacturing. *Polymers*, 15(19), 2023.

[122] V. Slavković, B. Hanželič, V. Plesec, S. Milenković, and G. Harih. Thermo-Mechanical Behavior and Strain Rate Sensitivity of 3D-Printed Polylactic Acid (PLA) below Glass Transition Temperature (Tg). *Polymers*, 16(11), 2024.

[123] N. Vidakis, M. Petousis, E. Velidakis, M. Liebscher, V. Mechtcherine, and L. Tzounis. On the strain rate sensitivity of fused filament fabrication (Fff) processed pla, abs, petg, pa6, and pp thermoplastic polymers. *Polymers*, 12(12):1–15, 2020.

[124] N. Vidakis, M. Petousis, A. Korlos, E. Velidakis, N. Mountakis, C. Charou, and A. Myftari. Strain rate sensitivity of polycarbonate and thermoplastic polyurethane for various 3d printing temperatures and layer heights. *Polymers*, 13(16), 2021.

[125] R. K. Dhanapal, V. Alagumalai, and V. Shanmugam. Exploring the dynamic mechanical properties of fused filament fabrication printed polyetheretherketone with various infill patterns. *Progress in Additive Manufacturing*, 10(4):2911–2926, 2024.

[126] N. Giani, L. Mazzocchetti, T. Benelli, F. Picchioni, and L. Giorgini. Towards sustainability in 3D printing of thermoplastic composites: Evaluation of recycled carbon fibers as reinforcing agent for FDM filament production and 3D printing. *Composites Part A: Applied Science and Manufacturing*, 159:107002, 2022.

[127] B. Huang, S. H. Masood, M. Nikzad, P. R. Venugopal, and A. Arivazhagan. Dynamic mechanical properties of fused deposition modelling processed polyphenylsulfone material. *American Journal of Engineering and Applied Sciences*, 9(1):1–11, 2015.

[128] C. Jameson, D. M. Devine, G. Keane, and N. M. Gately. A Comparative Analysis of Mechanical Properties in Injection Moulding (IM), Fused Filament Fabrication (FFF), and Arburg Plastic Freeforming (APF) Processes. *Polymers*, 17(7):990, 2025.

[129] O. A. Mohamed, S. H. Masood, and J. L. Bhowmik. Experimental Investigations of Process Parameters Influence on Rheological Behavior and Dynamic Mechanical Properties of FDM Manufactured Parts. *Materials and Manufacturing Processes*, 31(15):1983–1994, 2016.

[130] M. A. Ramirez, E. Barocio, J. T. Tsai, and R. B. Pipes. Temperature-Dependent Mechanical Properties of Additive Manufactured Carbon Fiber Reinforced Polyethersulfone. *Applied Composite Materials*, 29(6):2293–2319, 2022.

[131] J. Pu, C. McIlroy, A. Jones, and I. Ashcroft. Understanding mechanical properties in fused filament fabrication of polyether ether ketone. *Additive Manufacturing*, 37:101673, 2021.

[132] J. Struz, M. Trochta, L. Hruzik, D. Pistacek, S. Stawarz, W. Kucharczyk, and M. Rucki. Wear and Dynamic Mechanical Analysis (DMA) of Samples Produced via Fused Deposition Modelling (FDM) 3D Printing Method. *Polymers*, 16(21):3018, 2024.

[133] S. Thumsorn, W. Prasong, T. Kurose, A. Ishigami, Y. Kobayashi, and H. Ito. Rheological Behavior and Dynamic Mechanical Properties for Interpretation of Layer Adhesion in FDM 3D Printing. *Polymers*, 14(13):1–22, 2022.

[134] M. Aberoumand, D. Rahmatabadi, K. Soltanmohammadi, E. Soleyman, I. Ghasemi, M. Baniassadi, K. Abrinia, M. Bodaghi, and M. Baghani. Stress recovery and stress relaxation behaviors of PVC 4D printed by FDM technology for high-performance actuation applications. *Sensors and Actuators A: Physical*, 361:114572, 2023.

[135] T. Kozior and C. Kundera. Evaluation of the Influence of Parameters of FDM Technology on the Selected Mechanical Properties of Models. *Procedia Engineering*, 192:463–468, 2017.

[136] P. N. Reis, S. Valvez, and J. A. Ferreira. Creep and stress relaxation behaviour of 3D printed nanocomposites. *Procedia Structural Integrity*, 37(C):934–940, 2022.

[137] Y. C. Niranjan, S. Krishnapillai, R. Velmurugan, and S. K. Ha. Effect of Annealing Time and Temperature on Dynamic Mechanical Properties of FDM Printed PLA. In S. Krishnapillai, R. Velmurugan, and S. K. Ha, editors, *Composite Materials for Extreme Loading*, pages 143–160. Springer Singapore, Singapore, 2022.

[138] A. M. Baker, J. McCoy, B. S. Majumdar, B. Rumley-Ouellette, J. Wahry, A. N. Marchi, J. D. Bernardin, and D. Spernjak. Measurement and Modelling of Thermal and Mechanical Anisotropy of Parts Additively Manufactured Using Fused Deposition Modelling (FDM). In *Proceedings of the Eleventh International Workshop on Structural Health Monitoring*, Stanford, CA, September 2017.

[139] M. Bharvirkar, P. Nguyen, and C. Pistor. Thermo-mechanical analysis of parts fabricated via Fused Deposition Modeling (FDM). *Solid Freeform Fabrication Proceedings*, pages 343–350, 1999.

[140] B. Rădulescu, A. M. Mihalache, A. Hrițuc, M. Rădulescu, L. Slătineanu, A. Munteanu, O. Dodun, and G. Nagîț. Thermal Expansion of Plastics Used for 3D Printing. *Polymers*, 14(15):1–17, 2022.

[141] O. Huseynov, S. Hasanov, and I. Fidan. Influence of the matrix material on the thermal properties of the short carbon fiber reinforced polymer composites manufactured by material extrusion. *Journal of Manufacturing Processes*, 92:521–533, 2023.

[142] M. F. Arif, H. Alhashmi, K. M. Varadarajan, J. H. Koo, A. J. Hart, and S. Kumar. Multifunctional performance of carbon nanotubes and graphene nanoplatelets reinforced PEEK composites enabled via FFF additive manufacturing. *Composites Part B: Engineering*, 184:107625, 2020.

[143] H. Wu and L. T. Drzal. Effect of graphene nanoplatelets on coefficient of thermal expansion of polyetherimide composite. *Materials Chemistry and Physics*, 146(1-2):26–36, 2014.

[144] J. L. Faust, P. G. Kelly, B. D. Jones, and J. D. Roy-Mayhew. Effects of coefficient of thermal expansion and moisture absorption on the dimensional accuracy of carbon-reinforced 3D printed parts. *Polymers*, 13(21), 2021.

[145] I. M. Kalogeras. Glass-Transition Phenomena in Polymer Blends. In *Encyclopedia of Polymer Blends*, pages 1–134. Wiley Online Books, 2016.

[146] ASTM International. ASTM D3418 Standard Test Method for Transition Temperatures and Enthalpies of Fusion and Crystallization of Polymers by Differential Scanning. *Annual Book of ASTM Standards*, pages 1–7, 2012.

[147] Deutsches Institut für Normung. DIN EN ISO 11357-1 Plastics – Differential scanning calorimetry (DSC) – Part 1: General principles. *Beuth Verlag GmbH*, 2023.

[148] Deutsches Institut für Normung. DIN EN ISO 11357-2 Plastics – Differential scanning calorimetry (DSC) – Part 2: Determination of glass transition temperature and step height. *Beuth Verlag GmbH*, 2020.

[149] Deutsches Institut für Normung. DIN EN ISO 11357-3 Plastics – Differential scanning calorimetry (DSC) – Part 3: Determination of temperature and enthalpy of melting and crystallization. *Beuth Verlag GmbH*, 2018.

[150] F. Yang and R. Pitchumani. Healing of thermoplastic polymers at an interface under nonisothermal conditions. *Macromolecules*, 35(8):3213–3224, 2002.

[151] D. Yang, K. Wu, L. Wan, and Y. Sheng. A Particle Element Approach for Modelling the 3D Printing Process of Fibre Reinforced Polymer Composites. *Journal of Manufacturing and Materials Processing*, 1(1):10, 2017.

[152] K.-I. Kanatani. Distribution of directional data and fabric tensors. *International journal of engineering science*, 22(2):149–164, 1984.

[153] S. G. Advani and C. L. Tucker. The Use of Tensors to Describe and Predict Fiber Orientation in Short Fiber Composites. *Journal of Rheology*, 31(8):751–784, 1987.

[154] N. N. Kermani, S. G. Advani, and J. Férec. Orientation predictions of fibers within 3D printed strand in material extrusion of polymer composites. *Additive Manufacturing*, 77:103781, 2023.

[155] B. P. Heller, D. E. Smith, and D. A. Jack. Effects of extrudate swell and nozzle geometry on fiber orientation in Fused Filament Fabrication nozzle flow. *Additive Manufacturing*, 12:252–264, 2016.

[156] B. Šeta, M. Sandberg, M. Brander, M. T. Mollah, D. K. Pokkalla, V. Kumar, and J. Spangenberg. Numerical modeling of fiber orientation in multi-layer, isothermal material-extrusion big area additive manufacturing. *Additive Manufacturing*, 92:104396, 2024.

[157] E. Bertevas, J. Férec, B. C. Khoo, G. Ausias, and N. Phan-Thien. Smoothed particle hydrodynamics (SPH) modeling of fiber orientation in a 3D printing process. *Physics of Fluids*, 30(10), 2018.

[158] P. Pibulchinda, E. Barocio, A. J. Favaloro, and R. B. Pipes. Influence of printing conditions on the extrudate shape and fiber orientation in extrusion deposition additive manufacturing. *Composites Part B: Engineering*, 261:110793, 2023.

[159] M. T. Mollah, A. Moetazedian, A. Gleadall, J. Yan, W. E. Alphonso, R. Comminal, B. Seta, T. Lock, and J. Spangenberg. Investigation on Corner Precision at Different Corner Angles in Material Extrusion Additive Manufacturing: An Experimental and Computational Fluid Dynamics Analysis. In *Proceedings of*

the Solid Freeform Fabrication Symposium 2022: 33rd Annual Meeting, pages 872–881, Austin, Texas, United States, 2022. University of Texas at Austin.

[160] A. Pricci and G. Percoco. Towards a Digital Twin of Extrusion-Based Additive Manufacturing: An Experimentally Validated Numerical Model of Ironing Process. *Progress in Additive Manufacturing*, 10(9):6491–6506, 2025.

[161] M. Makino, D. Fukuzawa, T. Murashima, M. Kawakami, and H. Furukawa. Analysis of deposition modeling by particle method simulation. *Microsystem Technologies*, 23(5):1177–1181, 2017.

[162] Z. Ouyang, E. Bertevas, D. Wang, B. C. Khoo, J. Férec, G. Ausias, and N. Phan-Thien. A smoothed particle hydrodynamics study of a non-isothermal and thermally anisotropic fused deposition modeling process for a fiber-filled composite. *Physics of Fluids*, 32(5), 2020.

[163] J.-F. Agassant, F. Pigeonneau, L. Sardo, and M. Vincent. Flow analysis of the polymer spreading during extrusion additive manufacturing. *Additive Manufacturing*, 29:100794, 2019.

[164] P. Pibulchinda, E. Barocio, C. V. Evans, and R. B. Pipes. Intralayer fusion bonding of additive manufactured fiber-reinforced polymer composites. *Composites Part A: Applied Science and Manufacturing*, 195:108941, 2025.

[165] M. E. Yildizdag. Numerical modeling and simulation of material extrusion-based 3-D printing processes with a material point method framework. *Continuum Mechanics and Thermodynamics*, 36(5):1361–1378, 2023.

[166] J. Meng, J. Liu, H. Xia, X. Ao, and W. Zhang. A reduced-order model of thermo-viscoelastic filaments in a material extrusion process. *Additive Manufacturing*, 91:104343, 2024.

[167] A. Elmoghazy, A. Heuer, A. Kneer, M. Reder, A. Prahs, D. Schneider, W. V. Liebig, and B. Nestler. Phase-field Modeling of the Morphological and Thermal Evolution of Additively Manufactured Polylactic Acid Layers and Their Influence on the Effective Elastic Mechanical Properties. *Progress in Additive Manufacturing*, 10(8):5093–5115, 2025.

[168] A. Benarbia, V. Sobotka, N. Boyard, and C. Roua. Fused filament fabrication: Numerical adhesion modeling suitable for semicrystalline polymers. *Materials Research Proceedings*, 28:139–148, 2023.

[169] Y. Mahmoud, J. Lyu, J. Akhavan, K. Xu, and S. Manoochehri. Thermal history based prediction of interlayer bond strength in parts manufactured by material extrusion additive manufacturing. *International Journal of Advanced Manufacturing Technology*, 126(9-10):3813–3829, 2023.

[170] T. J. Coogan and D. O. Kazmer. Prediction of interlayer strength in material extrusion additive manufacturing. *Additive Manufacturing*, 35:101368, 2020.

[171] A. A. Oskolkov, I. I. Bezukladnikov, and D. N. Trushnikov. Mathematical Model of the Layer-by-Layer FFF/FGF Polymer Extrusion Process for Use in the Algorithm of Numerical Implementation of Real-Time Thermal Cycle Control. *Polymers*, 15(23):4518, 2023.

[172] H. Xia, J. Lu, and G. Tryggvason. Fully resolved numerical simulations of fused deposition modeling. Part II – solidification, residual stresses and modeling of the nozzle. *Rapid Prototyping Journal*, 24(6):973–987, 2018.

[173] H. Xia, J. Lu, and G. Tryggvason. A numerical study of the effect of viscoelastic stresses in fused filament fabrication. *Computer Methods in Applied Mechanics and Engineering*, 346:242–259, 2019.

[174] M. Lukhi, C. Mittermeier, and J. Kiendl. Multi-physics simulation of a material extrusion-based additive manufacturing process: towards understanding stress formation in the printed strand. *Progress in Additive Manufacturing*, 10(9):6839–6853, 2025.

[175] B. Brenken, A. Favaloro, E. Barocio, and B. Pipes. Development of a Model to Predict Temperature History and Crystallization Behavior of 3D-Printed Parts Made from Fiber-Reinforced Thermoplastic Polymers. In *SAMPE Conference Proceedings*, Long Beach, CA, May 2016. Society for the Advancement of Material and Process Engineering, Purdue University.

[176] K. Nakamura, T. Watanabe, K. Katayama, and T. Amano. Some aspects of nonisothermal crystallization of polymers. I. Relationship between crystallization

temperature, crystallinity, and cooling conditions. *Journal of Applied Polymer Science*, 16(5):1077–1091, 1972.

[177] K. Nakamura, K. Katayama, and T. Amano. Some aspects of nonisothermal crystallization of polymers. II. Consideration of the isokinetic condition. *Journal of Applied Polymer Science*, 17(4):1031–1041, 1973.

[178] K. Nakamura, T. Watanabe, T. Amano, and K. Katayama. Some aspects of nonisothermal crystallization of polymers. III. Crystallization during melt spinning. *Journal of Applied Polymer Science*, 18(2):615–623, 1974.

[179] C. McIlroy and R. S. Graham. Modelling flow-enhanced crystallisation during fused filament fabrication of semi-crystalline polymer melts. *Additive Manufacturing*, 24:323–340, 2018.

[180] A. E. Likhtman and R. S. Graham. Simple constitutive equation for linear polymer melts derived from molecular theory: Rolie–Poly equation. *Journal of Non-Newtonian Fluid Mechanics*, 114(1):1–12, 2003.

[181] Y. Zhang and Y. K. Chou. Three-dimensional finite element analysis simulations of the fused deposition modelling process. *Proceedings of the Institution of Mechanical Engineers, Part B: Journal of Engineering Manufacture*, 220(10):1663–1671, 2006.

[182] Y. Zhang and K. Chou. A parametric study of part distortions in fused deposition modelling using three-dimensional finite element analysis. *Proceedings of the Institution of Mechanical Engineers, Part B: Journal of Engineering Manufacture*, 222(8):959–967, 2008.

[183] Dassault Systèmes Simulia Corp. *SIMULIA User Assistance - About Additive Manufacturing Process Simulation*, 2024. Version 2024. Accessed: May 23, 2025. Available at: `https://help.3ds.com/2024/english/DSSIMULIA_Established/SIMACAEANLRefMap/simaanl-c-amabout.htm?contextscope=all`.

[184] B. Courter, V. Savane, J. Bi, S. Dev, and C. J. Hansen. Finite Element Simulation of the Fused Deposition Modelling Process. In *Proceedings of NAFEMS World Congress*, Stockholm, Sweden, June 2017. NAFEMS.

[185] Hexagon AB and/or its subsidiaries. *Digimat-AM User Guide*, 2023. Version 2023.3. Accessed: May 23, 2025. Available at: `https://documentation-be.hexagon.com/bundle/Digimat_2023.3_AM_User_Guide/raw/resource/enus/Digimat_2023.3_AM_User_Guide.pdf`.

[186] ANSYS, Inc. *DED Simulation Guide*, 2025. Release 2025 R1. Accessed: June 03, 2025. Available at: `https://ansyshelp.ansys.com/public/account/secured?returnurl=/Views/Secured/corp/v251/en/add_ded/add_ded.html`.

[187] G. Chen, D. Wang, W. Hua, W. Wu, W. Zhou, Y. Jin, and W. Zheng. Simulating and Predicting the Part Warping in Fused Deposition Modeling by Thermal-Structural Coupling Analysis. *3D Printing and Additive Manufacturing*, 10(1):70–82, 2023.

[188] A. Al Rashid and M. Koç. Experimental validation of numerical model for thermomechanical performance of material extrusion additive manufacturing process: Effect of infill design & density. *Results in Engineering*, 17:100860, 2023.

[189] A. Sahu, S. S. Gorthi, and M. Arora. Warpage Estimation in Fused Filament Fabrication of ABS Parts Using Finite Element Method. In A. Chakrabarti and V. Singh, editors, *Design in the Era of Industry 4.0, Volume 2*, pages 903–913. Springer Nature Singapore, Singapore, 2023.

[190] H. Tanabi, W. Ndacyayisenga, and M. Ghaziani. A multi-objective investigation of warpage and mechanical performance in FDM-printed thermoplastic composites. *Journal of Composite Materials*, 59(21):2465–2483, 2025.

[191] H. Yang and S. Zhang. Numerical simulation of temperature field and stress field in fused deposition modeling. *Journal of Mechanical Science and Technology*, 32(7):3337–3344, 2018.

[192] B. Jiang, Y. Chen, L. Ye, L. Chang, and H. Dong. Residual stress and warpage of additively manufactured SCF/PLA composite parts. *Advanced Manufacturing: Polymer & Composites Science*, 9(1):2171940, 2023.

[193] A. El Moumen, M. Tarfaoui, and K. Lafdi. Modelling of the temperature and residual stress fields during 3D printing of polymer composites. *International Journal of Advanced Manufacturing Technology*, 104(5-8):1661–1676, 2019.

[194] J. Wang and P. Papadopoulos. Coupled thermomechanical analysis of fused deposition using the finite element method. *Finite Elements in Analysis and Design*, 197:103607, 2021.

[195] Y. Zhou, H. Lu, G. Wang, J. Wang, and W. Li. Voxelization modelling based finite element simulation and process parameter optimization for Fused Filament Fabrication. *Materials and Design*, 187:108409, 2020.

[196] B. Brenken. *Extrusion deposition additive manufacturing of fiber reinforced semi-crystalline polymers*. PhD thesis, Purdue University, School of Aeronautics & Astronautics, West Lafayette, Indiana, USA, 2017.

[197] A. A. Samy, A. Golbang, E. Harkin-Jones, E. Archer, and A. McIlhagger. Prediction of part distortion in Fused Deposition Modelling (FDM) of semi-crystalline polymers via COMSOL: Effect of printing conditions. *CIRP Journal of Manufacturing Science and Technology*, 33:443–453, 2021.

[198] A. Cattenone, S. Morganti, G. Alaimo, and F. Auricchio. Finite element analysis of additive manufacturing based on fused deposition modeling: Distortions prediction and comparison with experimental data. *Journal of Manufacturing Science and Engineering, Transactions of the ASME*, 141(1):1–17, 2019.

[199] A. Corvi, L. Collini, C. Sciancalepore, and A. Lutey. Influence of process parameters on temperature field and residual strain in FFF-printed parts. *Journal of Mechanical Science and Technology*, 37(11):5521–5527, 2023.

[200] J. Han, J. Tong, X. Tian, L. Xia, and D. Ma. Thermal Simulation and Warping Deformation Experimental Study of PEEK in Material Extrusion. *Macromolecular Theory and Simulations*, 30(2):1–13, 2021.

[201] B. Brenken, A. Favaloro, E. Barocio, V. Kunc, and R. B. Pipes. Thermoviscoelasticity in Extrusion Deposition Additive Manufacturing Process Simulations. In *American Society for Composites 2017*, Lancaster, PA, 2017. DEStech Publications, Inc.

[202] Q. Xia, G. Sun, J. Kim, and Y. Li. Multi-scale modeling and simulation of additive manufacturing based on fused deposition technique. *Physics of Fluids*, 35(3):034116, 2023.

[203] P. Kulkarni and D. Dutta. Deposition Strategies and Resulting Part Stiffnesses in Fused Deposition Modeling. *Journal of Manufacturing Science and Engineering*, 121(1):93–103, 1999.

[204] L. Li, Q. Sun, C. Bellehumeur, and P. Gu. Composite Modeling and Analysis for Fabrication of FDM Prototypes with Locally Controlled Properties. *Journal of Manufacturing Processes*, 4(2):129–141, 2002.

[205] C. Ziemian, R. Ziemian, and K. Haile. Characterization of stiffness degradation caused by fatigue damage of additive manufactured parts. *Materials & Design*, 109:209–218, 2016.

[206] L. Sánchez-Balanzar, F. Velázquez-Villegas, L. Ruiz-Huerta, and A. Caballero-Ruiz. A multiscale analysis approach to predict mechanical properties in fused deposition modeling parts. *The International Journal of Advanced Manufacturing Technology*, 115(7):2269–2279, 2021.

[207] S. Sharafi, M. Santare, J. Gerdes, and S. Advani. A multiscale modeling approach of the Fused Filament Fabrication process to predict the mechanical response of 3D printed parts. *Additive Manufacturing*, 51:102597, 2022.

[208] M. Lei, Y. Wang, Q. Wei, M. Li, J. Zhang, and Y. Wang. Micromechanical modeling and numerical homogenization calculation of effective stiffness of 3D printing PLA/CF composites. *Journal of Manufacturing Processes*, 102:37–49, 2023.

[209] A. Nasirov, S. Hasanov, and I. Fidan. Prediction of Mechanical Properties of Fused Deposition Modeling Made Parts using Multiscale Modeling and Classical Laminate Theory. *Solid Freeform Fabrication 2019: Proceedings of the 30th Annual International Solid Freeform Fabrication Symposium – An Additive Manufacturing Conference; Austin, TX*, pages 1373–1382, 2019.

[210] X. Liu and V. Shapiro. Homogenization of material properties in additively manufactured structures. *Computer-Aided Design*, 78:71–82, 2016.

[211] E. Barocio. *Fusion Bonding of Fiber Reinforced Semi-Crystalline Polymers in Extrusion Deposition Additive Manufacturing*. Phd thesis, Purdue University, School of Materials Engineering, West Lafayette, Indiana, USA, 2017.

[212] J. Knirsch, F. Frölich, L. Hof, F. Wittemann, and L. Kärger. pyGCodeDecode: A Python package for time-accurate GCode simulation in material extrusion processes. *Journal of Open Source Software*, 9(99):6465, 2024.

[213] J. Knirsch, F. Frölich, L. Hof, F. Wittemann, and L. Kärger. pyGCodeDecode (1.1.0). Zenodo, 2024. https://doi.org/10.5281/zenodo.13747299.

[214] MarlinFirmware Contributors. Marlin Firmware. https://github.com/MarlinFirmware, 2025. Accessed on August 4, 2025.

[215] GRBL Project Contributors. GRBL Firmware. https://github.com/grbl/grbl/tree/master, 2025. Accessed on August 4, 2025.

[216] Prusa Research. planner.cpp - Motion planning module in Prusa Firmware (line 195). https://github.com/prusa3d/Prusa-Firmware-Buddy/blob/818d812f954802903ea0ff39bf44376fb0b35dd2/lib/Marlin/Marlin/src/module/planner.cpp#L195, 2021. Accessed on August 4, 2025.

[217] Ultimaker. planner.cpp - Motion planning module in Ultimaker Firmware (line 840). https://github.com/Ultimaker/UM2.1-Firmware/blob/f6e69344c00d7f300dace730990652ba614a2105/Marlin/planner.cpp#L840, 2016. Accessed on August 4, 2025.

[218] Anisoprint. planner.cpp - Junction Handling in MKA Firmware (line 1830). https://github.com/anisoprint/MKA-firmware/blob/6e02973b1b8f325040cc3dbf66ac545ffc5c06b3/src/core/planner/planner.cpp#L1830, 2025. Accessed on August 4, 2025.

[219] MarlinFirmware. planner.cpp - Motion planning module in Marlin Firmware (line 2762). https://github.com/MarlinFirmware/Marlin/blob/8ec9c379405bb9962aff170d305ddd0725bd64e2/Marlin/src/module/planner.cpp#L2762, 2023. Accessed on August 4, 2025.

[220] chilipeppr. Add support for PWM spindle speed control. https://github.com/grbl/grbl/pull/47/files, 2014. GitHub Pull Request #47, accessed on August 4, 2025.

[221] Onehossshay. Improving GRBL Cornering Algorithm. `https://onehossshay.wordpress.com/2011/09/24/improving_grbl_cornering_algorithm/`, 2011. Blog post, accessed on August 4, 2025.

[222] L. Bechtloff. Entwicklung einer Prüfmethodik zur Charakterisierung der orientierungsabhängigen Materialeigenschaften von FFF-Strukturen. Bachelor's thesis (in German, instructed by F. Frölich, B. Scheuring, and A. Heuer), Karlsruhe Institute of Technology (KIT), Institute of Vehicle Systems Technology and Institute for Applied Materials, Karlsruhe, 2022.

[223] F. Frölich, L. Bechtloff, B. M. Scheuring, A. L. Heuer, L. Kärger, and W. V. Liebig. Development of a test method for characterization of the orientation dependent material properties of FFF structures. In *Proceedings of the 23rd International Conference on Composite Materials*, Belfast, UK, 2023.

[224] M. Montero, S. Roundy, D. Odell, S. H. Ahn, and P. K. Wright. Material Characterization of Fused Deposition Modeling (FDM) ABS by Designed Experiments. *Society of Manufacturing Engineers*, 10:1–21, 2001.

[225] E. H. Baran and H. Y. Erbil. Surface Modification of 3D Printed PLA Objects by Fused Deposition Modeling: A Review. *Colloids and Interfaces*, 3(2):43, 2019.

[226] A. D. Banjo, V. Agrawal, M. L. Auad, and A. D. N. Celestine. Moisture-induced changes in the mechanical behavior of 3D printed polymers. *Composites Part C: Open Access*, 7:100243, 2022.

[227] L. Englert, A. Heuer, M. K. Engelskirchen, F. Frölich, S. Dietrich, W. V. Liebig, L. Kärger, and V. Schulze. Hybrid material additive manufacturing: interlocking interfaces for fused filament fabrication on laser powder bed fusion substrates. *Virtual and Physical Prototyping*, 17(3):508–527, 2022.

[228] A. Nogales, E. Gutiérrez-Fernández, M. C. García-Gutiérrez, T. A. Ezquerra, E. Rebollar, I. Šics, M. Malfois, S. Gaidukovs, E. Gē Cis, K. Celms, and G. Bakradze. Structure Development in Polymers during Fused Filament Fabrication (FFF): An in Situ Small- And Wide-Angle X-ray Scattering Study Using Synchrotron Radiation. *Macromolecules*, 52(24):9715–9723, 2019.

[229] Y. Shmueli, Y. C. Lin, S. Lee, M. Zhernenkov, R. Tannenbaum, G. Marom, and M. H. Rafailovich. In Situ Time-Resolved X-ray Scattering Study of Isotactic

Polypropylene in Additive Manufacturing. *ACS Applied Materials and Interfaces*, 11(40):37112–37120, 2019.

[230] D. Vaes, M. Coppens, B. Goderis, W. Zoetelief, and P. Van Puyvelde. The extent of interlayer bond strength during fused filament fabrication of nylon copolymers: An interplay between thermal history and crystalline morphology. *Polymers*, 13(16), 2021.

[231] A. Posselt. Erweiterung einer virtuellen Prozesskette für die Materialextrusion zur Untersuchung von prozessinduziertem Verzug und Eigenspannungen unter der Berücksichtigung einzelner Nachbearbeitungsschritte. Bachelor's thesis (in German, instructed by F. Frölich), Karlsruhe Institute of Technology (KIT), Institute of Vehicle Systems Technology, Karlsruhe, 2023.

[232] E. W. Fischer, H. J. Sterzel, and G. Wegner. Investigation of the structure of solution grown crystals of lactide copolymers by means of chemical reactions. *Kolloid-Zeitschrift & Zeitschrift für Polymere*, 251(11):980–990, 1973.

[233] J. M. Svanberg and J. A. Holmberg. Prediction of shape distortions Part I. FE-implementation of a path dependent constitutive model. *Composites Part A: Applied Science and Manufacturing*, 35(6):711–721, 2004.

[234] A. A. Johnston. *An Integrated Model of the Development of Process-Induced Deformation in Autoclave Processing of Composite Structures*. Phd thesis, University of British Columbia, Department of Metals and Materials Engineering, Vancouver, Canada, 1997.

[235] J. K. Bauer and T. Böhlke. On the dependence of orientation averaging mean field homogenization on planar fourth-order fiber orientation tensors. *Mechanics of Materials*, 170:104307, 2022.

[236] C. Krauß, J. K. Bauer, J. Mitsch, T. Böhlke, and L. Kärger. On the Averaging and Closure of Fiber Orientation Tensors in Virtual Process Chains. *Journal of Elasticity*, 156(1):279–306, 2024.

[237] M. E. Di Nardo. Development of a numerical method for the trajectory consideration in a MEX process simulation on macroscale. Master's thesis (instructed by F. Frölich), Karlsruhe Institute of Technology (KIT), Institute of Vehicle Systems Technology, Karlsruhe, 2024.

[238] M. E. Di Nardo, F. Frölich, L. Kärger, and P. Carlone. Modeling time-dependent anisotropy in MEX component-scale process simulation. In *Materials Research Proceedings*, volume 41, pages 603–612, Toulouse, France, 2024. Materials Research Forum LLC.

[239] T. Schultz and G. Kindlmann. A Maximum Enhancing Higher-Order Tensor Glyph. *Computer Graphics Forum*, 29(3):1143–1152, 2010.

[240] A. E. H. Love. A Treatise on the Mathematical Theory of Elasticity. *Nature*, 105(2643):511–512, 1920.

[241] H. D. Baehr and K. Stephan. *Heat and mass transfer*. Springer-Verlag Berlin Heidelberg, Berlin, Heidelberg, 3. edition, 2011.

[242] P. Gkertzos, A. Kotzakolios, G. Mantzouranis, and V. Kostopoulos. Nozzle temperature calibration in 3D printing. *International Journal on Interactive Design and Manufacturing*, 18(2):879–899, 2024.

[243] C.-L. Tang, S. Seeger, and M. Röllig. Improving the comparability of FFF-3D printing emission data by adjustment of the set extruder temperature. *Atmospheric Environment: X*, 18:100217, 2023.

[244] H. Alzyod and P. Ficzere. Thermal Evaluation of Material Extrusion Process Parameters and Their Impact on Warping Deformation. *Jordan Journal of Mechanical and Industrial Engineering*, 17(4):617–624, 2023.

[245] X. Ao, S. Lin, J. Liu, H. Xia, and J. Meng. Modeling and self-supporting printing simulation of fuse filament fabrication. *Scientific Reports*, 14(1):16275, 2024.

[246] ASTM International. ASTM E1269 Standard Test Method for Determining Specific Heat Capacity by Differential Scanning. *ASTM International*, 11(Reapproved):1–6, 2011.

[247] I. Blanco, G. Cicala, G. Recca, and C. Tosto. Specific Heat Capacity and Thermal Conductivity Measurements of PLA-Based 3D-Printed Parts with Milled Carbon Fiber Reinforcement. *Entropy*, 24(5):654, 2022.

[248] V. Cojocaru, D. Frunzaverde, C. O. Miclosina, and G. Marginean. The Influence of the Process Parameters on the Mechanical Properties of PLA Specimens Produced by Fused Filament Fabrication—A Review. *Polymers*, 14(5), 2022.

[249] M. Domingo-Espin, J. M. Puigoriol-Forcada, A.-A. Garcia-Granada, J. Llumà, S. Borros, and G. Reyes. Mechanical property characterization and simulation of fused deposition modeling Polycarbonate parts. *Materials & Design*, 83:670–677, 2015.

[250] A. J. Favaloro, E. Barocio, B. Brenken, R. B. Pipes, E. Barocio, and R. B. Pipes. Simulation of Polymeric Composites Additive Manufacturing using Abaqus. In *Dassault Systèmes' Science in the Age of Experience*, Chicago, IL, May 2017.

[251] F. Frölich, L. Bechtloff, B. M. Scheuring, A. Heuer, L. Kärger, and W. V. Liebig. Development of a test-method for characterization of the orientation dependent material properties of FFF structures. Poster presented at the 23rd International Conference on Composite Materials (ICCM 2023), Belfast, United Kingdom, July 30–August 4, 2023, 2023.

[252] M. Lecoublet, M. Ragoubi, N. Leblanc, and A. Koubaa. Dielectric and viscoelastic properties of 3D-printed biobased materials. *Industrial Crops and Products*, 212:118354, 2024.

[253] G. Liao, Z. Li, C. Luan, Z. Wang, X. Yao, and J. Fu. Additive Manufacturing of Polyamide 66: Effect of Process Parameters on Crystallinity and Mechanical Properties. *Journal of Materials Engineering and Performance*, 31(1):191–200, 2022.

[254] O. Lietaer, S. Bouillon, E. Seignobos, and L. Berger. Multi-scale Material Modeling and Print Simulation for "First Time Right" Additive Manufacturing. In *Proceedings of the SAMPE Conference 2019*, pages 1519–1526, Charlotte, NC, 2019. SAMPE.

[255] A. A. Mishra, A. Momin, M. Strano, and K. Rane. Implementation of viscosity and density models for improved numerical analysis of melt flow dynamics in the nozzle during extrusion-based additive manufacturing. *Progress in Additive Manufacturing*, 7(1):41–54, 2022.

[256] O. A. Mohamed, S. H. Masood, and J. L. Bhowmik. Experimental investigation of the influence of fabrication conditions on dynamic viscoelastic properties of PC-ABS processed parts by FDM process. *IOP Conference Series: Materials Science and Engineering*, 149(1), 2016.

[257] C. O'Mahony, E. Gkartzou, E. U. Haq, S. Koutsoumpis, C. Silien, C. A. Charitidis, and S. A. Tofail. Determination of thermal and thermomechanical properties of biodegradable PLA blends: for additive manufacturing process. *Journal of Thermal Analysis and Calorimetry*, 142(2):715–722, 2020.

[258] British Standards Institute. BS ISO 11359-1:2023 Plastics — Thermomechanical analysis (TMA) — Part 1: General principles. *British Standards Institute*, 2023.

[259] British Standards Institute. BS 11359-2:2021 Part 2: Determination of coefficient of linear thermal expansion and glass transition temperature. *British Standards Institute*, 2021.

[260] F. Talagani, S. Dormohammadi, D. Technologies, C. Godines, and H. Baid. Numerical Simulation of Big Area Additive Manufacturing (3D Printing) of a Full Size Car. *SAMPE Journal*, 51(4):27–36, July 2015.

[261] Z. Wang, C. Luo, Z. Xie, and Z. Fang. Three-dimensional polymer composite flow simulation and associated fiber orientation prediction for large area extrusion deposition additive manufacturing. *Polymer Composites*, 44(10):6720–6735, 2023.

[262] K. P. Weiss, N. Bagrets, C. Lange, W. Goldacker, and J. Wohlgemuth. Thermal and mechanical properties of selected 3D printed thermoplastics in the cryogenic temperature regime. *IOP Conference Series: Materials Science and Engineering*, 102(1), 2015.

[263] Z. Weng, J. Wang, T. Senthil, and L. Wu. Mechanical and thermal properties of ABS/montmorillonite nanocomposites for fused deposition modeling 3D printing. *Materials and Design*, 102:276–283, 2016.

[264] Y. Yu, B. Jiang, Y. Chen, and L. Ye. Modelling and characterising FFF process of semi-crystalline polymers: Warpage formation and mechanism analysis. *Polymers and Polymer Composites*, 32:1–11, 2024.

[265] R. J. Zaldivar, D. B. Witkin, T. McLouth, D. N. Patel, K. Schmitt, and J. P. Nokes. Influence of processing and orientation print effects on the mechanical and thermal behavior of 3D-Printed ULTEM ® 9085 Material. *Additive Manufacturing*, 13:71–80, 2017.

List of Publications

Journal articles

- F. Frölich, L. Bechtloff, B. M. Scheuring, A. L. Heuer, F. Wittemann, L. Kärger, and W. V. Liebig. Evaluation of mechanical properties characterization of additively manufactured components. *Progress in Additive Manufacturing*, 10(2):1217-1229, 2025.
- F. Frölich, L. Hof, C. Zimmerling, F. Wittemann, and L. Kärger. A submodeling approach for efficient prediction of local temperature profiles in component-scale additive manufacturing. *The International Journal of Advanced Manufacturing Technology*, 136(3):1561-1576, 2025.
- F. Frölich, M. E. Di Nardo, C. Krauß, A. Heuer, W. V. Liebig, F. Wittemann, P. Carlone, and L. Kärger. An orientation-based homogenization approach for predicting process-induced deformations in extrusion-based additive manufacturing. *Additive Manufacturing*, 113:105023, 2025.

Conference contributions

With proceedings (peer-reviewed)

- F. Frölich and L. Kärger. Thermal Modeling of Laser Powder Bed Fusion during Printing on Temperature-Unstable Materials Considering Local Sintering.

Key Engineering Materials, 926:331-340, ESAFORM 2022, Braga/Portugal, 2022.

- F. Frölich, D. Dörr, A. Jackstadt, F. Wittemann, and L. Kärger. Mechanical and kinetic characterization of additively manufactured PLA structures for improved process and warpage modeling. *Materials Research Proceedings*, 54:2281-2290, ESAFORM 2025, Salerno/Italy, 2025.

With posters

- F. Frölich, L. Bechtloff, B. M. Scheuring, A. Heuer, L. Kärger, and W. V. Liebig. Development of a test-method for characterization of the orientation dependent material properties of FFF structures. *23rd International Conference on Composite Materials*, KITopen-ID: 1000161267, Belfast/United Kingdom, 2023.

Without proceedings/posters

- F. Frölich, L. Bechtloff, B. M. Scheuring, A. Heuer, L. Kärger, and W. V. Liebig. Challenges in characterization of polylactic acid (PLA) for thermo-mechanical material modeling in material extrusion. *11th European Solid Mechanics Conference*, KITopen-ID: 1000148773, Galway/Irland, 2022.

Software publications

- J. Knirsch, F. Frölich, L. Hof, F. Wittemann, and L. Kärger. pyGCodeDecode: A Python package for time-accurate GCode simulation in material extrusion processes. *Journal of Open Source Software*, 19(99):6465, 2024.

Co-authored journal articles

- L. Englert, A. Heuer, M. K. Engelskirchen, F. Frölich, S. Dietrich, W. V. Liebig, L. Kärger, and V. Schulze. Hybrid material additive manufacturing: interlocking interfaces for fused filament fabrication on laser powder bed fusion substrates. *Virtual and Physical Prototyping*, 17(3):1-20, 2022.

Co-authored conference contributions

With proceedings (peer-reviewed)

- A. Jackstadt, F. Frölich, K. Weidemann, and L. Kärger. Modeling the Mullins effect of rubbers used in constrained-layer damping applications. *Proceedings in Applied Mathematics and Mechanics (PAMM)*, 21(1), GAMM 2021, Kassel/Germany, 2021.

- J. Kesten, F. Frölich, F. Wittemann, J. Knirsch, F. Bechler, L. Kärger, P. Eberhard, F. Henning, and M. Doppelbauer. Design Approach for a Novel Multi Material Variable Flux Synchronous Reluctance Machine without Rare Earth Magnets. *2022 International Conference on Electrical Machines (ICEM)*, 2304-2310, ICEM 2022, Valencia/Spain, 2022.

- A. Schäfer, M. Baranowski, M. Springmann, L. Hof, F. Frölich, A. Peter, N. Parspour, J. Fleischer, P. Middendorf, L. Kärger, and A. Michalowski. Design concept of a repairable YASA axial flux machine with a hybrid cooling system. *IET Conference Proceedings*, 2023(17):119-128, PEMD 2023, Brussels/Belgium, 2023.

- J. Kesten, D. Ambruster, F. Frölich, L. Kärger, C. Bonten, and M. Doppelbauer. Electromechanical optimization of high reluctance torque variable flux machines under structural mechanical constraints. *Electromechanical Drive Systems 2023*, 172:189-194, 9. ETG-Fachtagung "Elektromechanische Antriebssysteme", Vienna/Austria, 2023.

- M. E. Di Nardo, F. Frölich, L. Kärger, and P. Carlone. Modeling time-dependent anisotropy in MEX component-scale process simulation. *Materials Research Proceedings*, 41:603-612, ESAFORM 2024, Toulouse/France, 2024.
- L. Hof, F. Frölich, F. Wittemann, and L. Kärger. Modelling bead deposition in material extrusion using the smoothed particle hydrodynamics framework PySPH. *Materials Research Proceedings*, 5:68-77, ESAFORM 2025, Salerno/Italy, 2025.

With proceedings

- S. Dietrich, C. Dohmen, F. Frölich, A. Jackstadt, F. Wittemann, and L. Kärger. Investigation of the thermoviscoelastic behavior of a closed-cell polymer structural foam under pressure for processing in hybrid LCM processes. *Proceedings of the 21st European Conference on Composite Materials*, 2:548-554, ECCM 2024, Nantes/France, 2024.

With posters

- L. Hof, F. Frölich, F. Wittemann, and L. Kärger. Homogenization of the Anisotropic Thermal Conductivity of Mesostructures in Material Extrusion. *21st European Conference on Composite Materials*, KITopen-ID: 1000172308, Nantes/France, 2024.

Without proceedings/posters

- A. Jackstadt, F. Frölich, W. V. Liebig, L. Kärger, and K. Weidemann. Investigation into the influence of the Mullins effect on the dynamic behavior of hybrid laminates. *11th European Solid Mechanics Conference*, KITopen-ID: 1000148762, Galway/Irland, 2022.